

Université Paris Cité

En cotutelle avec Shanghai Jiao Tong University

Laboratoire Astroparticule et Cosmologie (APC-Paris)

École Doctorale des Sciences de la Terre et de l'Environnement
et Physique de l'Univers de Paris, ED 560

Constraints on the Higgs Self-coupling at the LHC with $\sqrt{s} = 13$ TeV and Long-lived Particles Searches with a Future Lepton Collider

Par YULEI ZHANG

Thèse de doctorat en PHYSIQUES DE L'UNIVERS

Dirigée par GREGORIO BERNARDI

Et par LIANG LI

Présentée et soutenue publiquement le 18 Décembre 2023

Devant un jury composé de:

MME.	SUZANNE SHOTKIN-GASCON	PROFESSEUR	UNIVERSITÉ CLAUDE BERNARD, LYON	RAPPORTEUR
M.	YAQUAN FANG	PROFESSEUR	IHEP, UNIVERSITY OF BEIJING	RAPPORTEUR
MME.	VALENTINA CAIRO	STAFF CERN	CERN	EXAMINATEUR
M.	MATTEO CACCIARI	PROFESSEUR	UNIVERSITÉ PARIS CITÉ	EXAMINATEUR
M.	KUN LIU	ASS. PROFESSEUR	TD LEE INSTITUTE, SHANGHAI	EXAMINATEUR
M.	HAIJUN YANG	PROFESSEUR	SJTU UNIVERSITY OF SHANGHAI	EXAMINATEUR
M.	GREGORIO BERNARDI	DR	APC-PARIS	DIRECTEUR
M.	LIANG LI	PROFESSEUR	SHANGHAI JIAO TONG UNIVERSITY	DIRECTEUR

Résumé

Titre: Contraintes sur l'auto-couplage du boson de Higgs au LHC avec $\sqrt{s} = 13$ TeV et recherches de particules à longue durée de vie avec un futur collisionneur de leptons

Résumé: Le Modèle Standard (MS) de la physique des particules fournit un cadre complet qui a été vérifié expérimentalement à un degré impressionnant, avec le boson de Higgs comme élément central. Les investigations sur les interactions di-Higgs offrent des aperçus essentiels sur le comportement d'auto-couplage du boson de Higgs et pourraient potentiellement élucider les mécanismes sous-jacents à la brisure de la symétrie électrofaible. De plus, le boson de Higgs agit comme une voie prospective pour explorer une multitude de théories au-delà du Modèle Standard, avec les Particules à Longue Durée de Vie (LLP) représentant juste un des plusieurs modèles intrigants encore à explorer pleinement.

Dans la première analyse de la thèse, l'attention est centrée sur la production de paires de bosons de Higgs du MS (HH) se désintégrant en états finals multileptons, en particulier à 3 leptons. En utilisant 140 fb^{-1} de données de collisions proton-proton à $\sqrt{s} = 13$ TeV provenant du détecteur ATLAS lors du Run 2, l'étude explore principalement la production de HH par fusion de gluons (ggF), avec une contribution additionnelle par fusion de bosons vectoriels (VBF). Essentiel à ce travail est l'atténuation du bruit de fond principal WZ , abordée par repondération pour prendre en compte la mauvaise modélisation à de grandes multiplicités de jets, et le bruit de fond de faux leptons, estimé via la méthode "Template Fit". Un arbre de décision boosté par gradient est utilisé pour une discrimination optimale signal-bruit, affinée en outre par une technique d'entraînement triple et un réglage exhaustif des hyperparamètres. De façon remarquable, ce canal à 3 leptons atteint une limite supérieure de 28.1 la section efficace HH par rapport au MS, constituant une amélioration de 9,4 fois par rapport aux analyses précédentes. Lors de la prise en compte de tous les canaux multileptons, la limite supérieure attendue est de $9.74^{+13.91}_{-7.02}$, faisant du résultat du canal à 3 leptons l'une des meilleures limites parmi les canaux de désintégration purement leptoniques.

Le deuxième aspect clé de cette thèse concerne l'analyse $HH \rightarrow b\bar{b}\tau^+\tau^-$, s'appuyant sur 140 fb^{-1} de données complètes de Run 2 d'ATLAS. Ce travail se distingue par le raffinement ciblé des approches méthodologiques, en particulier en ce qui concerne les modificateurs de couplage κ_λ et κ_{2V} . En utilisant des techniques avancées d'analyse multivariée (MVA), l'analyse est optimisée séparément pour les modes de production par fusion de gluons et par Fusion de Bosons Vectoriels. En particulier, la catégorisation des événements est basée sur la masse invariante (m_{HH}) de la paire de Higgs dans la région ggF, avec une catégorie VBF supplémentaire introduite pour améliorer la sensibilité à κ_{2V} . L'utilisation des sorties MVA comme ultimes discriminants a engendré des améliorations significatives par rapport aux données précédentes: une amélioration en sensibilité de 17% sur μ_{HH} , et des améliorations de 11.9% et 19.8% dans les intervalles de confiance à 95% pour κ_λ et κ_{2V} , respectivement.

L'analyse combinée $HH+H$ conclut les investigations di-Higgs de la thèse. Cette synthèse incorpore les principaux canaux di-Higgs ($b\bar{b}b\bar{b}$, $b\bar{b}\gamma\gamma$, et $b\bar{b}\tau^+\tau^-$) avec les observables de Higgs simples pour imposer des contraintes strictes sur les modificateurs de couplage clés, spécifiquement κ_λ et κ_{2V} . Dans un ajustement complet, où κ_t , κ_b , κ_τ , et κ_V sont autorisés à varier librement, l'analyse atteint un intervalle de confiance à 95% de $-1.4 < \kappa_\lambda < 6.1$, qui se rapproche étroitement de la plage attendue de $-2.2 < \kappa_\lambda < 7.7$. La stabilité de ces résultats est corroborée par une sensibilité minimale aux fluctuations de κ_{2V} , affectant les contraintes observées sur κ_λ de moins de 5%. Cela confirme la concordance de tous les modificateurs de couplage analysés avec le MS, dans les limites des incertitudes associées.

Dans la dernière partie de la thèse, l'enquête se tourne vers l'examen des modes de désintégration du boson de Higgs dans le domaine de la physique BSM, ciblant spécifiquement les LLP. À cette fin, des algorithmes d'apprentissage automatique de pointe, tels que les réseaux neuronaux convolutionnels (CNN) et les réseaux neuronaux en graphes (GNN), sont déployés pour une analyse directe sur la sortie brute du détecteur, ce qui améliore considérablement l'efficacité de sélection du signal attendu. Par exemple, dans le cas d'une LLP de 50 GeV avec une durée de vie de 1 ns, l'efficacité du signal attendu atteint 99%. Cette recherche atteint une limite supérieure attendue de 4×10^{-6} pour le rapport de branchement du Higgs se désintégrant en LLP sous l'hypothèse de 10^6 de Higgs, ce qui dépasse significativement la limite supérieure de 1×10^{-3} actuellement établie par ATLAS et CMS. Pour les LLP avec des durées de vie supérieures à 1 ns, l'analyse produit une limite supérieure attendue qui est un ordre de grandeur meilleur que les résultats attendus du Collisionneur Linéaire International.

Enfin, la section d'annexe de la thèse décrit une étude préliminaire sur les recherches de photons sombres via une expérience cible fixe proposée avec des électrons de 8 GeV reculant à partir d'une cible métallique à grand-Z.

Mots clefs: Physique des Hautes Énergies, Collisionneur, di-Higgs, multilepton, $b\bar{b}\tau^+\tau^-$, Particules à Longue Durée de Vie, Apprentissage automatique, techniques avancées, Intelligence Artificielle

Résumé étendu

Qu'est ce qui constitue le tissu même de l'univers ? Comment ses plus petits constituants interagissent-ils pour former le monde tel que nous le comprenons ? Ces questions fondamentales sont centrales dans le domaine de la physique des particules, qui étudie les particules élémentaires constituant la matière. Les collisionneurs à haute énergie, machines qui accélèrent les particules à une vitesse proche de celle de la lumière et les font se percuter, offrent des opportunités uniques pour aborder ces questions en permettant aux scientifiques d'étudier les interactions de particules dans des conditions imitant l'univers primordial.

Le Modèle Standard de la physique des particules, une théorie bien établie développée au cours du dernier demi-siècle, explique avec succès ces interactions. Il fournit un cadre pour comprendre comment les particules connues, comme les quarks et les électrons, interagissent à travers des forces fondamentales - à savoir, les forces électromagnétique, faible et forte. La découverte du boson de Higgs en 2012 au Grand Collisionneur de Hadrons (LHC) du CERN, un anneau de 27 kilomètres sous la frontière France-Suisse, a fourni la pierre angulaire de ce modèle. Le boson de Higgs explique pourquoi certaines particules ont une masse, affirmant le succès monumental du Modèle Standard.

Malgré ces succès, il y a des phénomènes qui ne peuvent pas être expliqués par le Modèle Standard, tels que la matière noire, une substance mystérieuse qui constitue environ 27% de l'univers mais n'émet, n'absorbe ni ne reflète aucun rayonnement électromagnétique. Ces lacunes dans la compréhension appellent à l'exploration au-delà de la physique du Modèle Standard (BSM). Une voie intéressante est l'étude des particules à longue durée de vie (LLPs), qui sont des particules hypothétiques qui ne se désintègrent pas aussi rapidement que les autres et pourraient interagir faiblement avec la matière normale.

En réponse aux défis et opportunités posés par ces questions, les scientifiques ont déployé le Grand Collisionneur de Hadrons et planifient de futures machines connues sous le nom de collisionneurs de leptons. Cela inclut des projets tels que le Collisionneur Linéaire International (ILC), le Collisionneur Électron-Positron Circulaire (CEPC) et le Futur Collisionneur Circulaire (FCC-ee). Ces collisionneurs visent à fournir des mesures plus précises du boson de Higgs et à explorer de nouvelles physiques potentielles.

La découverte du boson de Higgs marque un jalon monumental en physique des particules, servant à la fois de confirmation du Modèle Standard et de porte d'entrée vers de nouvelles explorations. Ma recherche contribue à la prochaine phase cruciale de ce domaine en se concentrant sur la recherche di-Higgs, où deux bosons de Higgs sont produits simultanément. C'est un domaine d'étude pivot pour comprendre des aspects uniques du Higgs, en particulier son auto-couplage, qui régit la manière dont le boson de Higgs interagit avec lui-même. Mes analyses se concentrent particulièrement sur les événements avec des états finaux multileptons et $b\bar{b}\tau^+\tau^-$.

De plus, pour fournir une compréhension plus complète du secteur du Higgs, mon travail intègre une combinaison d'événements de production de Higgs simples et doubles. Cette approche intégrée vise à contraindre l'auto-couplage du boson de Higgs avec une précision accrue, offrant ainsi des aperçus critiques sur la physique du Modèle Standard et au-delà.

Au-delà du champ d'analyse di-Higgs et simple-Higgs, ma recherche s'étend aux phénomènes BSM, en se concentrant particulièrement sur les LLPs. Utilisant des techniques d'apprentissage automatique qui interprètent directement les données brutes du détecteur, j'ai développé une méthodologie novatrice pour distinguer ces particules hypothétiques des particules du Modèle Standard dans des simulations.

Enfin, alors que le corps principal de cette thèse se concentre sur des expériences basées sur des collisionneurs, mes intérêts s'étendent à d'autres formes de recherche en physique des particules. En particulier, j'ai travaillé sur une expérience visant à détecter des photons sombres, particules proposées comme vecteurs de force pour la matière noire, en utilisant une expérience à cible fixe qui utilise des faisceaux d'électrons à haute énergie.

En résumé, cette thèse offre un récit cohérent de mon parcours de recherche en doctorat. Elle couvre de l'investigation de questions fondamentales en physique des particules à des contributions significatives tant dans les études de bosons de Higgs basées sur des collisionneurs que dans les recherches de particules à longue durée de vie BSM, tout en s'aventurant également dans des expériences au-delà des collisionneurs. Chacune de ces entreprises de recherche ajoute une pièce au puzzle complexe de la compréhension de l'univers à son niveau le plus basique. Cette thèse est organisée comme suit :

- **Chapitre 2** : Fournit un aperçu de la physique du Higgs dans le Modèle Standard et au-delà.
- **Chapitre 3** : Discute du Grand Collisionneur de Hadrons et de l'expérience ATLAS.
- **Chapitre 4** : Se concentre sur les techniques de simulation et de reconstruction d'événements dans ATLAS.
- **Chapitre 5** : Présente les recherches di-Higgs SM dans les états finals multileptons.
- **Chapitre 6** : Couvre les recherches di-Higgs SM dans les états finals $b\bar{b}\tau^+\tau^-$.
- **Chapitre 7** : Vise à contraindre l'auto-couplage du boson de Higgs en utilisant des données de production de Higgs simples et doubles.
- **Chapitre 8** : Discute des stratégies de recherche pour les particules à longue durée de vie avec les futurs collisionneurs de leptons.
- **Chapitre 9** : Résume les découvertes et discute des perspectives futures.
- **Annexe** : Décrit une expérience à cible fixe pour sonder le photon sombre en utilisant un faisceau d'électrons de 8 GeV.

Recherche de la production di-Higgs avec des états finals multileptons

Dans cette étude, nous examinons la production de paires de bosons de Higgs (HH) via la fusion de gluons, en utilisant les données du détecteur ATLAS basées sur des collisions proton-proton à une énergie au centre de masse de $\sqrt{s} = 13$ TeV. L'ensemble de données englobe une luminosité totale de 140 fb^{-1} , collectée pendant la seconde phase du Grand Collisionneur de Hadrons. En accord avec les analyses existantes des collaborations ATLAS et CMS, cette recherche mène une recherche exhaustive à travers de multiples canaux de désintégration, incluant $VVVV$, $VV\tau\tau$, $\tau\tau\tau\tau$, $\gamma\gamma VV$, et $\gamma\gamma\tau\tau$, où V représente les bosons W^\pm ou Z . Spécifiquement, l'étude se concentre sur les désintégrations HH en $b\bar{b}ZZ$, avec les bosons Z se désintégrant en leptons. Étant donné la variété des états finals dans les analyses multileptons, cette thèse restreint son champ d'application au canal à 3 leptons, un choix motivé par la phénoménologie complexe et l'intracacité du canal.

Concluant cette étude, l'analyse du canal à 3 leptons basée sur 140 fb^{-1} de données de collision proton-proton à $\sqrt{s} = 13$ TeV collectées par le détecteur ATLAS est présentée. L'accent a été mis sur la production de paires de Higgs SM (HH), principalement à travers la fusion de gluons (ggF) avec la fusion de bosons vectoriels (VBF) comme rendement supplémentaire. Le bruit de fond principal, WZ , a été ajusté pour tenir compte d'une modélisation incorrecte dans les multiplicités de jets élevées à l'aide d'une fonction d'ajustement. Le bruit de fond secondaire, résultant de faux leptons, a été estimé par la méthode d'Ajustement de Modèle, avec des facteurs de normalisation dérivés de multiples régions de contrôle. Une méthode d'Arbres de Décision à Gradient Boosté, améliorée par une stratégie d'entraînement en trois étapes et un réglage détaillé des hyperparamètres, a été employée pour la discrimination signal-bruit. L'étude a atteint une signification

maximale du signal de 0.073 dans le canal à 3 leptons, avec une limite supérieure de la section efficace $HH \rightarrow 3\ell$ de $23.13^{+10.21}_{-6.66}$ par rapport au SM, s'améliorant à $28.09^{+12.81}_{-7.86}$ en incluant toutes les incertitudes. Ceci représente une avancée significative par rapport aux analyses précédentes. Dans les résultats multileptons combinés, la limite supérieure attendue est de $8.93^{+12.69}_{-6.44}$ statistiquement, et $9.74^{+13.91}_{-7.02}$ avec toutes les incertitudes systématiques incluses. Le canal à 3 leptons émerge comme l'un des plus robustes dans les canaux purement leptoniques, rivalisant étroitement avec le canal leader $\gamma\gamma + 1\ell$.

Recherche de la production di-Higgs avec des états finals $b\bar{b}\tau^+\tau^-$

Dans l'exploration de la production SM de paires de bosons de Higgs (HH), cette étude met l'accent sur le canal de désintégration $b\bar{b}\tau^+\tau^-$, notable pour sa signature unique et son utilité analytique. Malgré une fraction de branchement plus faible de 7,3% par rapport aux canaux $b\bar{b}b\bar{b}$ et $b\bar{b}WW$, le canal $b\bar{b}\tau^+\tau^-$ offre une signature expérimentale plus claire, essentielle pour une détection et une analyse précises. La désintégration des leptons τ en électrons ou en muons (τ_{lep}) ou en hadrons chargés et neutres (τ_{had}) conduit à la considération de deux sous-canaux spécifiques : $b\bar{b}\tau_{\text{lep}}\tau_{\text{had}}$ et $b\bar{b}\tau_{\text{had}}\tau_{\text{had}}$, les événements $b\bar{b}\tau_{\text{lep}}\tau_{\text{lep}}$ étant analysés dans un canal distinct $b\bar{b}\ell\ell$.

Cette analyse complète s'appuie sur des études précédentes, qui se concentraient principalement sur le mode de production SM par fusion de gluons (ggF). L'analyse précédente avait fixé une limite supérieure à la section efficace HH à 130 (110) fb à 95% CL, correspondant à 4,7 (3,9) fois la prédiction du SM. Cette étude, avec ses raffinements méthodologiques et catégorisations supplémentaires, vise à avancer ces résultats, en particulier concernant les modificateurs κ_λ et κ_{2V} . Les améliorations significatives de cette analyse incluent :

- Une réoptimisation de κ_λ en mettant en œuvre une catégorisation d'événements basée sur la masse invariante du système HH (m_{HH}) dans la région ggF, permettant des mesures et des contraintes plus précises sur ce paramètre.
- L'introduction d'une catégorie dédiée à la fusion de bosons vectoriels (VBF) améliore la sensibilité de l'étude au paramètre κ_{2V} , élargissant la portée de l'analyse.
- L'adoption de techniques avancées d'Analyse Multivariée (MVA) pour maximiser la discrimination signal-bruit. Cette approche a été cruciale pour affiner l'analyse, avec les sorties MVA servant de discriminants finaux dans l'ajustement.

Les résultats de cette analyse démontrent une amélioration marquée par rapport aux études précédentes. Une amélioration de 17% sur la sensibilité de μ_{HH} a été atteinte, indiquant une mesure plus robuste et précise du taux de production de paires de bosons de Higgs. De plus, les intervalles de confiance pour κ_λ et κ_{2V} ont été resserrés, avec une amélioration de 11,9% de l'intervalle de confiance à 95% pour κ_λ et une amélioration encore plus notable de 19,8% pour κ_{2V} . Ces avancées soulignent l'efficacité des améliorations méthodologiques et des catégorisations supplémentaires introduites dans cette étude. L'analyse raffinée fournit non seulement des contraintes plus strictes sur les paramètres clés mais aussi une compréhension plus complète des processus de production et de désintégration HH , en particulier dans le canal $b\bar{b}\tau^+\tau^-$.

Contraintes sur l'auto-couplage du Higgs avec la production de Higgs simple et double

Suite à la découverte du boson de Higgs par les collaborations ATLAS et CMS, le Grand Collisionneur de Hadrons (LHC) a joué un rôle déterminant dans la mesure méticuleuse des propriétés

du boson de Higgs. Cette entreprise vise à corroborer les prédictions du Modèle Standard (SM) ou à révéler de nouveaux phénomènes physiques. Dans le cadre du SM, le boson de Higgs est central dans la brisure de la symétrie électrofaible, donnant de la masse aux particules élémentaires et assurant l'unitarité perturbative. L'auto-couplage trilineaire du boson de Higgs, λ_{HHH} , lié à la masse du Higgs m_H et à la constante de Fermi G_F , est un point central de cette étude.

Cette analyse consolide les données des trois canaux de désintégration double-Higgs les plus sensibles : $b\bar{b}\gamma\gamma$, $b\bar{b}\tau^+\tau^-$, et $b\bar{b}b\bar{b}$, en utilisant les données d'ATLAS collectées entre 2015 et 2018. Ces données, correspondant à une luminosité intégrée de 126–139 fb⁻¹ à $\sqrt{s} = 13$ TeV, sont employées pour évaluer le modificateur de couplage κ_λ , défini comme $\kappa_\lambda = \lambda_{HHH}/\lambda_{HHH}^{\text{SM}}$. De plus, l'étude incorpore les résultats de la production de Higgs simple, en considérant d'importantes corrections électrofaibles d'ordre suivant (NLO), pour obtenir des contraintes plus complètes sur κ_λ .

Des études précédentes d'ATLAS, utilisant des données partielles de Run 2, ont établi une limite supérieure sur la production de HH SM, et la collaboration CMS a rapporté des résultats similaires. Cependant, cette étude fait progresser ces efforts en intégrant les principales analyses de double-Higgs avec les résultats de Higgs simple, améliorant la précision sur κ_λ et κ_{2V} . En employant un ajustement qui permet la variation de multiples modificateurs de couplage, y compris κ_t , κ_b , κ_τ , et κ_V , l'analyse présente un intervalle de confiance à 95% pour κ_λ de $-1.4 < \kappa_\lambda < 6.1$, un résultat qui reflète étroitement les limites attendues de $-2.2 < \kappa_\lambda < 7.7$. Notamment, l'impact des variations de κ_{2V} sur les limites de κ_λ est minimal, moins de 5%, renforçant la force et la fiabilité de ces contraintes. Ce résultat est significatif car il confirme la cohérence de tous les autres modificateurs de couplage avec les prédictions du SM dans leurs incertitudes respectives, consolidant ainsi la compréhension fondamentale du boson de Higgs dans le contexte du Modèle Standard.

Recherche de particules à longue durée de vie avec les futurs collisionneurs de leptons

La physique des particules est apparue comme une discipline distincte avec la découverte du muon en 1936 et du kaon en 1947, leurs durées de vie macroscopiques étant détectables avec la technologie de la chambre à nuages du début du 20e siècle. La progression vers des technologies modernes telles que les traceurs en silicium et les chambres de projection temporelle n'a pas diminué l'importance de la mesure des longueurs de désintégration en physique des particules. Malgré le changement d'orientation vers des énergies et des luminosités plus élevées avec l'avènement de grands accélérateurs de particules, la mesure des durées de vie des particules reste un aspect fondamental du domaine. Ceci est particulièrement évident dans la recherche de particules exotiques à longue durée de vie (LLPs) dans des installations telles que LEP et Tevatron, où les LLPs sont considérées cruciales pour des découvertes potentielles au-delà du Modèle Standard (SM), en particulier dans le domaine de la supersymétrie. Les approches théoriques se sont élargies pour englober une plus large gamme de signatures LLP, soutenues par des avancées dans les algorithmes de déclenchement et de reconstruction et une compréhension plus approfondie du bruit de fond dans les recherches de LLP.

Le lien entre les LLPs et le boson de Higgs est particulièrement intéressant. Le mécanisme de Higgs, central à la brisure de symétrie électrofaible et à l'acquisition de masse pour les bosons W et Z , peut également être une porte d'entrée vers de nouveaux secteurs en physique des particules. La nature scalaire et la structure de couplage du boson de Higgs en font un candidat probable pour se désintégrer en états exotiques, produisant potentiellement des LLPs détectables. Ces LLPs induits par le Higgs offrent une perspective unique pour sonder à la fois les propriétés structurelles du secteur Higgs et les nouvelles frontières de la physique. Des paramètres clés tels que le taux de production, la longueur de désintégration et la dilatation du temps sont cruciaux pour évaluer

la détectabilité et l'interprétation de tels événements de désintégration exotiques. S'appuyant sur cette prémisse, l'étude actuelle se penche sur les désintégrations du Higgs en LLPs, en employant un cadre analytique de pointe adapté aux futurs Collisionneurs de Leptons. Tirant parti des réseaux de neurones convolutifs (CNNs) et des réseaux de neurones graphiques (GNNs) appliqués directement aux données brutes du détecteur, cette approche a non seulement rationalisé l'analyse mais a également obtenu des résultats remarquables. L'étude rapporte une limite supérieure attendue d'environ 4×10^{-6} pour les LLPs, une amélioration significative par rapport aux limites de 1×10^{-3} établies par des collisionneurs hadroniques comme ATLAS et CMS. De plus, cette méthode dépasse les capacités des collisionneurs de leptons, telles que démontrées par les expériences auprès du Collisionneur Linéaire International (ILC), d'environ un ordre de grandeur dans les limites d'exclusion attendues pour les LLPs avec des durées de vie supérieures à 1 ns.

Contribution de l'auteur

Dans l'étude diHiggs vers multileptons, mes rôles clés comprenaient la direction de la stratégie d'analyse à 3 leptons, agissant en tant qu'éditeur de la note interne, et représentant notre groupe lors des réunions du comité éditorial et des discussions d'approbation de demande de dévoilement.

Pour l'analyse $HH \rightarrow b\bar{b}\tau^+\tau^-$, je me suis concentré sur l'application et l'optimisation des Arbres de Décision Boostés (BDTs) pour la séparation des régions ggF et VBF, et pour la différenciation signal-bruit. Cela impliquait une étude détaillée et un réglage fin des hyperparamètres et des variables d'entrée des BDT, ayant un impact significatif sur les résultats finaux.

Dans le travail de combinaison HH+H, j'ai joué un rôle crucial dans la consolidation des espaces de travail double-Higgs pour l'intégration dans l'analyse du Higgs simple.

Quant à l'étude des Particules à Longue Durée de Vie (LLPs) avec les futurs collisionneurs de leptons, j'ai servi en tant que premier auteur, dirigeant la recherche et rédigeant l'étude.



上海交通大学博士学位论文

在 13 TeV 对撞能量下利用大型强子对撞机对
希格斯粒子自耦合作用的约束研究以及在未
来轻子对撞机上寻找长寿命粒子

姓 名：张 宇 雷

学 号：019072210002

导 师：李亮教授, Gregorio Bernardi 教授

院 系：物理与天文学院

学 科/专 业：粒子物理

申 请 学 位：理学博士

2023 年 12 月 18 日

A Dissertation Submitted to
Shanghai Jiao Tong University for Doctoral Degree

**CONSTRAINTS ON THE HIGGS SELF-COUPLING
AT THE LHC WITH $\sqrt{s} = 13$ TEV AND LONG-LIVED
PARTICLES SEARCHES WITH A FUTURE LEPTON
COLLIDER**

Author: Yulei Zhang

Supervisor: Prof. Liang Li, Prof. Gregorio Bernardi

School of Physics and Astronomy

Shanghai Jiao Tong University

Shanghai, P.R. China

December 18th, 2023

上海交通大学
学位论文原创性声明

本人郑重声明：所呈交的学位论文，是本人在导师的指导下，独立进行研究工作所取得的成果。除文中已经注明引用的内容外，本论文不包含任何其他个人或集体已经发表或撰写过的作品成果。对本文的研究做出重要贡献的个人和集体，均已在文中以明确方式标明。本人完全知晓本声明的法律后果由本人承担。

学位论文作者签名：Yukei Kong

日期：2023 年 12 月 18 日

上海交通大学
学位论文使用授权书

本人同意学校保留并向国家有关部门或机构送交论文的复印件和电子版，允许论文被查阅和借阅。

本学位论文属于：

☒ 公开论文

☐ 内部论文，保密 ☐ 1 年 / ☐ 2 年 / ☐ 3 年，过保密期后适用本授权书。

☐ 秘密论文，保密 ____ 年（不超过 10 年），过保密期后适用本授权书。

☐ 机密论文，保密 ____ 年（不超过 20 年），过保密期后适用本授权书。

（请在以上方框内选择打“√”）

学位论文作者签名：Yukei Kong

指导教师签名：李亮

日期：2023 年 12 月 18 日

日期：2023 年 12 月 18 日

摘 要

粒子物理中的标准模型提供了一个在实验上已经获得广泛证实的理论框架。在该框架内,希格斯粒子起到了至关重要的作用,成为了研究标准模型以及寻找该模型以外新物理现象的关键。对双希格斯产生过程的研究不仅有助于我们深入了解希格斯粒子的自耦合性质,还有望揭示电弱对称破缺现象背后更深刻的物理机制,科学意义重大。此外,长寿命粒子作为一种新物理的候选粒子,它们可以由希格斯粒子发生稀有衰变而产生。一旦在实验上找到长寿命粒子,它们将为超出标准模型的新物理提供旗帜鲜明的信号,因此长寿命粒子的寻找一直是高能物理领域的重要研究课题之一。

本论文的首个分析研究了标准模型下希格斯粒子对 (HH) 衰变到多轻子末态反应道,尤其三轻子末态的衰变道。该分析使用了 ATLAS 探测器在 2015-2018 年第二阶段取数期间的 140 fb^{-1} 的全部质子-质子碰撞数据,主要涵盖了由胶子-胶子融合引发的希格斯粒子对产生,同时还考虑了矢量玻色子融合作为附加的信号贡献。三轻子末态的主要背景过程为 WZ , 其在多强子喷注区域的动力学模拟存在一定的偏差,因此该研究采用了拟合函数并通过真实数据对其进行修正。次要的背景过程为假轻子背景,通过模版拟合使用了数据驱动方法进行估算。三轻子末态使用梯度提升决策树作为研究方法区分 HH 信号和主要本底,得到了信号和背景的鉴别函数,极大提升了信噪比 (S/B)。三轻子末态在 95% 置信度下预期截面上限为 $28.09^{+12.81}_{-7.86}$ 倍标准模型 HH 的产生截面,比 2019 年发表的结果好了 9.4 倍。在考虑到所有多轻子末态后,预计的截面上限为 $9.74^{+13.91}_{-7.02}$ 倍标准模型产生截面。三轻子末态反应道在多轻子末态中是测量结果最为灵敏的通道之一。

论文的第二部分侧重于分析 $HH \rightarrow b\bar{b}\tau^+\tau^-$ 的衰变过程,该分析采用了 ATLAS 探测器在 2015-2018 年第二阶段取数期间收集的 140 fb^{-1} 全部质子-质子碰撞数据。相较于 2022 年的 $b\bar{b}\tau^+\tau^-$ 分析,该分析针对耦合强度因子 κ_λ 和 κ_{2V} 等相关参数进行了特别的优化。通过应用多变量分析的方法,对胶子-胶子融合和矢量玻色子融合这两种主要的希格斯粒子对产生的途径进行了定向优化。希格斯粒子对在胶子-胶子融合模式下的不变质量 (m_{HH}) 作为判别变量对事件进行了分类,同时为了提高对 κ_{2V} 的灵敏度,额外引入了一个矢量玻色子融合的分类。通过使用多变量分析的输出作为判别因子,相较于 2022 年的分析结果,信号强度 (μ_{HH}) 提高了 17%。同时, κ_λ 和 κ_{2V} 在 95% 置信区间内的灵敏度分别提升了 11.9% 和 19.8%。

作为一项关于标准模型双希格斯的综合研究，本论文的第三部份焦点在希格斯粒子的对产生与单希格斯粒子产生的联合分析上。这一综合研究整合了主要的双希格斯衰变末态，包括 $b\bar{b}b\bar{b}$ ， $b\bar{b}\gamma\gamma$ 和 $b\bar{b}\tau^+\tau^-$ ，以及所有的单希格斯粒子产生道。其主要目的是对希格斯耦合强度因子，尤其是 κ_λ 和 κ_{2V} ，施加严格的约束。该研究采用了多种情况下的拟合，允许各个耦合强度因子在不同假设下变化。在对 κ_t ， κ_b ， κ_τ 和 κ_V 不施加任何假设的情况下， κ_λ 观测到的 95% 置信区间为 $-1.4 < \kappa_\lambda < 6.1$ ，与预期的范围 $-2.2 < \kappa_\lambda < 7.7$ 非常接近。同时，在只允许 κ_{2V} 自由变化和假设为标准模型的情况对比中， κ_λ 的观察拟合结果的波动不超过 5%。目前观察到的所有耦合强度因子都在误差范围内与标准模型一致。

在超标准模型中，希格斯粒子的稀有衰变产物中包含长寿命粒子。论文的较后部分针对此类长寿命粒子进行了寻找。该研究采用了先进的机器学习技术，包括卷积神经网络和图神经网络，直接利用了探测器的原始信息展开了分析研究，在最大限度排除背景事例的前提下，和传统方法相比大大提高了信号的预期选择效率，例如在长寿命粒子质量 50 GeV 和寿命 1 纳秒的情况下，信号预期效率达到了 99%。该研究在 10^6 希格斯粒子的统计量下对 $H \rightarrow \text{LLPs}$ 的衰变分支比给出了最低 4×10^{-6} 的预期排除上限，这显著优于 ATLAS 和 CMS 目前设定的 1×10^{-3} 的上限。在粒子寿命大于 1 纳秒的情形下，该分析给出的预期排除上限比国际直线对撞机的相关研究结果好了一个数量级。

最后，本论文的附录部分描述了一项利用固定靶实验寻找暗光子的预先研究。该实验利用 8 GeV 的高能电子轰击重金属靶并寻找在电子散射过程中可能产生的暗光子。

关键词：高能物理，对撞机，双希格斯粒子，多轻子末态， $b\bar{b}\tau^+\tau^-$ ，长寿命粒子，机器学习

ABSTRACT

The Standard Model (SM) of particle physics provides a comprehensive framework that has been experimentally verified to an impressive degree, with the Higgs boson as a pivotal element. Investigations into di-Higgs interactions offer vital insights into the self-coupling behavior of the Higgs boson and potentially elucidate the mechanisms underlying electroweak symmetry breaking. Moreover, the Higgs boson acts as a prospective avenue for exploring a multitude of theories beyond the Standard Model, with Long-Lived Particles (LLPs) representing just one of several intriguing models yet to be fully explored.

In the dissertation's first analysis, attention is centered on the production of SM Higgs boson pairs (HH) decaying to multilepton final states, especially 3-lepton. Utilizing 140 fb^{-1} of proton-proton collision data at $\sqrt{s} = 13 \text{ TeV}$ from the ATLAS detector's Run 2, the study predominantly explores HH production via gluon-gluon fusion, with Vector Boson Fusion contributing additional signal yield. Critical to this work is the mitigation of the primary WZ background, addressed through reweighting to account for mismodeling at high jet multiplicities, and the secondary fake-lepton background, estimated via the Template Fit method. A Gradient Boosted Decision Tree is employed for optimal signal-background discrimination, further refined through a 3-fold training technique and exhaustive hyperparameter tuning. Remarkably, this 3-lepton channel achieves an upper limit of $28.09^{+12.81}_{-7.86}$ on the HH cross-section over SM, constituting a 9.4-fold enhancement over previous analyses. When considering all multilepton channels, the expected upper limit stands at $9.74^{+13.91}_{-7.02}$, making the 3-lepton channel result as one of the best limits among pure leptonic decay channels.

The second key facet of this dissertation revolves around the $HH \rightarrow b\bar{b}\tau^+\tau^-$ analysis, building on 140 fb^{-1} of Full Run 2 ATLAS data. This work distinguishes itself by the targeted refinement of methodological approaches, particularly concerning the κ_λ and κ_{2V} coupling modifiers. Employing advanced Multivariate Analysis (MVA) techniques, the analysis optimizes for both gluon-gluon fusion and Vector Boson Fusion production modes. Specifically, event categorization is influenced by the invariant mass (m_{HH}) of the Higgs pair in the ggF region, with an additional VBF category introduced to enhance sensitivity to κ_{2V} . Utilizing MVA outputs as the ultimate discriminants has engendered significant improvements over legacy data: a 17% boost in the systematic-adjusted baseline for μ_{HH} , and 11.9% and 19.8%

enhancements in the 95% confidence intervals for κ_λ and κ_{2V} , respectively.

The HH+H combination analysis concludes the dissertation's SM di-Higgs investigations. This synthesis incorporates the primary di-Higgs channels ($b\bar{b}b\bar{b}$, $b\bar{b}\gamma\gamma$, and $b\bar{b}\tau^+\tau^-$) with single-Higgs observables to impose stringent constraints on key coupling modifiers, specifically κ_λ and κ_{2V} . In a comprehensive fit, where κ_t , κ_b , κ_τ , and κ_V are allowed to vary freely, the analysis attains a 95% confidence interval of $-1.4 < \kappa_\lambda < 6.1$, which closely approximates the expected range of $-2.2 < \kappa_\lambda < 7.7$. The stability of these results is corroborated by a minimal sensitivity to κ_{2V} fluctuations, affecting the observed κ_λ constraints by less than 5%. This substantiates the concordance of all analyzed coupling modifiers with the SM, within the limits of the associated uncertainties.

In the later part of the dissertation, the investigation transitions to scrutinizing decay modes of the Higgs boson in the realm of BSM physics, specifically targeting LLPs. To this end, state-of-the-art machine learning algorithms, such as Convolutional Neural Networks (CNNs) and Graph Neural Networks (GNNs), are deployed for direct analysis on raw detector output, which significantly enhances the expected signal selection efficiency. For example, in the case of a 50 GeV LLP with a lifetime of 1 ns, the expected signal efficiency reaches 99%. This research achieves an expected upper limit of 4×10^{-6} for the branching ratio of Higgs decaying to LLPs under the assumption of 10^6 Higgs, which significantly outperforms the upper limit of 1×10^{-3} currently established by ATLAS and CMS. For LLPs with lifetimes greater than 1 ns, the analysis yields an expected upper limit that is one order of magnitude better than the expected results from the International Linear Collider.

Last but not least, the appendix section of the dissertation describes a preliminary study on dark photon searches via a proposed fixed target experiment with 8 GeV electrons recoiling from a High-Z metal target.

Key words: High Energy Physics, Collider, di-Higgs, multilepton, $b\bar{b}\tau^+\tau^-$, LLP, Machine learning

Contents

Chapter 1 Introduction	1
Chapter 2 Higgs Physics in Standard Model and Beyond	5
2.1 Introduction to the Standard Model	7
2.1.1 Fermions and Bosons	7
2.1.2 The Quantum Field Theory and the Lagrangian of the Standard Model	8
2.2 Electroweak Symmetry Breaking and the Brout-Englert-Higgs Mechanism ...	10
2.2.1 Electroweak unification	10
2.2.2 The role of the Higgs field in symmetry breaking	12
2.3 Higgs Physics at the LHC	14
2.3.1 Higgs boson production	14
2.3.2 Di-Higgs production	17
2.4 Long-Lived Particles (LLPs) and Beyond Standard Model Search	19
Chapter 3 The Large Hadron Collider and ATLAS Experiment	21
3.1 Introduction to the Large Hadron Collider (LHC)	22
3.1.1 Accelerator design and parameters	22
3.1.2 Operation status	26
3.2 The ATLAS Experiment	29
3.2.1 Overview and scientific goals	29
3.2.2 Detector subsystems and components	33
Chapter 4 Event Simulation and Reconstruction in ATLAS	47
4.1 Event Simulation	47
4.1.1 Simulation Overview and Large-Scale Production System	47
4.1.2 Event generation	49
4.1.3 Detector simulation and response	53
4.2 Object Reconstruction	55
4.2.1 Tracks	55

4.2.2	Electrons	58
4.2.3	Photons	68
4.2.4	Muons	78
4.2.5	Hadronically decaying taus	83
4.2.6	Jets and b-jets	84
4.2.7	Missing Transverse Energy	87
Chapter 5 SM Di-Higgs Searches in Multi-Lepton Final States		89
5.1	Introduction	89
5.2	Data and Monte Carlo samples	90
5.2.1	Data Preparation and Analytical Framework	90
5.2.2	Data Collection and Quality	91
5.2.3	Monte Carlo Simulations	91
5.3	Analysis Strategy	93
5.3.1	Object definitions	94
5.3.2	Jet and b-jet	97
5.3.3	Overlap Removal	98
5.3.4	Event Selection	99
5.3.5	Background Modelling	100
5.3.6	Multivariate Analysis	106
5.3.7	Validation Plots	109
5.4	Systematic Uncertainties	117
5.4.1	Experimental uncertainties	117
5.4.2	Theory uncertainties	118
5.4.3	WZ reweighting uncertainties	118
5.4.4	Uncertainties on data-driven background estimation	120
5.5	Statistical Interpretation	121
5.5.1	Statistical model	121
5.5.2	Statistical analysis and Results	123
5.6	Combination Results	125
5.6.1	Overview of other channels	125
5.6.2	Treatment of the Normalization Factors (NFs)	128

Chapter 6 SM Di-Higgs Searches in $b\bar{b}\tau^+\tau^-$ Final States	131
6.1 Introduction	131
6.2 Data and Monte Carlo samples	132
6.2.1 Simulation of Signal Datasets	133
6.2.2 Background Simulation Samples	135
6.3 Event selection	136
6.3.1 Object Reconstruction	138
6.3.2 Trigger Selection	143
6.3.3 $\tau_{\text{had}}\tau_{\text{had}}$ Event Selection	143
6.3.4 Event Categorization	147
6.3.5 Z+HF control region	148
6.4 Background Modelling	151
6.4.1 Multijet with fake- τ backgrounds in the $\tau_{\text{had}}\tau_{\text{had}}$ channel	152
6.4.2 $t\bar{t}$ with fake- τ_{had} in the $\tau_{\text{had}}\tau_{\text{had}}$ channel with scale-factor method	153
6.5 Multivariate signal extraction	154
6.5.1 General MVA and optimisation strategy	154
6.5.2 $\tau_{\text{had}}\tau_{\text{had}}$ MVAs	157
6.6 Systematic uncertainties	175
6.7 Statistical interpretation	177
6.7.1 Fit step	177
6.7.2 Binning	178
6.7.3 Blinding strategy	179
6.8 Results	179
6.8.1 Fits	179
6.8.2 Data-driven $t\bar{t}$ Modelling	180
6.8.3 $\tau_{\text{had}}\tau_{\text{had}}$ Fitting Results	181
6.8.4 Limits and scans	184
Chapter 7 Constraining the Higgs boson self-coupling from single- and double-Higgs production	189
7.1 Introduction	189
7.2 Theoretical framework	189

7.3 Individual channel measurements	191
7.4 Statistical Methodology and Analysis Combination	192
7.5 Di-Higgs Combined Results	193
7.5.1 Global signal strength	193
7.5.2 Constraints on Higgs self-coupling	194
7.6 Single- and Di-Higgs Combined Results	195
Chapter 8 Search for Long-Lived Particle with the Future Lepton Collider	199
8.1 Introduction	199
8.1.1 Methods and Subsystems for LLP Detection in Collider Experiments	199
8.1.2 Challenges and Considerations in LLP Detection	199
8.1.3 Signatures of Neutral Long-Lived Particles	200
8.2 Event Generation and Simulation at CEPC	203
8.2.1 Overview of CEPC	203
8.2.2 Event generation and simulation	205
8.2.3 LLP Signal Production	206
8.3 Analysis Strategy	207
8.3.1 General Training Configuration	208
8.3.2 Image-based Deep Learning Analysis (CNN)	210
8.3.3 Graph-based Deep Learning Analysis (GNN)	213
8.3.4 Event selection with XGBoost	216
8.3.5 Efficiency comparison between CNN and GNN	217
8.4 Results	218
8.5 Discussion and Summary	221
8.5.1 Comparison with Hadron Colliders: ATLAS and CMS	221
Chapter 9 Summary and Future prospects	225
Bibliography	231
Appendix A DarkSHINE Experiment	261
A.1 Theory Assumption	262
A.2 Experimental Setup	263

A.2.1 SHINE Facility	263
A.2.2 Detector Design	264
A.3 Simulation	267
A.3.1 Signal Sample Production	268
A.3.2 Background Sample Production	269
A.4 Signal Region Definition	271
A.5 Background Estimation	274
A.5.1 Extrapolation from rare processes simulation	275
A.5.2 Validation from inclusive background simulation	278
A.5.3 Invisible background estimation	280
A.5.4 Background Estimation Summary	281
A.6 Sensitivity study	282
A.7 Summary	284
Acknowledgements	287
List of Research Achievements	289

List of Figures

Figure 2–1	The properties of elementary particles in the Standard Model.	8
Figure 2–2	The illustration of Higgs potential $V(\phi)$. Point B represents for the non-zero vacuum expectation value (VEV) of the field.	14
Figure 2–3	A collection of the primary Feynman diagrams at leading order contributing to Higgs boson production. (a) Represents the gluon fusion process, (b) showcases Vector-boson fusion, (c) displays Higgs-strahlung or associated production with a gauge boson arising from a quark-quark interaction at the tree level, (d) outlines associated production with a gauge boson from a gluon-gluon interaction at the loop level, (e) depicts the associated production with a pair of top quarks (a similar diagram would represent the associated production with a pair of bottom quarks), (e-f) illustrates the process of production in association with a single top quark.	15
Figure 2–4	(Left) The production cross sections of the SM Higgs boson as a function of the center of mass energy, \sqrt{s} , for proton-proton collisions ^[21] . The VBF process is denoted here as qqH . (Right) Branching ratios for the primary decays of the SM Higgs boson near a mass (m_H) of 125 GeV ^[20] . Bands represent theoretical uncertainties.	16
Figure 2–5	The major Feynman diagrams for the production of two Higgs bosons via gluon fusion. (Left) Triangle diagram sensitive to the self-coupling vertex κ_λ , (Right) Box diagram, which interferes destructively at the self-coupling vertex κ_λ	18
Figure 2–6	Depiction of Vector Boson Fusion (VBF) processes in Higgs boson pair production: (a) the VVHH vertex process, (b) the trilinear coupling, and (c) the VVH production mode.	18
Figure 3–1	Diagram of CERN’s sequential accelerator system ^[35]	24

Figure 3–2	Public ATLAS Luminosity Results for Run-2 of the LHC ^[36] . Left: Delivered Luminosity Over Time (2011-2018): The graph depicts the cumulative luminosity delivered to ATLAS as a function of time during stable beams and for high-energy p-p collisions. Right: Interactions per Crossing (2015-2018 at 13 TeV): This illustration shows the luminosity-weighted distribution of the average interactions per crossing. The data encompasses all records from ATLAS during stable beams between 2015 and 2018. The integrated luminosity and the mean μ value are indicated. The average interactions per crossing align with the Poisson distribution's mean, ascertained for each bunch.	27
Figure 3–3	The layout of the whole ATLAS detector ^[40]	32
Figure 3–4	Illustration of the global track coordinate with respect to perigee.	33
Figure 3–5	The layout of the ATLAS Inner Detector ^[42] . Left: Overview of the ID; Right: Cross-sectional view of the Inner Detector, with layers from innermost to outermost being the pixel detector, SCT, and TRT.	36
Figure 3–6	The layout of the ATLAS calorimeters ^[44]	38
Figure 3–7	The layout of the ATLAS muon system ^[46]	41
Figure 3–8	The layout of the ATLAS magnet system ^[48]	42
Figure 3–9	Left: A schematic view of the ATLAS trigger system ^[49] ; Right: Block scheme of the first level trigger ^[49]	44
Figure 3–10	A schematic view of the ATLAS DAQ system ^[50]	45

Figure 4–1	Schematic representation of a $pp \rightarrow t\bar{t}$ event as simulated by PYTHIA ^[64] , with certain simplifications for visual clarity. 1) The number of shower branchings and final-state hadrons is reduced compared to an actual PYTHIA simulation; 2) Recoil effects are not depicted to scale; 3) Weak decays of light-flavor hadrons are omitted, implying, for example, a K_S^0 meson is shown as stable; 4) Incoming momenta are illustrated as inversed ($p \rightarrow -p$), necessitating that the momentum direction for both beam remnants and ISR branchings should be interpreted as outward-facing to avoid diagrammatic complexity. This convention prevents the need for beam remnants and ISR emissions to intersect in the central region of the figure.	51
Figure 4–2	Overview of Track Candidate Progression within the Ambiguity Solver ^[83]	58
Figure 4–3	A conceptual diagram depicting an electron’s journey through the various components of the detector ^[91] . The solid red line represents the speculated path of an electron as it moves initially through the tracking system, starting with the pixel detectors, followed by the silicon-strip detectors, and finally through the TRT, before entering the electromagnetic calorimeter. The dotted red line illustrates the trajectory of a photon generated due to the electron’s interaction with the tracking system’s material.	60
Figure 4–4	Algorithm flow diagram for the new electron and photon reconstruction ^[88]	61
Figure 4–5	Efficiency plots of electron ID working points ^[96]	65
Figure 4–6	Efficiency plots of electron Isolation working points ^[88]	67
Figure 4–7	Efficiency measurements for unconverted and converted photons across different η bins ^[98]	69
Figure 4–8	Flowchart of the ambiguity resolution procedure for electron and photon objects ^[97]	70
Figure 4–9	The distribution of reweighting scale factor (signal over background) in each p_T and η bin for both unconverted and converted case.	73

Figure 4–10	The 1D basic kinematic distributions before (top) and after (bottom) reweighting the basic kinematics of $Z \rightarrow e^+e^-$ to those of $\gamma + \text{jets}$ events.	73
Figure 4–11	The ROC performance of rectangular optimization for all p_T and η bins. The grey line is signal efficiency of 80%.	78
Figure 4–12	Comparison of Photon Conversion Efficiency: Rows correspond to 80%, 60%, and 50% efficiency levels. Each row comprises unconverted and converted γ for signal and background.	79
Figure 4–13	Efficiency vs η and p_T for different WPs in simulated $t\bar{t}$ events ^[107] .	81
Figure 4–14	Rejection power for different prong configurations of $\tau_{\text{had-vis}}$ candidates, comparing RNN-based and BDT-based algorithms ^[112] .	84
Figure 4–15	Flow chart depicting the sequential steps of the Particle Flow algorithm from track selection to energy subtraction in the calorimeter ^[115] . The end result comprises charged particles, unmodified topo-clusters, and topo-cluster remnants with partially removed energy.	85
Figure 4–16	Comparison of light-jet (left) and c-jet (right) rejection against b-tagging efficiency for jets with $p_T > 20 \text{ GeV}$ and $ \eta < 2.5$. Statistical errors are within 3%. MV2c10 serves as a high-level BDT-based benchmark, incorporating both IP3D and additional vertex metrics from JetFitter and SV1 ^[122] .	87
Figure 5–1	Overview of the multi-lepton final states considered.	89
Figure 5–2	The pre-fit (let) and post-fit (right) nJets distribution plots of the WZ control regions, using fitting function of Eq.5–1. Both statistical uncertainties and systematic errors are accounted for.	103
Figure 5–3	From left to right shows the pre-fit (top) and post-fit (bottom) plots of the HF-E, HF-MU, External Conversion control regions. All entries represent uncorrected Monte Carlo simulations.Both statistical uncertainties and systematic errors are accounted for.Additionally, the WZ background is adjusted using a fitted scaling function.	105
Figure 5–4	The correlation matrix of MVA variables for signal and background (pure MC) training samples.	108

Figure 5–5	Training results of BDTG: Receiver Operating Characteristic (ROC) curve for 3-lepton channel, illustrating the trade-off between signal efficiency (True Positive Rate) and background inefficiency (False Positive Rate). ..	109
Figure 5–6	The pre-fit and post-fit distributions of the BDTG score in low BDT VR and WZ-enriched region. Scaling factors for External Conversion, HF(electron), and HF(muon) are applied. Additionally, the WZ background is adjusted using a fitted scaling function.Both statistical uncertainties and systematic errors are accounted for.	110
Figure 5–7	The post-fit distribution of distance of lepton pairs and jets, where all the events are required to pass the pre-selection and BDTG score ≤ 0.55 . Scaling factors for External Conversion, HF(electron), and HF(muon) are applied. Additionally, the WZ background is adjusted using a fitted scaling function.Both statistical uncertainties and systematic errors are accounted for.	111
Figure 5–8	The post-fit distribution of invariant mass of lepton pairs and jets, where all the events are required to pass the pre-selection and BDTG score ≤ 0.55 . Scaling factors for External Conversion, HF(electron), and HF(muon) are applied. Additionally, the WZ background is adjusted using a fitted scaling function.Both statistical uncertainties and systematic errors are accounted for.	112
Figure 5–9	The post-fit distribution of the remaining kinematics, where all the events are required to pass the pre-selection and BDTG score ≤ 0.55 . Scaling factors for External Conversion, HF(electron), and HF(muon) are applied. Additionally, the WZ background is adjusted using a fitted scaling function.Both statistical uncertainties and systematic errors are accounted for.	113
Figure 5–10	The post-fit distribution of distance of lepton pairs and jets, where all the events are required to pass the pre-selection. Scaling factors for External Conversion, HF(electron), and HF(muon) are applied. Additionally, the WZ background is adjusted using a fitted scaling function.Both statistical uncertainties and systematic errors are accounted for.	114

Figure 5–11	The post-fit distribution of invariant mass of lepton pairs and jets, where all the events are required to pass the pre-selection. Scaling factors for External Conversion, HF(electron), and HF(muon) are applied. Additionally, the WZ background is adjusted using a fitted scaling function. Both statistical uncertainties and systematic errors are accounted for.	115
Figure 5–12	The post-fit distribution of the remaining kinematics, where all the events are required to pass the pre-selection. Scaling factors for External Conversion, HF(electron), and HF(muon) are applied. Additionally, the WZ background is adjusted using a fitted scaling function. Both statistical uncertainties and systematic errors are accounted for.	116
Figure 5–13	The systematics plots for reweighted WZ samples in WZ enriched region.	120
Figure 5–14	Fitting results for 3ℓ channel, including all systematics and data-driven nuisance parameters.	123
Figure 5–15	The correlation matrix in 3ℓ channel. All systematics and data driven nuisance parameters included.	124
Figure 5–16	Correlation scheme of the systematic uncertainties in the analysis.	129
Figure 5–17	Expected individual and combined upper limits in channels, with full systematic uncertainties (left) and statistics only (right).	130
Figure 6–1	Invariant mass (m_{HH}) distribution at the parton level for the ggF HH signal in the $\tau_{had}\tau_{had}$ channel, with overlaid κ_λ values of 1.0 and 10.0.	134
Figure 6–2	Inclusive distributions of VBF HH samples for varying κ_{2V} at parton-level, presented for the $\tau_{had}\tau_{had}$ and $\tau_{lep}\tau_{had}$ channels. Couplings are adjusted as outlined in Table 6–2.	135
Figure 6–3	Schematic representation of the analysis strategy.	137
Figure 6–4	Sub-leading b -jet DL1r quantiles. Figure (a) shows the SM ggF, ggF ($\kappa_\lambda = 10.0$) and SM VBF signals, along with the sum of the backgrounds. Figure (b) shows the same variable for each background component.	142

Figure 6–5	Event categorisation into low- m_{HH} ggF, high- m_{HH} ggF, and VBF signal regions.	147
Figure 6–6	Data/MC comparison in the prior $Z + HF$ control region.	149
Figure 6–7	Comparison of $V p_T$ shapes between the SRs and the Z CR.	149
Figure 6–8	(a) Quantification of the $V p_T$ shape uncertainty, representing the full discrepancy between data and nominal MC forecast in the Z CR. (b) The subsequent discrete parameterization of the shape uncertainty.	151
Figure 6–9	Schematic illustration of the application of the fake-factor method for estimating multi-jet backgrounds featuring fake- $\tau_{had-vis}$ in the $\tau_{had}\tau_{had}$ channel. In all control regions, non-multi-jet backgrounds are simulated and subsequently deducted from the observed data, as denoted by ‘Subtracted Non-Multi-Jet Backgrounds’ in the legend.	152
Figure 6–10	Fake factors for 1-prong DTT (top), 3-prong DTT (middle), and STT (bottom) for the data-taking periods 15-16 (left), 17 (centre), and 18 (right) for the di-Higgs $\tau_{had}\tau_{had}$ channel.	153
Figure 6–11	Illustrative summary of the data-corrected scale-factor technique employed for evaluating $t\bar{t}$ background containing fake- $\tau_{had-vis}$ in the $\tau_{had}\tau_{had}$ channel.	154
Figure 6–12	Performance progression of the ggF/VBF classification BDT as supplementary variables are incrementally appended to the baseline variables, which consist of m_{jj} and $\Delta\eta_{jj}$.	158
Figure 6–13	Histograms of input variables for the ggF/VBF BDT in the $\tau_{had}\tau_{had}$ channel, illustrating the distinction between ggF HH events (signal in blue) and VBF HH events (background in red).	159
Figure 6–14	Variation of binned significance, as assessed on the validation partitions, with respect to the ensemble’s tree count (NTrees) and each tree’s maximum depth (MaxDepth).	160
Figure 6–15	Dependence of HH signal strengths on the ggF vs VBF BDT cut value for the refined set of variables (left). The right figure shows the aggregate signal-to-background ratio also as a function of the cut value. A vertical dashed line marks the chosen cut value of 0.1.	160

Figure 6–16	Distribution of ggF/VBF BDT scores for various VBF processes under signal region preselection conditions.	161
Figure 6–17	Impact of the NTrees and MaxDepth hyperparameters on the validation significance for the respective BDT training sets in the $\tau_{\text{had}}\tau_{\text{had}}$ channel. ..	162
Figure 6–18	Trajectory of the validation significance as additional predictor variables are incorporated. The baseline set consists of m_{jj} , m_{bb} , $m_{\tau\tau}^{\text{MMC}}$, ΔR_{bb} , and $\Delta R_{\tau\tau}$. Red curves (trafo60_5_total_sig_val) represent binned significance with at least 5.0 expected background events per bin, whereas black curves (trafo60_total_sig_val) require only a minimum of 1.0 expected background events per bin.	164
Figure 6–19	Representative set of pre-fit MVA input variable distributions in the $\tau_{\text{had}}\tau_{\text{had}}$ SRs.	167
Figure 6–20	Representative set of pre-fit MVA input variable distributions in the $\tau_{\text{had}}\tau_{\text{had}}$ SRs.	168
Figure 6–21	Categorisation BDT variable distributions in the $\tau_{\text{had}}\tau_{\text{had}}$ SRs.	168
Figure 6–22	Pre-fit BDT score distributions in the $\tau_{\text{had}}\tau_{\text{had}}$ signal regions.	169
Figure 6–23	Prefit yields of the main background components, the total signal, as well as the total background in the most signal-like BDT bins in the $\tau_{\text{had}}\tau_{\text{had}}$ SRs.	169
Figure 6–24	Top row: Sensitivity as a function of the cut on the ggF vs VBF classification BDT for different variable sets. Bottom row: Inclusive S/B as a function of the cut on the ggF vs VBF classification BDT for different variable sets.	174
Figure 6–25	Post-fit values of the NPs included in the fit of the di-lepton invariant mass distribution in the CR.	180
Figure 6–26	Post-fit modelling of the di-lepton invariant mass (left) and p_T (right) distribution in the CR. In both cases the NP extracted from the fit to m_{ll} are used.	181
Figure 6–27	a Post-fit modelling of the di-lepton invariant mass distribution in the CR, when the $t\bar{t}$ contribution is taken from a dedicated $e\mu$ CR. b Post-fit values of the nuisance parameters included in the fit.	181

Figure 6–28	Nuisance parameter ranking in the $\tau_{\text{had}}\tau_{\text{had}}$ fit using the Asimov dataset.	182
Figure 6–29	Correlations among NPs in the $\tau_{\text{had}}\tau_{\text{had}}$ SM fit to the Asimov dataset (left) and real data (right). MC statistical uncertainties are purposefully omitted.	183
Figure 6–30	Post-fit BDT score distributions in the $\tau_{\text{had}}\tau_{\text{had}}$ signal regions.	184
Figure 6–31	Negative logarithm of the likelihood ratio comparing different κ_λ (a) and κ_{2V} (b) hypotheses to an Asimov dataset constructed under the SM hypothesis in the $\tau_{\text{had}}\tau_{\text{had}}$ channel.	185
Figure 6–32	Negative log-likelihood ratios assessing various κ_λ and κ_{2V} scenarios, in reference to an Asimov dataset created under the SM framework. Analyses incorporate both individual channels and their amalgamation. Solid lines intersecting dashed horizontal lines indicate 68% and 95% confidence levels.	187
Figure 7–1	Illustration of the observed and expected 95% CL upper bounds on the signal strength μ_{HH} for the considered decay channels and their statistical amalgamation. The SM prediction assumes $m_H = 125.09$ GeV.	193
Figure 7–2	95% CL constraints on κ_λ and κ_{2V} from the combined analysis. The red lines indicate the theory constraints, while the solid lines represent observed limits.	194
Figure 7–3	Observed (a) and projected (b) test statistics in terms of κ_λ .	195
Figure 7–4	Constraints in the κ_λ – κ_t parameter space.	196
Figure 8–1	The schematic representation of LLPs' decaying process in the detector.	200
Figure 8–2	Feynman diagrams illustrating LLP production via the Higgsstrahlung process.	207
Figure 8–3	Illustration of image built from raw detector hits for four different processes.	211
Figure 8–4	Illustration of the architecture of ResNet-18 based neural network.	212
Figure 8–5	Illustration of the architecture of the GNN-based neural network.	215
Figure 8–6	The product of signal efficiencies and acceptance for different assumptions of LLPs' mass and lifetime obtained with CNN-based (solid) and GNN-based (dot) approaches.	218

- Figure 8–7 The 95% C.L. upper limit on $\text{BR}(h \rightarrow X_1 X_2)$ for the process $e^+ e^- \rightarrow Zh$ with the condition of ϵ_V fixed (left) and ϵ_V floated (right), where $\epsilon_V := \frac{\text{BR}(X \rightarrow \nu \bar{\nu})}{\text{BR}(X \rightarrow q \bar{q})}$. Different colored lines indicate different LLPs masses. Shaded area indicate statistical and systematic uncertainties combined. ... 220
- Figure 8–8 The 95% C.L. 2-D upper limit on $(\mathcal{B}_{2\text{-jet}}, \mathcal{B}_{4\text{-jet}})$ for the process $e^+ e^- \rightarrow Zh$ for three LLPs masses 50 GeV (left), 10 GeV (middle), 1 GeV (right). Different colored lines indicate different LLPs lifetimes. The uncertainties on the limits are omitted and a few limits are scaled by a factor for better visibility. 220
- Figure 8–9 The 2D fitting for $(\mathcal{B}_{2\text{-jet}}, \mathcal{B}_{4\text{-jet}})$. From top to bottom, the mass is 50, 10, 1 GeV/ c^2 ; From left to right, the lifetime is 0.0001, 0.1, 1.0, 10 ns. 221

List of Tables

Table 2–1	Production cross sections of the Standard Model Higgs boson, with a mass of 125 GeV, in proton-proton collision	16
Table 3–1	Circumference, curvature radius ρ , and beam momentum upon injection for the primary accelerators in the LHC injection sequence ^[32]	25
Table 3–2	Summary of integrated luminosities post standard data-quality checks, alongside uncertainties for the calibration of each yearly data sample from Run 2 pp at $\sqrt{s} = 13$ TeV, including the cumulative sample ^[37] . The table presents the integrated luminosities, total uncertainties, a detailed split of contributions to the vdM calibration’s absolute accuracy, extra uncertainties associated with the physics data sample, and the overall relative uncertainty in percentage.	28
Table 3–3	Summary of the resolution and η coverage for various subdetectors. ECAL and HCAL represent for electromagnet calorimeter and hadronic calorimeter, respectively. The listed resolutions for trackers and the ECAL are parametrized forms dependent on either p_T or E (in GeV), while the Muon Spectrometer provides a specific resolution at a given p_T value. The η coverage is further categorized into measurement and trigger regions.	34
Table 3–4	Inner Detector Parameters and Resolutions ^[41] : The provided resolutions are indicative values (the precise resolution in each detector varies with $ \eta $).	36
Table 3–5	Specifications for the four subsystems of the muon detector ^[47] : The stated spatial resolution (in columns 3 and 4) excludes uncertainties from chamber alignment. The intrinsic time accuracy for each chamber type is detailed in column 5, with additional time required for signal propagation and electronic factors. Numbers in parentheses relate to the full detector setup anticipated for 2009.	40

Table 4–1	Quantities of materials, solids, logical volumes, physical volumes, and aggregate volumes essential for the assembly of diverse segments of the ATLAS detector are outlined. The term "Inner Detector" encompasses components such as the beampipe, BCM, pixel tracker, SCT, and TRT. ...	54
Table 4–2	Summary of Quantities for Electron Identification.	64
Table 4–3	Description of electron isolation benchmarks and their corresponding performance metrics. For the Gradient strategy, the transverse momentum (p_T) is expressed in GeV. A consistent cone dimension of $\Delta R = 0.2$ is employed for both calorimeter and track-based isolation methods, with a maximum cone size of $\Delta R_{\max} = 0.2$ designated for track isolation.	67
Table 4–4	Definition of the photon isolation working points ^[97]	70
Table 4–5	Single Photon signal samples and $Z \rightarrow e^+e^-$ background samples.	72
Table 4–6	Yields of pre-selected ambiguous events and total pre-selected events before ambiguity requirement for $\gamma + \text{jets}$ and $Z \rightarrow e^+e^-$	74
Table 4–7	Separation power of shower shapes, topo-cluster, and ambiguity variables, which are retrieved from the BDT method from TMVA package, since the kCut method does not provide the variable ranking	77
Table 4–8	Definitions of the muon isolation WPs.	82
Table 5–1	Good Run List XML Files by Year.	91
Table 5–2	Event generation configurations for signal and background processes.	92
Table 5–3	List of lowest p_T -threshold, un-prescaled single lepton and di-lepton triggers used for 2015-2018 data taking.	95
Table 5–4	Definitions of Baseline, Loose, and Tight criteria in multilepton channels.	96
Table 5–5	Summary of Overlap Removal Criteria in Multilepton Channels.	98
Table 5–6	The raw yields with pre-selection cut-flow for the 3ℓ analysis.	100
Table 5–7	Summary of Monte Carlo (MC) samples with applied normalization factors and re-weighted WZ contributions, alongside data for all control and validation regions in the 3ℓ channel. Only the principal background processes are enumerated.	101
Table 5–8	The systematics of three fake sources and the corresponding yields in the signal region, which is estimated by the template fit method.	106

Table 5–9	Discriminant variables used in BDTG training for 3ℓ channel.	107
Table 5–10	The background sample normalizations and their uncertainties were used in the analysis. The uncertainties on the inclusive cross sections are taken from the ATLAS Physics Modelling Group Twiki.	119
Table 5–11	Correlation and Covariance Matrix for Parameters A, B, and C.	120
Table 5–12	Eigenvalues and Eigenvectors of the Covariance Matrix for Parameters A, B, and C.	120
Table 5–13	Expected Upper limits in 3ℓ channel. First row: Limits with stats only; Second row: Limits with systematics.	125
Table 5–14	Selection criteria applied to each of the control and validation regions defined in each channel. The requirements that guarantees orthogonality with respect to the corresponding signal region are highlighted in blue.	126
Table 5–15	Selection criteria applied to each channel to form the signal regions.	127
Table 5–16	Summary table of employed normalization factors, detailing individual and composite fit values. Specific channels without normalization factors are also indicated.	128
Table 5–17	Table of 95% C.L. upper limits on signal strength for multi-lepton channels. Limits are derived using Asimov datasets under varying scenarios of statistical and systematic uncertainties.	130
Table 6–1	Summary of MC samples for signal and background processes.	132
Table 6–2	Considered κ_λ , κ_{2V} , and κ_V coupling modifiers for VBF HH simulations.	134
Table 6–3	Coupling modifier values for generating alternative VBF HH samples.	135
Table 6–4	Summary of the event selections, shown separately for events that are selected by different triggers.	138
Table 6–5	Summary of overlap-removal procedures with the standard working point.	142
Table 6–6	Data-taking triggers for the $\tau_{\text{had}}\tau_{\text{had}}$ channel.	144
Table 6–7	SM ggF HH signal cutflow (POWHEG + PYTHIA 8) in the $\tau_{\text{had}}\tau_{\text{had}}$ sub-channel.	145
Table 6–8	SM VBF HH signal cutflow (POWHEG + PYTHIA 8) in the $\tau_{\text{had}}\tau_{\text{had}}$ sub-channel.	146

Table 6–9	Demarcation of the simulated event pools used for the learning, fine-tuning, and scrutiny of the BDT algorithms.	155
Table 6–10	Input variables used for the ggF/VBF BDT training in the $\tau_{\text{had}}\tau_{\text{had}}$ channel.	158
Table 6–11	Chosen hyperparameters for the ggF/VBF BDT training in the $\tau_{\text{had}}\tau_{\text{had}}$ channel.	159
Table 6–12	Training hyperparameters chosen for the BDTs used in the three $\tau_{\text{had}}\tau_{\text{had}}$ analysis categories.	163
Table 6–13	Input variables used for the low- m_{HH} ggF BDT training in the $\tau_{\text{had}}\tau_{\text{had}}$ channel.	165
Table 6–14	Input variables used for the high- m_{HH} ggF BDT training in the $\tau_{\text{had}}\tau_{\text{had}}$ channel.	166
Table 6–15	Input variables used for the VBF BDT training in the $\tau_{\text{had}}\tau_{\text{had}}$ channel.	166
Table 6–16	Prefit yields of the individual background components and the total ggF+VBF HH signal (labelled signal) in the four most signal-like BDT bins, shown for the $\tau_{\text{had}}\tau_{\text{had}}$ high- m_{HH} region.	170
Table 6–17	Prefit yields of the individual background components and the total ggF+VBF HH signal (labelled signal) in the four most signal-like BDT bins, shown for the $\tau_{\text{had}}\tau_{\text{had}}$ low- m_{HH} region.	171
Table 6–18	Prefit yields of the individual background components and the total ggF+VBF HH signal (labelled signal) in the four most signal-like BDT bins, shown for the $\tau_{\text{had}}\tau_{\text{had}}$ VBF region.	172
Table 6–19	Comparison of BDT configurations for ggF/VBF in relation to the ultimate fit outcomes. These limits are derived from a fit that incorporates solely floating normalizations and MC statistical uncertainties. A consistent BDT threshold of 0.1 is employed across all scenarios. The percentage enhancement relative to the 15-var BDT outcome is indicated in parentheses.	173
Table 6–20	Summarized 95% CL expected upper boundaries on HH signal strength and intervals for κ_λ and κ_{2V} , categorized by production mode in the $\tau_{\text{had}}\tau_{\text{had}}$ channel. All estimations with and without systematic uncertainties are included.	185

Table 6–21	Expected 95% CL limits on HH signal strength and intervals for κ_λ and κ_{2V} from the combined fit. The statistics are reported both with and without systematic uncertainties.....	186
Table 7–1	Summary of datasets for each contributing analysis channel, with their corresponding integrated luminosities in fb^{-1} . Detailed descriptions of each channel can be found in the last column's references.	191
Table 7–2	Comprehensive summary of κ_λ constraints.	197
Table 8–1	Projected Operational Modes of CEPC and Corresponding Yields of Higgs, W, and Z Bosons; calculations Based on Two Interaction Points and Integrated Luminosity.....	203
Table 8–2	Fundamental Specifications and Efficacy Metrics of the CEPC Detector System.	204
Table 8–3	Cross-Section of Higgs and Background Processes at CEPC	206
Table 8–4	Signal Acceptance for Different Mass and Lifetime Parameters.....	207
Table 8–5	Node and edge features defined in the heterogenous graph.	214
Table 8–6	Signal efficiencies for different assumptions of LLPs' mass and lifetime obtained with CNN-based and GNN-based approaches.....	217
Table 8–7	The 95% C.L. exclusion limit on $\text{BR}(h \rightarrow X_1 X_2)$ for all signal channels: fixed and floated ϵ_V , based on CNN's efficiency.....	219

Chapter 1 Introduction

What makes up the very fabric of the universe? How do its smallest constituents interact to form the world as we understand it? These overarching questions are central to the field of particle physics, which investigates the fundamental particles that make up matter. High-energy colliders, machines that accelerate particles to nearly the speed of light and smash them together, offer unique opportunities to address these questions by allowing scientists to study particle interactions in conditions that mimic the early universe.

The Standard Model of particle physics, a well-established theory developed over the past half-century, successfully explains these interactions. It provides a framework for understanding how known particles, like quarks and electrons, interact through fundamental forces—namely, the electromagnetic, weak, and strong forces. The discovery of the Higgs boson in 2012 at CERN’s Large Hadron Collider, a 27-kilometer ring beneath the France-Switzerland border, provided the capstone to this model. The Higgs boson explains why some particles have mass, affirming the monumental success of the Standard Model.

Despite these successes, there are phenomena that cannot be fully accounted for by the Standard Model alone, such as dark matter, a mysterious substance that makes up about 27% of the universe but doesn’t emit, absorb, or reflect any electromagnetic radiation. These gaps in understanding call for exploration into Beyond the Standard Model (BSM) physics. One interesting avenue is the study of long-lived particles (LLPs), which are hypothetical particles that do not decay as rapidly as others and could possibly interact weakly with normal matter.

In response to the challenges and opportunities posed by these questions, scientists have deployed the Large Hadron Collider and are planning future machines known as lepton colliders. These include projects like the International Linear Collider (ILC), the Circular Electron-Positron Collider (CEPC), and the Future Circular Collider (FCC-ee). These colliders aim to provide more precise measurements of the Higgs boson and to explore potential new physics.

The discovery of the Higgs boson marks a monumental milestone in particle physics, serving as both a confirmation of the Standard Model and a gateway to further explorations. My research contributes to the next crucial phase of this field by focusing on di-Higgs search, where two Higgs bosons are produced simultaneously. This is a pivotal area of study to understand unique aspects of the Higgs, particularly its self-coupling, which governs how

the Higgs boson interacts with itself. My analyses particularly center on events with multi-lepton and $b\bar{b}\tau^+\tau^-$ final states.

Additionally, to provide a more comprehensive understanding of the Higgs sector, my work incorporates a combination of both single- and double-Higgs production events. This integrated approach aims to constrain the Higgs boson self-coupling with increased precision, thereby offering critical insights into both Standard Model and Beyond the Standard Model physics.

Beyond the scope of di-Higgs and single-Higgs analyses, my research extends to BSM phenomena, particularly focusing on LLPs. Utilizing machine learning techniques that directly interpret raw detector data, I've developed a novel methodology for distinguishing these hypothetical particles from Standard Model particles in simulations.

Finally, while the main body of this dissertation focuses on collider-based experiments, my interests extend to other forms of particle physics research. Specifically, I have worked on an experiment aiming to detect dark photons, particles that are proposed as force carriers for dark matter, using a fixed-target experiment that utilizes high-energy electron beams.

In sum, this dissertation offers a coherent narrative of my Ph.D. research journey. It spans from probing fundamental questions in particle physics to making significant contributions in both collider-based Higgs boson studies and BSM long-lived particle searches, while also venturing into experiments beyond colliders. Each of these research endeavors adds a piece to the complex puzzle of understanding the universe at its most basic level. This dissertation is organized as follows:

- **Chapter 2:** Provides an overview of Higgs physics within the Standard Model and beyond.
- **Chapter 3:** Discusses the Large Hadron Collider and the ATLAS experiment.
- **Chapter 4:** Focuses on event simulation and reconstruction techniques in ATLAS.
- **Chapter 5:** Presents SM di-Higgs searches in multi-lepton final states.
- **Chapter 6:** Covers SM di-Higgs searches in $b\bar{b}\tau\tau$ final states.
- **Chapter 7:** Aims to constrain the Higgs boson self-coupling using data from single- and double-Higgs production.
- **Chapter 8:** Discusses search strategies for long-lived particles with future lepton colliders.

- **Chapter 9:** Summarizes the findings and discusses future prospects.
- **Appendix A:** Describes a fixed-target experiment to probe dark photon using 8 GeV electron beam.

Chapter 2 Higgs Physics in Standard Model and Beyond

The Standard Model (SM) of particle physics is the pinnacle of over a century's worth of scientific research, culminating in our current understanding of the fundamental particles and the forces that govern their interactions. It is one of the most complicated theories, yet elegant in both mathematics and physics that has stood the test of time and experimental scrutiny.

The story of the Standard Model starts in the mid 20th century, when quantum electrodynamics (QED) was born. This theory is developed by the great physicist Richard Feynman^[1], Julian Schwinger^[2], Sin-Itiro Tomonaga, and Freeman Dyson, describing how photons interact with electrons and positrons. The development of QED was a major achievement, as it successfully reconciled quantum mechanics, which governs the small scale, with special relativity, which describes the fast-moving world. It provided a framework that could make incredibly precise predictions, many of which have been confirmed by experiments. QED was the first example of a quantum field theory, which would serve as the template for the rest of the Standard Model.

In the 1960s and 70s, the understanding of the strong nuclear force, one of the four fundamental forces of nature, underwent a significant revolution with the introduction of partons, namely quarks and gluons. This force is responsible for holding together the protons and neutrons inside atomic nuclei, and the particles that mediate this force are called gluons. The theory that describes the strong force is called quantum chromodynamics (QCD), developed by scientists such as Murray Gell-Mann^{[3][4]} and Harald Fritzsch^[5]. The particles involved in this force, quarks and gluons, carry a property called "color charge" (analogous to electric charge in electromagnetism), and the theory gets its name from this color charge. QCD provided a framework for understanding how quarks combine to form protons, neutrons, and other particles.

Meanwhile, scientists were also making progress on understanding the weak nuclear force, which is responsible for radioactive decay and plays a key role in nuclear fusion in stars. The weak force was initially puzzling because it is very different from the other forces, which is much weaker (hence the name), and it only operates at very short distances. In the 1960s, Sheldon Glashow^[6], Abdus Salam^[7], and Steven Weinberg^[8] developed a theory that

unified the weak force with electromagnetism, resulting in the "electroweak" theory. This theory predicted the existence of three new particles, the W^+ , W^- , and Z , which mediate the weak force. These particles were later discovered in experiments at CERN in the 1980s.

The final piece of the puzzle was electroweak symmetry breaking, and this happens through the Brout-Englert-Higgs mechanism. This mechanism necessitates the existence of a Higgs field, and after EWS breaking, a scalar boson (the Higgs boson) appears. This particle was predicted in 1964 by several scientists, including Peter Higgs, François Englert, and Robert Brout. According to the theory, particles, especially for fermions, gain mass by interacting with this field, which means the more they interact, the more mass they have. The Higgs boson remained elusive for many years, but it was finally discovered in 2012 at CERN's Large Hadron Collider^[9], in one of the most celebrated scientific achievements of the 21st century.

The discovery of the Higgs boson was indeed a watershed moment in the history of particle physics, confirming the last missing piece of the Standard Model puzzle. However, it is important to note that the Higgs boson itself is not the end of the story. Its discovery opened up new avenues of research, including the study of its properties and the search for possible new particles and forces associated with it.

Moreover, the Standard Model, while extraordinarily successful, does not account for some observed phenomena, indicating that there is physics beyond it - often referred to as "Beyond the Standard Model" (BSM) physics. One of the major areas of research in BSM physics involves long-lived particles (LLPs). These are hypothetical particles that do not decay immediately after being produced in high-energy collisions, as most known particles do. Instead, they would travel a significant distance before decaying, potentially leaving a distinctive signature in detectors at particle accelerators. This unusual behavior could be linked to the mysteries of dark matter, neutrino masses, or the imbalance between matter and antimatter in the universe.

This chapter delves into the intricacies of the Standard Model and its fundamental components, beginning with an overview in Section 2.1. Next, Section 2.2 illuminates the concept of Electroweak Symmetry Breaking and the Brout-Englert-Higgs Mechanism. The subsequent focus in Section 2.3 is on the research surrounding the Higgs bosons at the Large Hadron Collider (LHC). Finally, Section 2.4 delves into the frontier of Long-Lived Particles (LLPs)

and their potential to further the understanding of physics beyond the Standard Model.

2.1 Introduction to the Standard Model

2.1.1 Fermions and Bosons

The SM theoretical framework categorizes elementary particles into two principal classes, known as fermions and bosons, each with distinctive characteristics and roles in the cosmos, as summarized in Figure 2-1.

Fermions comprise the building blocks of matter and adhere to the Pauli Exclusion Principle, implying that they cannot simultaneously occupy identical quantum states. Characterized by half-integer spins, fermions are sub-categorized into two classes: quarks and leptons.

- **Quarks:** There exist six flavors of quarks: up, down, charm, strange, top, and bottom. The up, charm, and top quarks carry a fractional electric charge of $+2/3$, while the down, strange, and bottom quarks carry a fractional charge of $-1/3$. Quarks are unique in that they interact via all three fundamental non-gravitational forces: strong, weak, and electromagnetic. Additionally, quarks carry an intrinsic property termed 'color charge', which mediates their interaction via the strong force. There are 3 color charges (and 3 opposite charges) for each flavor.
- **Leptons:** Analogous to quarks, leptons are also divided into six types across three generations: electron, muon, tau particles, and their corresponding neutrinos. The electron, muon, and tau each carry a unit negative charge and interact via the weak and electromagnetic forces. Neutrinos, on the other hand, being neutral, solely partake in weak interactions.

Bosons, contrarily, are force mediators and possess integer spins, permitting them to inhabit the same quantum state. The Standard Model recognizes the following bosons: photon, W and Z bosons, gluons, and the Higgs boson.

- **Photon:** The photon is the force carrier for the electromagnetic force, governing interactions between electrically charged particles. It is a massless particle that propagates at the speed of light.
- **W and Z bosons:** These are the mediators of the weak nuclear force, which controls certain types of nuclear decay, such as beta decay. The W bosons carry a unit positive

or negative charge, while the Z boson is electrically neutral. Their considerable masses lead to the short-range nature of the weak force.

- **Gluons:** Gluons mediate the strong nuclear force, responsible for binding quarks within protons, neutrons, and other hadronic particles. They carry a color charge, allowing them to interact among themselves.
- **Higgs boson:** The Higgs boson is associated with the Higgs field, as proposed by the Brout-Englert-Higgs mechanism, which also explains the unique "Yukawa" interaction^[10] through which particles acquire mass.

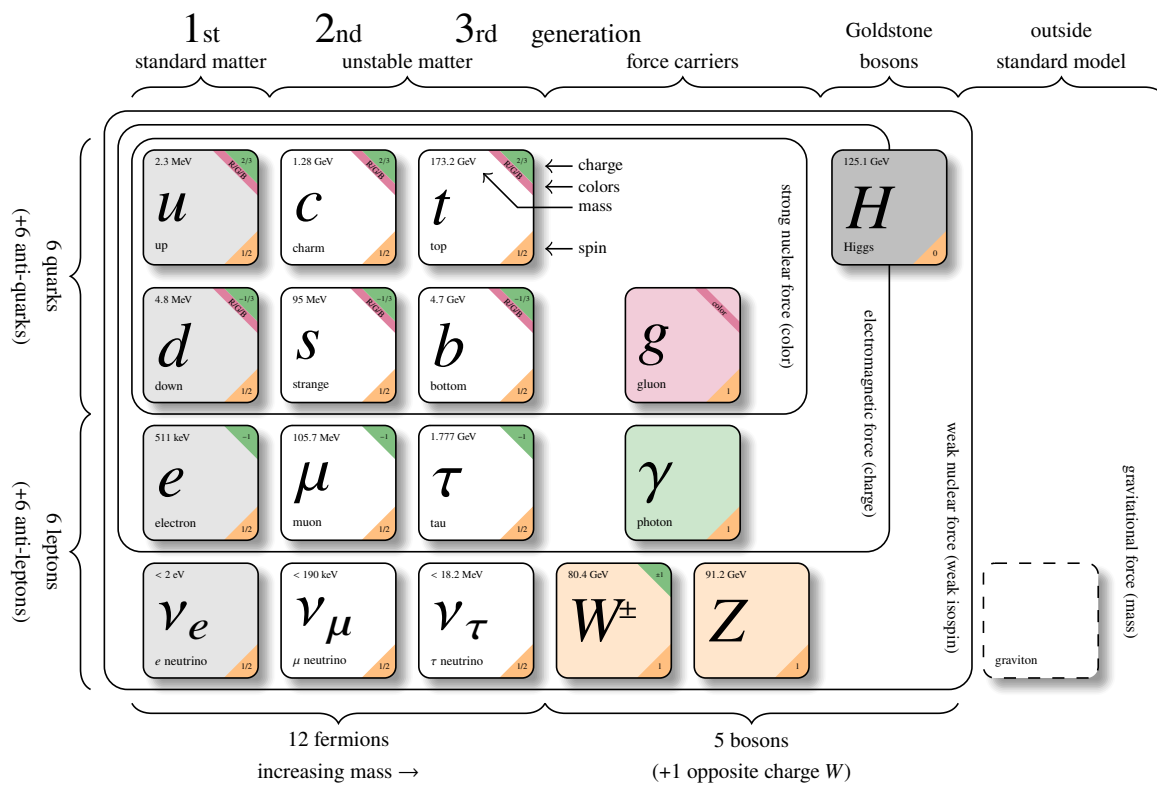


Figure 2-1 The properties of elementary particles in the Standard Model.

2.1.2 The Quantum Field Theory and the Lagrangian of the Standard Model

Quantum Field Theory (QFT) is the theoretical framework that combines classical field theory^[11], quantum mechanics, and special relativity. QFT treats particles as excited states, or quanta, of underlying quantum fields. These fields are mapped across spacetime, and particles are represented by field oscillations. The most successful application of QFT is the

Standard Model of particle physics. The mathematical structure that describes the dynamics and interactions of the quantum fields in the Standard Model is given by the so-called Standard Model Lagrangian. This Lagrangian includes terms for each of the particles and their interactions in the model.

To describe the Standard Model in the language of QFT, the concept of gauge symmetry is introduced. This is a fundamental symmetry principle that states that the laws of physics should not change under certain transformations, known as gauge transformations. In the context of QFT, gauge transformations change the phase of the quantum fields, and different types of gauge transformations lead to different types of forces.

The Lagrangian of the Standard Model encompasses all known elementary particles and their interactions, excluding gravity. The full Lagrangian is the sum of these parts:

$$L = -\frac{1}{4}F_{\mu\nu}F^{\mu\nu} + i\bar{\psi}\not{D}\psi + h.c. + \psi_i y_{ij} \psi_j \phi + h.c. + |D_\mu \phi|^2 - V(\phi), \quad (2-1)$$

which is usually divided into several parts that describe different kinds of interactions^[12]:

1. $-\frac{1}{4}F_{\mu\nu}F^{\mu\nu}$ This term represents the kinetic energy of the matter fields. It describes the propagation of matter particles in space and time. This term includes the fields of quarks and leptons, which are the building blocks of matter.
2. $i\bar{\psi}\not{D}\psi$ This term describes the interactions between matter particles and force particles. It includes the electromagnetic interaction, the strong interaction, and the weak interaction. The electromagnetic interaction is mediated by the photon, the strong interaction by the gluon, and the weak interaction by the W and Z bosons. The weak interaction is unique in that it can transform one type of matter particle into another.
3. $h.c.$ This term represents the 'hermitian conjugate' of term 2. The hermitian conjugate is necessary if arithmetic operations on matrices produce complex numbers.
4. $\psi_i y_{ij} \psi_j \phi$ This term represents how matter particles couple to the Brout-Englert-Higgs (BEH) field ϕ and thereby obtain mass. It includes the coupling of quarks and leptons to the Higgs field.
5. $h.c.$ This term describes is necessary since this hermitian conjugate of term 4 describes the same interaction, but with antimatter particles.
6. $|D_\mu \phi|^2$ This term represents how the propagator particles of weak interaction couple to the BEH field. It only applies to the W and Z bosons, because photons and gluons are massless.

7. $-V(\phi)$ This term describes the Brout-Englert-Higgs field potential and how Higgs bosons couple to each other.

The specific form of each of these terms is dictated by the principles of gauge symmetry, special relativity, and quantum mechanics. The parameters in the Lagrangian (the particle masses, the coupling constants, etc.) are determined by experiments. In this framework, particles interact by exchanging gauge bosons. For instance, two electrons repel each other by exchanging a photon, the gauge boson of the electromagnetic field. Similarly, quarks interact by exchanging gluons, the gauge bosons of the strong force. The Higgs field, as introduced in the Lagrangian, plays a critical role in the Standard Model. When the Higgs field undergoes spontaneous symmetry breaking, it gives rise to the masses of the other particles. The interaction of the particles with the Higgs field is proportional to their mass. More details about the Higgs field are discussed in Section [2.2](#).

2.2 Electroweak Symmetry Breaking and the Brout-Englert-Higgs Mechanism

2.2.1 Electroweak unification

Electroweak unification is a fundamental concept in particle physics that ties together two of the four known forces of nature, namely the weak nuclear force and electromagnetism. This unification is a cornerstone of the Standard Model (SM) of particle physics, providing an elegant theoretical framework to understand the interactions of elementary particles.

At the heart of electroweak unification is the realization that at high enough energies, electromagnetism, mediated by photons (γ), and the weak nuclear force, mediated by W and Z bosons (W^+ , W^- , and Z^0), manifest as facets of the same force: the electroweak force. The connection between these two fundamental interactions was initially proposed by Sheldon Glashow, Abdus Salam, and Steven Weinberg, earning them the Nobel Prize in Physics in 1979.

The theory begins with an invariant Lagrangian under the $SU(2)_L \times U(1)_Y$ gauge group, with $SU(2)_L$ and $U(1)_Y$ representing the weak isospin and hypercharge symmetries, respectively. The gauge fields corresponding to these symmetries are W_μ^a ($a = 1, 2, 3$) and B_μ . The

electroweak part of the SM Lagrangian can be written as follows:

$$\mathcal{L}_{EW} = -\frac{1}{4}W_{\mu\nu}^a W^{a\mu\nu} - \frac{1}{4}B_{\mu\nu}B^{\mu\nu} \quad (2-2)$$

Here, $W_{\mu\nu}^a$ and $B_{\mu\nu}$ are the field strength tensors for the $SU(2)_L$ and $U(1)_Y$ gauge fields, defined as:

$$W_{\mu\nu}^a = \partial_\mu W_\nu^a - \partial_\nu W_\mu^a + g\epsilon^{abc}W_\mu^b W_\nu^c \quad (2-3)$$

$$B_{\mu\nu} = \partial_\mu B_\nu - \partial_\nu B_\mu \quad (2-4)$$

Here, ϵ^{abc} is the totally antisymmetric tensor, g is the $SU(2)_L$ gauge coupling constant, and μ, ν are space-time indices. This Lagrangian describes four massless gauge bosons, which correspond to the three generators of $SU(2)_L$ and the generator of $U(1)_Y$. However, empirical evidence contravenes this: the weak force has a short range because its mediators, the W and Z bosons, are massive, while the photon is massless.

To reconcile this discrepancy, the Brout-Englert-Higgs mechanism is invoked, which introduces a complex scalar field, the Higgs field. This field spontaneously breaks the $SU(2)_L \times U(1)_Y$ symmetry down to $U(1)_{em}$, the gauge group of electromagnetism. Consequently, three of the original massless gauge bosons acquire mass, becoming the W and Z bosons, while the fourth remains massless, recognized as the photon.

It is worth noting that the electroweak symmetry breaking also involves the generation of fermion masses through their Yukawa couplings to the Higgs field. As we know it, without this mechanism, the elementary particles would all be massless, zipping through space at the speed of light, and the universe would not exist.

The unification of the electromagnetic and weak forces happens at a sufficiently high energy scale, known as the electroweak scale, at approximately 100 GeV. At energies below this scale, the weak and electromagnetic forces appear distinct because of the large masses of the W and Z bosons. Above the electroweak scale, however, the distinction between these forces blurs, and they behave as a singular electroweak force.

Experimental confirmation of electroweak unification came in the 1980s with the discovery of W and Z bosons at CERN's Super Proton Synchrotron^[13]. Further, precision measurements at the HERA^[14] ($e-p$ collider), the Large Electron-Positron (LEP) collider^[15] and the Tevatron^[16] confirmed the predictions of the electroweak theory, solidifying it as an integral

part of the SM. At HERA we could see the unification of charged current (CC) and neutral current (NC) cross sections at high Q^2 (squared momentum transfer)^[17].

2.2.2 The role of the Higgs field in symmetry breaking

The Standard Model of particle physics provides an extraordinarily successful framework for understanding elementary particles and their interactions. Central to the model is the electroweak theory, which describes electromagnetism and the weak nuclear force as two aspects of a unified electroweak force. However, in order to reconcile the massless nature required by gauge invariance with the observed massive particles, we need to introduce the Brout-Englert-Higgs (BEH) mechanism, which is a process of spontaneous symmetry breaking.

The spontaneous symmetry breaking^[18] occurs in the scalar sector of the electroweak theory, which contains the Higgs field^[19], denoted by Φ . The Lagrangian density responsible for this process is given by:

$$\mathcal{L} = (D^\mu \Phi)^\dagger (D_\mu \Phi) - V(\Phi) \quad (2-5)$$

where D_μ is the covariant derivative that contains the W and B fields, and $V(\Phi)$ is the Higgs potential. In the Standard Model, Φ is a doublet of complex scalar fields given by:

$$\Phi = \frac{1}{\sqrt{2}} \begin{pmatrix} 0 \\ v + h(x) \end{pmatrix} \quad (2-6)$$

where v is the vacuum expectation value (VEV) of the field and $h(x)$ signifies the real scalar field representing fluctuations about the vacuum. The Higgs potential $V(\Phi)$ is given by:

$$V(\Phi) = \mu^2 \Phi^\dagger \Phi + \lambda (\Phi^\dagger \Phi)^2 \quad (2-7)$$

with the parameters satisfying $\mu^2 < 0$ and $\lambda > 0$. The negative μ^2 term allows for a non-zero minimum of the potential away from the origin, while the positive λ term ensures that the potential is bounded from below. This generates a "Mexican hat" shape in the Higgs potential. Figure 2-2 illustrates the Higgs potential for $\mu^2 < 0$ and $\mu^2 > 0$.

This non-zero minimum of the potential, also known as the vacuum expectation value (VEV), is given by $v = \sqrt{\frac{-\mu^2}{2\lambda}}$. It is around this value that the Higgs field oscillates, not around zero, and thus the electroweak symmetry is spontaneously broken, resulting in the W and Z bosons acquiring mass. It's also beneficial to understand that the fluctuations about this vacuum state, represented by $h(x)$, correspond to the physical Higgs boson.

Upon expanding the kinetic term $(D^\mu\Phi)^\dagger(D_\mu\Phi)$ and the potential $V(\Phi)$ around the vacuum expectation value, we find terms proportional to $W^\mu W_\mu$, $B^\mu B_\mu$, and h^2 , which give rise to the masses of the W boson, Z boson, and the Higgs boson, respectively. Specifically, the Higgs boson mass can be identified as $m_H = \sqrt{2\lambda}v$.

The mass generation for fermions is also an outcome of the Higgs mechanism, however it involves a different process, namely the Yukawa interaction between fermions and the Higgs field. After the spontaneous symmetry breaking, the Higgs doublet acquires a vacuum expectation value v , and the Yukawa interaction term in the Standard Model Lagrangian becomes:

$$\mathcal{L}_{\text{Yukawa}} = -\frac{y_f v}{\sqrt{2}} \bar{\Psi}_f \Psi_f - \frac{y_f h}{\sqrt{2}} \bar{\Psi}_f \Psi_f + \text{h.c.} \quad (2-8)$$

The first term now clearly signifies the mass term for the fermions, $m_f = y_f v / \sqrt{2}$, which is non-zero due to the non-zero vacuum expectation value of the Higgs field. This is how fermions acquire their mass in the Higgs mechanism. The second term represents the interaction of the Higgs boson with the fermions, which is proportional to the mass of the fermions. These interactions are crucial for the production and decay of the Higgs boson at colliders. In the Standard Model, the Yukawa couplings y_f are free parameters and must be determined by experiment.

The Brout-Englert-Higgs (BEH) mechanism and its associated spontaneous symmetry breaking are fundamental components of the Standard Model of particle physics. They provide a consistent framework that unifies the weak nuclear force and electromagnetism, offering a profound explanation for the observed masses of fundamental particles. The mechanism relies on the Higgs field, which has a non-zero vacuum expectation value and plays a crucial role in this process. Rather than actually "breaking" the symmetry, the mechanism merely conceals it. The underlying theory remains symmetric, but the ground state does not exhibit this symmetry. This distinction is crucial for our modern understanding of particle physics.

It is worth emphasizing that direct mass terms for gauge bosons would violate gauge invariance, which is a foundational symmetry of the Standard Model. The Higgs mechanism becomes indispensable in this regard. Starting from a massless theory that requires gauge invariance, the Higgs field and its corresponding mechanism give rise to effective mass terms for particles after electroweak symmetry breaking (EWSB). This ingenious solution ensures that the theory remains consistent and gauge invariant while also explaining the origin of

mass for particles.

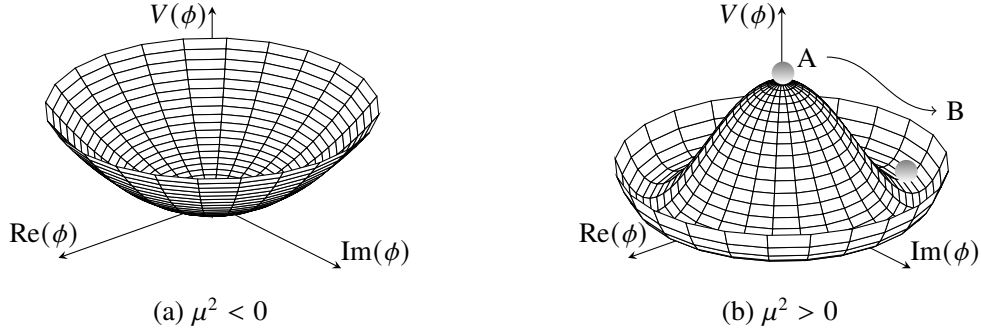


Figure 2-2 The illustration of Higgs potential $V(\phi)$. Point B represents for the non-zero vacuum expectation value (VEV) of the field.

2.3 Higgs Physics at the LHC

2.3.1 Higgs boson production

The key production mechanisms for the Higgs boson at the Large Hadron Collider (LHC) include gluon fusion (ggF), vector-boson fusion (VBF), associated production with a gauge boson (VH), as well as associated production with a pair of top quarks ($t\bar{t}H$) or with a single top quark (tHq). Figure 2-3 illustrates these dominant Higgs boson production processes. In 2-4 (left), the cross sections corresponding to the production of a SM Higgs boson are presented as a function of the center of mass energy, \sqrt{s} , for proton-proton (pp) collisions. This representation also includes bands to indicate theoretical uncertainties.

A comprehensive discussion on uncertainties in the theoretical calculations, resulting from missing higher-order effects and the experimental uncertainties on the determination of SM parameters used in the calculations, can be found in references^[20]. These sources also offer advanced discussions on the impact of parton distribution function (PDF) uncertainties, Quantum Chromodynamics (QCD) scale uncertainties, uncertainties stemming from different procedures for including higher-order corrections matched to parton shower simulations, as well as uncertainties due to hadronisation and parton-shower events.

Table 2-1 tabulates the production cross sections for a SM Higgs boson with a mass of 125 GeV in proton-proton collisions. These values are presented as functions of the center-of-mass energy \sqrt{s} . The projections for the Large Hadron Collider (LHC) energies have been

sourced from reference^[20]. The estimates for the ggF channel at the LHC are inclusive of the most recent next-to-next-to-next-to leading order (N3LO) results, which have significantly cut down the theoretical uncertainties by approximately a factor of two, in comparison to the next-to-next-to leading order plus next-to leading logarithm (NNLO+NLL) results. It's worth noting that the total uncertainties were calculated under the assumption of no correlations between strong coupling constant (α_s) and PDF uncertainties.

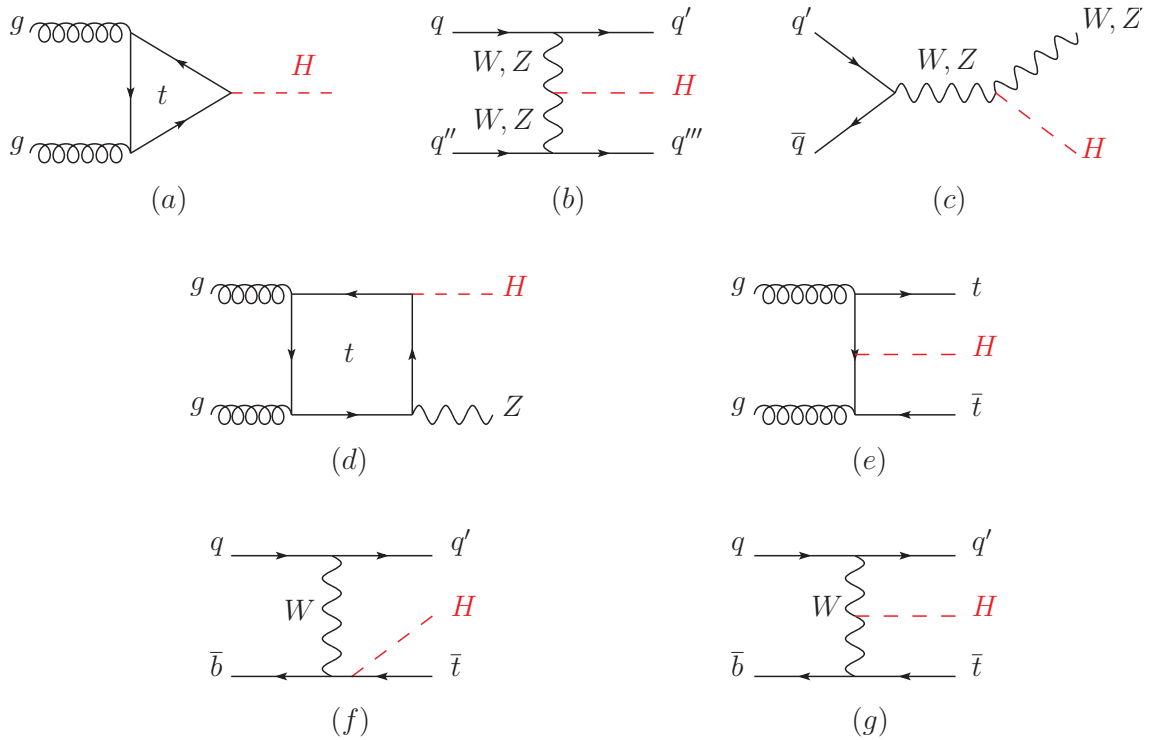


Figure 2–3 A collection of the primary Feynman diagrams at leading order contributing to Higgs boson production. (a) Represents the gluon fusion process, (b) showcases Vector-boson fusion, (c) displays Higgs-strahlung or associated production with a gauge boson arising from a quark-quark interaction at the tree level, (d) outlines associated production with a gauge boson from a gluon-gluon interaction at the loop level, (e) depicts the associated production with a pair of top quarks (a similar diagram would represent the associated production with a pair of bottom quarks), (e-f) illustrates the process of production in association with a single top quark.

At the LHC, two of the most prominent higgs production modes are the ggF and VBF.

The ggF is the dominant production mechanism for Higgs boson at the LHC. This process is a quantum loop process, where two gluons (g) emitted by incoming protons interact to produce a Higgs boson (H), with the help of a top quark loop. Although gluons are massless

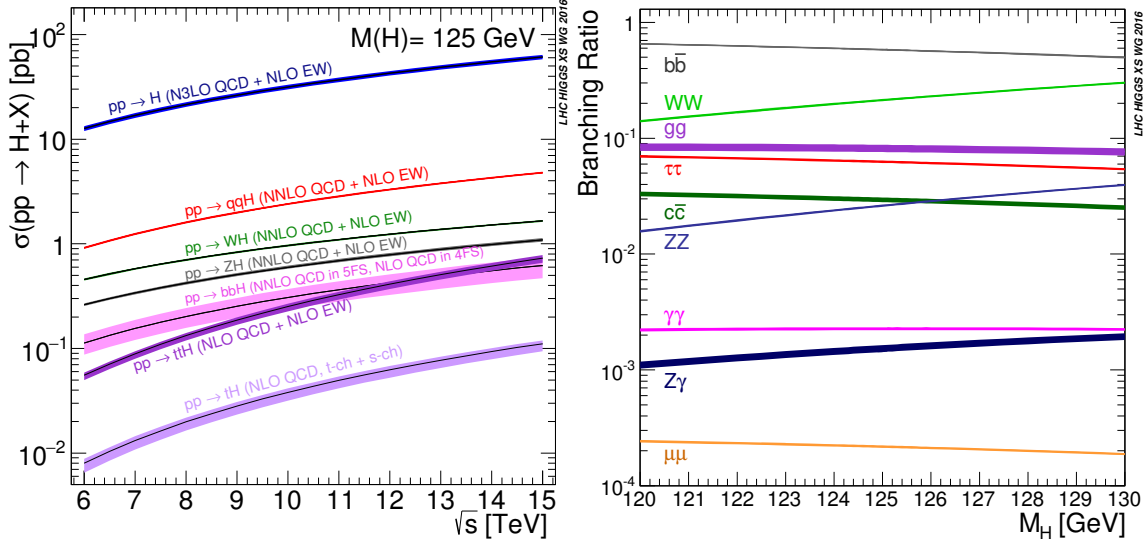


Figure 2–4 (Left) The production cross sections of the SM Higgs boson as a function of the center of mass energy, \sqrt{s} , for proton-proton collisions^[21]. The VBF process is denoted here as qqH . **(Right)** Branching ratios for the primary decays of the SM Higgs boson near a mass (m_H) of 125 GeV^[20]. Bands represent theoretical uncertainties.

$\sqrt{s}(\text{TeV})$	Production cross section (in pb) for $m_H = 125\text{GeV}$					
	ggF	VBF	WH	ZH	$t\bar{t}H$	total
7	$16.9^{+4.4\%}_{-7.0\%}$	$1.24^{+2.1\%}_{-2.1\%}$	$0.58^{+2.2\%}_{-2.3\%}$	$0.34^{+3.1\%}_{-3.0\%}$	$0.09^{+5.6\%}_{-10.2\%}$	19.1
8	$21.4^{+4.4\%}_{-6.9\%}$	$1.60^{+2.3\%}_{-2.1\%}$	$0.70^{+2.1\%}_{-2.2\%}$	$0.42^{+3.4\%}_{-2.9\%}$	$0.13^{+5.9\%}_{-10.1\%}$	24.2
13	$48.6^{+4.6\%}_{-6.7\%}$	$3.78^{+2.2\%}_{-2.2\%}$	$1.37^{+2.6\%}_{-2.6\%}$	$0.88^{+4.1\%}_{-3.5\%}$	$0.50^{+6.8\%}_{-9.9\%}$	55.1
14	$54.7^{+4.6\%}_{-6.7\%}$	$4.28^{+2.2\%}_{-2.2\%}$	$1.51^{+1.9\%}_{-2.0\%}$	$0.99^{+4.1\%}_{-3.7\%}$	$0.60^{+6.9\%}_{-9.8\%}$	62.1

Table 2–1 Production cross sections of the Standard Model Higgs boson, with a mass of 125 GeV, in proton-proton collision

and the Higgs boson couples to particles with mass, the strong coupling between gluons and top quarks allows this process via quantum loops. The process can be represented as $g + g \rightarrow H + X$. Given the high abundance of gluons in the proton at the LHC energies, this process has a high rate of occurrence, making it the primary channel for Higgs boson production at the LHC.

VBF is the second most common process for producing Higgs bosons at the LHC. In this process, the two protons each emit a W or Z boson, which then interact to produce the Higgs boson. This can be represented as $q + q \rightarrow q' + q' + H$, where q and q' are quarks.

Unlike ggF, this process is not a loop process but a t-channel process. The scattered quarks usually result in two forward jets in the detector, with the Higgs boson produced centrally. This characteristic jet activity often assists in distinguishing the VBF process from other production mechanisms.

2.3.2 Di-Higgs production

The production of two Higgs bosons, a process referred to as double Higgs boson production, is of significant interest due to the wealth of information it provides about the Higgs potential. Specifically, this process gives insights into the trilinear self-coupling of the Higgs. The primary mechanism for double Higgs production is through gluon fusion ($gg \rightarrow HH$), which accounts for more than 90% of the total cross-section. Figure 2-5 depicts the major Feynman diagrams for the production of two Higgs bosons via gluon fusion. These two diagrams interfere destructively, leading to a very small HH cross-section, namely $\sigma_{\text{ggF}, HH}^{SM} = 31.05 \pm 3\%$ (PDF+ α_s) $^{+6\%}_{-23\%}$ (Scale + m_{top}) fb, calculated at next-to-next-to-leading-order (NNLO) accuracy in the finite top-quark mass approximation for $m_H = 125$ GeV and $\sqrt{s} = 13$ TeV

Under the conditions at the LHC ($\sqrt{s} = 14\text{TeV}$), the cross-section for the bbH mode can reach up to 550fb, albeit this is still two orders of magnitude below the cross-section for ggF. It is noteworthy that in alternative models such as the two Higgs doublet model or a SUSY model, the Higgs self-coupling is proportional to the ratio of neutral Higgs boson vacuum expectation values. For large values of this ratio, the coupling undergoes significant amplification, potentially elevating the bbH mode to be the dominant mechanism for Higgs boson production, a deviation from the Standard Model predictions. Other sub-leading production mechanisms are also present, including VBF $HHjj$ ($\sigma_{\text{VBF}, HH}^{SM} = 1.726 \pm 2.1\%$ (PDF+ α_s) $^{+0.03\%}_{-0.04\%}$ (Scale) fb at $\sqrt{s} = 13\text{TeV}$) (Figure 2-6), HHW (0.50fb), HHZ (0.36fb), and $ttHH$ (0.8fb). QCD corrections, computed in the infinite top mass limit, significantly influence the cross-section, effectively doubling it from LO to NLO^[22] and further enhancing it by around 20% from NLO to NNLO^[23].

In the recent past, complete NLO corrections incorporating all top quark mass effects^[24] have been determined numerically. These findings reveal a k-factor less flat than that predicted in large top mass approximations^[24]. This unexpected dependency of the results on

the renormalisation scheme and scale for the top quark mass raises questions about the assessment of scale uncertainty and calls for a more accurate NNLO computation, although such a task is likely to remain challenging for some time.

On the differential level, the destructive interference between the box and triangle contributions makes the predictions made in the infinite top mass limit for both the HH invariant mass and the leading Higgs boson p_T distributions complex. With an inclusive cross-section of around 35 fb at $\sqrt{s} = 13$ TeV and challenging signal-background discrimination, the double Higgs boson production remains a difficult channel to probe and is expected to significantly benefit from the high-luminosity run of the LHC^[25].

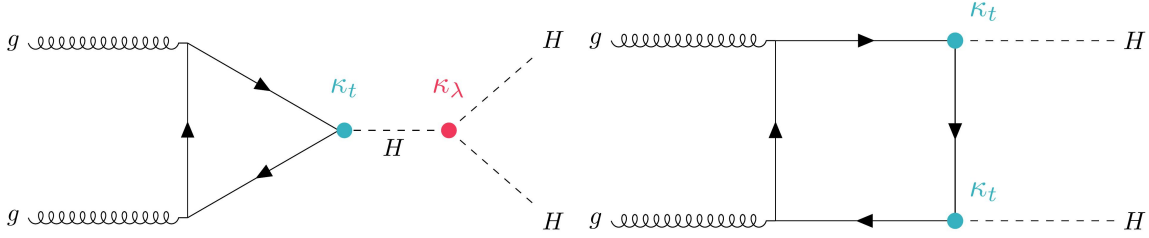


Figure 2-5 The major Feynman diagrams for the production of two Higgs bosons via gluon fusion. (Left) Triangle diagram sensitive to the self-coupling vertex κ_λ , (Right) Box diagram, which interferes destructively at the self-coupling vertex κ_λ .

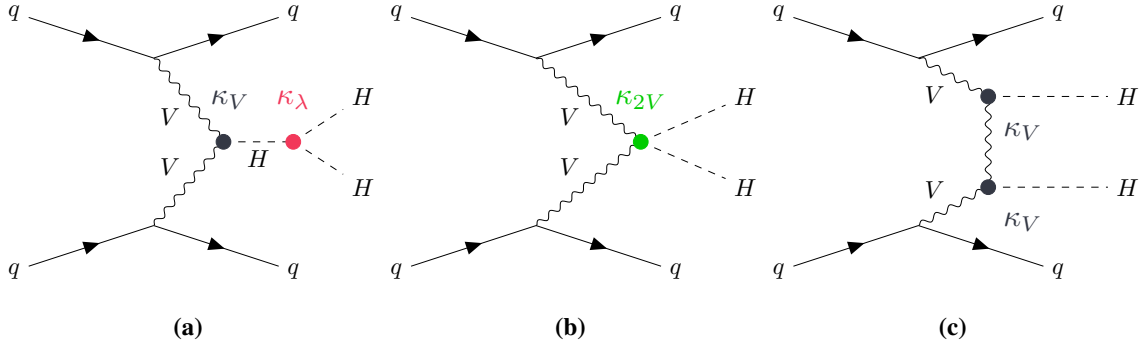


Figure 2-6 Depiction of Vector Boson Fusion (VBF) processes in Higgs boson pair production: (a) the VVHH vertex process, (b) the trilinear coupling, and (c) the VVH production mode.

Investigations into both resonant and non-resonant Higgs boson pair production can reveal intriguing insights into various BSM theories. Resonant production involves the creation of unstable, heavier particles that decay into two Higgs bosons, thereby forming a characteristic peak in the energy spectrum. Non-resonant production, however, involves processes

that create two Higgs bosons directly, without the intermediate step of a heavier particle. These mechanisms offer different perspectives and carry distinctive signatures, broadening the scope of the search for new physics. During Run 1 and Run 2, both ATLAS and CMS experiments performed searches for resonant and non-resonant Higgs boson pair production via the following channels:

1. $HH \rightarrow bb\gamma\gamma$,
2. $HH \rightarrow bb\tau^+\tau^-$,
3. $HH \rightarrow bbbb$,
4. $HH \rightarrow bbVV$,
5. $HH \rightarrow blll$,
6. Final states containing multiple leptons (electrons or muons), covering the WW^*WW^* , WW^*ZZ^* , ZZ^*ZZ^* , $ZZ^*\tau^+\tau^-$, $WW^*\tau^+\tau^-$, ZZ^*bb , and $\tau^+\tau^-\tau^+\tau^-$ channels,

2.4 Long-Lived Particles (LLPs) and Beyond Standard Model Search

Particle physics as a distinct field was demarcated by the discoveries of the muon in 1936 and the kaon in 1947. These particles exhibited macroscopic lifetimes detectable via early 20th-century cloud chamber technology. Transitioning to modern silicon trackers and time projection chambers has preserved the significance of measuring decay lengths. While the advent of large particle accelerators shifted focus to higher energies and luminosities, the measurement of particle lifetimes remains integral. This is evidenced by pivotal searches for exotic long-lived particles (LLPs) at earlier facilities like LEP^[26] and Tevatron^[27].

LLPs have always been considered critical for discoveries beyond the Standard Model, particularly in the context of supersymmetry. The theoretical paradigms have evolved to consider a broader range of LLP signatures, beyond hard signals like high-energy photons or jets^[28]. This expansion is also aided by a nuanced understanding of modern trigger and reconstruction algorithms, as well as background noise in LLP searches.

The study of LLPs has a rich theoretical and experimental background, with roles both in the discoveries within the Standard Model and in theories that extend it. LLPs are at the forefront of modern particle physics, offering sophisticated understandings of decay mechanisms and cosmological implications. In the SM, while most particles decay promptly, exceptions such as the neutron can have suppressed decay widths due to phase space suppression^[29-30].

In the context of the SM, LLPs can be produced through the decay of a heavier resonance Y , which can either be a Standard Model particle like the Higgs boson and the top quark, or can represent particles from new physics. These LLPs manifest certain common characteristics, such as production rate, decay length (d), and time dilation (γ), thereby offering a unified framework for analysis.

The connection between LLPs and the Higgs boson is especially compelling. The Higgs mechanism, responsible for electroweak symmetry breaking and mass acquisition for W and Z bosons, could also serve as a conduit to new, uncharted sectors in particle physics. Specifically, the Higgs boson, given its scalar nature and coupling structure, could decay into exotic states, thereby producing LLPs that can be detected.

In summary, Higgs-induced LLPs offer a unique lens through which both the structural properties of the Higgs sector and realms of new physics can be investigated. Parameters such as production rate, decay length, and time dilation are pivotal in determining the detectability and interpretability of such exotic decay events. Consequently, the continued study of LLPs produced via Higgs decay is a promising avenue for discovering new physics beyond the Standard Model.

Chapter 3 The Large Hadron Collider and ATLAS Experiment

The Large Hadron Collider (LHC)^{[B1][B2]} and the ATLAS experiment^[B3] are two of the most significant scientific endeavors of the modern era. They represent the culmination of decades of research and development, as well as the collaborative efforts of thousands of scientists from around the world.

The history of the LHC and ATLAS experiment is a testament to humanity's unrelenting quest for knowledge. It all began in the aftermath of the Second World War, when a war-torn Europe sought avenues for unity, collaboration, and rediscovery of its scientific prowess. In 1954, the European Organization for Nuclear Research^[B4], or CERN, was established, marking a new dawn for European physics. Located near Geneva at the Franco-Swiss border, CERN became a beacon of international collaboration.

The years that followed saw CERN launching multiple accelerators, each more sophisticated than its predecessor. The Proton Synchrotron, completed in 1959, was a marvel of its time, accelerating protons to energies previously unattained. But the scientists at CERN had a grander vision.

By the late 1980s, the Large Electron-Positron Collider^[L5] (LEP) was inaugurated. It was an accelerator designed to collide electrons and positrons at energies that allowed the discovery of the W and Z bosons. These particles, crucial to the electroweak theory, solidified the Standard Model's foundations.

However, while the LEP was a significant achievement, the dream for an even grander machine was taking shape. The field of particle physics was abuzz with questions surrounding the Higgs boson, a particle that had been theorized in the 1960s but had eluded detection. The LHC was envisioned as a solution to this problem.

Conceived in the 1980s and 1990s, the LHC was a monumental undertaking, not only in terms of physics but also engineering. To house such a colossal machine, CERN's underground tunnel, previously used for LEP, was repurposed, marking an evolution from electron-positron collisions to hadron collisions.

But a machine of the LHC's caliber required detectors of exceptional finesse. This need

birthed the ATLAS experiment. Beginning in the early 1990s, ATLAS was an audacious plan, with its blueprint promising unparalleled resolution and detection capabilities. The experiment was to be a melting pot of international collaboration, with scientists, engineers, and students from around the globe contributing to its design, construction, and eventual data analysis. The name "ATLAS" was reminiscent of the Titan of Greek mythology, reflecting the experiment's grandeur and ambition.

The years of meticulous planning and construction bore fruit in 2008 with the LHC's inauguration. The world watched with bated breath, and in 2012, a groundbreaking announcement followed: the discovery of the Higgs boson by the ATLAS and CMS experiments. This seminal moment was not just a triumph for CERN but also a testament to decades of collaborative science, realizing Peter Higgs' and other physicists' 1960s vision.

The LHC and ATLAS are not just about the Higgs boson, however. They represent the spirit of scientific inquiry. This chapter provides broad information about the LHC and ATLAS experiments. Section 3.1 discusses the design and general information of the accelerator, as well as its current operational status. Section 3.2 introduces the ATLAS experiment, from the subsystems of the detector to its performance.

3.1 Introduction to the Large Hadron Collider (LHC)

3.1.1 Accelerator design and parameters

The complex array of accelerators at CERN has been meticulously constructed to prepare and accelerate beams of particles to unprecedented energies, with each accelerator playing a distinct role. The pipeline's efficiency ensures that particles, mainly protons, achieve near-light speeds, making them fit for the high-energy collisions that the LHC facilitates. Followed the details of the accelerator system shown in figure 3-1, the journey of the particles go through 5 main stages:

- **Linear Accelerators:** Particles begin in the Linac 4, a linear accelerator. Here, protons are derived from hydrogen gas by stripping away the electrons from hydrogen atoms. These protons are then accelerated to an energy of about 160 MeV using radio-frequency quadrupole (RFQ) and drift tube linac (DTL) structures.
- **Proton Synchrotron Booster (PSB):** After Linac 4, the protons move to the PSB. This

is where they are grouped into bunches and further accelerated. Using magnetic fields, the PSB boosts the protons to energies up to 2 GeV.

- **Proton Synchrotron (PS):** The next phase of acceleration occurs in the PS. A circular accelerator with a circumference of approximately 628 meters, the PS elevates the proton energies to 25 GeV. The PS is also responsible for compressing the proton bunches, ensuring they're even tighter and more focused before they're passed onto the next stage.
- **Super Proton Synchrotron (SPS):** Acting as the final preparatory accelerator before the LHC, the Super Proton Synchrotron is a large circular accelerator with a circumference of 7 kilometers. Here, the proton bunches are further accelerated to energies of 450 GeV. Beyond serving the LHC, the SPS has its own experimental halls and has been pivotal in numerous significant discoveries in particle physics over the years.
- **Large Hadron Collider (LHC):** The culmination of this sequential system is the LHC, where the protons, now moving at 99.9999991% of the speed of light, undergo their final acceleration. Within the LHC's 27-kilometer ring, the protons reach energies up to 6.5 TeV. The LHC's twin beam pipes ensure that proton bunches can be accelerated and steered in opposite directions, leading to head-on collisions at four main interaction points where the primary experiments are situated.

The complex infrastructure of the LHC's accelerators is characterized by a series of technical parameters, fundamental to understanding their capabilities. There's a summary of some basic beam parameters of the accelerators in table [3-1](#).

The starting point, Linac 4, accelerates protons to an energy of 160 MeV. From here, they are directed to the Proton Synchrotron Booster (PSB), where their energy is further boosted to 2 GeV. The Proton Synchrotron (PS) then takes over, its 628-meter circumference serving to escalate the proton energy to 25 GeV. Beyond this, the Super Proton Synchrotron (SPS), with its vast 7-kilometer ring, elevates the energy of these protons to 450 GeV. Ultimately, the protons find their way to the LHC, where they are accelerated to a staggering 6.5 TeV per beam, resulting in a collision energy of 13 TeV.

In the LHC, approximately 2,808 bunches are operated per beam. Intriguingly, each of these bunches holds roughly 1.2×10^{11} protons, leading to a dense traffic of particles that enhance the collision chances. The measure of this potential for collisions is captured by the

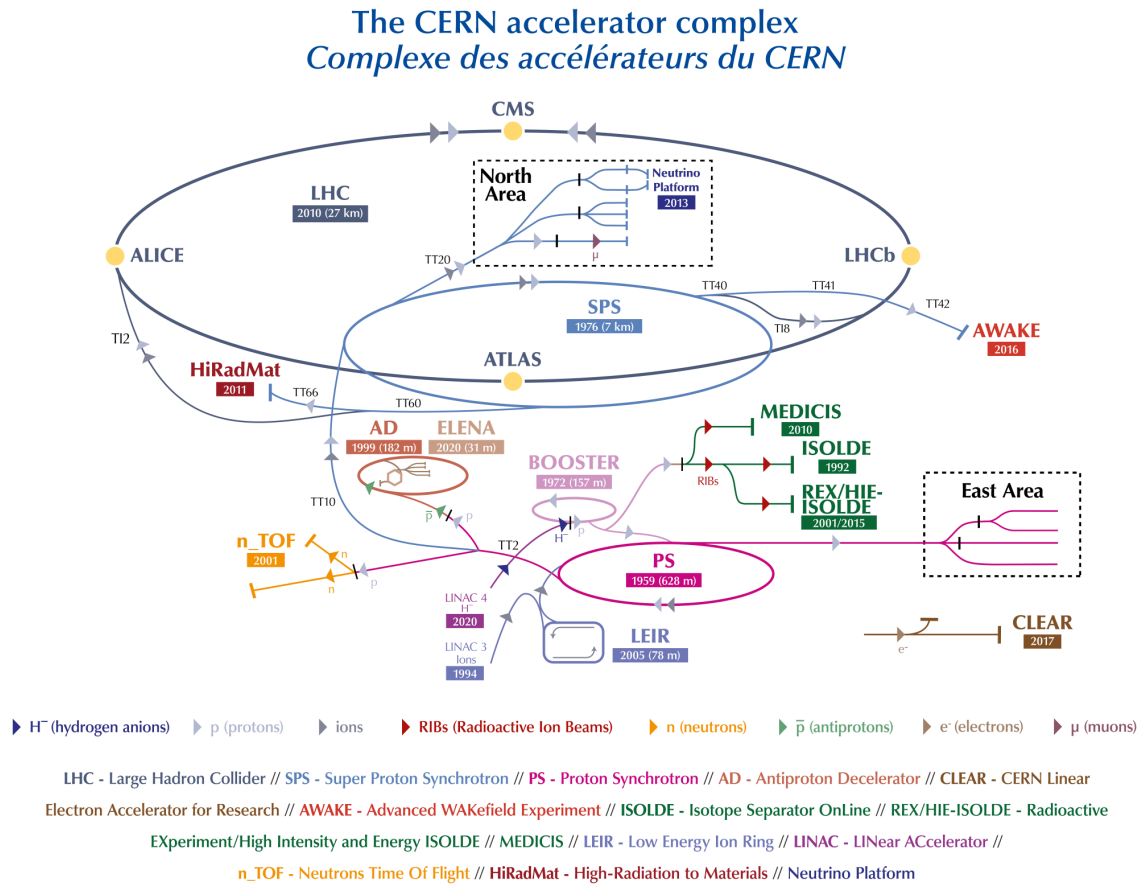


Figure 3–1 Diagram of CERN’s sequential accelerator system^[8].

concept of luminosity. For the LHC, its peak luminosity stands around $1 \times 10^{34} \text{ cm}^{-2} \text{ s}^{-1}$, a figure indicative of the LHC’s exceptional capability to produce particle interactions.

Complementing this data, it’s worth noting the LHC’s revolution frequency, registering at about 11.245 kHz. When it comes to beam operations, after being injected into the LHC at 450 GeV, the energy of the beam is ramped up to its operational 6.5 TeV in a timespan of approximately 20 minutes.

The accelerator works at a chilling 1.9 K. This ultra-cold environment is essential to ensure the superconducting state of its magnets, which in turn produce a magnetic field of 8.33 T, a critical factor in directing the high-energy beams along the 27-km ring.

machine	L[m]	relative	ρ [m]	beam momentum [GeV/c]	bunches
LINAC	30		-	10^{-4}	4×2
PSB	157		8.3	0.05	4×2
PS	628.318	1	70.676	1.4	72
SPS	6911.56	$11 \times$ PS	741.257	26	4×72
LHC	26658.883	$27/7 \times$ SPS	2803.98	450	2×2808

Table 3–1 Circumference, curvature radius ρ , and beam momentum upon injection for the primary accelerators in the LHC injection sequence^[32].

The instantaneous luminosity is given by

$$L = \frac{N_1 N_2 n_b f_{\text{rev}}}{\pi \sqrt{(\sigma_{x,1}^2 + \sigma_{x,2}^2)} \sqrt{(\sigma_{y,1}^2 + \sigma_{y,2}^2)}} FH, \quad (3-1)$$

where:

- f_{rev} is the revolution frequency,
- n_b is the number of bunches colliding at the IP,
- $N_{1,2}$ represent the number of particles in each bunch,
- $\sigma_{x,1,2}$ and $\sigma_{y,1,2}$ are the horizontal and vertical beam sizes of the colliding bunches respectively,
- F signifies the geometric luminosity reduction factor due to transverse offset or crossing angle collisions at the IP,
- H denotes the reduction factor for the hourglass effect significant when the bunch length is similar or larger than the β -functions at the IP.

Assuming round beams at the IP and neglecting any spurious dispersion at the IP one can write the instantaneous luminosity in the LHC IPs as:

$$L = \frac{\gamma f_{\text{rev}} n_b N_b^2}{4\pi \epsilon_n \beta^*} F. \quad (3-2)$$

Maximizing the instantaneous luminosity in the LHC therefore implies (in order of priority):

- Ensure optimum overlap of the two beams at the IP, which for head-on collisions entails matching the optics functions and steering the beam orbits transversely.
- Minimize beam size at the IPs. This doesn't necessarily increase total beam power but demands adequate aperture.

- Increase the number of particles per bunch.
- Maximize the number of bunches in the collider. In the LHC, operating with more than 150 bunches necessitates a crossing angle at the IP to prevent undesired parasitic beam interactions.

3.1.2 Operation status

In the context of assessing the operational status of the LHC, it is paramount to examine the data from its detectors, as the collider itself does not record collision outcomes. Among the suite of detectors around the LHC's ring, ATLAS stands as one of the primary general-purpose instruments, meticulously capturing a wide range of physics events. Given our affiliation with the ATLAS collaboration, and its comprehensive dataset covering numerous runs and periods, we will focus on the data from ATLAS to provide an illustrative example of the LHC's operational status over the years. The following figures and tables offer a detailed insight into the luminosities achieved and the associated uncertainties throughout different operational periods.

The graph on the left of Figure 3-2 details the evolution of luminosity delivered to ATLAS across the years 2011 to 2018. This measurement pertains specifically to stable beams and high-energy proton-proton (p-p) collisions. The LHC's primary function is to provide high luminosity, ensuring that ATLAS and other experiments have a sufficient number of collision events to carry out precision measurements and search for new phenomena. The increase in luminosity over the years is a testament to the constant enhancements in the LHC's machine operation and maintenance. Each point on the curve represents a specific operational period, and the rise in luminosity can be attributed to various machine upgrades, operational optimizations, and the introduction of more intense beams. The increase in delivered luminosity means that a larger number of collisions is available for data analysis, thus enhancing the potential for scientific discoveries.

While the right one offers insight into the average interactions per crossing from 2015 to 2018 at a center-of-mass energy of 13 TeV. During this phase, the LHC resumed operations after its initial extended shutdown, operating at an energy level nearly double that of its inaugural run, signaling a significant advancement in its operational capabilities. The displayed data encompasses all records from ATLAS during stable beams within this time frame. A

key feature of the graph is the indication of the integrated luminosity and the mean value of μ (denoted as the average number of interactions per crossing). This average is aligned with the Poisson distribution's mean, a statistical measure used to predict the probability of events in a fixed interval of time or space. The formula $\mu = \mathcal{L}_{\text{bunch}} \times \sigma_{\text{inel}} / f$ used in the caption provides a method for calculating this average. Here, $\mathcal{L}_{\text{bunch}}$ represents the instantaneous luminosity for each bunch. In layman terms, it measures the density of particles in a specific beam bunch. On the other hand, σ_{inel} denotes the inelastic cross-section, with its value approximated at 80 mb for 13 TeV collisions. It provides a measure of the probability of a particular interaction between particles. Lastly, f stands for the LHC revolution frequency, indicating how frequently the particles in the beam complete one circuit of the main ring of the accelerator. In collider physics, the number of interactions per crossing determines the event complexity. A higher value means more simultaneous interactions. This increases the chance of significant events, but also requires advanced techniques to isolate desired signals from numerous interactions.

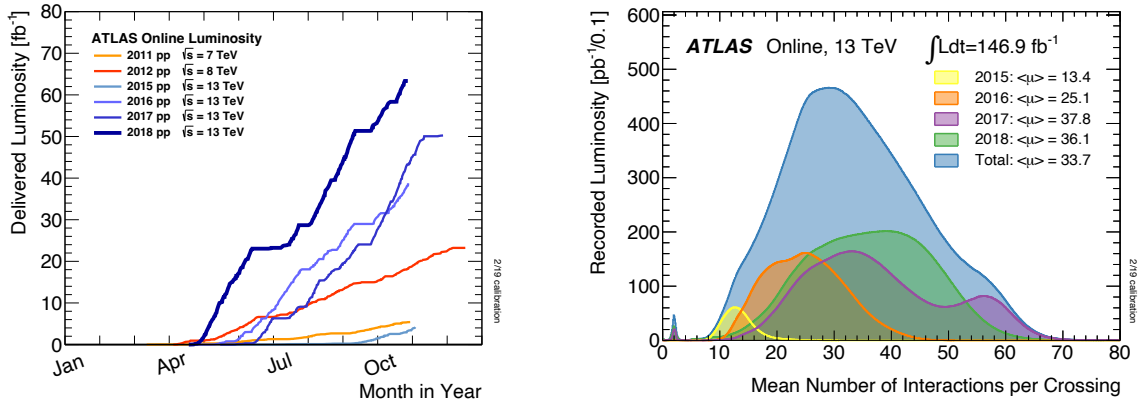


Figure 3–2 Public ATLAS Luminosity Results for Run-2 of the LHC^[36]. **Left: Delivered Luminosity Over Time (2011-2018):** The graph depicts the cumulative luminosity delivered to ATLAS as a function of time during stable beams and for high-energy p-p collisions. **Right: Interactions per Crossing (2015-2018 at 13 TeV):** This illustration showcases the luminosity-weighted distribution of the average interactions per crossing. The data encompasses all records from ATLAS during stable beams between 2015 and 2018. The integrated luminosity and the mean μ value are indicated. The average interactions per crossing align with the Poisson distribution's mean, ascertained for each bunch.

In the ATLAS experiment during the LHC Run 2 at $\sqrt{s} = 13$ TeV, a comprehensive summary of integrated luminosities, post rigorous data-quality checks, is provided in Table 3–2.

Data sample	2015	2016	2017	2018	Comb
Integrated luminosity [fb^{-1}]	3.24	33.40	44.63	58.79	140.07
Total uncertainty [fb^{-1}]	0.04	0.30	0.50	0.64	1.17
Uncertainty contributions [%]:					
Statistical uncertainty	0.07	0.02	0.02	0.03	0.01
Fit model*	0.14	0.08	0.09	0.17	0.12
Background subtraction*	0.06	0.11	0.19	0.11	0.13
FBCT bunch-by-bunch fractions*	0.07	0.09	0.07	0.07	0.07
Ghost-charge and satellite bunches*	0.04	0.04	0.02	0.09	0.05
DCCT calibration*	0.20	0.20	0.20	0.20	0.20
Orbit-drift correction	0.05	0.02	0.02	0.01	0.01
Beam position jitter	0.20	0.22	0.20	0.23	0.13
Non-factorisation effects*	0.60	0.30	0.10	0.30	0.24
Beam-beam effects*	0.27	0.25	0.26	0.26	0.26
Emittance growth correction*	0.04	0.02	0.09	0.02	0.04
Length scale calibration	0.03	0.06	0.04	0.04	0.03
Inner detector length scale*	0.12	0.12	0.12	0.12	0.12
Magnetic non-linearity	0.37	0.07	0.34	0.60	0.27
Bunch-by-bunch σ_{vis} consistency	0.44	0.28	0.19	0.00	0.09
Scan-to-scan reproducibility	0.09	0.18	0.71	0.30	0.26
Reference specific luminosity	0.13	0.29	0.30	0.31	0.18
Subtotal vdM calibration	0.96	0.70	0.99	0.93	0.65
Calibration transfer*	0.50	0.50	0.50	0.50	0.50
Calibration anchoring	0.22	0.18	0.14	0.26	0.13
Long-term stability	0.23	0.12	0.16	0.12	0.08
Total uncertainty [%]	1.13	0.89	1.13	1.10	0.83

Table 3–2 Summary of integrated luminosities post standard data-quality checks, alongside uncertainties for the calibration of each yearly data sample from Run 2 pp at $\sqrt{s} = 13$ TeV, including the cumulative sample^[37]. The table presents the integrated luminosities, total uncertainties, a detailed split of contributions to the vdM calibration’s absolute accuracy, extra uncertainties associated with the physics data sample, and the overall relative uncertainty in percentage.

The luminosity data span the years 2015 to 2018, presenting an ascending trend: from 3.24 fb^{-1} in 2015, the values increase progressively to 33.40, 44.63, and 58.79 fb^{-1} in 2016, 2017, and 2018, respectively. The cumulative sample across these years totals an impressive 140

fb^{-1} . This table not only enumerates the integrated luminosities for each year but also delves into the specific uncertainties associated with the calibration of each yearly data sample. Importantly, certain contributors to uncertainty, marked with an asterisk (*), are considered to be fully correlated across the years. In contrast, other sources of uncertainty are treated as uncorrelated. This meticulous breakdown serves as an essential resource, quantifying both the vast amount of collision data ATLAS has accumulated during this period and the precision with which the luminosity measurements were made. The various factors influencing the absolute accuracy of the vdM calibration and the overall relative uncertainty percentages further underscore the diligence and detail invested in these measurements.

3.2 The ATLAS Experiment

3.2.1 Overview and scientific goals

Situated at CERN, the European Organization for Nuclear Research, the ATLAS (A Toroidal LHC ApparatuS) experiment is one of the largest collaborative efforts in the domain of experimental particle physics. It is a general-purpose particle detector with a forward-backward symmetric cylindrical geometry and nearly $4 - \pi$ coverage in solid angle. ATLAS is not just an experiment, but a testament to international collaboration, with over 3,000 physicists from 38 countries and 180 institutions coming together for a common scientific pursuit. It stands as tall as a five-story building at about 25 meters and stretching 44 meters in length. It weighs approximately 7,000 tons.

ATLAS is a particle detector that has several scientific goals^[88]. One of its primary goals is to search for the Higgs boson, a particle predicted by the Standard Model to explain why other particles possess mass. This quest bore fruit in 2012 when the ATLAS and CMS collaborations announced the discovery of the Higgs boson. ATLAS is also constantly searching for discrepancies with Standard Model predictions that could be indicative of new physics phenomena, including probing supersymmetry, a popular extension to the Standard Model, and hunting for dark matter candidates directly or via potential mediators. In addition, by analyzing lead-lead ion collisions, ATLAS seeks to understand the state of matter known as quark-gluon plasma, which is believed to have been prevalent shortly after the Big Bang. Finally, ATLAS aims to provide a deeper understanding of the forces and particles that make up

our universe. It investigates the properties of the top quark, probes the electroweak symmetry breaking mechanism, and studies various aspects of quantum chromodynamics.

The conceptualization of the ATLAS detector was influenced by a range of intricate physics analyses. The fundamental design principles of the detector were shaped around the following core objectives^[88-89]:

- Achieve superior electromagnetic calorimetry to accurately identify and measure electrons and photons. This should be supplemented by comprehensive hadronic calorimetry to ensure precise measurements of jets and missing transverse energy (E_T^{miss}).
- Ensure high-precision measurements of muon momentum. The design must facilitate accurate measurements even at peak luminosity, relying primarily on the external muon spectrometer.
- Maintain efficient tracking capabilities during high luminosities. This is vital for measurements of high- p_T lepton momentum, identification of electrons, photons, τ -leptons, and heavy flavors, as well as enabling a complete event reconstruction during periods of lower luminosity.
- The detector must offer a broad acceptance in pseudorapidity (η), combined with nearly complete azimuthal angle (ϕ) coverage. Here, ϕ denotes the angle measured around the beam's axis, while η is associated with the polar angle (θ), where θ represents the angle from the z-direction.
- The design should support low- p_T threshold triggers and measurements, ensuring high-efficiency capture of most physics processes that are integral to LHC operations.

The fundamental design principles of the ATLAS detector were meticulously crafted to cater to a spectrum of intricate physics studies. These principles revolve around ensuring precise measurements, large acceptance, and robust performance even under the challenging environment of high luminosities. Each subsystem^[89] of the detector is designed with specific characteristics that when combined, form the complete and formidable capability of the ATLAS detector.

- **Magnet Configuration:** The detector is equipped with an inner superconducting solenoid, surrounding the inner detector, and large external superconducting toroids having an eight-fold symmetry.
- **Inner Detector (ID):** Situated within a 7 m by 1.15 m cylinder, the ID functions in a

2 T solenoidal magnetic field. The inner part comprises semiconductor pixel and strip detectors for accuracy, while the outer portion contains straw-tube trackers ensuring a wide tracking range.

- **Calorimetry:** Liquid-argon (LAr) electromagnetic calorimetry offers precise energy and position measurements up to $|\eta| < 3.2$. The end-caps, using LAr technology, stretch this to $|\eta| = 4.9$. Most hadronic measurements come from the uniquely designed scintillator-tile calorimeter, segmented into a barrel and two extended barrels.
- **Dimensions and Weight:** The LAr calorimetry is contained in a 2.25 m by ± 6.65 m cylinder. Adjacent to it, the tile calorimeter spans an outer radius of 4.25 m and a half-length of 6.10 m, together weighing around 4,000 Tons.
- **Muon Spectrometer:** Surrounding the calorimeters, the spectrometer features an air-core toroid system. It boasts three stations of high-precision tracking chambers, ensuring stellar muon momentum resolution, supplemented by rapid-response trigger chambers.
- **Overall Dimensions:** The muon spectrometer determines the detector's vast scale. Its boundaries, at about 11 m in radius, combined with the 12.5 m barrel toroid coils and 23 m distant forward muon chambers, sum up the detector's total weight to an impressive 7,000 Tons.

The ATLAS detector is designed with a comprehensive framework consisting of various subsystems and components, of which a computer generated image is shown in figure 3-3. These elements collectively contribute to its functionality, enabling it to fulfill its scientific objectives effectively. In the subsequent sections, we will provide a detailed explanation of each subsystem, outlining its design, functionality, and its vital role within the broader goals of the ATLAS experiment.

3.2.1.1 Detector Coordinate

The LHC beam's direction sets the z-axis, while the x-y plane is perpendicular to this beam direction. The positive x-axis extends from the interaction point towards the LHC ring's center, and the positive y-axis points upward. The azimuthal angle, ϕ , is determined around the beam direction, while θ represents the angle from this axis. Pseudorapidity is expressed as η , defined as $\eta \equiv -\ln \tan(\theta/2)$. Both the transverse momentum $p_T = \sqrt{p_x^2 + p_y^2}$

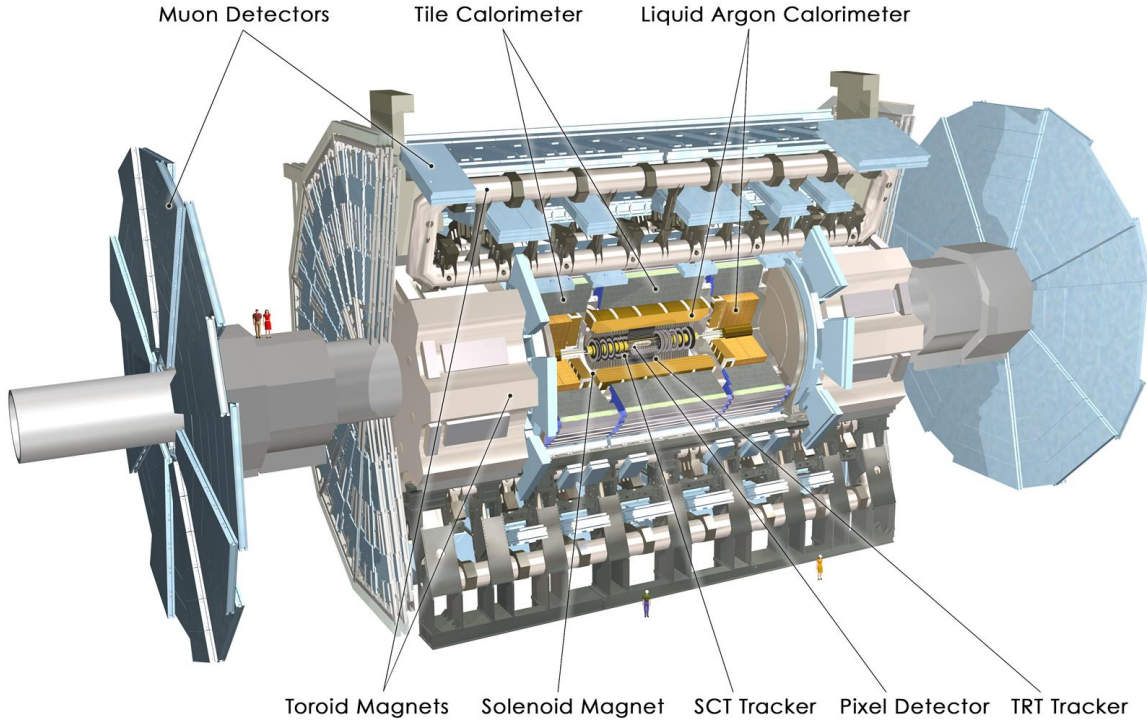


Figure 3–3 The layout of the whole ATLAS detector^[40].

and the transverse energy $E_T = \sqrt{p_T^2 + m^2}$, as well as the missing transverse energy E_T^{miss} , are generally defined in the x-y plane. The distance ΔR in $\eta - \phi$ space is given by $\Delta R = \sqrt{\Delta^2 \eta + \Delta^2 \phi}$.

Charged particle trajectories in a consistent magnetic field are characterized using five parameters of a helix. In ATLAS, a specific helix parameterization ($d_0, z_0, \theta, \phi, q/p$) is employed, which is shown in figure 3–4, considering all measurements at the point nearest to the beam line where x and y are zero. Parameters in x – y plane are:

- d_0 : The transverse impact parameter, which is the sideways distance from the beam axis at the closest approach point. Its sign is determined by the reconstructed angular momentum of the track around the axis.
- ϕ : Azimuthal angle, where $\tan \phi \equiv p_y/p_x$, ranged from $[0, \pi]$.
- q/p_T : The charge-to-momentum ratio in the transverse plane. "q" is the charge of the particle (either +1 or -1 for singly charged particles) and " p_T " is the transverse

momentum. It determines the curvature of the trajectory.

Parameters in the $R - z$ plane are:

- θ : the polar angle, where $\cot \theta \equiv p_z/p_T$.
- z_0 : The longitudinal impact parameter, which is the z -coordinate of the track at the closest approach point.

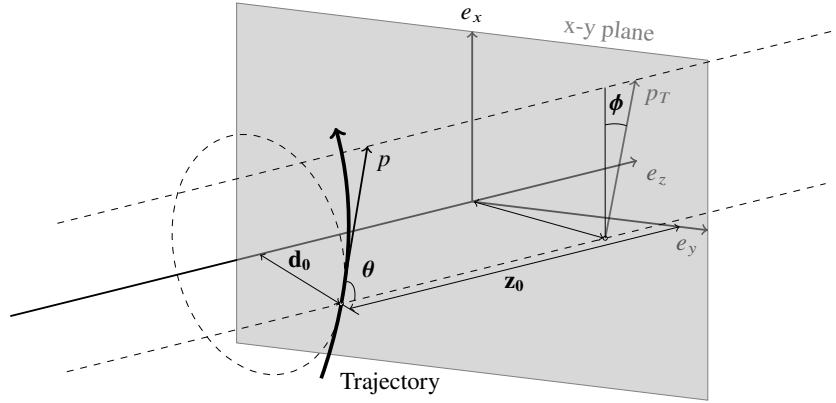


Figure 3-4 Illustration of the global track coordinate with respect to perigee.

3.2.2 Detector subsystems and components

In this section, a comprehensive overview of the subsystems that constitute the ATLAS detector is provided, progressing from the innermost components to the outer structures. Each subsystem is pivotal in the detection, tracking, and measurement of particles, contributing to the high precision and reliability for which the ATLAS detector is known. The performance characteristics of these integral components are summarized in Table 3-3.

3.2.2.1 Inner tracking system

In every 25 ns proton bunch collision event, approximately 1,000 particles emerge from the collision point, producing extremely dense tracks within the detector region of $|\eta| \leq 2.5$. To achieve the momentum and vertex requirements necessary for measuring critical physical processes, a fine granularity of the detector is essential for precise measurements. The ATLAS Inner tracking system is pivotal in this context and is responsible for detecting and measuring these charged particles. Designed to offer full tracking coverage over $|\eta| \leq 2.5$, it employs high-resolution detectors at inner radii and continuous tracking elements at outer radii. The incorporation of Semiconductor Tracking (SCT) detectors and the TRT

Subdetectors	Resolution	η coverage	
		Measurement	Trigger
Trackers	$\sigma_{p_T}/p_T = 0.05\% p_T \oplus 1\%$	± 2.5	
ECAL	$\sigma_E/E = 10\% \sqrt{E} \oplus 0.7\%$	± 3.2	± 2.5
HCAL(jets)			
Barrel & Cap	$\sigma_E/E = 50\% \sqrt{E} \oplus 3\%$	± 3.2	± 3.2
Forward	$\sigma_E/E = 100\% \sqrt{E} \oplus 10\%$	$3.1 < \eta < 4.9$	$3.1 < \eta < 4.9$
Muon Spectrometer	$\sigma_{p_T}/p_T = 10\%$ at $p_T = 1\text{TeV}$	± 2.7	± 2.4

Table 3–3 Summary of the resolution and η coverage for various subdetectors. ECAL and HCAL represent for electromagnet calorimeter and hadronic calorimeter, respectively. The listed resolutions for trackers and the ECAL are parametrized forms dependent on either p_T or E (in GeV), while the Muon Spectrometer provides a specific resolution at a given p_T value. The η coverage is further categorized into measurement and trigger regions.

(Transition Radiation Tracker) further accentuates the precision of these measurements.

The Inner Detector (ID) is mechanically divided into three units^[41]:

- **Pixel Detector:** The pixel detector, positioned closest to the interaction point in the ATLAS Inner Detector, provides three high-precision measurements across its full acceptance, aiding in identifying short-lived particles like b-quarks and τ -leptons. With its 140 million elements, each sized $50\text{ }\mu\text{m}$ in the $R - \phi$ direction and $300\text{ }\mu\text{m}$ in z , the pixel detector offers unambiguous two-dimensional space point segmentation. It comprises three barrels at average radii of approximately 4 cm, 11 cm, and 14 cm, complemented by four disks on each side, spanning radii from 11 to 20 cm. This modular system consists of about 1500 identical barrel modules and 1000 disk modules. Each barrel module, measuring 62.4 mm by 22.4 mm, is equipped with 61440 pixel elements, serviced by 16 readout chips. The design ensures overlapping modules for hermetic coverage, and the thickness of each layer in the simulation is less than 1.39% of a radiation length.
- **Semiconductor Tracker (SCT):** The SCT system, positioned in the intermediate radial range of the ATLAS Inner Detector, provides four precision measurements per track, contributing to momentum, impact parameter, vertex positioning, and pattern

recognition via its high granularity. The SCT system boasts a significantly larger surface area compared to previous silicon microstrip detectors, and it is designed to withstand radiation intensities that can modify the inherent characteristics of its silicon wafers. The barrel SCT utilizes four layers of silicon microstrip detectors, each measuring $6.36 \times 6.40 \text{ cm}^2$ with 768 readout strips at an $80 \text{ }\mu\text{m}$ pitch. A module encompasses four detectors, and the system's readout comprises a front-end amplifier and discriminator connected to a binary pipeline. The detector covers a surface of 61 m^2 , having 6.2 million readout channels, offering a spatial resolution of $16 \text{ }\mu\text{m}$ in $R-\phi$ and $580 \text{ }\mu\text{m}$ in z . This structure is further enhanced with specific design elements for cooling, and thermal stability, using materials with minimal thermal expansion coefficients and a unique cooling method employing a methanol-water mixture.

- **Transition Radiation Tracker (TRT):** The TRT employs straw detectors, recognized for their capability to handle very high rates due to their small diameter and the isolation of their sense wires. Enhanced by xenon gas, these detectors can identify electrons by detecting transition-radiation photons produced in a specific radiator positioned between the straws. The design accommodates the LHC's high counting rates and large occupancy. Each straw is 4 mm in diameter and can span up to 150 cm in length. In total, the system integrates about 420,000 electronic channels which offer a spatial resolution of $170 \text{ }\mu\text{m}$ per straw. The barrel structure encompasses modules that range radially from 56 to 107 cm . In contrast, the two end-caps are structured with 18 wheels, covering various radial ranges to maintain consistent straw crossing. The system's design priority is to deliver high performance under substantial occupancy and counting rates. Even at peak rates, the majority of straws provide accurate drift time measurements, ensuring a track measurement precision under $50 \text{ }\mu\text{m}$. The TRT enhances the momentum measurement precision in the Inner Detector and plays a pivotal role in pattern recognition and electron-hadron differentiation.

The fundamental design specifications and space-point measurement resolutions are detailed in Table 3-4. Additionally, an overview and a cross-sectional view of the Inner Detector, showing layers from the innermost to the outermost, is provided in Figure 3-5.

System	Position	Area (m ²)	Resolution σ (μm)	Channels (10 ⁶)	η coverage
Pixels	1 removable barrel layer	0.2	$R\phi = 12, z = 66$	16	± 2.5
	2 barrel layers	1.4	$R\phi = 12, z = 66$	81	± 1.7
	4 end-cap disks on each side	0.7	$R\phi = 12, R = 77$	43	$1.7 - 2.5$
Silicon strips	4 barrel layers	34.4	$R\phi = 16, z = 580$	3.2	± 1.4
	9 end-cap wheels on each side	26.7	$R\phi = 16, R = 580$	3.0	$1.4 - 2.5$
TRT	Axial barrel straws		170 (per straw)	0.1	± 0.7
	Radial end-cap straws		170 (per straw)	0.32	$0.7 - 2.5$

Table 3–4 Inner Detector Parameters and Resolutions^[41]: The provided resolutions are indicative values (the precise resolution in each detector varies with $|\eta|$).

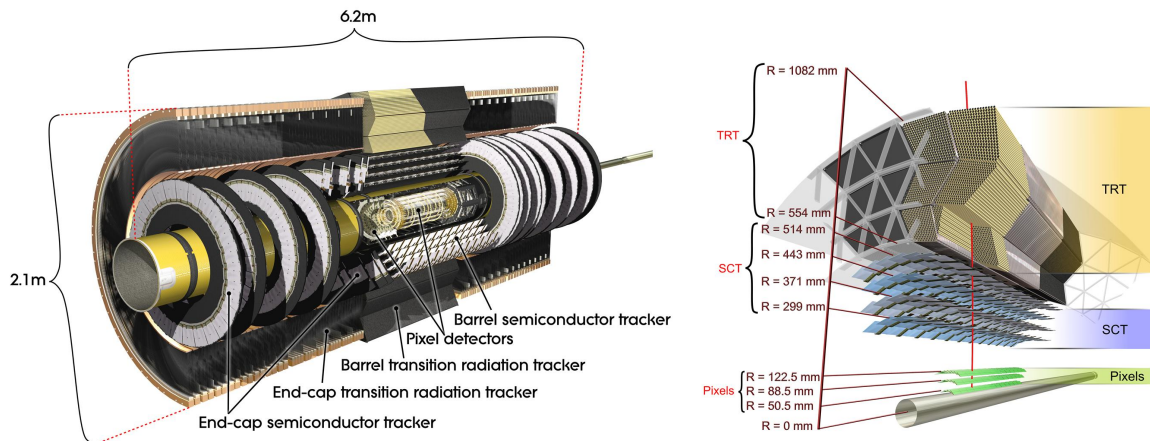


Figure 3–5 The layout of the ATLAS Inner Detector^[42]. Left: Overview of the ID; Right: Cross-sectional view of the Inner Detector, with layers from innermost to outermost being the pixel detector, SCT, and TRT.

3.2.2.2 Electromagnetic and hadronic calorimeters

The physics requirements for calorimeters at LHC^[43], are of utmost importance. They must accurately measure the energy and position of electrons and photons, the energy and direction of jets, and the missing transverse momentum of events. Particle identification, event selection at the trigger level, and high radiation resistance are also crucial. The LHC's high luminosity and energy range require fast detector response, fine granularity, and rejec-

tion of backgrounds such as jets faking photons. The performance specifications come from benchmark channels such as the search for a Higgs boson through the decays $H \rightarrow \gamma\gamma$ and $H \rightarrow 4e$, and the search for heavy vector bosons (W' , Z') with masses up to 5 – 6 TeV through the decays $W' \rightarrow e\nu$ and $Z' \rightarrow e^+e^-$. The SM Higgs search imposes specific requirements on the hadronic calorimetry, such as $W \rightarrow jj$ mass reconstruction, forward jet tagging, and $H \rightarrow b\bar{b}$ mass reconstruction using jet spectroscopy. These requirements are critical for discovering high and low mass Higgs bosons, studying top physics, and detecting non-interacting particles in supersymmetric models.

The ATLAS Electromagnetic calorimeter^[43] (ECAL) has stringent requirements tailored to its pivotal role in ATLAS experiments. It boasts a broad rapidity coverage and possesses the capability to reconstruct electrons within an energy range spanning from 1 – 2 GeV up to 5 TeV. In terms of energy resolution, the device excels, demonstrating exceptional performance over the energy bracket of 10 – 300 GeV. With a structural robustness, it maintains a total thickness of at least 24 radiation lengths at $\eta = 0$. Its dynamic range is set between 50 MeV and 3 TeV, and it stands out with its energy-scale precision of 0.1%. The linearity of its response is noteworthy, surpassing benchmarks by remaining better than 0.5% for energies up to 300 GeV. One of its notable features is its ability to measure the shower direction in θ , achieving a resolution of approximately 50 mrad per the square root of the energy in GeV. As for particle differentiation, the calorimeter has an exceptional capacity for photon/jet, electron/jet, and τ /jet separations. Furthermore, it is designed to have a rapid response, low noise, and offers high granularity. The coherent noise level is maintained below $E = 3$ MeV for each channel, and it is adept at identifying individual bunch crossings.

The EM calorimeter of the LHC is divided into a central barrel ($|\eta| < 1.475$) and two end-caps ($1.375 < |\eta| < 3.2$). The barrel consists of two half-barrels, while each end-cap is further segmented into outer and inner wheels. Designed as a lead-LAr detector, the calorimeter features accordion-shaped Kapton electrodes to ensure complete ϕ symmetry without azimuthal gaps. The thickness of the calorimeter varies, exceeding $24X_0$ in the barrel and $26X_0$ in the end-caps. Within the precision-focused region ($|\eta| < 2.5$), it is divided into three longitudinal layers.

- **First Sampling (Preshower Detector):** This layer has a consistent thickness of $6X_0$ and is furnished with narrow strips oriented in the η direction. It acts primarily as a

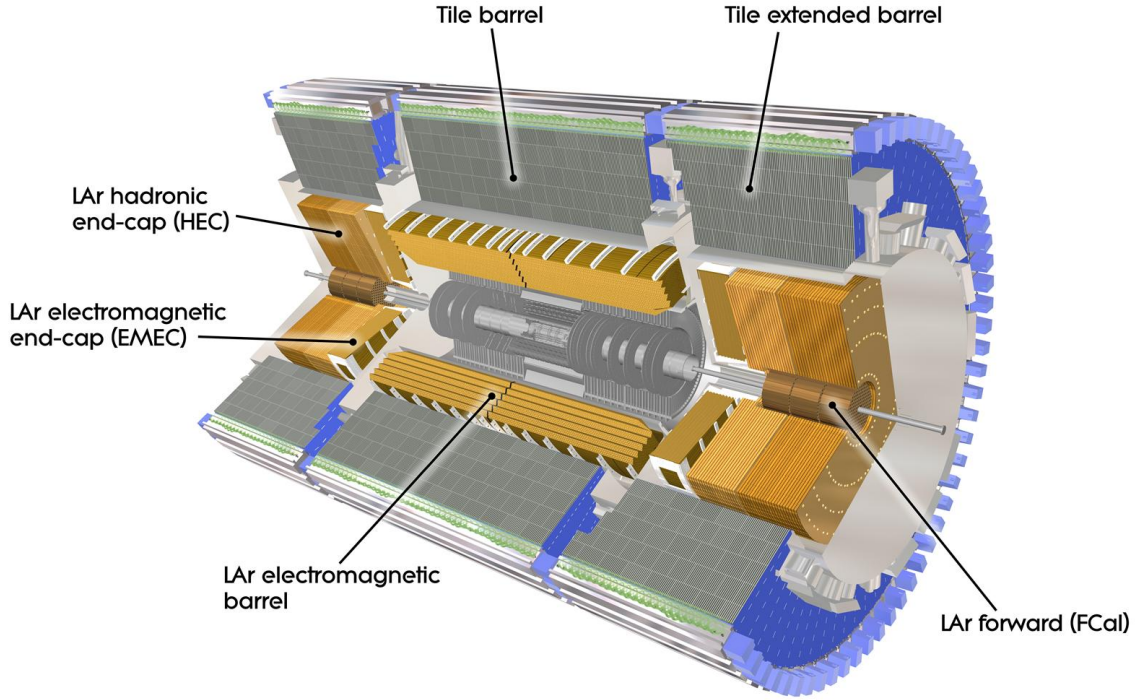


Figure 3–6 The layout of the ATLAS calorimeters^[44].

”preshower” detector, aiding in particle identification and precise position measurements in the η dimension.

- **Second Sampling:** This layer is divided into square towers each spanning $\Delta\eta \times \Delta\phi = 0.025 \times 0.025$. By the end of this second sampling, the total calorimeter thickness reaches around $24 X_0$.
- **Third Compartment:** This final layer has coarser granularity in the η direction and its thickness varies between $2X_0$ and $12X_0$.

In total, the calorimeter has about 190,000 channels. Materials in front of the calorimeter, including the inner detector and solenoid coil, sum up to about $1.8X_0$ at $\eta = 0$. Signals from the calorimeter are routed to external preamplifiers, digitized upon trigger events, and forwarded to the Data Acquisition system using a three-gain scale for optimum noise management.

The ATLAS hadronic calorimetry^[43] (HCAL) covers a pseudo-rapidity range of $|\eta| < 5$, employing various techniques tailored for the radiation environment and diverse require-

ments. The barrel and extended barrel Tile calorimeters, which span up to $|\eta| < 1.6$, use iron-scintillating-tiles. The Liquid Argon calorimetry is employed from $\sim 1.5 < |\eta| < 4.9$. Total calorimeter thickness at $\eta = 0$ is 11 interaction lengths, providing sufficient containment for hadronic showers and reducing punch-through for the muon system.

- **Tile Calorimeter:** The hadronic barrel calorimeter operates as a sampling device, using iron as the absorber and scintillating tiles as the active medium. Tiles, 3 mm thick, are oriented perpendicular to the colliding beams and staggered in depth with a periodic structure along the z-axis. Both tile sides are readout using wavelength shifting fibers, channeling into two separate photomultiplier tubes (PMTs). Comprising one barrel and two extended barrels, the calorimeter spans from an inner radius of 2.28 m to 4.23 m. It features three layers segmented to thicknesses of approximately 1.4, 4.0, and 1.8 interaction lengths at $\eta = 0$. The granularity results in a $\Delta\eta \times \Delta\phi = 0.1 \times 0.1$ (or 0.2×0.1 in the last layer). The calorimeter is positioned behind the EM calorimeter and the solenoid coil, leading to a total active calorimeter thickness of 9.2 interaction lengths at $\eta = 0$. An Intermediate Tile Calorimeter (ITC) enhances the thickness in the gap between the barrel and extended barrels.
- **End-cap Liquid Argon calorimetry:** The end-cap Liquid Argon calorimetry, covering $\sim 1.5 < |\eta| < 3.2$, features two wheels of equal diameter. The first wheel uses 25 mm copper plates, while the second wheel has 50 mm plates. The gap between consecutive plates is 8.5 mm, segmented with 3 electrodes, forming 4 drift spaces of around 1.8 mm each. The first wheel is bifurcated into two longitudinal segments, consisting of 8 and 16 layers, while the second has a single 16-layer segment. The end-cap's active portion has a thickness of around 12 interaction lengths.
- **Forward Liquid Argon calorimetry:** Located within the end-cap cryostat, the forward calorimeter covers $3.2 < |\eta| < 4.9$. Its close proximity to the interaction point (5 meters) exposes it to high radiation levels. Its design ensures uniformity of coverage, minimizing crack and dead space effects around $\eta = 3.1$. This calorimeter is high-density, with three longitudinal sections: the first is copper, and the subsequent two are tungsten. Each section features a metal matrix with spaced channels filled with rods, with Liquid Argon serving as the sensitive medium in the gaps. The forward calorimeter's electronic noise for a jet cone of $\Delta R = 0.5$ is roughly 1 GeV E_T at $\eta = 3.2$,

decreasing sharply to 0.1 GeV E_T at $\eta = 4.6$.

The overall layout of the ATLAS ECAL and HCAL is shown in Figure 3-6.

3.2.2.3 Muon spectrometer

Theoretically, particles that can pass through the entire depth of the calorimeter without interacting, or only weakly interacting, include neutrinos and muons which do not deposit their full energy. The muon spectrometer is used to identify muons and calculate the energy that is not detected.

The ATLAS Muon Spectrometer^[45], as shown in Figure 3-7, includes a barrel region and three wheel-shaped endcap regions. In the barrel region ($|\eta| < 1.4$), the magnetic field is provided by barrel toroidal magnets. In the endcap region ($1.6 < |\eta| < 2.7$), the magnetic field is provided by the endcap toroidal magnets in Section 3.2.2.4. In the transition region of $1.4 < |\eta| < 1.6$, the magnetic field is jointly provided by the endcap and barrel toroidal magnets. The muon spectrometer employs four drift chamber technologies: Monitored Drift Tubes (MDTs), Cathode Strip Chambers (CSCs), Resistive Plate Chambers (RPCs), and Thin Gap Chambers (TGCs). In the barrel region, the drift chambers are arranged in three concentric cylindrical layers along the beam axis. In both endcap regions, the drift chambers are also divided into three layers placed on discs perpendicular to the beam direction.

Type	Function	Chamber resolution (RMS) in			Measurements/track		Number of	
		z/R	ϕ	time	barrel	end-cap	chambers	channels
MDT	tracking	35 μm (z)	-	-	20	20	1088(1150)	339k(354k)
CSC	tracking	40 μm (R)	5 mm	7 ns	-	4	32	30.7k
RPC	trigger	10 mm(z)	10 mm	1.5 ns	6	-	544(606)	359k(373k)
TGC	trigger	2 – 6 mm(R)	3 – 7 mm	4 ns	-	9	3588	318k

Table 3-5 Specifications for the four subsystems of the muon detector^[47]: The stated spatial resolution (in columns 3 and 4) excludes uncertainties from chamber alignment. The intrinsic time accuracy for each chamber type is detailed in column 5, with additional time required for signal propagation and electronic factors. Numbers in parentheses relate to the full detector setup anticipated for 2009.

The muon spectrometer is divided into two sets of systems: precision chambers and trigger chambers. High-precision track measurements are based on MDTs in the barrel and CSCs in the endcaps, providing 6-8 measurement points. MDTs cover the region $|\eta| < 2.7$

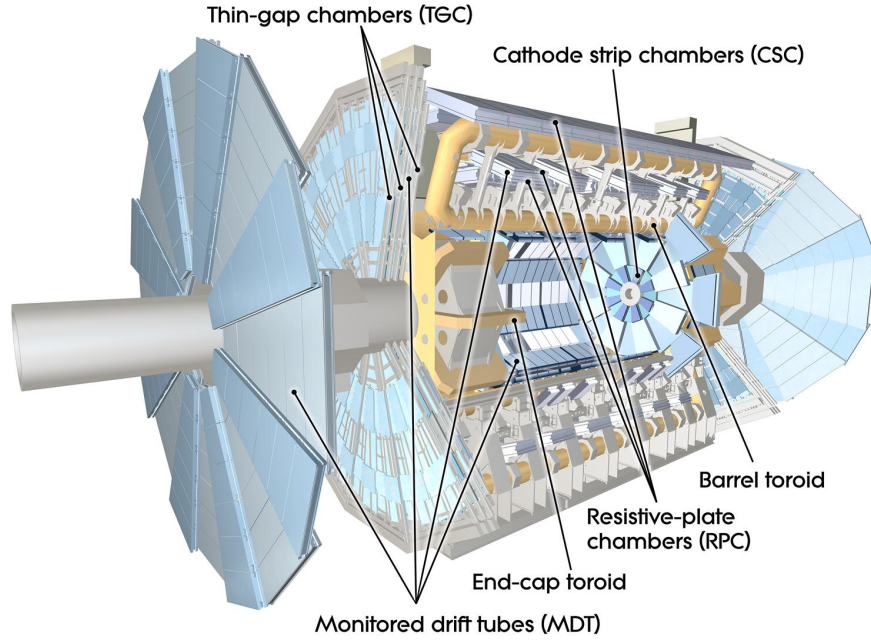


Figure 3–7 The layout of the ATLAS muon system^[44].

and consist of drift tubes with a diameter of 3 cm and 50 μm tungsten-rhenium signal wires, filled with a mixture of 93% argon gas and 7% carbon dioxide. They operate under a voltage of 3kV and function similarly to the TRT, working in a drift chamber mode with a maximum drift time of 750 ns. A single drift tube offers a spatial resolution of $(R - \phi)$ 80 μm , while the average resolution of MDTs can reach 35 μm . In a region of higher pseudorapidity ($2.0 < |\eta| < 2.7$), closer to the interaction point, higher granularity CSCs are used to adapt to higher particle flux and beam background. CSCs are based on Multiwire Proportional Chamber (MRPC) detectors, with a maximum drift time of 40 ns.

Trigger chambers are primarily used for rapid triggering of muon events and are based on RPCs and TGCs. These detectors achieve intrinsic time resolutions of 1.5 ns and 4 ns, respectively. Additionally, the trigger chambers provide a second set of position measurements independent of the precision measurements (for $|\eta| < 2.4$), aligned approximately with the magnetic field lines, though with slightly inferior spatial resolution (5-10 mm). RPCs operate as MRPC detectors in saturation mode, filled with a mixture of 55% carbon dioxide and 45% n-pentane, covering the barrel region ($1.05 < |\eta| < 2.4$). RPCs function as parallel plate detectors in amplification mode, filled with $\text{C}_2\text{H}_2\text{F}_4$, with electrode distances of 2 mm, covering the barrel region ($|\eta| < 1.05$). Detailed parameters are given in Table 3–5.

3.2.2.4 Magnet system

The ATLAS experiment is equipped with a distinctive combined system comprising four extensive superconducting magnets. Spanning a diameter of 22 m and extending 26 m in length, this magnetic setup houses an energy storage capacity of 1.6 GJ. Following roughly a decade and a half dedicated to its design, its assembly in industrial settings, and the eventual integration at CERN, this system now stands fully operational in its subterranean chamber. This section describes the characteristics of these magnets along with their auxiliary services.

Illustrated in Figure 3-8 is the overarching design, spotlighting the four primary layers of detectors as well as the quartet of superconducting magnets responsible for generating the magnetic field across a vast expanse of about 12000 m^3 (this volume is demarcated by regions where the field strength surpasses 50 mT). Central attributes of the ATLAS magnetic system encompass:

- A central solenoid, strategically positioned along the beam trajectory, furnishing a 2T axial magnetic field purposed for the inner detector. This ensures the reduction of radiative thickness ahead of the barrel electromagnetic calorimeter.
- A cylindrical barrel toroid paired with twin end-cap toroids. Together, they generate a toroidal magnetic field, averaging between 0.5T in the core region and amplifying up to 1T for the muon detectors located at the end-cap zones.

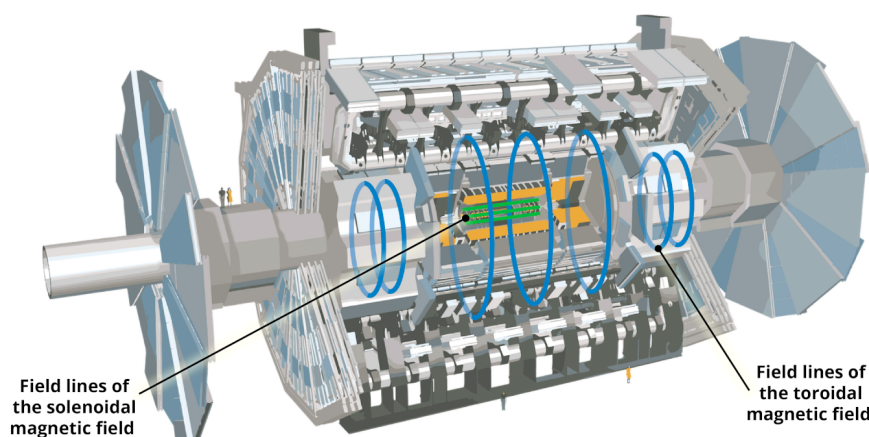


Figure 3-8 The layout of the ATLAS magnet system^[48].

3.2.2.5 Trigger and data acquisition systems

The ATLAS experiment employs a sophisticated, multi-level event selection mechanism, often referred to as the "trigger system". This system has been designed to sift through the vast number of potential event candidates, selecting only those of highest interest for in-depth analysis.

The trigger system is divided into three hierarchical stages, which is shown in Figure 3-9:

1. **Level-1 (L1) Trigger:** The most immediate and rapid-fire of the selection processes. Designed with custom electronics, it employs low-resolution data from select detectors, chiefly the Resistive Plate Chambers (RPC) and Thin-Gap Chambers (TGC) for high- p_T muons, along with all calorimeter sub-systems to detect electromagnetic clusters, jets, τ -leptons, missing transverse energy E_T^{miss} , and overall large transverse energy. This stage primarily searches for signatures from high- p_T muons, electrons/photons, jets, and τ -leptons that decay into hadrons. It is tailored to make fast decisions, with a decision window of just $2.5 \mu\text{s}$ post a bunch-crossing. It operates at an impressive maximum rate of 75 kHz, which holds the potential to be upgraded to 100 kHz.
2. **Level-2 (L2) Trigger (High-Level Trigger - HLT):** Unlike L1, this stage is powered primarily by commercial computing and networking equipment. The L2 trigger operates in a more refined environment, with its activities being directed by the Regions-of-Interest (RoI's) highlighted by the L1 trigger. These RoI's are essentially detector zones where potential event candidates have been spotted. The L2 trigger then utilizes the RoI data to curtail the data volume that needs to be fetched from the detector readout, thereby optimizing the event selection process. At this stage, event rates are scaled down to a manageable 3.5 kHz, while maintaining an average processing time of around 40 ms.
3. **Event Filter:** This serves as the final layer of online event selection. Adopting offline analysis techniques on completely assembled events, it filters the event rate down to approximately 200 Hz. This stage, with an average processing duration of about 4 seconds, ensures only the most pertinent events are stored for further offline scrutiny. The algorithms deployed within the HLT use the full detail of the calorimeter, muon chamber data, and data from the inner detector to perfect their selections. Improved data on energy deposition aids in refining threshold limits, while inner detector track

reconstruction considerably augments particle identification capabilities, such as differentiating between electrons and photons.

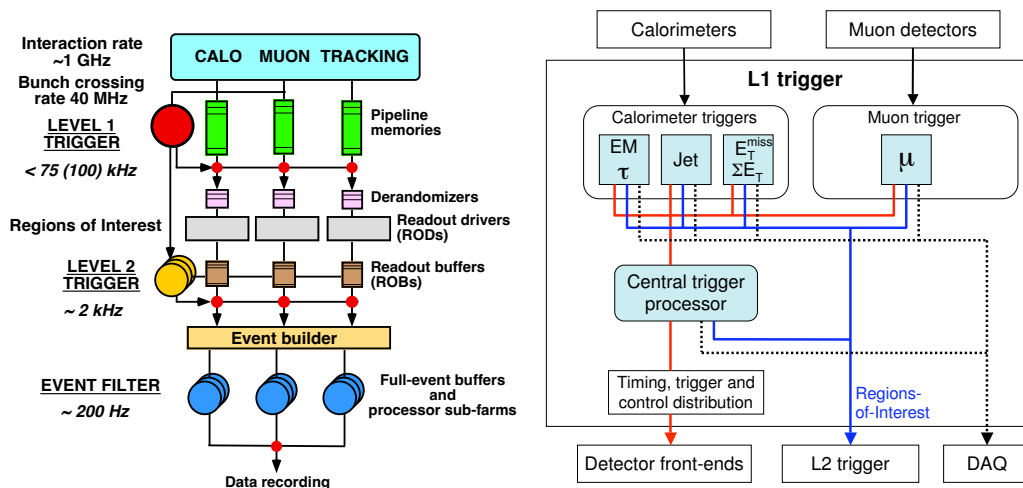
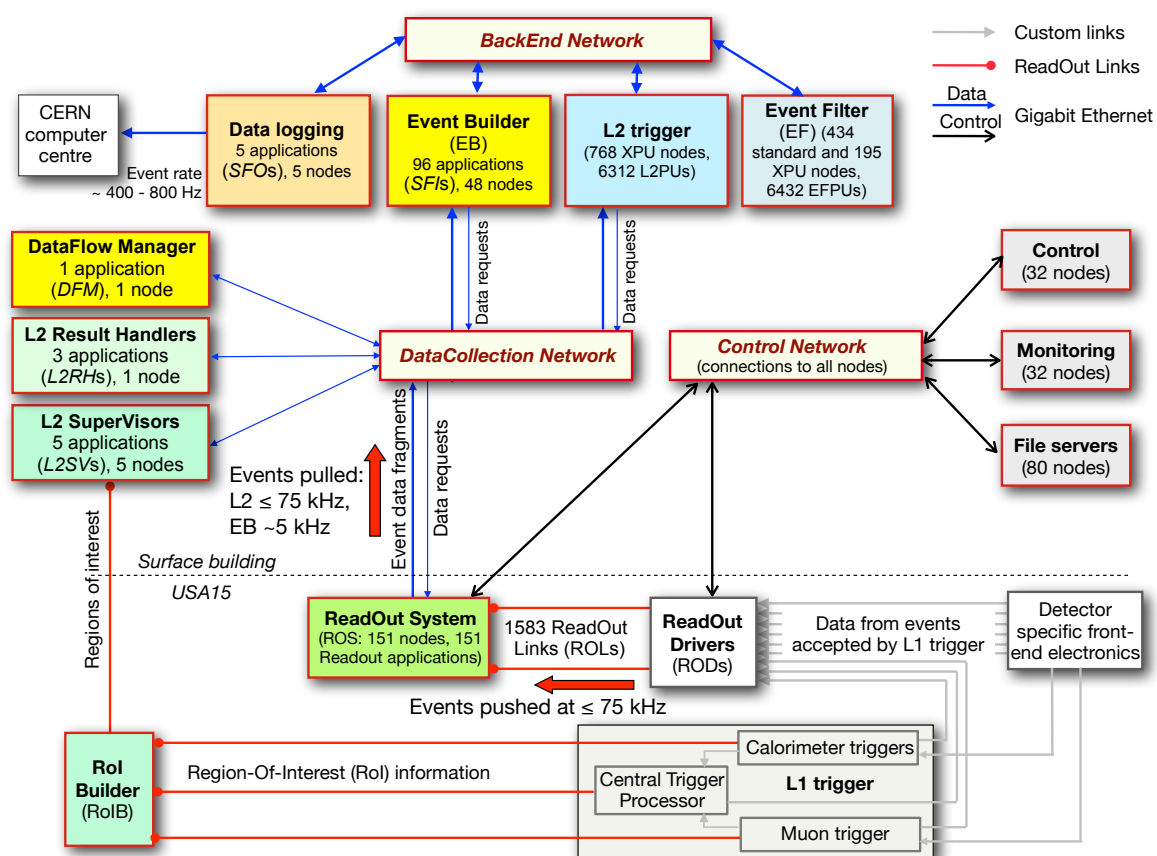


Figure 3-9 Left: A schematic view of the ATLAS trigger system^[49]; Right: Block scheme of the first level trigger^[49].

Alongside the trigger system, the Data Acquisition System (DAQ)^[47,50] plays a pivotal role, as illustrated in Figure 3-10. It is the backbone that oversees the capture, buffering, and transmission of event data from the specialized readout hardware at the L1 trigger rate. Through dedicated point-to-point Readout Links (ROL's), the DAQ dispatches data requested by the L2 trigger, predominantly related to the RoI's. Upon fulfilling L2 selection criteria, events are compiled and then shuttled by the DAQ to the event filter. Events that pass this stringent filter are then preserved in a permanent storage system.

Additionally, the DAQ is not just a passive data handler. It actively aids in orchestrating the configuration, control, and oversight of the entire ATLAS detector during data collection phases. For hands-on supervision of the myriad elements of the detector infrastructure, like gas systems and power supplies, the Detector Control System (DCS) is brought into play.

In summary, the interplay of the multi-layered trigger system and the DAQ ensures the ATLAS experiment efficiently manages the vast influx of data, making informed selections and effectively archiving events of significance.

Figure 3-10 A schematic view of the ATLAS DAQ system^[50].

Chapter 4 Event Simulation and Reconstruction in ATLAS

4.1 Event Simulation

4.1.1 Simulation Overview and Large-Scale Production System

In the ATLAS experiment, the role of numerical simulation is critical for experimental design and data interpretation. Each aspect of the event process, from initial particle collision to detector response, is replicated within the simulation framework. This approach enables the identification of potential outcomes and limitations, as well as the adjustment of experimental parameters.

Given the data volume generated by the ATLAS detector, which is on the order of petabytes per year, a detailed simulation is essential. It facilitates a robust methodology for the analysis of complex data sets, thereby ensuring that results conform to theoretical expectations within defined statistical limits.

By meticulously mimicking the complete event cycle, the simulation aids in refining analytical methods and optimizing detector settings. Thus, a high level of experimental accuracy is maintained, contributing to a more reliable exploration of particle physics phenomena within the constraints of the Standard Model and beyond.

Central to this simulation is the Athena program^[51], integrated into the ATLAS framework and powered by the Geant4 simulation toolkit^[52-53]. The simulation sequence is typically segmented into the following distinct phases^[54]:

1. **Event Generation:** In the initial stage of event generation, emphasis is placed on the production and decay of events, which encompasses the calculation of Matrix Elements (ME) and the processes of Parton Shower (PS) or hadronization. Events are generated and filtered in accordance with the HepMC standard format^[55], retaining only those that meet specific criteria such as leptonic decay or a predetermined missing energy threshold. Prompt decays, particularly those involving Z or W bosons, are primarily managed at this stage, while particles considered "stable" for detector traversal are retained. Notably, at this phase, consideration is restricted to immediate decays, making the geometric configuration of the detector irrelevant. Within each job, run and event numbers are systematically assigned to simulated data sets.

2. **Detector Simulation:** Once events are generated, they're integrated into the simulation. An exhaustive record of all particles from the generator is preserved, while user-defined cuts determine which particles undergo processing. Geant4 controls the path of each particle as it moves through the ATLAS detector. Energy deposited in the detector's sensitive areas is documented as "hits".
3. **Truth Information:** During both the event generation and detector simulation, every event is assigned a "truth" record. In the generation phase, this "truth" represents a history of particle interactions. In the simulation phase, it focuses on details of individual particle tracks and decays, highlighting events such as photon conversions in the inner detector.
4. **Digitization:** This phase converts "hit" outputs from the simulation into tangible detector signals, such as voltage or time. The pile-up effect is integrated here to ensure computational efficiency. Digitization's output materializes as a Raw Data Object (RDO) file, standing out from the detector's "bytestream" format due to the inclusion of truth information.
5. **High-Level Trigger and Reconstruction:** Both the ATLAS HLT and the subsequent reconstruction process are built on the RDO files. The reconstruction remains consistent for simulated and actual data, with the exception of truth information being exclusive to the simulation. The HLT, during real data acquisition, leans on bytestream files, though a thorough assessment can revert RDOs to this format.

4.1.1.1 Large-Scale Production System

As the ATLAS simulation process is computationally demanding and time-intensive, a large-scale production system becomes indispensable for distributing the workload and ensuring the timely completion of complex tasks. For this purpose, ATLAS employs the Worldwide LHC Computing Grid (WLCG)^[56], which allows tasks to be divided into multiple jobs based on their complexity and computational requirements. Each job is designed to be executed within a CPU's maximum allowed runtime, typically ranging from 2-3 days. The output from these jobs, including log files, is systematically registered with the ATLAS Distributed Data Management (DDM) system^[57] for meticulous bookkeeping and subsequent analysis.

To maintain software reliability and uniformity, complete software releases—incorporat-

ing all Athena software, external dependencies like Geant4, and generators—are distributed to production sites and end-users at regular intervals. These releases are further updated through periodic patches known as ‘production caches.’ Alongside these software packages, a set of data files containing database replicas, external data files, and sample output files are included for validation purposes.

Job distribution within the WLCG adheres to a well-structured protocol. Initially, a test batch of approximately 10 jobs is run, and the remaining jobs are queued only after the successful completion of this test batch. The process is often hierarchical; each step in a sequence of jobs (generation, simulation, and digitization) remains in the queue until the preceding job’s data are available. Multiple steps can also be configured to run concurrently for efficiency, with about one million events per day being produced using Geant4.

Modifications to each job are permitted but are kept minimal for the sake of consistency. These could involve slight adjustments to random number seeds, generator configurations, detector geometry, and other job options. Some specialized options are also available for unique simulation needs, such as non-standard vertex smearing or simulation of long-lived exotic particles.

Through this large-scale production system, ATLAS effectively tackles the computational challenges associated with its complex simulation processes, optimizing the use of resources for the production of high-quality simulated data.

4.1.2 Event generation

4.1.2.1 General-Purpose Monte Carlo Generators

General-purpose Monte Carlo (GPMC) generators like HERWIG^[58-59], PYTHIA^[60-61], and Sherpa^[62] are integral in simulating high energy particle collisions. These generators serve a dual purpose: first, as theoretical tools for probing Quantum Chromodynamics (QCD) beyond fixed-order perturbation, and second, as practical instruments for data analysis and experimental planning. They function at different scales, ranging from the perturbative to the nonperturbative, capturing the physics from sub-femtometer dimensions to the larger scales of hadron formation and decay.

The architecture of GPMC generators is organized into four fundamental components. Each component serves a distinct function in simulating high-energy particle interactions,

which are interrelated:

- **Short-Distance, Perturbative Phenomena:** At sub-femtometer scales, GPMC generators utilize perturbative QCD to model hard scattering and other partonic-level processes^[63]. Matrix Elements (ME) are employed to provide fixed-order calculations for specific scattering processes, and they often serve as the starting point for parton shower evolution. The parton shower (PS) technique further refines these calculations by capturing the sequential emission of gluons and quarks at lower transverse momenta. Additional features like Initial-State Radiation (ISR) and Final-State Radiation (FSR) are implemented to account for particle emissions both before and after the core hard-scattering event. These mechanisms collectively influence the kinematic attributes of the simulated collision. Furthermore, the strong coupling constant, denoted as α_s , serves as a key parameter in these simulations, dictating the strength of strong force interactions and contributing to theoretical uncertainties.
- **Nonperturbative Transition:** Beyond the perturbative regime, these generators employ phenomenological models like the Lund String or Cluster models to simulate the transition from quarks and gluons to observable hadrons.
- **Soft Hadron Physics Models:** For larger-scale, nonperturbative interactions, the generators incorporate models of the underlying event and minimum-bias interactions, along with specialized treatments for Bose-Einstein correlations and color reconnection.
- **MC Uncertainty Estimates and Tuning:** The generators also provide frameworks for uncertainty quantification and parameter tuning, which are crucial for assessing the reliability of simulation results.

In elucidating how pp collision events are simulated by PYTHIA^[64], Figure 4-1 offers a schematic overview, albeit with certain simplifications for the sake of visual clarity; these include a reduced number of shower branchings and final-state hadrons, approximate recoil effects, and the exclusion of weak decays in light-flavor hadrons, among other details (see caption for a complete list of simplifications).

4.1.2.2 Specialized Generators

Specialized generators serve as auxiliary tools in the high-energy physics ecosystem, designed to work in conjunction with GPMC generators such as PYTHIA and HERWIG. Unlike

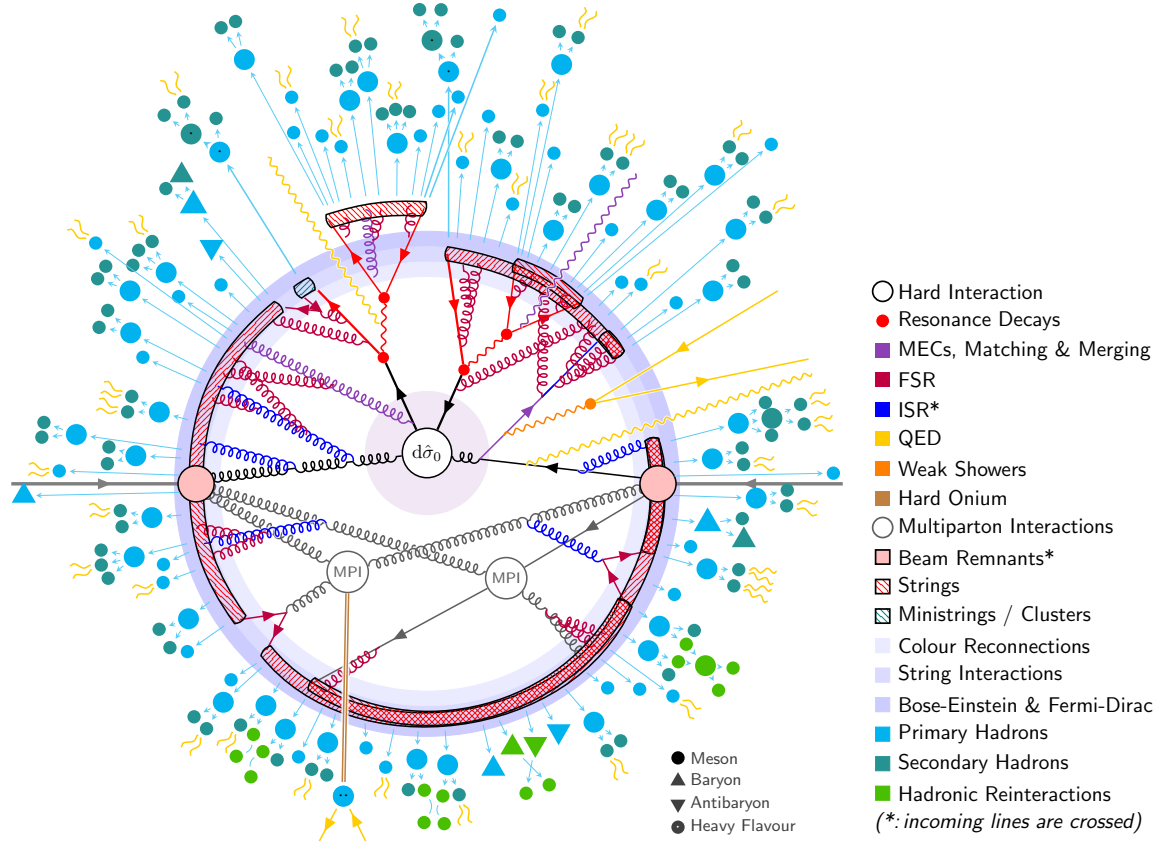


Figure 4-1 Schematic representation of a $pp \rightarrow t\bar{t}$ event as simulated by PYTHIA [64], with certain simplifications for visual clarity. 1) The number of shower branchings and final-state hadrons is reduced compared to an actual PYTHIA simulation; 2) Recoil effects are not depicted to scale; 3) Weak decays of light-flavor hadrons are omitted, implying, for example, a K_S^0 meson is shown as stable; 4) Incoming momenta are illustrated as inversed ($p \rightarrow -p$), necessitating that the momentum direction for both beam remnants and ISR branchings should be interpreted as outward-facing to avoid diagrammatic complexity. This convention prevents the need for beam remnants and ISR emissions to intersect in the central region of the figure.

GPMC, specialized generators do not produce complete events amenable to direct simulation. Instead, their function is to provide a more accurate representation of specific decay processes or specialized final states. These generators often employ advanced theoretical models and methodologies, ranging from next-to-leading order (NLO) perturbative calculations to intricate decay models. By generating partonic four-vectors in compatible formats, they enable seamless integration with GPMC generators, thereby enhancing the overall predictive power and accuracy of event simulations. These specialized generators often produce

outputs in ASCII formats compatible with "Les Houches" standards^[65], which are then read and processed by GPMC generators via interfaces like Athena.

EvtGen^[66], originally conceived by the CLEO collaboration, specializes in providing a nuanced description of B meson and hadron decays, thereby enhancing the default capabilities of general-purpose generators. Recent extensions of EvtGen have incorporated data from experiments at the Tevatron, BaBar, and Belle, allowing for more accurate modeling of B_s and b-baryon decays. EvtGen is unique in its incorporation of angular correlations, which are crucial for calculating the acceptance rates for certain decay modes of B mesons and baryons. It has been particularly useful in ATLAS studies that focus on exclusive B decays.

MC@NLO^[67], another specialized generator, operates as a standalone "Les Houches" type generator. It is notable for its employment of NLO QCD perturbation theory for evaluating hard scattering processes. This makes it especially relevant for generating events involving top quarks, offering a more precise representation of their transverse momentum distributions as compared to general-purpose generators. One of its defining features is the inclusion of one-loop corrections, resulting in events with both positive and negative weights that must be carefully accounted for in subsequent data analysis.

Parton Distribution Functions (PDFs) serve as essential components to model the internal structure of protons. These PDFs are incorporated into all event generators as external inputs. Specifically, ATLAS employs the Les Houches Accord PDF Interface (LHAPDF)^[68], a robust library that has effectively replaced the older PDFLIB^[69]. This library offers an extensive repository of PDFs, with the default being the CTEQ PDFs^[70]. It is noteworthy that MC@NLO employs NLO PDFs, whereas all other generators utilize Leading Order (LO) PDFs. The choice of PDFs is intrinsically tied to the tuning parameters associated with initial state radiation^[71-72]. Due to this interconnectedness, altering PDFs independently can result in inconsistent outcomes. Hence, whenever a new set of PDFs is adopted, a corresponding retuning of the event generator's parameters is performed to ensure result consistency.

Monte Carlo truth is preserved in a HepMC event record, serving as a complete list of particles that are directly produced or involved in high-energy interactions. These particles often serve as progenitors to a cascade of sub-processes and decays that ultimately interact with the detector. The MC truth at the generator level differentiates between particles originating from the initial collision and those produced through subsequent interactions or decays,

allowing for a precise understanding of the underlying physical processes. This granularity is essential for calibrating the simulation and validating the detector’s response to specific types of events.

4.1.3 Detector simulation and response

4.1.3.1 Detector Simulation

The ATLAS detector’s geometric model is highly detailed, with an extensive list of materials and physical volumes. Table 4-1 lists the specific quantities of each, broken down by detector component. This level of detail is essential for accurate predictions, particularly in variables like missing transverse energy and track reconstruction. To improve computational efficiency, the model uses volume parameterization, which allows the reuse of the same logical volume. Sub-picometer gaps are introduced between volumes to prevent computational issues like ‘stuck tracks’.

The system also allows for frequent updates and maintains backward compatibility, enabling older geometries to still function. Users have the option to enable or disable specific sections of the detector for resource optimization. The architecture supports the incorporation of various detector conditions like misalignments, which can be stored in a database and transferred across different data processing stages.

4.1.3.2 Digitization

The digitization stage in the ATLAS software framework translates simulated hits into detector readouts, commonly referred to as “digits.” These digits are generated based on predefined voltage or current thresholds within specific time windows for individual readout channels. The software also accounts for charge collection in each subdetector, including cross-talk, electronic noise, and channel-dependent variations.

The digitization software^[73-77] for each subdetector is orchestrated by a top-level Python package, which ensures a unified configuration across all subdetectors. The algorithms’ properties are optimized to match the real-world detector response as observed in lab tests, test beam data, and cosmic ray measurements. Dead channels and noise rates are incorporated from database tables to mirror real experimental conditions.

Raw Data Objects (RDOs) serve as the output of the digitization process. Depending on the subdetector, some may require a two-step conversion from hits to digits and then to

Subsystem	Materials	Solids	Logical Vol.	Physical Vol.	Total Vol.
Beampipe	43	195	152	514	514
BCM	40	131	91	453	453
Pixel	121	7,290	8,133	8,825	16,158
SCT	130	1,297	9,403	44,156	52,414
TRT	68	300	357	4,034	1,756,219
LAr Calorimetry	68	674	639	106,519	506,484
Tile Calorimetry	8	51,694	35,227	75,745	1,050,977
Inner Detector	243	12,501	18,440	56,838	1,824,614
Calorimetry	73	52,366	35,864	182,262	1,557,459
Muon System	22	33,594	9,467	76,945	1,424,768
ATLAS TOTAL	327	98,459	63,769	316,043	4,806,839

Table 4-1 Quantities of materials, solids, logical volumes, physical volumes, and aggregate volumes essential for the assembly of diverse segments of the ATLAS detector are outlined. The term "Inner Detector" encompasses components such as the beampipe, BCM, pixel tracker, SCT, and TRT.

RDOs, while others bypass the intermediate digit stage and generate RDOs directly from hits. Additionally, Simulated Data Objects (SDOs) may be generated, which offer details on particle interactions and energy contributions. These SDOs are crucial for assessing tracking efficiency and false track rates.

Moreover, the simulation process also accounts for multiple interactions within a single bunch crossing, including both the hard scattering event and any additional inelastic, non-diffractive interactions. These multiple events, often referred to as pile-up, are integrated into the digitization stage to produce a realistic detector response.

Finally, the conversion from bytestream data to RDO format is an essential step before running reconstruction algorithms. While the process from RDO to bytestream involves some data loss due to truncation, the reverse operation is essentially lossless. This bidirectional conversion capability facilitates evaluation of the conversion algorithms themselves.

4.1.3.3 Fast Simulation

In order to meet the demands of complex physics studies without sacrificing computational efficiency, various fast simulation methods have been developed to complement the

standard full simulation in the ATLAS experiment. These fast simulation approaches aim to offer a balance between accuracy and speed, targeting specific bottlenecks or computational requirements. Here are the key methods:

- **Fast G4 Simulation**^[78-79]: Targets the calorimeter simulations, which consume almost 80% of full simulation time. By replacing low-energy electromagnetic particles with pre-simulated showers, it reduces CPU time by a factor of three in hard scattering events such as $t\bar{t}$ production.
- **ATLFAST-I**^[80-81]: Ideal for studies requiring large statistics but not detailed complexity. It employs smeared truth objects to mimic physics objects from reconstruction, achieving a speed increase of up to 1000 times over full simulation.
- **ATLFAST-II**^[82]: Designed to offer a balance between speed and accuracy. It comprises Fast ATLAS Tracking Simulation (FAtlas) for inner detector and muon simulations, and Fast Calorimeter Simulation (FastCaloSim) for calorimeter simulations. Depending on its configuration, it can achieve a 10-time or 100-time speed improvement over full simulation.

4.2 Object Reconstruction

4.2.1 Tracks

In the ATLAS experiment, the accurate reconstruction of charged particle tracks is crucial for a wide array of physics analyses, from the study of the Higgs boson to the search for new phenomena beyond the Standard Model. These tracks provide key insights into the underlying collision events and are fundamental for vertex identification, momentum measurement, and isolation criteria, among other parameters. The structure of the ATLAS Inner Detector is introduced in Section 3.2.2.1, and the nomenclature of track coordinate is in Section 3.2.1.1. Accurate track reconstruction^[83-84] is especially vital for studies involving heavy flavor tagging, precision measurements of Standard Model processes, and the identification of long-lived particles. The process is complex, involving several steps to convert raw detector hits into particle trajectories. Each stage, from clusterization of signals to resolving track ambiguities, plays a critical role in ensuring the accuracy of the physics outcomes:

1. **The ID Reconstruction Sequences**^[84]: In contemporary ID track reconstruction, the

boundaries between pattern finding and track fitting have blurred. Many modern pattern finding strategies go beyond the classical histogram-based methods and include both global and local pattern recognition. In this context, track fitting is often incorporated into the pattern finding process. Similarly, modern track fitters, like the combinatorial extension of the standard Kalman filter^[85] or the deterministic annealing filter, integrate pattern recognition as part of the fitting process. Therefore, the sequence for ID reconstruction in ATLAS combines pattern finding and track fitting into a unified chain.

The ID reconstruction adopts two primary sequences: the main inside-out track reconstruction and a subsequent outside-in tracking. These sequences are heavily influenced by the pre-existing ATLAS ID reconstruction program XKALMAN but have been further enhanced with additional components following the NEWT approach. There's also a third sequence for the finding of V0 vertices, kink objects, and their associated tracks using common tracking tools and EDM, although this is not specific to the NEWT approach.

2. **The Inside-Out Sequence**^[84]: The inside-out tracking sequence begins with seed formation in the inner silicon tracker and progresses towards the outer regions of the ID. This process involves both global and local pattern recognition stages. The global stage narrows down the possibilities, and the local stage works on this reduced set of candidates. The first phase in the inside-out sequence is the construction of three-dimensional representations of the silicon detector measurements. Track seeds are formed from these 3D objects. A window search is then performed based on the seed direction to build track candidates. Hits from the detector elements that lie within this "road window" are collected and evaluated based on a simplified Kalman filtering-smoothing approach. These hits are then either added to the track candidates or rejected.
3. **Iterative Combinatorial Track Finding**^[83]: The process starts by forming track seeds from sets of three space-points. This is a trade-off to allow a large number of combinations while still getting a rough initial momentum estimate. The algorithm then estimates the impact parameters of these seeds with respect to the interaction region's center, assuming a perfect helical trajectory in a uniform magnetic field. Multiple cri-

teria are then applied to these seeds to ensure a high level of purity. These criteria include type-dependent momentum and impact parameter requirements, as well as the necessity for one additional space-point that is compatible with the estimated particle's trajectory. Subsequently, a Combinatorial Kalman filter^[86] is used to build track candidates by incorporating additional space-points from the remaining layers of the pixel and SCT detectors.

4. **Track Candidates and Ambiguity Solving**^[83-84]: The process begins by assigning a score to each track candidate based on a variety of factors that assess the quality of the track. This includes the number of clusters the track intersects with and the chi-square (χ^2) value of the track fit. After these scores are assigned, the track candidates are sorted in descending order. The candidates are processed individually in this order. This is under the premise that higher scores likely represent tracks that more accurately correspond to the trajectories of primary charged particles.

Once sorted, each track candidate is rigorously evaluated against a set of basic quality criteria. These criteria include a transverse momentum (p_T) greater than 400 MeV, and an absolute value of η that is less than 2.5. Additionally, the candidate must have a minimum of seven pixel and SCT clusters; although 12 are typically expected. Limits are also imposed on shared clusters: a maximum of one shared pixel cluster or two shared SCT clusters on the same layer can be a part of the track. Other parameters include not having more than two "holes" in the combined pixel and SCT detectors, not having more than one hole in the pixel detector alone, a transverse impact parameter ($|d_0^{BL}|$) less than 2.0 mm, and a longitudinal impact parameter ($|z_0^{BL} \sin \theta|$) less than 3.0 mm.

Following the application of quality criteria, the ambiguity solver moves on to resolve any issues with shared clusters. This step is crucial, as clusters can be attributed to more than one track. In such cases, preference is given to tracks that were processed earlier. Penalties are applied for sharing clusters that haven't been identified as 'merged'. If a track candidate doesn't meet any of the quality criteria, it gets rejected. The track is then re-scored and placed back into the list of remaining candidates for another round of processing. This ensures that only the most promising track candidates make it into the final dataset, thus enhancing the reliability and accuracy of particle track recon-

struction. An overview of this ambiguity solving procedures is shown in Figure 4-2.

5. **Neural-Network Pixel Clustering**^[83]: An artificial neural network^[87] is employed to assist in identifying merged clusters, clusters which are created by the charge deposits from multiple particles. This identification is based on the measured charge, relative positions of pixels within a cluster, and additional information about the particle's incident angle. The network has high efficiency in recognizing these merged clusters. However, it doesn't break down these merged clusters into individual energy deposits.
6. **Cluster Identification Logic**: Merged clusters can be identified in two distinct ways. First, they can be flagged by the neural network when they are used in multiple track candidates. Alternatively, clusters can be identified as merged if they appear on two consecutive layers and are used by the same track candidates. Clusters identified as merged are used without penalty, whereas clusters not identified as merged, but which are shared, can still be used but with a penalty as described earlier.

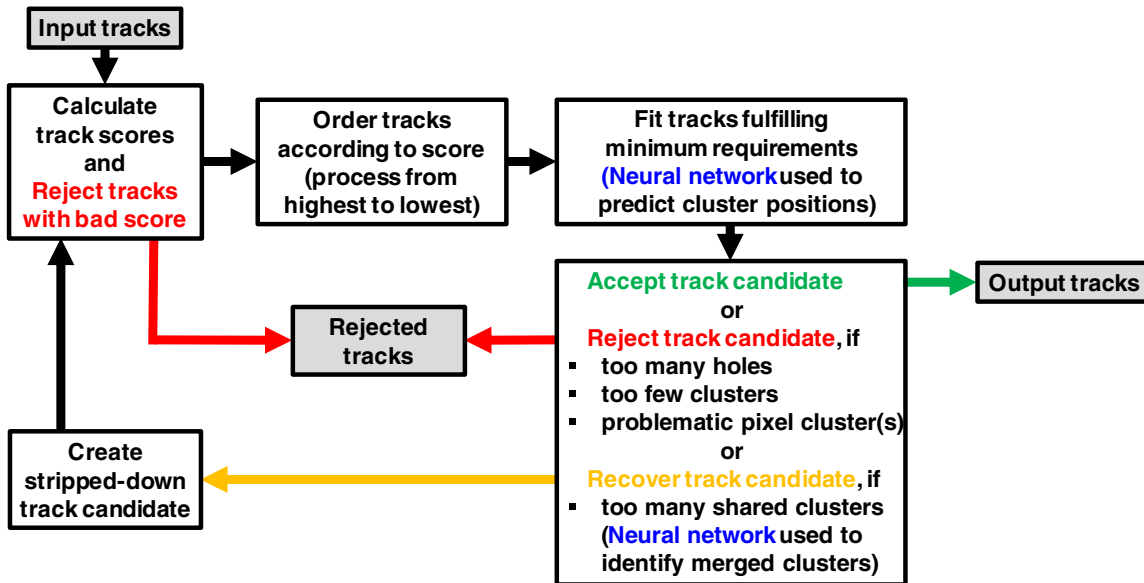


Figure 4-2 Overview of Track Candidate Progression within the Ambiguity Solver^[83].

4.2.2 Electrons

4.2.2.1 Electron Reconstruction

The updated algorithm^[88] for reconstructing electrons and photons commences by identifying topo-clusters that are viable candidates for forming these particles. Following this,

the tracks are refitted with an understanding of bremsstrahlung processes and then matched to the previously selected topo-clusters. The refitted tracks also serve as the foundation for constructing conversion vertices, which are then aligned with the selected topo-clusters.

Subsequent to this initial phase of track-cluster association and conversion vertex formation, separate routines for electron and photon superclustering are invoked concurrently. The resulting superclusters undergo preliminary positional adjustments, and are then matched with tracks for electrons and with conversion vertices for photons.

An electron is conventionally described as an entity that pairs a calorimeter-based supercluster with a compatible track or tracks. Conversely, a converted photon pairs a calorimeter cluster with one or multiple conversion vertices, while an unconverted photon pairs with neither an electron track nor a conversion vertex.

Because a single object can be simultaneously reconstructed as both an electron and a photon, a specialized ambiguity resolution step is employed to minimize such overlaps. However, a certain degree of overlap is deliberately preserved to ensure efficient reconstruction rates for both particle types, enabling subsequent physics analyses to apply more specialized criteria as needed.

The calibrated final forms of the electrons and photons are then produced, paving the way for the computation of various additional metrics that are essential for quality control and further ambiguity resolution. Prior methodologies for electron and photon reconstruction are detailed in References [89] and [90]. A visual representation summarizing the flow of the revamped algorithm for electron and photon reconstruction can be found in Figure 4-4, and a conceptual diagram depicting an electron's journey through the various components of the detector is shown in Figure 4-3.

In the formation of topological clusters (topo-clusters) within the ATLAS detector, the concept of cell significance plays a pivotal role. This is represented by the variable $\zeta_{\text{cell}}^{\text{EM}}$. The equation for calculating cell significance is given by:

$$\zeta_{\text{cell}}^{\text{EM}} = \frac{|E_{\text{cell}}^{\text{EM}}|}{\sigma_{\text{noise, cell}}^{\text{EM}}} \quad (4-1)$$

Here, $|E_{\text{cell}}^{\text{EM}}|$ is the absolute energy of the cell at the electromagnetic (EM) scale, and $\sigma_{\text{noise, cell}}^{\text{EM}}$ is the expected noise for that cell. The initial clustering process starts with seed cells having $\zeta_{\text{cell}}^{\text{EM}} \geq 4$. These seed cells then collect neighboring cells with $\zeta_{\text{cell}}^{\text{EM}} \geq 2$.

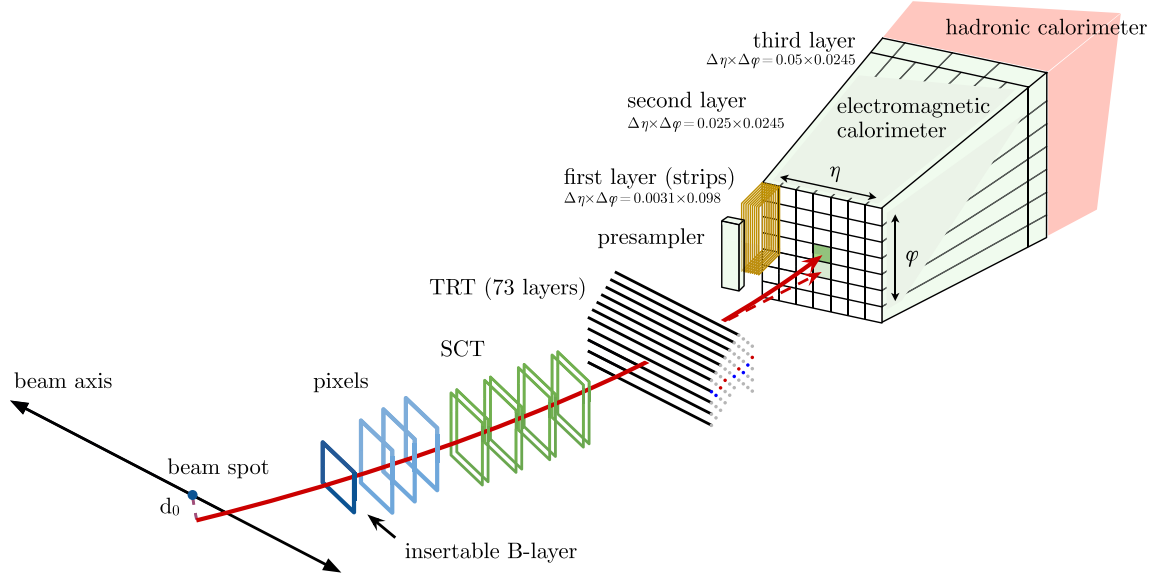


Figure 4-3 A conceptual diagram depicting an electron's journey through the various components of the detector^[91]. The solid red line represents the speculated path of an electron as it moves initially through the tracking system, starting with the pixel detectors, followed by the silicon-strip detectors, and finally through the TRT, before entering the electromagnetic calorimeter. The dotted red line illustrates the trajectory of a photon generated due to the electron's interaction with the tracking system's material.

When proto-clusters share a cell and the energy of that cell significantly exceeds the noise threshold, these proto-clusters are merged. After collecting all cells with energies above the noise threshold, an additional set of neighboring cells with $\zeta_{\text{cell}}^{\text{EM}} \geq 0$ are added to form the cluster. This process is often referred to as the "4-2-0" topo-cluster reconstruction methodology.

For clusters requiring splitting due to the presence of multiple local energy maxima, fractional cell weights are calculated based on cluster energies and distances from the cell to the centers of gravity of the clusters. The formulas for these weights^[92] are as follows:

$$w_{\text{cell},1} = \frac{E_{\text{clus},1}^{\text{EM}}}{E_{\text{clus},1}^{\text{EM}} + r E_{\text{clus},2}^{\text{EM}}} \quad (4-2)$$

$$w_{\text{cell},2} = 1 - w_{\text{cell},1} = \frac{r E_{\text{clus},2}^{\text{EM}}}{E_{\text{clus},1}^{\text{EM}} + r E_{\text{clus},2}^{\text{EM}}}$$

Here, $r = \exp(d_1 - d_2)$, where d_1 and d_2 are the distances of the cell to the centers of gravity of the first and second clusters, respectively.

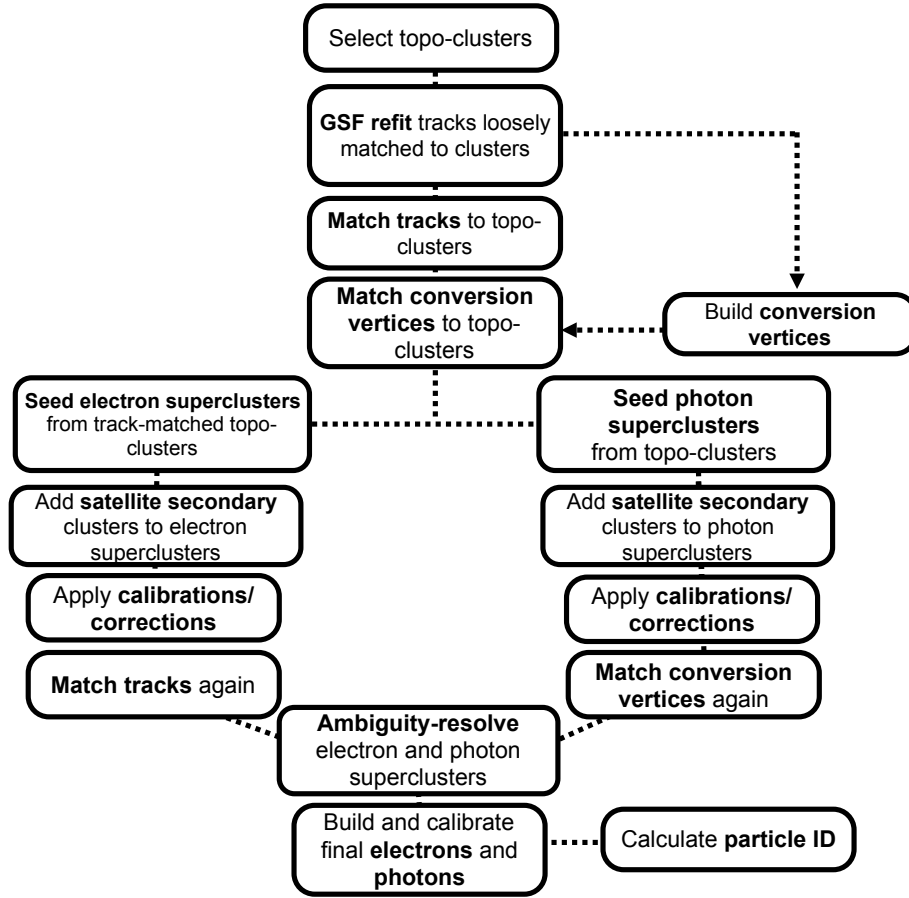


Figure 4–4 Algorithm flow diagram for the new electron and photon reconstruction^[88].

Electromagnetic (EM) topological clusters (topo-clusters) are constructed by an algorithm that initially uses the universal ”4-2-0” rules but later refines these to consider only cells from the EM calorimeter. This procedure serves multiple broader detector goals, including particle flow reconstruction and future isolation calculation enhancements.

The algorithm starts by duplicating the existing set of 4-2-0 topo-clusters. It then focuses on isolating clusters originating primarily from EM showers by applying an EM fraction (f_{EM}) criterion, calculated as follows:

$$f_{\text{EM}} = \frac{E_{L1} + E_{L2} + E_{L3} + w \cdot (E_{E4} + E_{\text{PS}})}{E_{\text{clus}}}, \quad w = \begin{cases} 1, & 1.37 < |\eta| < 1.63 \\ 0, & \text{otherwise} \end{cases} \quad (4-3)$$

Here, w takes different values based on the η region of the cluster, E_{Lx} is the energy in

layer x of the calorimeter, and E_{clus} is the total cluster energy. After removing cells from the hadronic calorimeter to reduce noise, the cluster's kinematics are recalculated.

A minimum energy threshold of $E_T > 400$ MeV is enforced to eliminate noise and irrelevant clusters. Through extensive Monte Carlo simulations, the f_{EM} value was optimized, leading to a pre-selection requirement of $f_{\text{EM}} > 0.5$. This criterion successfully filters out approximately 60% of pile-up-induced clusters while maintaining efficient electron identification.

In the electron track matching procedure, refitted tracks that are loosely matched initially undergo more stringent selection to be matched to EM clusters. This selection is defined with tighter constraints in η and ϕ . When there are multiple candidate tracks for a single cluster, a hierarchy is applied to determine the track that will define the electron's properties:

1. Tracks with hits in the pixel detector are prioritized.
2. Next, preference is given to tracks with hits in the SCT, but not in the pixel detector.

Within each category, tracks are further ranked based on their ΔR in $\eta - \phi$ space. Two types of ΔR calculations are performed:

1. The track momentum is rescaled to the cluster energy for the first calculation.
2. The second calculation uses the original, unrescaled track momentum.

The track with the better ΔR match is preferred, unless the differences are minimal, in which case the track with more pixel hits is chosen. Special weight is given to a hit in the innermost pixel layer. Momentum rescaling aids in achieving better track-cluster matching, especially when track momentum undergoes significant changes due to bremsstrahlung radiation. Distance-related variables between the track and cluster are also utilized for this matching, as detailed in the referenced studies^[89].

The electron supercluster reconstruction^[93] occurs in two main stages:

1. **Seed Cluster Identification:** EM topoclusters are scrutinized to act as seed cluster candidates. A cluster needs to have a minimum E_T of 1 GeV and must be associated with a track having at least four hits in the silicon trackers to qualify as a seed.
2. **Satellite Cluster Identification:** EM topoclusters near the seed are identified as potential satellite clusters, which can arise from bremsstrahlung radiation or topo-cluster splitting. If these satellite clusters satisfy specific criteria, they are added to the seed cluster to form the final supercluster.

Spatial criteria for defining a satellite cluster involve two conditions:

- A cluster is categorized as a satellite if it lies within a $\Delta\eta \times \Delta\phi = 0.075 \times 0.125$ window around the seed cluster barycenter.
- For electrons, a cluster is also considered a satellite if it is within a $\Delta\eta \times \Delta\phi = 0.125 \times 0.300$ window, and its 'best-matched' track is also the best-matched track for the seed cluster.

After superclusters are assembled, initial energy calibration is performed. The superclusters, therefore, improve the energy resolution of electron candidates, quantified by the IQE (Interquartile Energy), defined as:

$$\text{IQE} = \frac{Q_3 - Q_1}{1.349} \quad (4-4)$$

Here, Q_1 and Q_3 are the first and third quartiles of the $E_{\text{calib}}/E_{\text{true}}$ distribution. The normalization factor of 1.349 ensures that the IQE for a Gaussian distribution is equivalent to its standard deviation.

4.2.2.2 Electron Identification

One commonly used approach for electron identification^[94] is the likelihood-based (LH) method, which excels in differentiating prompt electrons from other similar signals, such as jets or non-prompt electrons.

The LH method utilizes a series of measurements obtained from both the tracking and calorimeter systems of the detector. These measurements are modeled using probability density functions (PDFs). Mathematically, the likelihoods for signal L_S and background L_B are calculated using the equation

$$L_{S(B)}(x) = \prod_{i=1}^n P_{S(B),i}(x_i). \quad (4-5)$$

To make a decision based on these likelihoods, a discriminant d_L is formed as $d_L = \frac{L_S}{L_S + L_B}$. However, d_L has a sharp peak, making it difficult to set a threshold for identification. To mitigate this, d_L is further transformed using an inverse sigmoid function: $d'_L = -\tau^{-1} \ln(d_L^{-1} - 1)$, where τ is a constant set to 15^[95]. This transformation makes it easier to differentiate between signal and background.

In the Table 4-2 that summarizes quantities for electron identification, various metrics are presented that are instrumental for the identification of prompt electrons. Columns la-

Type	Description	Name	Rejects			Usage
			LF	γ	HF	
Hadronic leakage	Ratio of E_T in the first layer of the hadronic calorimeter to E_T of the EM cluster (used over the range $\ \eta\ < 0.8$ or $\ \eta\ > 1.37$)	R_{had1}	x	x		LH
	Ratio of E_T in the hadronic calorimeter to E_T of the EM cluster (used over the range $0.8 < \ \eta\ < 1.37$)	R_{had}	x	x		LH
Third layer of EM calorimeter	Ratio of the energy in the third layer to the total energy in the EM calorimeter. This variable is only used for $E_T < 80\text{GeV}$, due to inefficiencies at high E_T , and is also removed from the LH for $\ \eta\ > 2.37$, where it is poorly modelled by the simulation.	f_3	x			LH
Second layer of EM calorimeter	Lateral shower width, $\sqrt{(\sum E_i \eta_i^2) / (\sum E_i) - ((\sum E_i \eta_i) / (\sum E_i))^2}$, where E_i is the energy and η_i is the pseudorapidity of cell i and the sum is calculated within a window of 3×5 cells	$w_{\eta 2}$	x	x		LH
	Ratio of the energy in 3×3 cells over the energy in 3×7 cells centred at the electron cluster position	R_ϕ	x	x		LH
	Ratio of the energy in 3×7 cells over the energy in 7×7 cells centred at the electron cluster position	R_η	x	x	x	LH
First layer of EM calorimeter	Shower width, $\sqrt{(\sum E_i (i - i_{\text{max}})^2) / (\sum E_i)}$, where i runs over all strips in a window of $\Delta\eta \times \Delta\phi \approx 0.0625 \times 0.2$, corresponding typically to 20 strips in η , and i_{max} is the index of the highest-energy strip, used for $E_T > 150\text{GeV}$ only	w_{stot}	x	x	x	C
	Ratio of the energy difference between the maximum energy deposit and the energy deposit in a secondary maximum in the cluster to the sum of these energies	E_{ratio}	x	x		LH
	Ratio of the energy in the first layer to the total energy in the EM calorimeter	f_1	x			LH
Track conditions	Number of hits in the innermost pixel layer	n_{Blayer}		x		C
	Number of hits in the pixel detector	n_{Pixel}		x		C
	Total number of hits in the pixel and SCT detectors	n_{Si}		x		C
	Transverse impact parameter relative to the beam-line	d_0		x	x	LH
	Significance of transverse impact parameter defined as the ratio of d_0 to its uncertainty	$\ d_0/\sigma(d_0)\ $		x	x	LH
	Momentum lost by the track between the perigee and the last measurement point divided by the momentum at perigee	$\Delta p/p$	x			LH
TRT	Likelihood probability based on transition radiation in the TRT	eProbabilityHT	x			LH
Track-cluster matching	$\Delta\eta$ between the cluster position in the first layer and the extrapolated track	$\Delta\eta_1$	x	x		LH
	$\Delta\phi$ between the cluster position in the second layer of the EM calorimeter and the momentum-rescaled track, extrapolated from the perigee, times the charge q	$\Delta\phi_{\text{res}}$	x	x		LH
	Ratio of the cluster energy to the track momentum, used for $E_T > 150\text{GeV}$ only	E/p	x	x		C

Table 4–2 Summary of Quantities for Electron Identification.

beled “Rejects” are provided to indicate the discriminative power of each metric against other signals such as light-flavour (LF) jets, photon conversions (γ), and non-prompt electrons originating from heavy-flavour (HF) quarks like b- or c-quarks. Another column, labeled “Usage,” is included to specify how each metric is used in the identification process. Metrics marked with “LH” are incorporated into the likelihood functions L_S and L_B , as specified in Equation 4-5. Metrics marked with “C” are utilized as direct selection criteria. For metrics that make use of the second layer of the calorimeter, notations like 3×3 , 3×5 , 3×7 , and 7×7 are employed to indicate the specific regions in $\Delta\eta \times \Delta\phi$ space that are covered, with each unit being 0.025×0.025 .

There are two major advantages to using the LH method over traditional cut-based identification techniques. First, it provides a more holistic evaluation of an electron candidate. In cut-based identification, failing to meet even a single condition could result in a false negative. In contrast, the LH method takes into account the collective information from all variables. Second, the LH method can include additional discriminating variables that may not be distinct enough for cut-based methods but still provide valuable information.

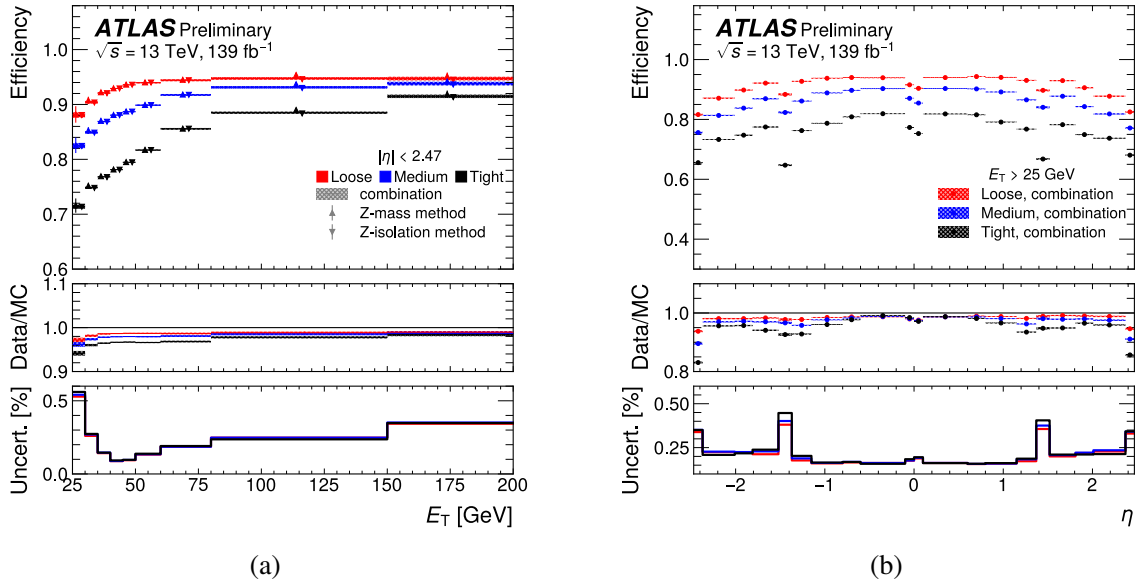


Figure 4-5 Efficiency plots of electron ID working points [96].

Figure 4-5 comprises two plots that present the efficiencies of various electron identification working points during the 2015-2018 Run 2 data from the LHC in $Z \rightarrow e^+e^-$ events. Figure 4-5a on the left illustrates these efficiencies as they relate to electron transverse en-

ergy (E_T). It not only showcases the aggregate data but also highlights the outcomes of individual efficiency assessment techniques, specifically the Z-mass and Z-isolation methods. These methods and working points can be found in the related study^[57]. Error indicators on this plot encompass both statistical and systematic uncertainties.

Figure 4-5b on the right focuses on the efficiencies as functions of the electron pseudorapidity (η). This plot also provides statistical and systematic uncertainty bands. A noteworthy feature of this plot is the decreased efficiency in the transitional zone between the electromagnetic calorimeter barrel and endcap, specifically for $1.37 < |\eta| < 1.52$, implemented to maintain manageable background levels.

4.2.2.3 Electron Isolation

Isolation for electrons in the study is quantified through two primary methods: calorimeter-based and track-based isolation variables.

In the calorimeter-based approach, the raw transverse energy $E_{T,\text{raw}}^{\text{isol}}$ is calculated by summing the transverse energies of topological clusters found within a specific cone around the electron or photon cluster center. The EM particle energy $E_{T,\text{core}}$ is subtracted out from this raw value. Corrections for energy leakage and pile-up are then applied. The final corrected calorimeter isolation variable is given by

$$E_T^{\text{coneXX}} = E_{T,\text{raw}}^{\text{isolXX}} - E_{T,\text{core}} - E_{T,\text{leakage}}(E_T, \eta, \Delta R) - E_{T,\text{pile-up}}(\eta, \Delta R), \quad (4-6)$$

where $\Delta R = \frac{XX}{100}$. For electron working points, a cone size of $\Delta R = 0.2$ is utilized, while for photons, cone sizes of $\Delta R = 0.2$ and $\Delta R = 0.4$ are employed.

The track isolation variable p_T^{coneXX} considers the transverse momentum of selected tracks within a cone centered around the electron or photon. For electrons, a variable cone size $p_T^{\text{varconeXX}}$ is used, defined as

$$\Delta R = \min\left(\frac{10}{p_T[\text{GeV}]}, \Delta R_{\text{max}}\right) \quad (4-7)$$

with ΔR_{max} typically being 0.2. The tracks in this approach must have $p_T > 1$ GeV and $|\eta| < 2.5$, along with certain hit and hole requirements in the silicon detectors.

The electron isolation strategies and their corresponding efficiencies are comprehensively detailed in Table 4-3. Figure 4-6 provides a comparative analysis of electron isolation efficiencies for $Z \rightarrow e^+e^-$ events collected during the 2018 Run 2 of the LHC. This figure

Working point	Calorimeter isolation	Track isolation
Gradient	$\epsilon = 0.1143 \times p_T + 92.14\%$ (with E_T^{cone20})	$\epsilon = 0.1143 \times p_T + 92.14\%$ (with $p_T^{\text{varcone20}}$)
HighPtCaloOnly	$E_T^{\text{cone20}} < \max(0.015 \times p_T, 3.5\text{GeV})$	-
Loose	$E_T^{\text{cone20}} / p_T < 0.20$	$p_T^{\text{varcone20}} / p_T < 0.15$
Tight	$E_T^{\text{cone20}} / p_T < 0.06$	$p_T^{\text{varcone20}} / p_T < 0.06$

Table 4-3 Description of electron isolation benchmarks and their corresponding performance metrics. For the Gradient strategy, the transverse momentum (p_T) is expressed in GeV. A consistent cone dimension of $\Delta R = 0.2$ is employed for both calorimeter and track-based isolation methods, with a maximum cone size of $\Delta R_{\text{max}} = 0.2$ designated for track isolation.

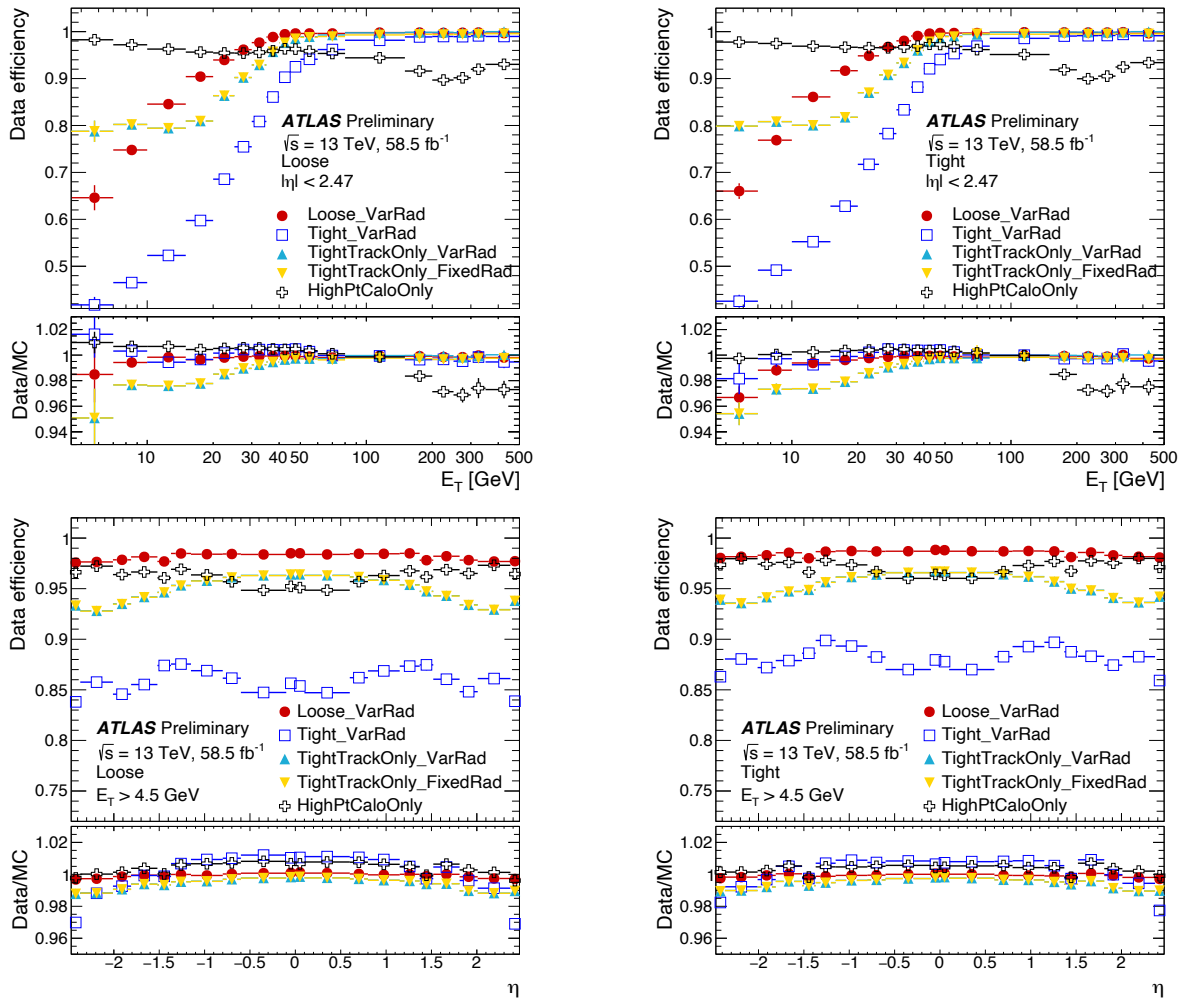


Figure 4-6 Efficiency plots of electron Isolation working points^[88].

presents data based on two crucial parameters—transverse energy E_T and pseudorapidity η , along with two selection criteria: Loose and Tight, which are derived from likelihood-based electron identification methods^[97].

4.2.3 Photons

In the ATLAS experiment, the techniques used for photon reconstruction closely parallel those used for electrons, as described in Section 4.2.2. Given the similarities in how both particles interact within the electromagnetic calorimeter, the foundational reconstruction and identification methodologies are almost identical. As such, this section will not revisit the reconstruction algorithms for photons, but will directly proceed to discuss the specific identification (ID) and isolation procedures tailored for photons.

4.2.3.1 Photon Identification and Isolation

The ATLAS experiment employs a multi-tiered identification system for photons, aimed to effectively segregate prompt, isolated photons from backgrounds predominantly from hadronic jets. This identification is based on a set of one-dimensional selection criteria, commonly referred to as shower shape variables in Table 4-2. The photon identification efficiencies are measured in 68 bins of photon E_T and η for both converted and unconverted photons. The bin edges are set at

$$E_T = \{10, 15, 20, 25, 30, 35, 40, 45, 50, 60, 80, 100, 125, 150, 175, 250, 350, \infty\} \text{ GeV}$$

and

$$|\eta| = \{0, 0.6, 1.37, 1.52, 1.81, 2.37\}.$$

No measurements are conducted for $|\eta| = \{1.37, 1.52\}$ due to its overlap with the transition region of the ATLAS calorimeter.

Three distinct methods are employed to measure photon identification efficiencies^[94]:

1. **Radiative Z:** Using probe photons from $Z \rightarrow \ell\ell\gamma$ decays with specific cuts on the invariant mass of the three-body system. The dominant uncertainty comes from low statistics at high E_T and MC generator modelling.
2. **Matrix Method:** Application of a matrix method on an inclusive photon sample. The efficiency for Loose photon candidates to pass the Tight identification is extracted and

corrected. The dominant systematic uncertainty arises from non-closure related to the assumption that isolation and identification efficiencies are independent.

3. **Electron Extrapolation:** Using electrons from $Z \rightarrow e^+e^-$ decays to emulate photon behavior. The method closure uncertainty is dominant at low E_T but decreases with increasing E_T .

The efficiencies, as shown in Figure 4-7 are first measured in MC simulation, and the photon shower shapes are corrected to better align with the data [94]. The data-to-MC simulation ratios are then applied to account for residual differences between identification selection efficiencies. These are determined from a weighted average of the three methods in each $E_T - \eta$ bin.

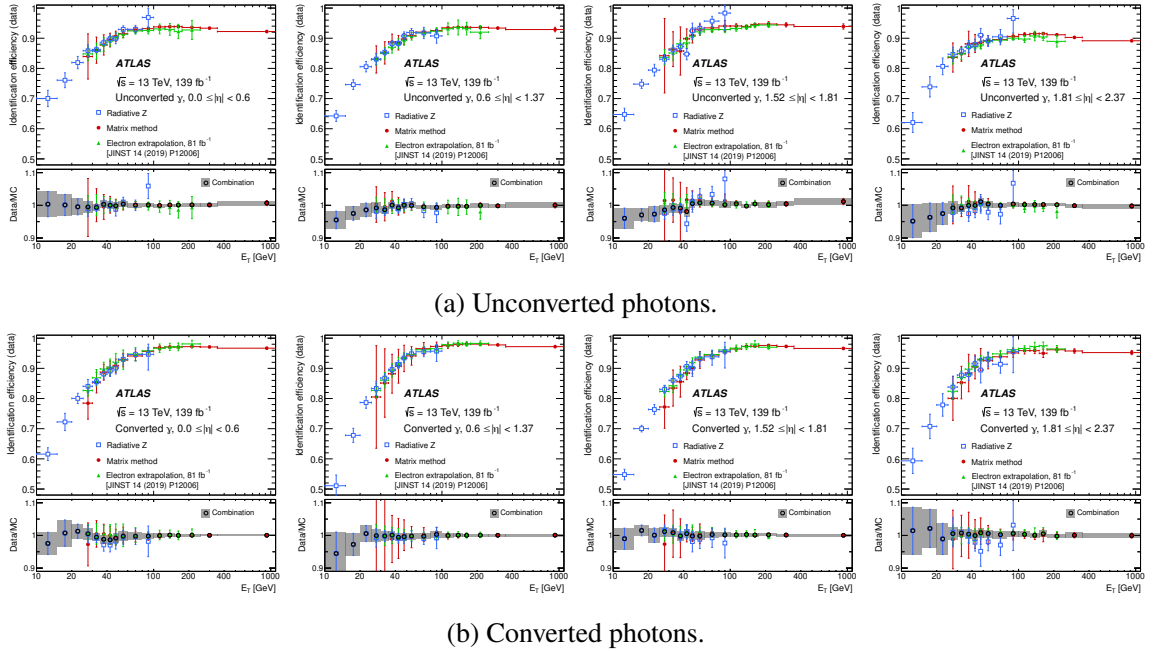


Figure 4-7 Efficiency measurements for unconverted and converted photons across different η bins [95].

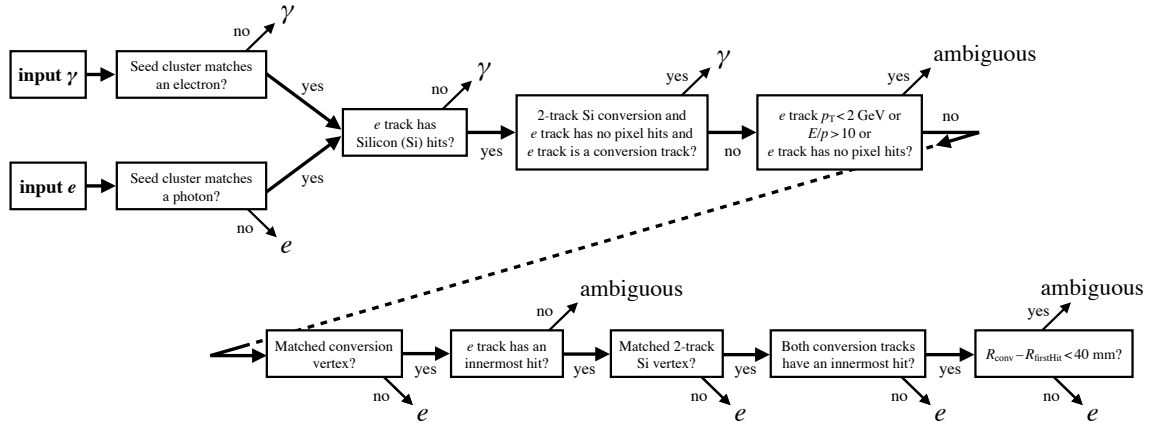
Table 4-4 outlines three distinct operating points for photon isolation, focusing on both calorimeter and track isolation variables. The study [97] identifies discrepancies between data and simulations in the calorimeter-based isolation variables, which are then corrected using data-driven shifts. The effectiveness of these corrections is examined across two primary photon signatures: radiative Z decays and inclusive photons.

Working point	Calorimeter isolation	Track isolation
Loose	$E_T^{\text{cone20}} < 0.065 \times E_T$	$p_T^{\text{cone20}} / E_T < 0.05$
Tight	$E_T^{\text{cone40}} < 0.022 \times E_T + 2.45\text{GeV}$	$p_T^{\text{cone20}} / E_T < 0.05$
TightCaloOnly	$E_T^{\text{cone40}} < 0.022 \times E_T + 2.45\text{GeV}$	-

Table 4–4 Definition of the photon isolation working points^[97].

4.2.3.2 Improvement of photon ID against electron fakes

The ATLAS experiment employs a sophisticated method for resolving ambiguities between electron and photon objects, primarily centered on a data structure known as a supercluster. These superclusters for electrons and photons are generated independently and are subjected to an initial round of energy calibration and position correction. Following this, tracks are correlated with electron superclusters, and conversion vertices are matched with photon superclusters using the same algorithmic approach that was employed for EM topo-clusters.

Figure 4–8 Flowchart of the ambiguity resolution procedure for electron and photon objects^[97].

A key point of differentiation arises here. If a seed cluster gives rise to both an electron and a photon supercluster, a specialized procedure outlined in Figure 4–8 is initiated. The aim is twofold: First, if a given object can be conclusively identified as a photon due to the absence of a 'good' associated track, then only a photon object is generated for downstream analysis. Similarly, if it can only be identified as an electron based on a good track and absence of a suitable photon conversion vertex, only an electron object is created. Second,

if the object is intrinsically ambiguous, both electron and photon objects are generated and marked explicitly for future classification depending on the requirements of specific analyses.

After this ambiguity resolution step, another round of energy recalibration is performed, given that the initial calibration precedes the final matching of tracks and conversion vertices. This recalibration is conducted according to a previously described procedure.

Lastly, discriminative variables such as shower shape are computed for both electrons and photons. Interestingly, lateral shower shapes are independent of the clustering algorithm used and are based solely on the position of the most energetically active cell. These variables are pivotal for the final identification and classification of the electron and photon objects.

With the current ambiguity solver, there is still a comparable amount of objects (electrons and photons) which are labelled as “ambiguity” type. With the mixture of pair production and photon conversion, separation between electrons and photons becomes challenging. This study is considered as the Qualification Task (QT) in the ATLAS experiment^[99]. In order to have better photon identification efficiency and high electron fake rejection efficiency, it is worth combining the topo-cluster information^[100] with the tracks information, which provides a set of variables with high separation power and is studied in the ambiguity tool. The ambiguity tool is a tool which is used during the EGamma reconstruction of electrons and photons. Due to the parallel reconstruction of electrons and photons, it occurs that the same constituents, such as topo-clusters and tracks, contribute to the formation of both electrons and photons. To avoid to save all the combinations the ambiguity tool removes the easiest cases when the reconstructed particles are “for sure not electron” or “for sure not photon”. In this cases the particles are saved only under one hypothesis. In the other case the reconstructed particles are saved both as electron and as photon and marked as “ambiguous”. Using the ambiguity objects is a good starting point to improve the photon identification criteria against photons faked by electrons.

The single photon process “ γ + jets” is chosen to be the physics sample in order to study the variables of truth prompt photon. There are two main mechanisms to produce photon + jets with p-p collision:

- quark-gluon Compton scattering, $qg \rightarrow q\gamma$
- quark-antiquark annihilation, $q\bar{q} \rightarrow g\gamma$

In order to study the photon and the electron fakes, two full simulated samples have

been considered, summarized in Table 4-5. The inclusive single photon sample generated with PYTHIA 8^[101], including the leading order $\gamma + \text{jets}$ events are treated as signal. The background samples are generated with POWHEG + PYTHIA 8^[102], including the $Z \rightarrow e^+e^-$ process.

Process	Generator	DSID	Tag
$\gamma + \text{jets}$	PYTHIA 8	423101	e3904_s3126_r9364_r9315_p4191
		423102-423106	e3791_s3126_r9364_r9315_p4191
		423107-423112	e4453_s3126_r9364_r9315_p4191
$Z \rightarrow e^+e^-$	PowhegPythia8EvtGen	361106	e3601_e5984_s3126_r10201_r10210_p4323

Table 4-5 Single Photon signal samples and $Z \rightarrow e^+e^-$ background samples.

In the $Z \rightarrow e^+e^-$ process, what is categorized as a "fake" photon is in fact one of the two electrons misidentified as a photon at the reconstruction level. Compared to a single-photon signal sample ($\gamma + \text{jets}$), these fake photons typically exhibit lower p_T values, a consequence of originating from the decay of a 90 GeV object. Given these differences in basic kinematic variables (p_T and η), it becomes essential to reweight the $|\eta| - p_T$ distribution of these fake photons in $Z \rightarrow e^+e^-$ events to align with the photon distribution in $\gamma + \text{jets}$ signal events. This ensures that the optimization procedures that distinguish true photons from fake ones are not biased by these kinematic discrepancies. Thus, the $Z \rightarrow e^+e^-$ process serves as an essential background process where one of the decay electrons is misclassified, affecting the overall kinematic distribution. By contrast, in true γ events, the kinematic variables are inherently different, necessitating this reweighting for a more accurate analysis.

A direct 2D (p_T and η) reweighting is applied on $Z \rightarrow e^+e^-$ background samples in order to scale the yields of background samples to signal yields in each p_T and η bins. The reweighting factor is simply dividing the weighted sum of yields of " $\gamma + \text{jets}$ " samples by the the weighted sum of yields of $Z \rightarrow e^+e^-$ samples for each p_T and η bins. In order to have finer reweighting, the kinematics binning strategy has been changed as followed:

- p_T [GeV]: 13 bins
 - [25, 30), [30, 35), [35, 40), [40, 45), [45, 50), [50, 60), [60, 80), [80, 100)
 - [100, 125), [125, 150), [150, 175), [175, 250), [250, 1500)
- $|\eta|$: 6 bins

– $[0.0, 0.6)$, $[0.6, 0.8)$, $[0.8, 1.37)$, $(1.52, 1.81)$, $[1.81, 2.01)$, $[2.01, 2.37)$

The 2D reweighting scale factors can be found in figure 4–9. The 1D basic kinematic distributions are summarized in figure 4–10.

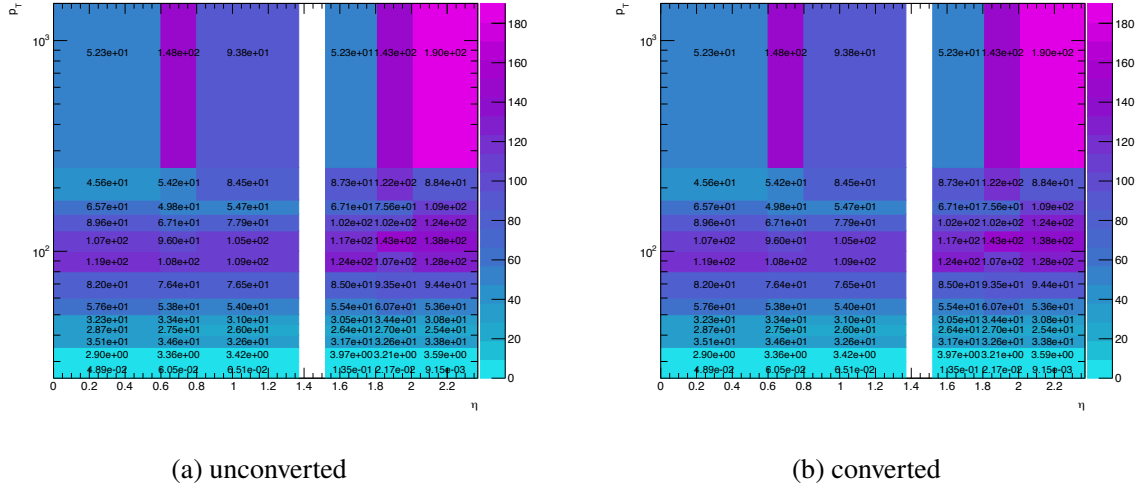


Figure 4–9 The distribution of reweighting scale factor (signal over background) in each p_T and η bin for both unconverted and converted case.

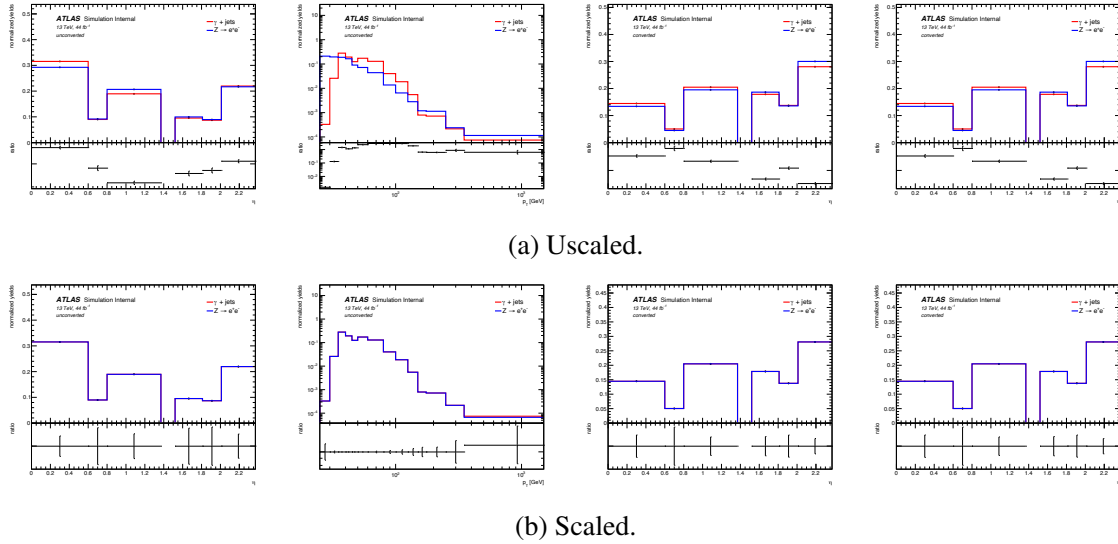


Figure 4–10 The 1D basic kinematic distributions before (top) and after (bottom) reweighting the basic kinematics of $Z \rightarrow e^+e^-$ to those of $\gamma + \text{jets}$ events.

In order to achieve good object quality, several basic selections need to be applied:

- Event Quality: duplicated events are removed.
- Truth matching: signal photons are required to be matched to the truth photon, while background photons should be matched to the truth electron.
- Object removal (only signal sample): each signal sample, aims at producing a definite photon p_T interval. Events out of the p_T intervals at the truth level are excluded.
- Loose photon ID: loose identification working point for photons is the minimal requirement for good object quality.
- Loose photon Isolation: FixedCutLoose_proRec¹ working point is used in order to maximize the selection of good photon quality.
- Ambiguity type: event is selected if there is at least one ambiguous photon. Yields of ambiguous events and total events are summarized in table 4-6.

		Ambiguous events	Total	Ratio
$\gamma + \text{jets}$	unconverted	679,097	5,368,897	11.3%
	converted	1,352,243	2,540,905	49.8%
$Z \rightarrow e^+e^-$	unconverted	1,564,090	3,125,334	50.7%
	converted	7,077,013	7,701,844	91.9%

Table 4-6 Yields of pre-selected ambiguous events and total pre-selected events before ambiguity requirement for $\gamma + \text{jets}$ and $Z \rightarrow e^+e^-$.

In order to improve the identification power to separate true photons from fake photons, this study uses a combination of variables from tracker and calorimeter. Many variables have been studied for distinguishing photon and photons faked by jets. They are the good starting to study photons faked by electrons. This analysis will focus on three sets of variables: shower shapes, Topo-clusters variables and ambiguity (tracker related) variables.

For shower shapes, most of the variables have already been introduced in Table 4-2 and R_{had} and R_{had1} has been combined as one variable with different $|\eta|$ region. Three new shower shape variables from EM first layer are added to this study:

- $w_{\eta1}$ or w_{s3} : Lateral shower width calculated from three strips around the strip with the highest energy deposit.
- F_{side} : Energy fraction outside core of three central cells, within seven cells

¹ isolation defined as $E_T^{\text{cone20}} < 0.065 p_T$ & $p_T^{\text{cone20}} < 0.05 p_T$

- ΔE : Difference between the energy of the cell associated with the second maximum, and the energy reconstructed in the cell with the smallest value found between the first and second maxima.

In total five topo-cluster variables are considered in this study (Only variables from the leading topo-cluster are included):

- E_{topo}^+ : total positive energy of the leading topo-cluster.
- $\sqrt{\langle r^2 \rangle}$: the second moment of the radial (shortest) distance of cell to the shower axis.
- $\sqrt{\langle \lambda^2 \rangle}$: the second moment of the longitudinal distance of cell from the cluster centre of gravity measured along shower axis.
- $|r|$: the radial (shortest) distance of cell to the shower axis, $\sqrt{x^2 + y^2 + z^2}$.
- λ_{center} : shower depth at its centroid of the topo-cluster.

These variables were studied in detail, and have been proved to be the most discriminating among all moments in the previous analysis^[100]. Other powerful variables such as signal moments can be studied in the future.

In the current cutflow of the ambiguity tools in figure 4-8, there are 13 variables used to help separating electrons, photons and ambiguity type. In order to optimize the ambiguity efficiency on photon and electron fakes, the following 5 variables are chosen:

- p_T^{amb} : the transverse momentum of the reconstructed electron which is reconstructed using the same cluster of the reconstructed photon.
- $p_T^{\text{amb,track}}$: the p_T measured using the track associated to the reconstructed electron which is using the same cluster of the reconstructed photon.
- E/P : the ratio of energy (measured from the cluster) and momentum (measured from the track) of the ambiguity object. If the track is a random track (for example if the object is a true unconverted photon and it is) this variable is expected to be far from 1. On the contrary if it is a real electron, this variable is expected to be close to 1.
- PixelHits: number of pixel hits from the track.
- SiliconHits: number of silicon hits from the track.

Due to the detector performance and the reconstruction efficiency, the behaviour of photons will be different in various p_T and η region. This prompts the kinematics region splitting so that in each region, an individual optimization is studied due to the distinct physics performance. The p_T and η binning is chosen to ensure enough statistics in both low p_T (large

$Z \rightarrow e^+e^-$ statistics) and high p_T (large γ + jets statistics) region:

- p_T [GeV]: 4 bins
 - [25, 40), [40, 55), [55, 80), [80, 1500)
- $|\eta|$: 5 bins
 - [0, 0.6), [0.6, 1.37), (1.52, 1.81), [1.81, 2.01), [2.01, 2.37)

Rectangular optimization is considered to be the strategy in this study. In some photon-related analyses such as the $H \rightarrow \gamma\gamma$ analysis, the selections in the photon identification need to be partially reversed in order to estimate photon fakes. For this specific reason, BDT or deep learning cannot be used in the optimization strategy. There are 19 available discriminating variables, which are unnecessary for rectangular optimization. Rectangular optimization does not heavily rely on the correlation and the underlying effect. So a better way is to shrink the size of available discriminating variables to a relatively small number, reducing the training time. The selection of this number depends on the overall performance of the final results. The cases of 5, 9, 10, and 19 have been tested for the final performance. Results with 9 variables are better than with 5, and give similar performance than when using more variables. It is thus better to use 9 discriminating variables to train for more stable and smooth performance^[99]. The variable separation ranking from the BDT method^[95] can be a good guide to select discriminating variables, as listed in table 4–7. There are two strategies for selecting variables:

1. Use the variable separation ranking from the inclusive region (not splitting p_T and η into finer bins) and then choose the fixed top 9 variables for all sub-regions.
2. Run the variable separation ranking for each p_T and η region, and then choose the top 9 variables for each region.

Both strategies have been studied and the difference in the final signal identification efficiency is small. This study will focus on the first strategy using fixed top 9 variables from the inclusive region. (The performance of these two methods is similar, but for simplicity and stability, method one is preferred.)

Table 4–7 shows that the most discriminating variable for both unconverted and converted cases is from the ambiguity variables, which follows the physics intuition that the main difference for photon and electron is if the track is well matching the cluster. For the converted case, the main separating variables are ambiguity variables and Shower shapes.

rank	variable	separation	variable	separation
	unconverted		converted	
1	E/P	0.057100	PixelHits	0.071860
2	$p^{\text{amb,track}}$	0.031760	SiliconHits	0.037530
3	R_ϕ	0.016490	R_ϕ	0.026240
4	PixelHits	0.016280	E/P	0.021060
5	SiliconHits	0.015300	ΔE	0.019500
6	$\sqrt{\langle r^2 \rangle}$	0.008835	F_1	0.018310
7	ΔE	0.008517	E_{ratio}	0.016430
8	E_{ratio}	0.006444	$w_{\eta 2}$	0.009212
9	$w_{\eta 2}$	0.004687	R_η	0.007168
10	F_1	0.004124	p_T^{amb}	0.005839
11	$\sqrt{\langle \lambda^2 \rangle}$	0.002756	$\sqrt{\langle r^2 \rangle}$	0.005554
12	λ_{center}	0.002653	λ_{center}	0.003968
13	p_T^{amb}	0.002644	E_{topo}^+	0.001319
14	R_{had1}	0.002242	$ r $	0.001108
15	R_η	0.001873	$\sqrt{\langle \lambda^2 \rangle}$	0.000545
16	$w_{\eta 1}$	0.001412	R_{had1}	0.000455
17	E_{topo}^+	0.000907	$w_{\eta 1}$	0.000274
18	$ r $	0.000466	$p^{\text{amb,track}}$	0.000051
19	w_{tots1}	0.000049	w_{tots1}	0.000004

Table 4–7 Separation power of shower shapes, topo-cluster, and ambiguity variables, which are retrieved from the BDT method from TMVA package, since the kCut method does not provide the variable ranking

Topo-cluster variables have a relatively low separation power compared with the other two sets of variables. But for the unconverted case, all three sets of variables play an important role in separation. E/P and R_ϕ have a high rank for both two cases. So the final top 9 discriminating variables are:

- **unconverted:** E/P , $p^{\text{amb,track}}$, $\sqrt{\langle r^2 \rangle}$, R_ϕ , ΔE , E_{ratio} , PixelHits, SiliconHits and $w_{\eta 2}$.
- **converted:** PixelHits, SiliconHits, E/P , E_{ratio} , ΔE , R_ϕ , F_1 , $w_{\eta 2}$, and R_η .

The finer rectangular optimization will be based on these 9 variables.

The real application of this rectangular optimization is based on full photon container, which includes both photons identified as photons and photons identified as ambiguous ob-

jects. The performance of this study can be measured using the background efficiency when the signal efficiency is at a certain level (80%, 60%, and 50%). The overall performance for the unconverted case is better than for the converted case. As expected, photons faked by electrons concentrate in the low p_T and low η regions. The fake photon rate decreases when p_T and η increase. The corresponding ROC curves are summarized in figure 4-11. Cut efficiencies both for γ + jets and $Z \rightarrow e^+e^-$ when signal efficiency is 80%, 60% and 50% respectively can be found in Figure 4-12.

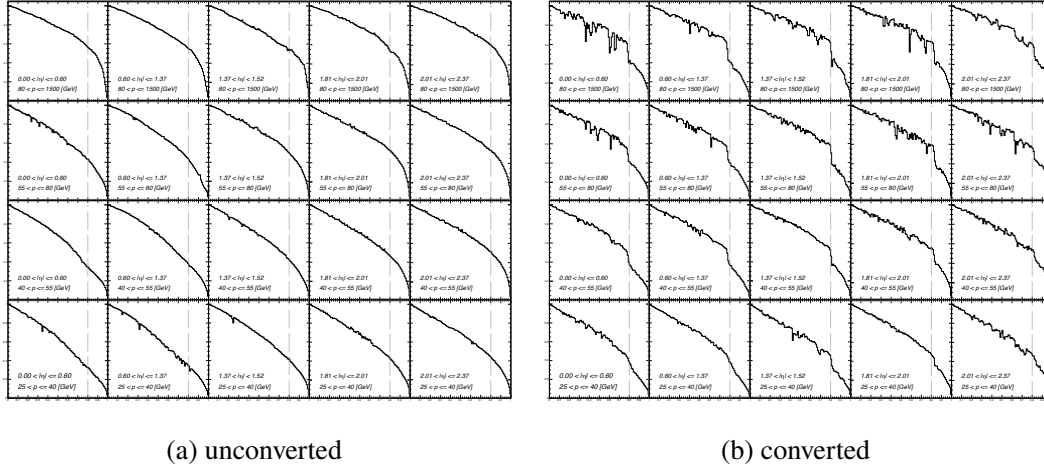


Figure 4-11 The ROC performance of rectangular optimization for all p_T and η bins. The grey line is signal efficiency of 80%.

4.2.4 Muons

4.2.4.1 Muon reconstruction

Muons in the ATLAS experiment are predominantly identified based on their minimum-ionizing particle signature. This is evident either through a track in the Muon Spectrometer (MS) or unique energy depositions in the calorimeters. The primary sources of information for muon reconstruction^[103-104] are the Inner Detector (ID) and MS tracking detectors, while calorimeter data is also used for refining track parameters and for MS-independent candidate tagging.

Track reconstruction in the MS initiates with the identification of local, straight-line track segments that are based on hits in individual MS stations. These segments are detected via a Hough transform^[105]. Preliminary track candidates are then formulated by applying a loose

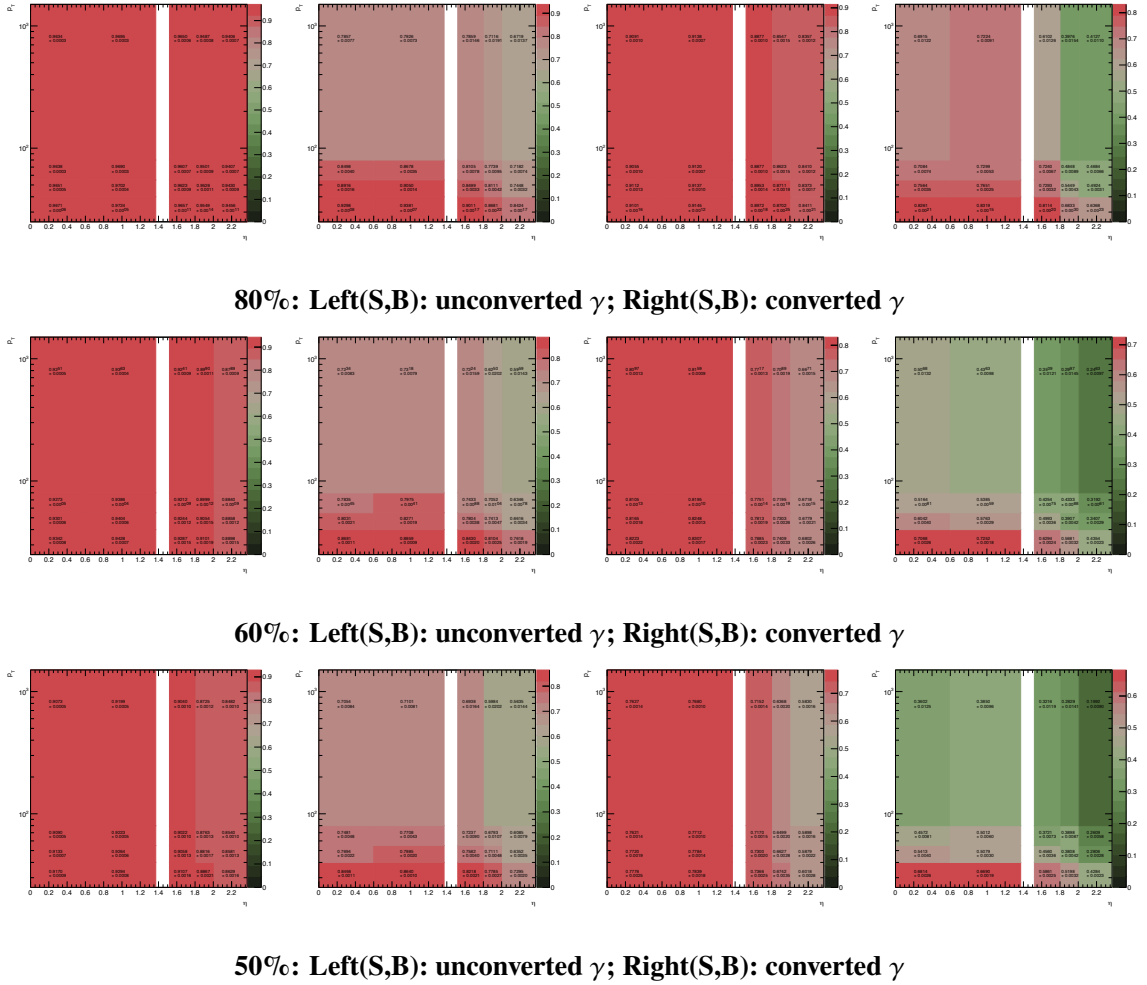


Figure 4-12 Comparison of Photon Conversion Efficiency: Rows correspond to 80%, 60%, and 50% efficiency levels. Each row comprises unconverted and converted γ for signal and background.

pointing constraint to the interaction point (IP) via a parabolic trajectory approximation. This accounts for the muon bending in the magnetic field. A global χ^2 fit is employed to optimize the muon trajectory, taking into account possible interactions in the detector material and potential misalignments between detector chambers.

Global muon reconstruction employs data from both the ID and MS along with calorimeter information. There are five main strategies for muon identification: combined (CB), inside-out combined (IO), muon-spectrometer extrapolated (ME), segment-tagged (ST), and calorimeter-tagged (CT). CB muons are identified by aligning MS and ID tracks followed by a combined track fit, factoring in energy loss in the calorimeters. For regions with $|\eta| > 2.5$, a specific class of muons, known as silicon-associated forward (SiF) muons, is identified.

IO muons are detected by extrapolating ID tracks to the MS and requiring at least three loosely-aligned MS hits. In cases where an MS track cannot be aligned with an ID track, it is extrapolated to the beamline to identify an ME muon, thereby extending the detector's acceptance to $|\eta| = 2.7$. ST muons necessitate tight angular matching between an ID track extrapolated to the MS and at least one MS segment. CT muons are identified by examining energy depositions in the calorimeters consistent with a minimum-ionizing particle, applying a p_T threshold of 5 GeV to mitigate background noise.

Several advancements have been made in muon reconstruction techniques as compared to earlier models^[106]:

- A parabolic trajectory in pattern recognition enhances segment matching across different stations.
- The introduction of SiF muons optimizes the utility of the ID near its acceptance boundaries.
- Alignment uncertainties are now incorporated into the track fits.
- The calorimeter-tagging algorithm has been fine-tuned for enhanced purity in regions with limited MS coverage.

4.2.4.2 Muon identification

After reconstruction, high-quality muon candidates used for physics analyses are selected based on a set of requirements concerning the number of hits in different ID subdetectors and MS stations, track fit properties, and compatibility tests between the ID and MS measurements. A specific set of requirements for each muon type, as described in Section 4.2.4.1, is called a selection working point (WP). Multiple WPs are defined to cater to a variety of physics analyses involving muons.

Different analyses necessitate varying levels of prompt-muon identification efficiency, momentum measurement resolution, and background rejection capabilities. Special attention is paid to differentiating between muon candidates originating from light hadrons and those from heavy-flavor hadrons. The selection WPs primarily target the rejection of light hadrons which produce lower-quality tracks due to in-flight decays within the detector.

The Loose, Medium, and Tight selection working points The selection working points (WPs) are parameterized by several numerical criteria, often dependent on the pseudorapidity

η and transverse momentum p_T of the muon candidate. For the Medium WP, the criteria are:

- ID Acceptance: $|\eta| < 2.5$
- Number of Precision Stations: ≥ 2 (Exception: $|\eta| < 0.1$ can have one)
- q/p Compatibility: < 7

For the Loose WP, it includes all muons passing the Medium WP plus additional cases:

- For $|\eta| < 0.1$: Includes CT and ST muons
- For $p_T < 7$ GeV and $|\eta| < 1.3$: Includes IO muons with only one precision station

Efficiency Increase: $\approx 20\%$ for $3 \text{ GeV} < p_T < 5 \text{ GeV}$; $\approx 1\% - 2\%$ for $p_T > 5 \text{ GeV}$. The Tight WP imposes additional constraints:

- $\chi^2/\text{ndf} < 8$ for the combined track fit
- Optimized q/p and ρ_0 based on p_T and $|\eta|$

Efficiency Loss: $\approx 6\%$ for $6 \text{ GeV} < p_T < 20 \text{ GeV}$; Background Reduction: $> 50\%$ compared to Medium WP.

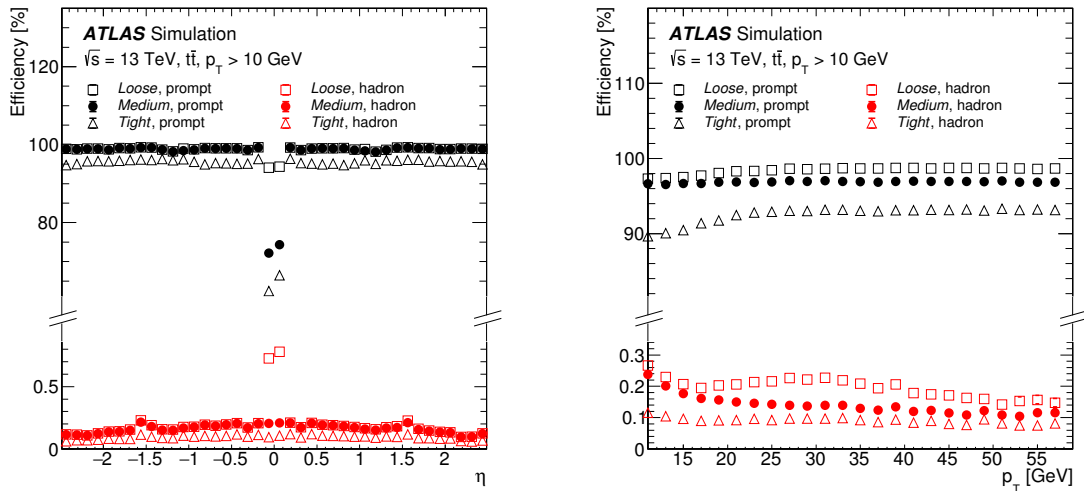


Figure 4-13 Efficiency vs η and p_T for different WPs in simulated $t\bar{t}$ events^[107].

In Figure 4-13, the efficiencies of various Working Points (WPs) are plotted as functions of pseudorapidity (η) and transverse momentum (p_T) under the scope of simulated $t\bar{t}$ events. The figure serves a dual purpose: first, it reveals how the efficiency of each WP correlates with η and p_T ; second, it differentiates between the efficiencies for muons that are promptly produced and those that result from hadron decays.

4.2.4.3 Muon isolation

Selection requirements are imposed on the impact parameters of the muon track to reject muons originating from hadron decays in-flight and from non-hard-scattering interactions. Two impact parameters are considered: the transverse impact parameter $|d_0|$ and the longitudinal impact parameter z_0 . The $|d_0|$ is measured relative to the actual beam position and is defined in terms of its significance, $|d_0|/\sigma(d_0)$, which is required to be less than three. The longitudinal distance $|z_0| \sin \theta$ is used, where θ is the polar angle of the muon track. For tracks with $p_T > 10 \text{ GeV}$, the impact parameter resolution is approximately $10 \mu\text{m}$ in the transverse plane and $50 \mu\text{m}$ in the longitudinal direction.

The isolation variable for track-based isolation is p_T^{cone} , defined as the scalar sum of p_T of ID tracks in an $\eta - \phi$ cone of size ΔR around the muon, excluding the muon itself. ΔR varies as either 0.2 or $\min(10 \text{ GeV}/p_T^\mu, 0.3)$. Calorimeter-based isolation is denoted as $E_T^{\text{topocone20}}$, defined in a cone $\Delta R = 0.2$ around the muon after correcting for pile-up effects. Particle-flow-based isolation combines track-based and calorimeter-based methods, using a weighting factor $w = 0.4$ to optimize for heavy-flavour hadron decays.

Several isolation WPs are defined to balance various performance metrics. These are categorized based on track-based isolation variables, possibly with additional criteria for calorimeter-based or particle-flow-based isolation.

Isolation WP	Definition	Track p_T requirement
PflowLoose*	$(p_T^{\text{varcone30}} + 0.4 \cdot E_T^{\text{neflow20}}) < 0.16 \cdot p_T^\mu$	$p_T > 500 \text{ MeV}$
PflowTight*	$(p_T^{\text{varcone30}} + 0.4 \cdot E_T^{\text{neflow20}}) < 0.045 \cdot p_T^\mu$	
Loose*	$p_T^{\text{varcone30}} < 0.15 \cdot p_T^\mu, E_T^{\text{topocone20}} < 0.3 \cdot p_T^\mu$	$p_T > 1 \text{ GeV}$
Tight*	$p_T^{\text{varcone30}} < 0.04 \cdot p_T^\mu, E_T^{\text{topocone20}} < 0.15 \cdot p_T^\mu$	
HighPtTrackOnly	$p_T^{\text{cone20}} < 1.25 \text{ GeV}$	$p_T > 1 \text{ GeV}$
TightTrackOnly*	$p_T^{\text{varcone30}} < 0.06 \cdot p_T^\mu$	
PLBDTLoose (PLBDTTight)	$p_T^{\text{varcone30}} < \max(1.8 \text{ GeV}, 0.15 \cdot p_T^\mu)$ BDT cut to mimic TightTrackOnly (Tight) efficiency	$p_T > 1 \text{ GeV}$

Table 4–8 Definitions of the muon isolation WPs.

The various isolation WPs are summarized in Table 4–8, which also provides the criteria used for each WP in its second column and the minimum track p_T requirements in the third column. Some WPs are marked with an asterisk (*) and exist in two variants: one where the cone ΔR parameter decreases with p_T^μ as $\min(10 \text{ GeV}/p_T^\mu, 0.3)$, and the other remaining

constant at $\Delta R = 0.2$ for $p_T^\mu > 50$ GeV. A track-only isolation WP is the most robust with respect to pile-up and suffers the lowest drop in efficiency from nearby objects. Two loose isolation WPs are defined using track isolation and either calorimeter or neutral particle-flow isolation, and are optimized for cases where high prompt-muon efficiency is prioritized over rejection of non-prompt muons. Two tight isolation WPs are defined using track isolation and either calorimeter or neutral particle-flow isolation, and are optimized for cases suffering from large backgrounds from non-prompt muons. Moreover, two isolation WPs are defined using the prompt lepton BDT: PLBDTLoose and PLBDTTight. In addition to a loose cut on the track isolation, a p_T -dependent BDT threshold selection is applied in each of these to achieve the same prompt-muon efficiency as the TightTrackOnly and Tight isolation WPs, respectively.

4.2.5 Hadronically decaying taus

The reconstruction of $\tau_{\text{had-vis}}$ candidates is based on seed jets formed using the anti- k_t algorithm with a distance parameter $R = 0.4$ ^[108]. The seed jets must fulfill $p_T > 10$ GeV and $|\eta| < 2.5$. The vertex is determined based on the highest p_T -weighted fraction of tracks with $p_T > 0.5$ GeV within $R = 0.2$ ^[109].

A set of BDTs classify tracks within $R = 0.4$ into core and isolation tracks. Energy calibration is applied via pile-up subtraction and response correction within $R = 0.2$ ^[106,110].

4.2.5.1 RNN Tau Identification

The RNN model uses a combination of low-level and high-level variables^[111]. Low-level variables include $p_{\text{track}T}$, $d_{\text{track}0}$, $z_{\text{track}0} \sin \theta$, $\Delta\eta_{\text{track}}$, $\Delta\phi_{\text{track}}$ and the number of hits in different detector layers. High-level variables comprise $p_{\text{seed jet}T}$, f_{cent} , $f_{\text{lead track}}^{-1}$, ΔR_{max} , $|S_{\text{lead track}}|$, $S_{\text{flight}T}$, f_{trackiso} , f_{EMtrack} , and $m_{\text{EM+track}}$.

4.2.5.2 Performance Metrics

The rejection power of the RNN-based tau identification is approximately twice as efficient as the BDT-based approach for both 1-prong and 3-prong $\tau_{\text{had-vis}}$ candidates^[109]. Working points are defined as Very Loose, Loose, Medium, and Tight, with the Tight working point having an RNN score threshold of > 0.55 .

The figure 4-14 accompanying this section illustrates the comparative rejection power of

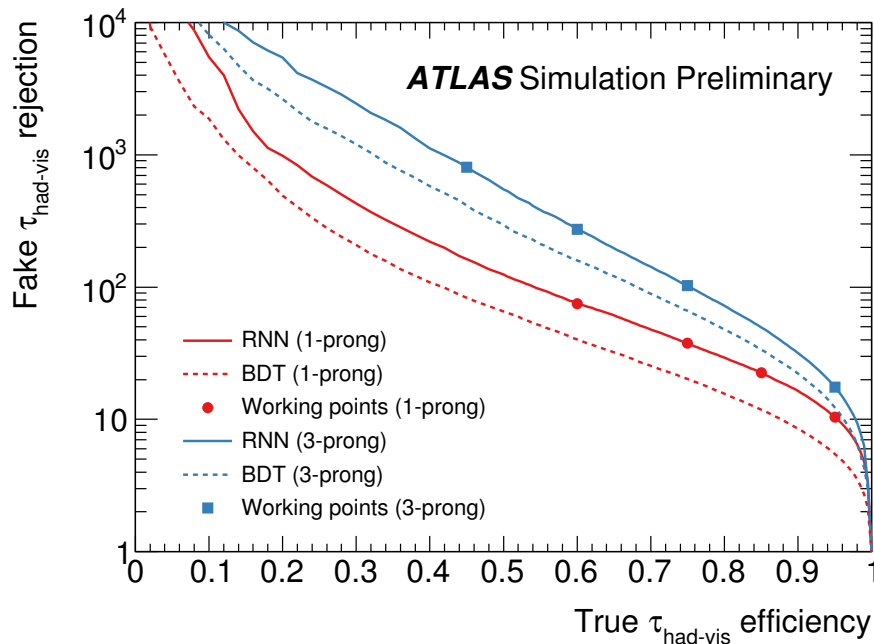


Figure 4-14 Rejection power for different prong configurations of $\tau_{had-vis}$ candidates, comparing RNN-based and BDT-based algorithms^[112].

RNN-based and BDT-based identification algorithms for 1-prong and 3-prong $\tau_{had-vis}$ candidates. The RNN-based algorithm demonstrates a significantly higher rejection power across both prong configurations.

4.2.6 Jets and b-jets

4.2.6.1 Jet Reconstruction using PFlow Algorithm

Two principal methodologies are used for jet reconstruction in the ATLAS experiment: calorimeter-based jet reconstruction and particle flow (PFlow) jet reconstruction. The former method utilizes topological clusters of calorimeter cells^[92] and employs a Jet Energy Scale (JES) correction factor for calibration^{[113][114]}. This approach, while widely used, has limitations in resolution. The latter, PFlow reconstruction^[115], integrates measurements from both the calorimeter and tracking systems to form an ensemble of 'particle flow objects,' aiming for enhanced granularity and resolution. The focus of the subsequent sections will be on the PFlow method, detailing its intricacies, advantages, and potential limitations in the jet reconstruction process.

The PFlow algorithm operates through a systematic, multi-step procedure to optimally

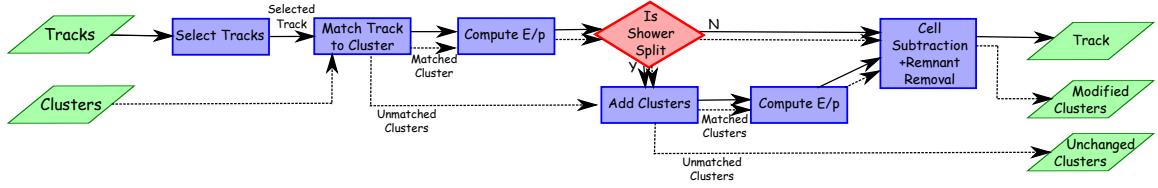


Figure 4–15 Flow chart depicting the sequential steps of the Particle Flow algorithm from track selection to energy subtraction in the calorimeter^[115]. The end result comprises charged particles, unmodified topo-clusters, and topo-cluster remnants with partially removed energy.

utilize both tracking and calorimetric information for the reconstruction of hadronic jets and soft activity. The procedure is shown in Figure 4–15. Initially, tracks are sorted in descending p_T order and selected based on stringent criteria. Each of these tracks is then matched to a single topo-cluster in the calorimeter. For each matched track-topo-cluster system, the algorithm calculates the expected energy deposition in the calorimeter based on the topo-cluster position and the track momentum. Given that a single particle may deposit energy in multiple topo-clusters, the algorithm evaluates this possibility and, when required, additional topo-clusters are added to the system to recover the full shower energy. Subsequently, cell-by-cell energy subtraction is performed for the matched topo-clusters. Any remnants that remain are removed if the residual energy aligns with the expected shower fluctuations of a single particle’s signal. This meticulous process is fundamental for the accurate calculation of the missing transverse momentum E_{miss}^T , in the event. The algorithm’s validation relies on single-pion and dijet Monte Carlo samples without pile-up, with charged pions typically contributing approximately two-thirds of the visible jet energy.

PFlow jets are reconstructed using the anti- k_t algorithm^[108] with a radius parameter $R = 0.4$. Topo-clusters and tracks are the primary inputs, selected based on $|z_0 \sin \theta| < 2$ mm to minimize pile-up contributions. Calorimeter jets employ the same algorithm but use LC-scale topo-clusters. For both jet types, jet ghost-area subtraction^[116–117] is applied for pile-up correction, while a numerical inversion restores the jet response. The transverse energy density, ρ , in PFlow jets is computed from both charged and neutral PFlow objects, and is found to have a lower per-event value compared to calorimeter jets due to the exclusion of pile-up tracks. JES corrections account for variables such as charged fraction and energy fractions in different calorimeter layers. Data/MC comparisons^[118] show a maximum deviation of 2% in jet characteristics, confirming the robustness of the PFlow algorithm for jet reconstruction.

4.2.6.2 b-jet Identification using RNN

Jet flavor tagging, particularly the identification of jets originating from bottom quarks (b-jets), plays an indispensable role in the ATLAS experiment. While the baseline high-level b-tagging algorithm termed MV2c10^[119-120] in ATLAS, utilizes a Boosted Decision Tree (BDT) in combination with kinematic features and algorithms like IP3D, SV1, and Jet-Fitter, the nature of the data prompts an exploration into more advanced machine learning techniques. One key observation is that the transverse impact parameter significances (S_{d0}) of charged particles emanating from a b-hadron decay are not independently distributed but exhibit intrinsic correlations. MV2c10 and IP3D, which calculate per-flavor conditional likelihoods in a product space of 29,400 bins—specifically $35 \times 20 \times 14 \times 3$ for S_{d0} , S_{z0} , and track category—operate under the assumption of feature independence and, thus, do not capture these interdependencies.

These limitations are addressed by employing Recurrent Neural Networks (RNNs)^[121], which are capable of processing sequences of arbitrary lengths and capturing time-dependent correlations. Mathematically, given a sequence of tracks $\{x_1, x_2, \dots, x_T\}$, an RNN computes its internal state h_t as follows:

$$h_t = \phi(W_{hh}h_{t-1} + W_{xh}x_t + b_h),$$

where ϕ is an activation function, and W_{hh}, W_{xh} are the weight matrices. The final state h_T serves as a fixed-dimensional representation of the jet's properties and can be further processed by a fully connected layer to yield a b-tagging discriminant. RNN variants like Long Short-Term Memory (LSTM) and Gated Recurrent Units (GRUs) further extend this capability, enabling the efficient learning of long-term dependencies via specialized gating mechanisms.

In an evaluation of the RNN-based b-tagging algorithm, both the b-tagging efficiency and background rejection were systematically examined across varying jet p_T values. A discriminant function D_{RNN} , defined as

$$D_{\text{RNN}} = \ln \left(\frac{p_b}{f_c \cdot p_c + f_\tau \cdot p_\tau + (1 - f_c - f_\tau) \cdot p_{\text{light}}} \right),$$

was employed, where $f_c = 0.07$ and $f_\tau = 0$. At a preset b-tagging efficiency of 70%, the RNN algorithm surpassed IP3D, the baseline algorithm. Specifically, RNN exhibited a 2.5-fold increase in light-jet rejection and a 1.2-fold increase in c-jet rejection compared to IP3D.

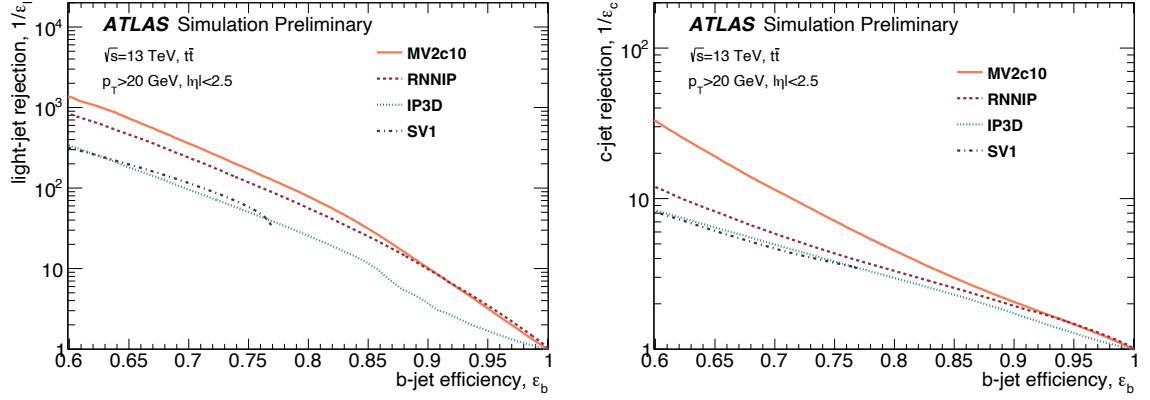


Figure 4-16 Comparison of light-jet (left) and c-jet (right) rejection against b-tagging efficiency for jets with $p_T > 20$ GeV and $|\eta| < 2.5$. Statistical errors are within 3%. MV2c10 serves as a high-level BDT-based benchmark, incorporating both IP3D and additional vertex metrics from JetFitter and SV1 [122].

The comparative performances of RNN and other algorithms are encapsulated in Figure 4-16.

4.2.7 Missing Transverse Energy

The reconstruction of E_T^{miss} in ATLAS is categorized into two contributions:

- **Hard-Event Signals:** Comprise electrons, photons, τ -leptons, muons, and jets.
- **Soft-Event Signals:** Consist of charged-particle tracks not associated with hard objects.

The key components are constructed from $E_{x(y)}^{\text{miss}}$ [123]:

$$E_{x(y)}^{\text{miss}} = - \sum_{i \in \text{hard objects}} p_{x(y),i} - \sum_{j \in \text{soft signals}} p_{x(y),j},$$

$$E_T^{\text{miss}} = \sqrt{(E_x^{\text{miss}})^2 + (E_y^{\text{miss}})^2},$$

$$\phi^{\text{miss}} = \tan^{-1} \left(\frac{E_y^{\text{miss}}}{E_x^{\text{miss}}} \right),$$

And the full missing transverse momentum formula is:

$$\begin{aligned}
 \mathbf{E}_T^{\text{miss}} &= - \sum_{\text{selected electrons}} \mathbf{p}_T^e - \sum_{\text{accepted photons}} \mathbf{p}_T^\gamma - \sum_{\text{accepted } \tau\text{-leptons}} \mathbf{p}_T^{\tau} - \sum_{\text{selected muons}} \mathbf{p}_T^\mu - \sum_{\text{accepted jets}} \mathbf{p}_T^{\text{jet}} - \sum_{\text{unused tracks}} \mathbf{p}_T^{\text{track}} \\
 &= \mathbf{E}_T^{\text{miss, e}} + \mathbf{E}_T^{\text{miss, } \gamma} + \mathbf{E}_T^{\text{miss, thad}} + \mathbf{E}_T^{\text{miss, } \mu} + \mathbf{E}_T^{\text{miss, jet}} + \mathbf{E}_T^{\text{miss, track}}
 \end{aligned}$$

In summary, the transverse missing energy does not play an important role in the di-Higgs $b\bar{b}\tau^+\tau^-$ analysis. And for the multilepton analysis, this variable proves valuable in distinguishing W-related processes from other standard model processes.

Chapter 5 SM Di-Higgs Searches in Multi-Lepton Final States

5.1 Introduction

This study focuses on the production of two Higgs bosons (HH) through the mechanism of gluon-gluon fusion. More details for a thorough understanding of HH physics can be found in Section 2.3.2. The data used in this research comes from the ATLAS detector and is based on proton-proton collisions at a center-of-mass energy of $\sqrt{s} = 13$ TeV. The dataset covers a total luminosity of 140 fb^{-1} , collected during the second run of the Large Hadron Collider.

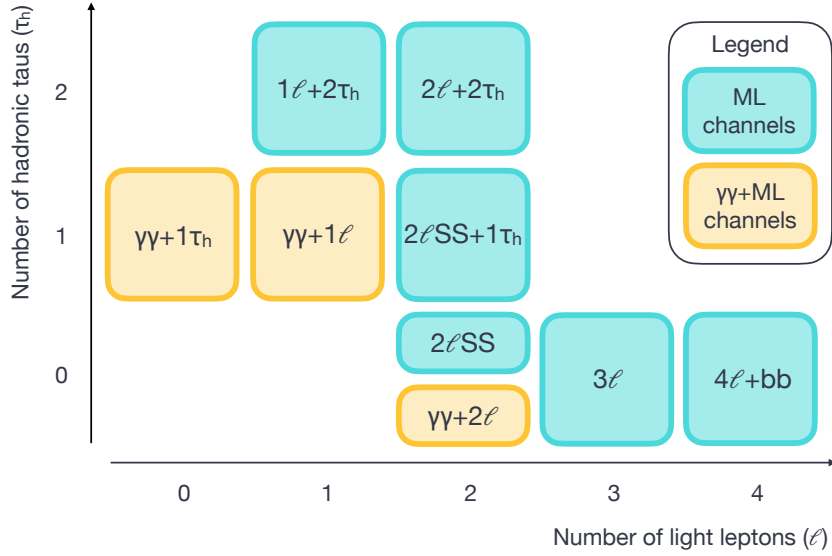


Figure 5-1 Overview of the multi-lepton final states considered.

In alignment with comprehensive analyses already undertaken by the ATLAS and CMS collaborations for this rare process, the present work performs a pioneering comprehensive search in multiple decay channels. These channels span $VVVV$, $VV\tau\tau$, $\tau\tau\tau\tau$, $\gamma\gamma VV$, and $\gamma\gamma\tau\tau$, where V can be either a W^\pm or Z boson. The study further encompasses HH decays into $b\bar{b}ZZ$, where the Z bosons subsequently decay into leptons. Figure 5-1 systematically categorizes the explored final states. Channels featuring a combination of diphoton and multiple leptons ($\gamma\gamma + ML$) are highlighted in yellow, while multi-lepton channels that also

involve hadronic taus are outlined in turquoise. Additionally, channels requiring both leptons to have identical electric charges are labeled with the acronym 'SS' (same-sign).

Six primary final states (pure-lepton), differentiated by the flavor and count of leptons, are considered:

- Tri-lepton channel without hadronic τ candidates (3ℓ).
- Quad-lepton final states from $H \rightarrow ZZ$ and accompanied by two b -jets ($b\bar{b} + 4\ell$).
- Di-lepton same-sign channel without hadronic τ candidates ($2\ell\text{SS}$).
- Channel with two same-sign light leptons and a single hadronic τ ($2\ell\text{SS} + \tau_{\text{had}}$).
- Channel with two light leptons and two hadronic τ candidates ($2\ell + 2\tau_{\text{had}}$).
- Single light lepton and two hadronic τ candidates ($\ell + 2\tau_{\text{had}}$).

An auxiliary set of final states involves one Higgs decaying to di-photons and the other Higgs decaying to WW , ZZ , or $\tau\tau$ ($\gamma\gamma + X$ channels):

- Single light lepton ($\gamma\gamma + \ell$).
- Single hadronic τ ($\gamma\gamma + \tau_{\text{had}}$).
- Di-lepton final state, flexible to include either light or hadronic τ leptons ($\gamma\gamma + 2\ell$).

Given the multiplicity of final states available in multi-lepton analyses, attention is often concentrated on individual channels to enable a thorough investigation. For the scope of this dissertation, our focus will be explicitly on the 3-lepton channel. The intrinsic complexities and rich phenomenology of this channel warrant a dedicated analysis. Subsequent to this targeted investigation, the results will be aggregated with other channels to provide a more comprehensive picture of the HH process in the results section.

5.2 Data and Monte Carlo samples

5.2.1 Data Preparation and Analytical Framework

The analytical process employs data initially structured in the xAOD format, which is subsequently transformed into the DxAOD format via the HIGG8D1 derivation framework. This transition, termed the GN1 framework, has been customized from the ttH multilepton analysis to specifically cater to signal events featuring multilepton final states.

Data size minimization is achieved through slimming (elimination of redundant variables), thinning (removal of entire objects from the event record), and event-level skimming

applied to both the collision data and Monte Carlo samples.

This framework has been particularly optimized for the $b\bar{b} + 4\ell$ channel, adhering to the lower p_T lepton thresholds as defined in the *baseline* lepton specification (see Section 5.3.1.3). Contrasting this, other multilepton channels employ more stringent lepton conditions (refer to Table 5-4), especially at the sample production phase (approximating the *Loose* criteria in Table 5-4 but utilizing FCLoose for lepton isolation).

It is noteworthy that channels involving $\gamma\gamma + X$ utilize a distinct derivation framework, named HIGG1D1, for their DxAOD production. This is complemented by the HGam framework, which inherently offers different lepton and τ_{had} definitions when compared to multi-lepton channels.

5.2.2 Data Collection and Quality

The current study utilizes a data set comprising 140 fb^{-1} of proton-proton collision records acquired by the ATLAS detector in the energy range of $\sqrt{s} = 13 \text{ TeV}$ spanning the years 2015-2018. The data have been collected with a bunch crossing interval of 25 ns, with the IBL (Insertable B-Layer) activated. Data quality verifications^[124] have been made in accordance with the predefined Good Run List (GRL). The GRLs used in this study are listed in Table 5-1.

Year	GRL XML File
2015	data15_13TeV.periodAllYear_DetStatus-v89-pro21-02_Unknown_PHYS_StandardGRL_All_Good_25ns.xml
2016	data16_13TeV.periodAllYear_DetStatus-v89-pro21-01_DQDefects-00-02-04_PHYS_StandardGRL_All_Good_25ns.xml
2017	data17_13TeV.periodAllYear_DetStatus-v99-pro22-01_Unknown_PHYS_StandardGRL_All_Good_25ns_TriggerNo17e33prim.xml
2018	data18_13TeV.periodAllYear_DetStatus-v102-pro22-04_Unknown_PHYS_StandardGRL_All_Good_25ns_TriggerNo17e33prim.xml

Table 5-1 Good Run List XML Files by Year.

5.2.3 Monte Carlo Simulations

The simulation framework relies on three distinct MC campaigns: mc16a, mc16d, and mc16e. These campaigns are tailored to replicate the conditions of the LHC runs for the years 2015-2016, 2017, and 2018, respectively, with particular emphasis on the interaction multiplicity per bunch crossing. To harmonize the simulated events with the actual collision data, a reweighting strategy is employed via the PileupReweightingTool^[125]. The event samples generated from these simulations are subsequently scaled according to their theoretical

cross-sections.

5.2.3.1 Background samples

Monte Carlo simulations for various signal and background processes are based on configurations specified in Table 5-2. These configurations are also employed to estimate systematic uncertainties (indicated in parentheses). Electroweak boson production (W or Z/γ^*) is denoted by V . Specific parton distribution functions (PDFs) and their roles in matrix element (ME) calculations and parton showers are clarified. The underlying-event tune for the parton shower generator and the software versions used in event generation are outlined. Heavy flavor hadron decays are modeled using EVTGEN 1.2.0, and photon emission is accounted for by either the parton shower generator or PHOTOS. The mass settings for the top quark and SM Higgs boson are at 172.5 GeV and 125 GeV, respectively.

Process	Generator	ME order	Parton shower	PDF	Tune
$t\bar{t}W$	SHERPA 2.2.10 (MG5_AMC)	NLO (NLO)	SHERPA (PYTHIA 8)	NNPDF3.0 NNLO (NNPDF3.0 NLO)	SHERPA default (A14)
$t\bar{t}t\bar{t}$	MG5_AMC (SHERPA 2.2.10)	NLO (NLO)	PYTHIA 8 (SHERPA)	NNPDF3.1 NLO (NNPDF3.0 NNLO)	A14 (SHERPA default)
$t\bar{t}H$	POWHEG-BOX ^{powhegtt} (Powheg-BOX) (MG5_AMC)	NLO (NLO) (NLO)	PYTHIA 8 (HERWIG7) (PYTHIA 8)	NNPDF3.0 NLO ^[126] (NNPDF3.0 NLO) (NNPDF3.0 NLO)	A14 (H7-UE-MMHT) (A14)
$t\bar{t}(Z/\gamma^* \rightarrow l^+l^-)$	SHERPA 2.2.11 (MG5_AMC)	NLO (NLO)	SHERPA (PYTHIA 8)	NNPDF3.0 NNLO (NNPDF3.0 NLO)	SHERPA default (A14)
$t\bar{t} \rightarrow W^+bW^-\bar{b}l^+l^-$	MG5_AMC	LO	PYTHIA 8	NNPDF3.0 LO	A14
$t(Z/\gamma^*)$	MG5_AMC	NLO	PYTHIA 8	NNPDF2.3 LO	A14
$tW(Z/\gamma^*)$	MG5_AMC	NLO	PYTHIA 8	NNPDF2.3 LO	A14
$t\bar{t}W^+W^-$	MG5_AMC	LO	PYTHIA 8	NNPDF2.3 LO	A14
$t\bar{t}$	POWHEG-BOX (POWHEG-BOX)	NLO (NLO)	PYTHIA 8 (HERWIG7.1.3)	NNPDF3.0 NLO (NNPDF3.0 NLO)	A14 (H7-UE-MMHT)
$t\bar{t}t$	MG5_AMC	LO	PYTHIA 8	NNPDF2.3 LO	A14
s -, t -channel, Wt single top	POWHEG-BOX ^{powhegstp.powhegstp2}	NLO	PYTHIA 8	NNPDF3.0 NLO	A14
$VV, qqVV,$ $lowm_{\ell\ell}, VVV$	SHERPA 2.2.2	NLO	SHERPA	NNPDF3.0 NNLO	SHERPA default
$Z \rightarrow l^+l^-$	SHERPA 2.2.1	NLO	SHERPA	NNPDF3.0 NLO	SHERPA default
$Z \rightarrow l^+l^-$ (matCO)	POWHEG-BOX	NLO	PYTHIA 8	CTEQ6L1 NLO	A14
$Z \rightarrow l^+l^-+(\gamma^*)$	POWHEG-BOX	NLO	PYTHIA 8	CTEQ6L1 NLO	A14
W +jets	SHERPA 2.2.1	NLO	SHERPA	NNPDF3.0 NLO	SHERPA default
VH	POWHEG-BOX	NLO	PYTHIA 8	NNPDF3.0 NLO	A14

Table 5-2 Event generation configurations for signal and background processes.

Pile-up is modeled through minimum-bias events generated via PYTHIA 8.186^[127], using

the NNPDF2.3LO PDFs and the A3 parameter set^[128]. These are then overlaid onto the primary hard-scatter events based on the luminosity profiles of the recorded data. The generated events are subjected to a simulation of the ATLAS detector's geometry and response through GEANT4^[129]. The same reconstruction software is applied as in the case of real data. Calibrations ensure that particle candidate selection efficiencies, energy scales, and resolutions are consistent with those determined from control samples in real data. The simulated datasets are normalized to their computed cross-sections, evaluated to the highest order available in perturbation theory.

5.2.3.2 Signal Samples

For ggF mode, events are generated at NLO accuracy using Powheg-Box-V2 for the matrix element and PYTHIA8 (A14 tune) for parton showering and hadronization. The PDF set employed is NNPDF 2.3 LO. Heavy-flavor hadron decays are modeled using EvtGen. Detector effects are accounted for by AlfastII (AF2). Lepton filters target multilepton final states, focusing on configurations such as $2\ell 0\tau$, $2\ell 1\tau$, $3\ell 0\tau$, among others. Lepton kinematics are restricted by a MultiLeptonFilter at $p_T > 7$ GeV and $|\eta| < 3$. Alternative ggF samples are produced with POWHEGBox-V2 interfaced to HERWIG7, employing the PDF4LHC15 PDF set to assess parton shower uncertainties. They adopt the same filtering strategy as the nominal samples.

For VBF mode, events are generated at LO with MADGRAPH5_AMC@NLO. Parton shower and hadronization are handled by PYTHIA8 using the A14 tune and the NNPDF 2.3 LO PDF set. HF hadron decays and detector effects are modeled similarly to the ggF case. Lepton filters are applied to target various final states.

5.3 Analysis Strategy

The analysis targets a final state characterized by three leptons, a channel that offers a relatively clean signal with a low branching ratio. The three-lepton requirement inherently acts as an effective filter against multi-jet backgrounds. This is augmented by employing advanced lepton identification and isolation working points, specifically the PromptLepton-Veto (PLV), thereby further mitigating backgrounds arising from fake leptons, which were dominant in prior analyses^[130]. Before any selection is applied, object definitions are estab-

lished for leptons, jets, and other relevant physics objects, which provide the foundation for the subsequent analysis stages. The major background contamination in this channel originates from the $WZ \rightarrow 3\ell 0\tau_h$ process. Given that the dominant backgrounds are largely EWK processes, targeted selection cuts are optimized to suppress these while retaining high signal efficiency.

The analysis pipeline comprises the following main stages:

1. **Pre-selection:** A set of baseline criteria applied to all events for initial filtering. Detailed pre-selection criteria are elaborated in Section 5.3.4.2.
2. **Background Modelling:** Four control regions (CRs) are defined to model various background contributions. These CRs are crucial for estimating background rates and for the validation of the analysis methodology. For details, refer to Section 5.3.5.
3. **Signal Region Optimization:** Multi-variate analysis techniques employing Boosted Decision Trees (BDT) are used to finely tune the selection criteria, maximizing signal significance in Section 5.3.6.
4. **Statistical Analysis:** A comprehensive statistical framework is employed for signal extraction, incorporating both statistical and systematic uncertainties, to derive the final results.

5.3.1 Object definitions

This section describes the methodologies for defining key objects with respect to multi-lepton channels. Criteria on data corruption or significant calorimeter noise result in event exclusion.

5.3.1.1 Selection of Primary Vertices

For multilepton channels, the primary vertex is designated as the one with the maximal $\sum p_T^2$ of its constituent tracks, following the criteria outlined in [131].

5.3.1.2 Event Triggering

In multilepton channels, an array of single-lepton and di-lepton triggers, pertinent to the 2015 - 2018 dataset, is listed in Table 5-3. These triggers are exempt from prescaling and are derived from the $t\bar{t}H$ multilepton 80 fb^{-1} analysis [132]. An inclusive OR condition is imposed between di-lepton (DL) and single-lepton (SL) triggers when at least two light leptons are

involved. For scenarios involving a single light lepton and two $\tau_{\text{had}}\tau_{\text{had}}$, non-prescaled single-lepton triggers are required.

Single lepton triggers (2015)	
μ	HLT_mu20_loose_L1MU15, HLT_mu50
e	HLT_e24_lhmedium_L1EM20VH, HLT_e60_lhmedium, HLT_e120_lhloose
Dilepton triggers (2015)	
$\mu\mu$ (asymm.)	HLT_mu18_mu8noL1
ee (symm.)	HLT_2e12_lhloose_L12EM10VH
$e\mu, \mu e$ (\sim symm.)	HLT_e17_lhloose_mu14
Single lepton triggers (2016)	
μ	HLT_mu26_ivarmedium, HLT_mu50
e	HLT_e26_lhtight_nod0_ivarloose, HLT_e60_lhmedium_nod0, HLT_e140_lhloose_nod0
Dilepton triggers (2016)	
$\mu\mu$ (asymm.)	HLT_mu22_mu8noL1
ee (symm.)	HLT_2e17_lhvloose_nod0
$e\mu, \mu e$ (\sim symm.)	HLT_e17_lhloose_nod0_mu14
Single lepton triggers (2017 / 2018)	
μ	HLT_mu26_ivarmedium, HLT_mu50
e	HLT_e26_lhtight_nod0_ivarloose, HLT_e60_lhmedium_nod0, HLT_e140_lhloose_nod0
Dilepton triggers (2017 / 2018)	
$\mu\mu$ (asymm.)	HLT_mu22_mu8noL1
ee (symm.)	HLT_2e24_lhvloose_nod0
$e\mu, \mu e$ (\sim symm.)	HLT_e17_lhloose_nod0_mu14

Table 5–3 List of lowest p_T -threshold, un-prescaled single lepton and di-lepton triggers used for 2015-2018 data taking.

Trigger corrections for simulation are computed event-wise with the TrigGlobalEfficiencyCorrection package^[133]. Any relevant scale factors for light lepton identification and isolation are appropriately integrated into the MC weight.

5.3.1.3 Lepton Working Points and Definitions

In signal events, leptons are primarily produced through the leptonic decays of WW/ZZ , which are themselves produced by Higgs decays. Harmonized Working Points (WPs) have been developed to optimize performance in both 2ℓ SS and 3ℓ channels while minimally affecting the tau-involved channels.

For multilepton channels, three distinct levels of light lepton selection criteria are implemented depending on the final state's object composition. These criteria are referred to as "Baseline" (B), "Loose" (L), and "Tight" (T), as defined in Table 5-4. The Baseline criteria are exclusively used in $b\bar{b} + 4\ell$ channels to augment the signal sensitivity. For categories other than $b\bar{b} + 4\ell$, the *Loose* definition is applied to establish channel orthogonality. Stricter definitions are utilized in channels with up to two light leptons and a single hadronically decaying tau to maximize signal sensitivity and minimize background interference. Specific lepton criteria for electrons, muons are elaborated in Sections 5.3.1.4, 5.3.1.5, respectively.

	e			μ		
	B	L	T	B	L	T
Isolation	None	PLVLoose	PLVTight	None	PLVLoose	PLVTight
Identification	LooseLH		TightLH	Loose		Medium
Charge MisID BDT	No	Yes	Yes	N/A	N/A	N/A
Ambiguity Resolution	No	Yes	Yes	N/A	N/A	N/A
$ d_0 /\sigma_{d_0}$	< 5			< 3		
$ z_0 \sin \theta $	< 0.5 mm					

Table 5-4 Definitions of Baseline, Loose, and Tight criteria in multilepton channels.

5.3.1.4 Electrons

The selection criteria for electron candidates in different multilepton channels involve several key elements:

- Electrons are reconstructed through matching energy deposits in the electromagnetic calorimeter with tracks in the inner detector.
- Baseline electrons are required to have $p_T > 4.5$ GeV and $|\eta| < 2.5$. Electrons within the calorimeter transition region $1.37 < |\eta| < 1.52$ are excluded.
- Stringent cuts on d_0 and z_0 ensure that electrons originate from a primary vertex.

- Employing a likelihood-based identification, the working points "LooseLH" and "TightLH" are used for Baseline/Loose and Tight electron candidates, respectively.
- Loose electrons should pass the *PLVLoose* working point¹ to ensure event isolation^[34].
- For stricter selection beyond Baseline, additional criteria like charge misidentification BDT and ambiguity selection (details in Section 4.2.3.2) are implemented to reduce background contributions.
- For Tight electrons, the *PLVTight* Isolation working point and the *TightLH* ID are mandated.

5.3.1.5 Muons

The selection criteria for muon candidates in multilepton channels are outlined below:

- Muons are reconstructed using data from both the Muon Spectrometer and the Inner Detector.
- Muon candidates must satisfy $p_T > 3$ GeV and $|\eta| < 2.5$.
- Two identification working points are used. Baseline muons are required to pass the "Loose" working point, while tighter criteria employ the "Medium" working point.
- Similar to electrons, muons must pass *PLVLoose* isolation criteria for baseline selection. Loose muons are required to fulfill *PLVLoose*, while Tight muons are selected from *PLVTight*.
- The criteria for both transverse and longitudinal impact parameters are harmonized with electrons. Specifically, $|d_0|/\sigma_{d_0} < 3$ and $z_0 < 0.5$ mm.

5.3.2 Jet and b-jet

The key elements concerning the selection and definition of jets and b-jets in the analysis are itemized below:

- The anti- k_t algorithm with a radius parameter $R = 0.4$ is used, operating on particle-flow (PFlow) objects.
- For ML channel, AntiKt4EMPFlowJets_BTagging201903 is employed.
- Events must pass the LooseBad working point as recommended by the Jet- E_T^{miss} group. A Tight Jet Vertex Tagger (JVT) working point is applied for $p_T < 60$ GeV and $|\eta| < 2.4$.

¹ PromptLeptonVeto

- Kinematic Selection:
 - $p_T > 25$ GeV
 - $|\eta| < 2.5$
 - $|y| < 4.4$
- Flavour Tagging: Utilizes a deep learning algorithm known as DL1r^[135], which has been re-optimized in 2019. The b-tagging working point with a 77% efficiency is selected.

The choices made for the jet and b-jet selections, including specific working points and efficiencies, are aimed at maximizing orthogonality to other diHiggs analyses. Associated scale factors for JVT and b-tagging are integrated into the MC event weight calculations. More details of these selection criteria can be found in the relevant studies^[136-137].

5.3.3 Overlap Removal

Overlap removal is essential to eliminate double-counting of reconstructed objects, which may occur due to the parallel use of different algorithms for object reconstruction. The procedure employed in this analysis is based on the ASG overlap removal tool in AnalysisTop^[138]. The criteria for overlap removal are listed in Table 5–5.

Kept Object	Removed Object	Condition
Electron	Calorimeter Muon	Sharing same track
Non-calorimeter Muon	Electron	Sharing same track
Electron	Jet	$\Delta R < 0.2$
Jet	Electron	$\Delta R < 0.4$
Muon	Jet	$n_{\text{track}} < 3$ and $\Delta R < 0.2$
Muon	Jet	$n_{\text{track}} < 3$ and Ghost-associated to muon ID track
Jet	Muon	$\Delta R < 0.4$
Electron	Tau	$\Delta R < 0.2$
Combined-type Muon	Tau	$p_T > 2$ GeV and $\Delta R < 0.2$
Tau	Jet	$\Delta R < 0.2$
Electron/Muon	Photon	$\Delta R < 0.4$
Photon	Jet	$\Delta R < 0.4$

Table 5–5 Summary of Overlap Removal Criteria in Multilepton Channels.

5.3.4 Event Selection

5.3.4.1 Signal Topology

In the targeted 3-lepton signal, we primarily focus on the di-Higgs decay channels $WWWW$, $WWZZ$, and $WW\tau\tau$, which collectively yield the combined final state of $3\ell 0\tau_h + \text{jets}$. Among these channels, $WWWW$ is dominant, comprising over 60% of the branching ratios.

The 3ℓ channel can be categorized into various sub-channels based on the lepton flavor composition:

- ℓee : Features a same-flavour, same-sign electron pair. Represented as $\mu^\mp e^\pm e^\pm$ or $e^\mp e^\pm e^\pm$.
- $\ell\mu\mu$: Features a same-flavour, same-sign muon pair. Represented as $\mu^\mp e^\pm e^\pm$ or $e^\mp \mu^\pm \mu^\pm$.
- $\ell e\mu$: Contains no same-flavour, same-sign lepton pairs. Represented by four combinations: $\mu^\mp e^\pm \mu^\pm$, $\mu^\mp \mu^\pm e^\pm$, $e^\mp \mu^\pm e^\pm$, $e^\mp e^\pm \mu^\pm$.

Due to statistical limitations in each sub-channel, the analysis treats these sub-channels inclusively. Variables that enhance the signal sensitivity are elaborated in Section 5.3.6. The analysis employs MVA techniques using BDT. Post-MVA, the background validation region and the signal region are defined based on the BDTG score, with $\text{BDTG} \leq 0.55$ and $\text{BDTG} > 0.55$ respectively, according to the maximum of significance.

5.3.4.2 Pre-Selection

Events are required to pass the following common selection, and the corresponding cut-flow is summarized in Table 5-6:

- **Trigger:**
 - Global Trigger Decision required.
 - Utilization of either single-lepton or di-lepton triggers.
- **Lepton multiplicity:**
 - Exactly three leptons with a total electric charge of ± 1 .
 - Events are classified by their lepton flavour/charge composition as $l_0 l_1 l_2$, where the lepton with opposite charge with respect to the other two is noted as lepton index "0". The remaining lepton that is nearest to l_0 in ΔR is given the index "1" and the final lepton is noted as lepton "2".
 - $p_T^0 > 10 \text{ GeV}$ and $p_T^{1,2} > 15 \text{ GeV}$.

- Lepton 0 is required to pass the loose selection while lepton 1 and 2 are required to pass the tight selection. The details of the corresponding working points can be found in Section 5.3.1.3.
- **Hadronic tau veto:** Events with at least one hadronic tau are vetoed.
- **Jet multiplicity:** Events with at least one jet are selected: $N_{\text{jet}} \geq 1$.
- **b-jet veto:** Veto events if they contain any b -tagged jets.
- **Low mass veto:**
 - To remove leptons from quarkonium decays, events with at least one same-flavour opposite-sign (SFOS) lepton pair with an invariant mass less than 12 GeV are vetoed.
- **Z-mass veto:**
 - Events with SFOS lepton pair with an invariant mass within a ± 10 GeV window around m_Z (91.2 GeV) are vetoed.
 - To remove potential backgrounds with Z decays to $ll\gamma^* \rightarrow ll'l'$ where one lepton has very low momentum and is not reconstructed, invariant mass of the tri-lepton within a ± 10 GeV window around m_Z are vetoed: $|m_{lll} - m_Z| > 10$ GeV

Selection Criteria	SM HH	prompt	fake	total bkg	S/B ($\times 1000$)	data
three leptons with a total charge of ± 1	6.32	75116.81	775243.60	850360.41	0.01	1213079
Triggers	5.88	69214.50	653599.08	722813.58	0.01	913339
Hadronic tau veto	5.88	69214.50	653599.08	722813.58	0.01	906509
Electron quality	5.38	63768.03	461547.24	525315.27	0.01	685064
$p_T^{0,1,2} > 10, 15, 15$ GeV	4.14	50731.84	152499.39	203231.22	0.02	251428
$N_{\text{jet}} \geq 1$	3.60	29312.65	94923.35	124236.00	0.03	145937
b-jet veto	3.21	25094.06	53653.52	78747.58	0.04	96919
Low mass veto	3.10	23760.92	51858.30	75619.22	0.04	78347
Z-mass veto	2.26	4169.97	19277.35	23447.32	0.10	25341
Lepton tight quality	1.23	2391.73	357.53	2749.25	0.45	2566

Table 5–6 The raw yields with pre-selection cut-flow for the 3ℓ analysis.

5.3.5 Background Modelling

In this analysis, two primary categories of backgrounds exist: prompt and non-prompt backgrounds. The prompt backgrounds, which consist predominantly of diboson processes, are composed of events that feature three prompt leptons in the final state. On the other hand,

the non-prompt backgrounds, often referred to as 'fakes,' emerge from events where jets or photons are misidentified as leptons.

The prompt backgrounds are rigorously modeled using Monte Carlo simulations. These include a variety of processes such as $t\bar{t}V$, VV , tV , VH , VVV , and $t\bar{t}H$. Notably, WZ processes account for over 85% of all prompt backgrounds. A specialized control region, optimized for a WZ -enriched environment, is introduced to refine this background estimation. Further details on this control region and its corresponding plots can be found in Sections 5.3.5.2 and 5.3.7.3.

The non-prompt backgrounds primarily involve $t\bar{t}$ and Z + jets processes. These backgrounds are estimated using a template fit method, detailed in Section 5.3.5.2. The non-prompt category also encompasses other processes such as W + jets and $V\gamma$, among others.

	HH: ggF	HH: VBF	WZ	ExtConv_e	HF_e	HF_m	Total Bkg	Data	Signal Contamination
ExtConv_e CR	0.00 ± 0.02	0.00 ± 0.00	2.59 ± 0.42	292.97 ± 17.59	0.02 ± 0.00	1.59 ± 0.32	303.64 ± 17.47	303.00	0.000% ± 0.005%
HF_e CR	0.00 ± 0.04	0.00 ± 0.00	1.03 ± 0.15	11.76 ± 2.39	145.97 ± 16.48	0.00 ± 0.00	239.98 ± 15.41	243.00	0.002% ± 0.018%
HF_m CR	0.01 ± 0.07	0.00 ± 0.00	2.32 ± 0.34	0.00 ± 0.00	0.00 ± 0.00	470.00 ± 24.89	566.38 ± 23.74	567.00	0.001% ± 0.013%
Low BDT VR	0.48 ± 5.51	0.03 ± 0.34	1558.72 ± 152.11	79.34 ± 13.74	60.52 ± 10.74	138.51 ± 13.98	2363.74 ± 165.71	2405.00	0.022% ± 0.234%
WZ CR	0.25 ± 2.90	0.01 ± 0.12	7137.60 ± 688.55	8.39 ± 6.18	54.13 ± 15.76	143.45 ± 22.88	8270.25 ± 704.82	8090.00	0.003% ± 0.035%

Table 5–7 Summary of Monte Carlo (MC) samples with applied normalization factors and re-weighted WZ contributions, alongside data for all control and validation regions in the 3ℓ channel. Only the principal background processes are enumerated.

A comprehensive summary of all defined control regions and validation regions is provided in Table 5–7.

5.3.5.1 Estimation of WZ Using fitting function

The WZ process serves as a crucial contributor to the prompt background within the 3ℓ channel. In order to optimize its simulation, a specialized control region is formulated. This region adheres to the general preselection criteria with two specific deviations:

- In contrast to the Signal Region, where a veto based on the invariant mass of the SFOS lepton pair is applied around m_Z , the control region is designed to *retain* such events. This invariant mass is confined within a ± 10 GeV window around m_Z , ensuring orthogonality with respect to the Signal Region.
- An additional constraint of $E_T^{\text{miss}} > 30$ GeV is introduced to further refine the WZ control region.

To address the recognized discrepancy in modeling the WZ background, particularly in

scenarios of high jet multiplicities, a fitting function that has been previously validated^[139] is applied. The function, given as

$$f(x) = \frac{b \times 2^c - a}{2^c - 1} + \frac{(b - a) \times 2^c}{(2^c - 1)x^c} \quad (5-1)$$

is used to fit the WZ sample in the dedicated control region. Here, x corresponds to the number of jets in the event. The fitting is performed using a least-squares method and results in the parameters $a = -0.706 \pm 0.018$, $b = -0.553 \pm 0.017$, and $c = 0.279 \pm 0.026$. For this fitting procedure, it should be noted that events with a jet count greater than 4 ($n_{\text{Jets}} > 4$) are treated as if they have exactly 4 jets ($n_{\text{Jets}} = 4$). This treatment is due to the known limitations in modeling WZ events with higher jet multiplicities.

The quality of the fit is exemplified by a χ^2/ndof value of 0.84, substantiating the fitting function as a robust modeling correction for WZ samples across all analytical regions. With this fitting function, it is consequently employed as an additional weighting factor for all WZ samples. This additional weight is used alongside the original sample weights to improve the representation of the WZ background in this analysis. Importantly, this fitting function is not just used in the control region where it was derived, but is also applied to all other relevant regions in the study. This ensures a consistent and improved modeling of the WZ background throughout the analysis.

Number of jets distributions pre- and post-fitting are visualized in Fig. 5-2, while additional kinematic distributions subsequent to the fitting are discussed in Sec. 5.3.7.3. The corresponding fitting uncertainties can be found in Section 5.4.3.

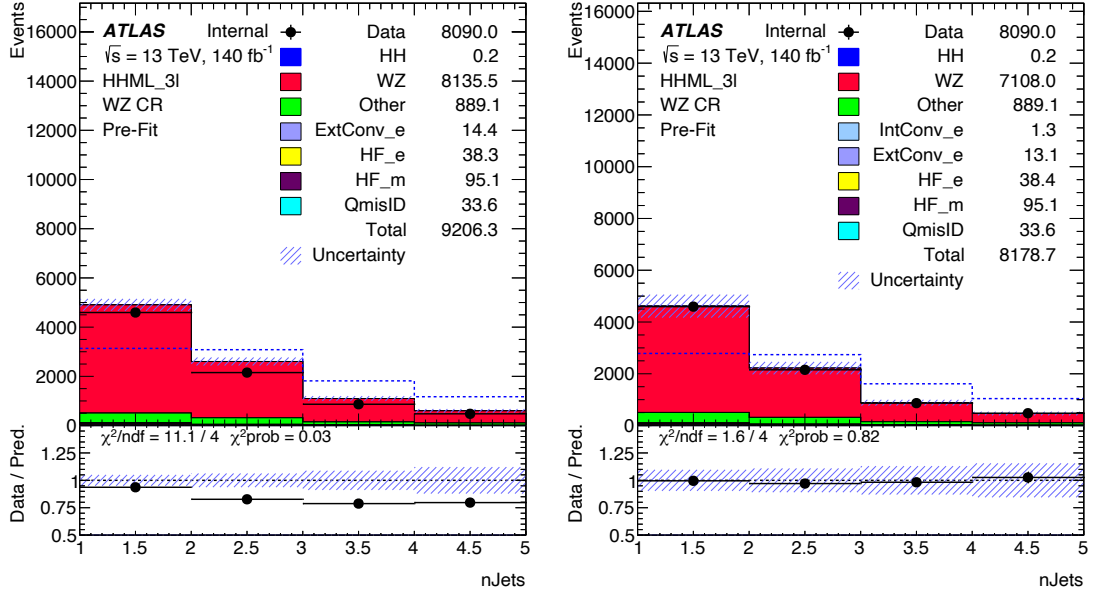


Figure 5–2 The pre-fit (let) and post-fit (right) $n\text{Jets}$ distribution plots of the WZ control regions, using fitting function of Eq.5–1. Both statistical uncertainties and systematic errors are accounted for.

5.3.5.2 Control regions and background estimation using template fit method

Despite strict lepton identification rules, fake leptons remain a significant background in the 3-lepton channel. For the purposes of this analysis, the fake background encompasses both non-prompt and fake leptons. Non-prompt leptons are primarily generated from heavy-flavor hadron decays (b or c hadrons), while other contributions may arise from photon conversions or hadronic jet misidentification. Owing to the intricate nature of fake backgrounds and the imprecision of MC simulations in adequately modeling these processes, a data-driven approach is essential for accurate estimation. The template fit method is employed as a semi-data-driven strategy. It involves a simultaneous fit of all processes contributing to the fake background. All backgrounds, including those arising from charge misidentifications, are extracted from MC simulations. Within this framework, normalization factors for different types of fakes are free parameters in a fit to data. These factors serve to correct MC estimates for fakes and are mainly derived from $t\bar{t}$ and Z +jets simulations.

Based on the truth classification of non-prompt lepton events, several key contributions are identified, with free-floating normalization factors (NF) as follows:

- NF_e^{HF} : For events with a non-prompt electron primarily from b or c decays.
- NF_μ^{HF} : For events with a non-prompt muon primarily from b or c decays.
- NF^{Conv} : For photon conversion events, predominantly from $V\gamma$ process.

Events are classified into the aforementioned categories based on their truth origin:

- Prompt leptons: leptons originating directly from electroweak processes.
- Conversion: leptons arising from photon conversions.
- B decay and C decay: non-prompt leptons originating from b or c hadron decays.
- Other: leptons from light quark decays or other minor sources.

Each CR is defined to be orthogonal to the SR, adhering to the general preselection criteria while incorporating several specialized variations. The following outlines the definition criteria for three key CRs:

- Electron from Heavy Flavor Decay Control Region (**HF-E CR**):
 - No isolation requirements; all set to loose isolation and tight ID.
 - Requires a minimum of 2 jets, including 2 or more b-jets to ensure orthogonality with the SR, which implements a b-jet veto.
 - Requires both same-sign leptons to be electrons (ℓee).
- Muon from Heavy Flavor Decay Control Region (**HF-MU CR**):
 - Adopts identical jet, b-jet, identification and isolation criteria as the HF-E CR for consistency.
 - Requires both same-sign leptons to be muons ($\ell \mu \mu$).
- Electron from External Conversion Control Region (**Conv CR**):
 - Loose Isolation for l_0 and Tight Isolation for l_1/l_2 , while omitting the standard ID requirement; all set to loose ID.
 - Requires the invariant mass of the three-lepton system to be within 10 GeV of the Z boson mass, thereby enriching $V\gamma$ backgrounds.
 - Adds a new condition for l_1 or l_2 : a conversion vertex should be present at a radius greater than 20 mm, and the mass of this vertex should be between 0 and 100 MeV. This condition further assures orthogonality with the SR.

To optimize the discrimination among the various NFs in the simultaneous template fit, specific kinematic distributions in different phase spaces are employed:

- For the estimation of the electron heavy flavor normalization factor NF_e^{HF} , the angu-

lar separation $\Delta R_{l_0 l_1}$ in the $\ell e e$ channel is utilized. This distribution is binned into 3 intervals, spanning $0 \leq \Delta R_{l_0 l_1} \leq 3$.

- Similarly, the muon heavy flavor normalization factor NF_{μ}^{HF} is estimated using the $\Delta R_{l_0 l_1}$ distribution in the $\ell \mu \mu$ channel, also segmented into 3 bins in the range $0 \leq \Delta R_{l_0 l_1} \leq 3$.
- The external conversion electron normalization factor NF_e^{Conv} is estimated using a single-bin distribution.

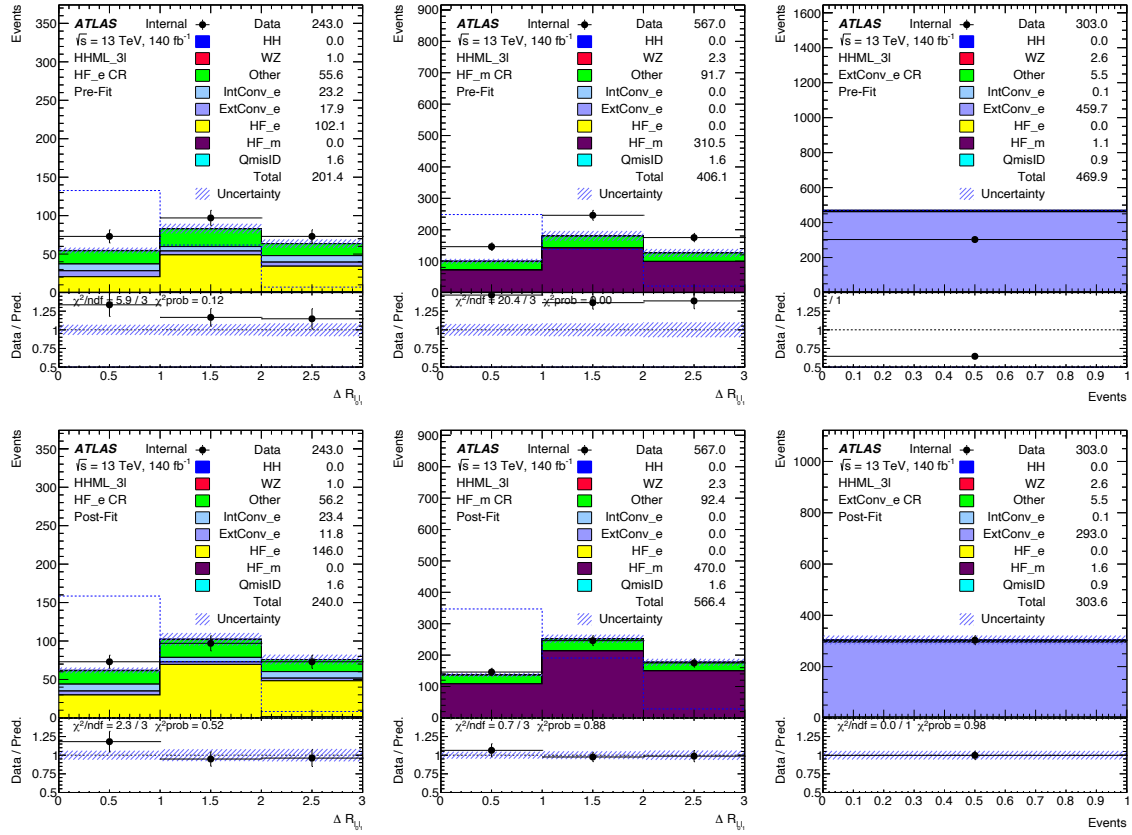


Figure 5–3 From left to right shows the pre-fit (top) and post-fit (bottom) plots of the HF-E, HF-MU, External Conversion control regions. All entries represent uncorrected Monte Carlo simulations. Both statistical uncertainties and systematic errors are accounted for. Additionally, the WZ background is adjusted using a fitted scaling function.

The Template Fit Control Regions are depicted in Figures 5–3, both before and after fitting to the data; the derived normalization factors are tabulated in Table 5–8. Due to the limited statistics in each specialized control region, additional sources of fake or non-prompt

leptons, such as internal conversions and light-flavor leptons, are amalgamated in these three CRs. Specifically, the NF for external conversions is also applied to internal conversion samples, and the NFs for heavy-flavor leptons encompass those for light-flavor and other leptonic sources.

Source	Norm Factor	Yields in SR	Uncertainty(%)
External Conversion	0.66 ± 0.13	2.8	13.29
Heavy Flavor (electron)	1.50 ± 0.50	11.3	30.52
Heavy Flavor (muon)	1.51 ± 0.23	29.5	13.12
Prompt Background	-	125.7	-

Table 5–8 The systematics of three fake sources and the corresponding yields in the signal region, which is estimated by the template fit method.

5.3.6 Multivariate Analysis

The analysis employs a multivariate approach using the Boosted Decision Trees (BDT) method, within the TMVA framework in ROOT 6.18/00^[40]. An enhanced version, Gradient BDT (BDTG), has also been implemented for this analysis. The training dataset comprises both prompt backgrounds, such as $t\bar{t}V$, VV , tV , VH , VVV , and $t\bar{t}H$, as well as the non-prompt processes, henceforth referred to as "fake background."

5.3.6.1 Input Variable and Correlation

Most of the Higgs bosons in 3-lepton channel are moderately boosted, thereby yielding leptons in the final state that are often spatially close due to the W-boson spin correlations in the Higgs decay processes. Variables coming from the lepton kinematics, such as $\Delta R_{l_i l_j}$, $m_{l_i l_j}$ are expected to have strong separation power, with W-boson can be partially reconstructed. Other variables like the missing transverse energy (\cancel{E}_T), sum of the transverse momentum of all objects (HT), and the invariant mass of all three leptons and two leading jets (m_{llljj}) are also expected to be useful in separating signal from background. The variables employed in BDTG training are itemized in Table 5–9, selected for their maximal discriminative power; the top 13 variables have been ranked according to their separation efficacy¹. Observable high correlations exist among certain invariant masses. Specifically, an 82% correlation between

¹ The variables were selected based on their separation power as quantified during BDT training.

m_{lll} and $m_{l_1 l_2}$, and a 90% correlation between m_{lll} and $m_{l_0 l_2}$ are in line with expectations. Similarly, an 83% correlation is noted between HT and m_{llljj} . The respective correlation matrix is shown in Figures 5-4a and 5-4b.

It is essential to note that despite these substantial correlations, the input variable set has been optimized based on the Area Under the Curve (AUC) metric. Empirical data substantiate a marked reduction in performance when the variable set is truncated. Consequently, the presence of high correlations among variables is tolerated in favor of optimized performance.

Variable	Description	Separation
$\Delta R_{l_0 l_1}$	Distance in $\eta - \phi$ space between lepton 0 and lepton 1	32.62%
$m_{l_0 l_1}$	Invariant mass of lepton 0 and lepton 1	26.90%
min. m_{ll}^{OS}	Minimum invariant mass of opposite-sign lepton pairs	26.23%
$\Delta R_{l_2 j}$	Distance in $\eta - \phi$ space between lepton 2 and nearest jet	23.90%
$\Delta R_{l_1 l_2}$	Distance in $\eta - \phi$ space between lepton 1 and lepton 2	12.67%
min. m_{ll}^{OSSF}	Minimum invariant mass of opposite-sign same-flavor lepton pairs	11.41%
$m_{ll}^{\text{Z-matched}}$	Invariant mass of lepton pair closest to Z mass	11.38%
m_{llljj}	Invariant mass of all three leptons and two leading jets	3.49%
m_{lll}	Invariant mass of all three leptons	2.94%
$m_{l_2 j}$	Invariant mass of lepton 2 and nearest jet	2.40%
$m_{l_0 l_2}$	Invariant mass of lepton 0 and lepton 2	2.11%
\cancel{E}_T	Missing transverse energy	1.80%
$\Delta R_{l_0 j}$	Distance in $\eta - \phi$ space between lepton 0 and nearest jet	1.20%
FlavorCategory	Categorization of lepton flavors, details in Sec. 5.3.4.1	1.17%
HT_{lep}	Scalar sum of lepton p_T 's and missing transverse momentum	0.96%
HT	Scalar sum of jet p_T 's	0.52%
$\Delta R_{l_1 j}$	Distance in $\eta - \phi$ space between lepton 1 and nearest jet	0.33%
$\Delta R_{l_0 l_2}$	Distance in $\eta - \phi$ space between lepton 0 and lepton 2	0.26%
$m_{l_1 j}$	Invariant mass of lepton 1 and nearest jet	0.19%
HT_{jets}	Scalar sum of jet p_T 's	0.05%
$m_{l_0 j}$	Invariant mass of lepton 0 and nearest jet	0.01%
$m_{l_1 l_2}$	Invariant mass of lepton 1 and lepton 2	0.01%

Table 5-9 Discriminant variables used in BDTG training for 3ℓ channel.

5.3.6.2 3-Fold Cross-Validation

Owing to the statistical constraints of the Monte Carlo training samples, a k -fold Cross-Validation (k -CV) strategy is employed, specifically 3-fold cross-validation. This approach

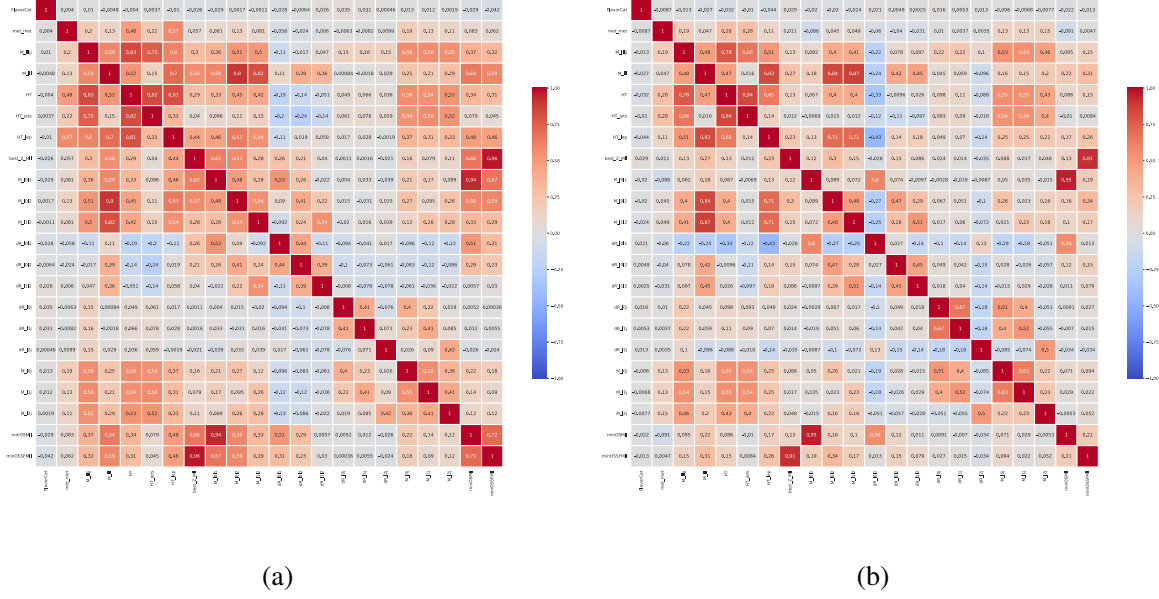


Figure 5-4 The correlation matrix of MVA variables for signal and background (pure MC) training samples.

uses the full statistical power of the dataset to generate robust training models and produce a smooth Receiver Operating Characteristic (ROC) curve.

In this setup, the MC samples are partitioned into three distinct sets: one for training, another for testing, and the third for application, thereby maintaining orthogonality between training and application sets. Event numbers are employed as the basis for fold assignment. During the training phase, no additional weights, including WZ-reweighting and fake normalization factors, are applied, as their impact has been found negligible. Conversely, in the application phase, these normalization factors are incorporated.

The training methodology remains consistent across all folds. For the BDTG, hyperparameter optimization targets the maximization of the AUC value for the testing set. The optimized hyperparameters are as follows:

- Number of Trees: 715
- Maximum Tree Depth: 4
- Boost Type: Gradient
- Bagged Boost Employed (Bagged Sample Fraction: 0.5)
- Number of Cuts (nCuts): 20

The ROC curves for each of the 3-fold cross-validation sets using the BDTG method are

compiled in Figure 5-5.

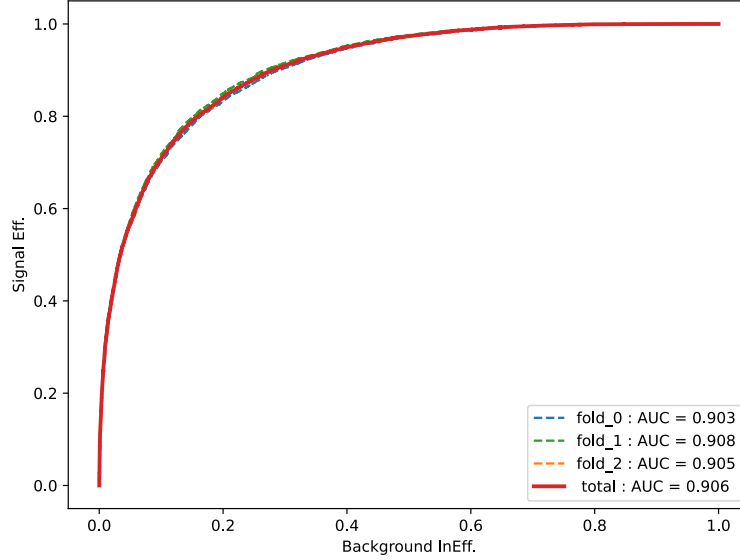


Figure 5-5 Training results of BDTG: Receiver Operating Characteristic (ROC) curve for 3-lepton channel, illustrating the trade-off between signal efficiency (True Positive Rate) and background inefficiency (False Positive Rate).

5.3.7 Validation Plots

5.3.7.1 BDTG score distribution in validation region

Figure 5-6 depicts the pre-fit and post-fit distributions of the BDTG score in both the low BDT Validation Region and the WZ-enriched region. The left panel showcases the BDTG score distributions before fitting, whereas the right panel reveals the distributions after the fitting process.

5.3.7.2 Control plots in low BDTG region

With satisfying the selections in Section 5.3.4.2, the region with low BDTG score¹ is defined as the validation region, with 0.012% signal contamination in table 5-7 (calculated as the ratio of raw yields between signal and total background). Invariant mass related variables are shown in figure 5-8. Distance related variables and HT are summarized in figure 5-7.

¹ BDTG score ≤ 0.55

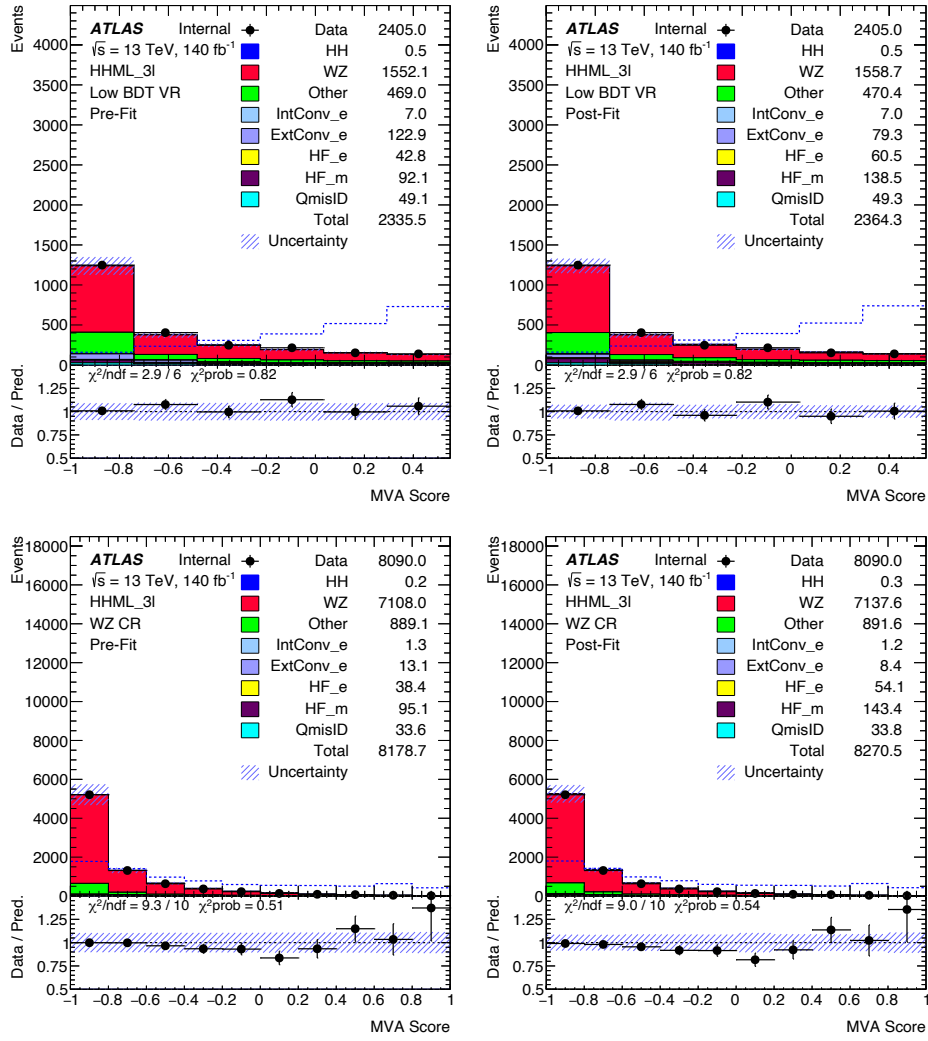


Figure 5-6 The pre-fit and post-fit distributions of the BDTG score in low BDT VR and WZ-enriched region. Scaling factors for External Conversion, HF(electron), and HF(muon) are applied. Additionally, the WZ background is adjusted using a fitted scaling function. Both statistical uncertainties and systematic errors are accounted for.

The rest of discriminant variables used in BDTG training is presented in figure [5-9](#).

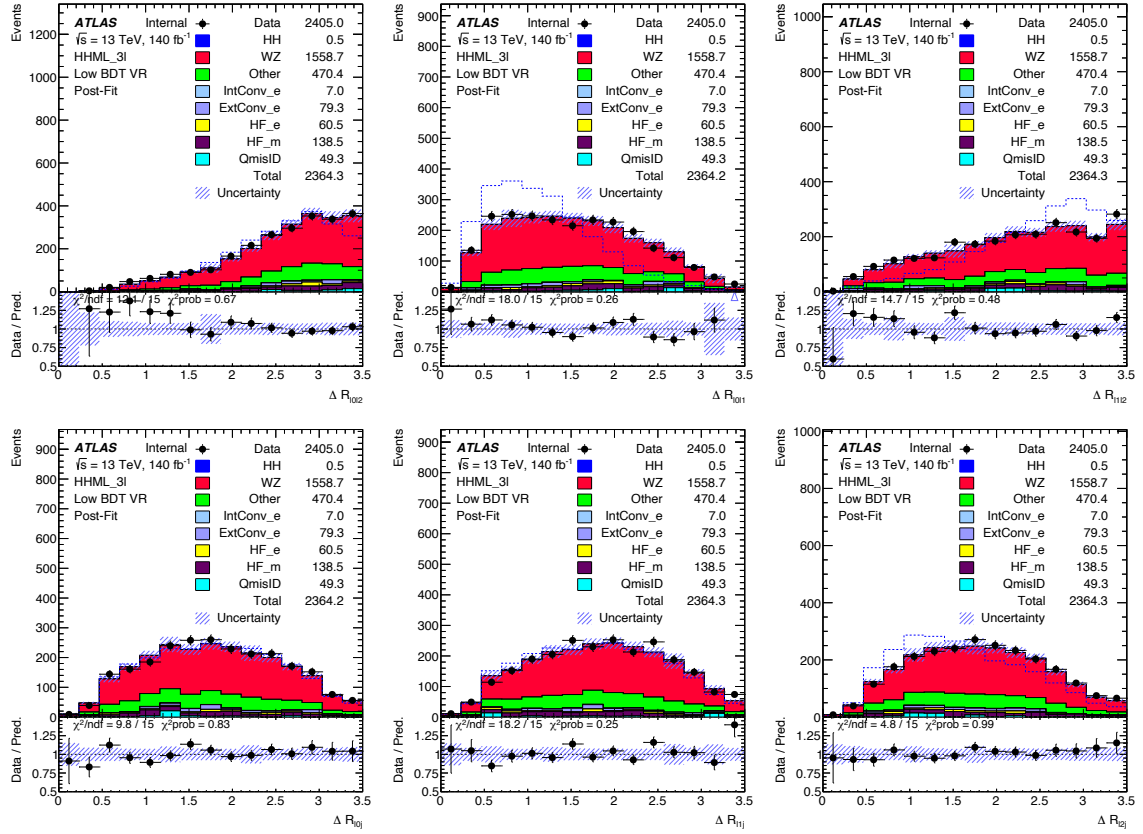


Figure 5-7 The post-fit distribution of distance of lepton pairs and jets, where all the events are required to pass the pre-selection and BDTG score ≤ 0.55 . Scaling factors for External Conversion, HF(electron), and HF(muon) are applied. Additionally, the WZ background is adjusted using a fitted scaling function. Both statistical uncertainties and systematic errors are accounted for.

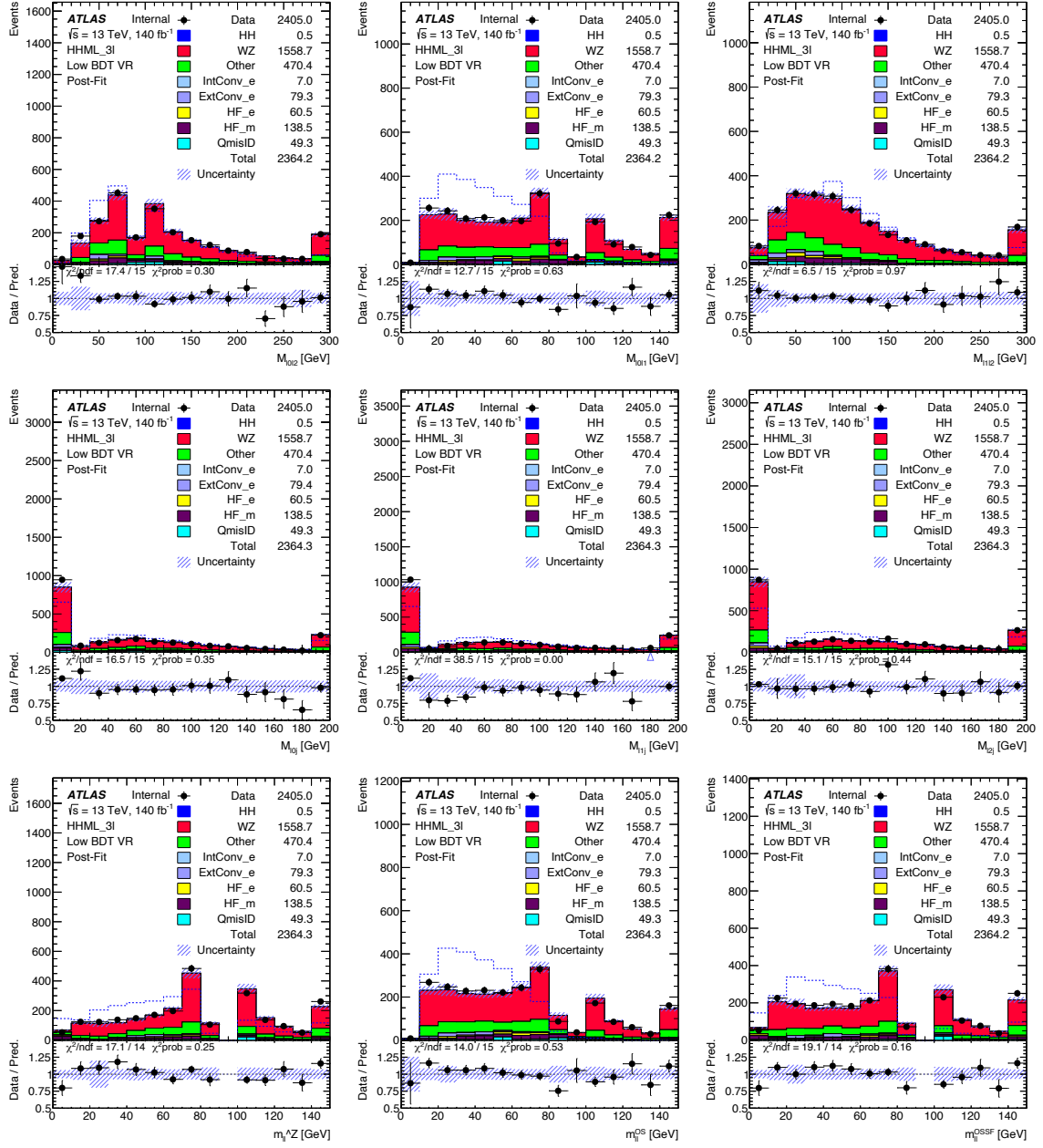


Figure 5–8 The post-fit distribution of invariant mass of lepton pairs and jets, where all the events are required to pass the pre-selection and BDTG score ≤ 0.55 . Scaling factors for External Conversion, HF(electron), and HF(muon) are applied. Additionally, the WZ background is adjusted using a fitted scaling function. Both statistical uncertainties and systematic errors are accounted for.

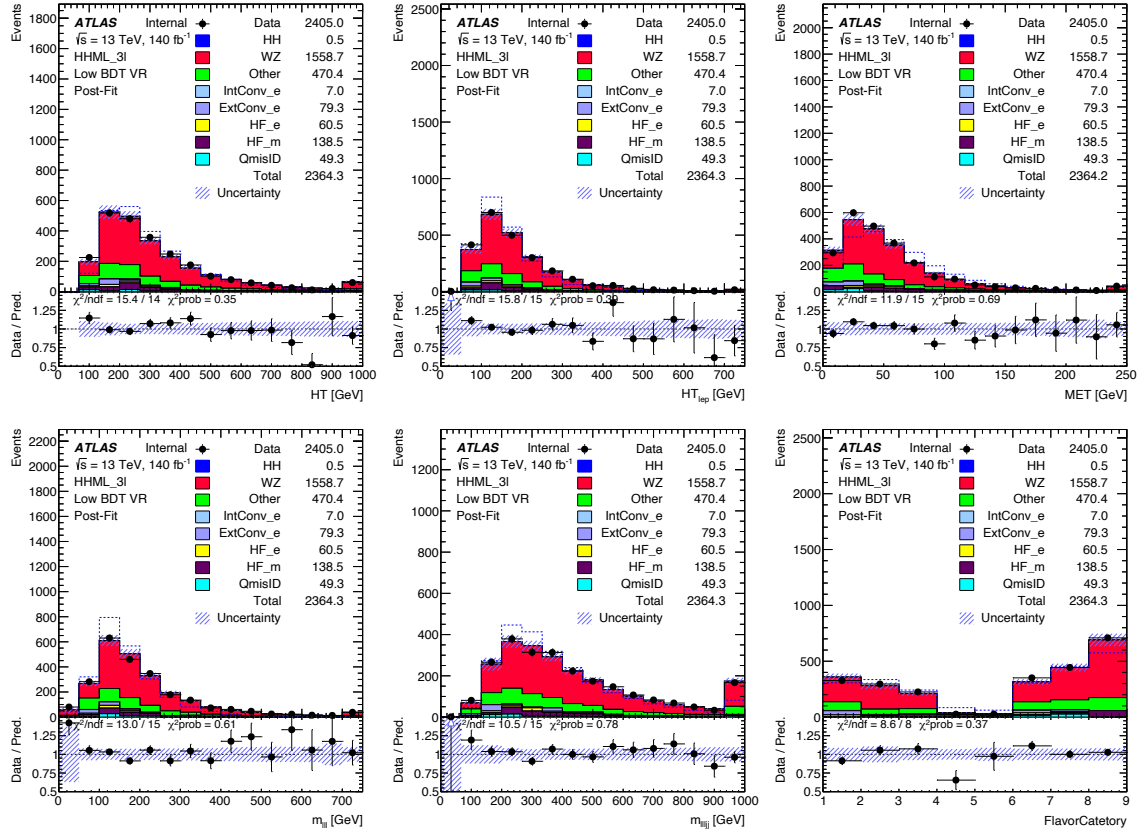


Figure 5-9 The post-fit distribution of the remaining kinematics, where all the events are required to pass the pre-selection and BDTG score ≤ 0.55 . Scaling factors for External Conversion, HF(electron), and HF(muon) are applied. Additionally, the WZ background is adjusted using a fitted scaling function. Both statistical uncertainties and systematic errors are accounted for.

5.3.7.3 Control plots in WZ control region

The definition of WZ control region is defined in Sec. 5.3.5.2, where events should pass all preselection but is required to have SFOS lepton pairs whose invariant mass is in the Z mass window. Invariant mass related variables are shown in figure 5-11. Distance related variables and HT are summarized in figure 5-10. The rest of discriminant variables used in BDTG training is presented in figure 5-12.

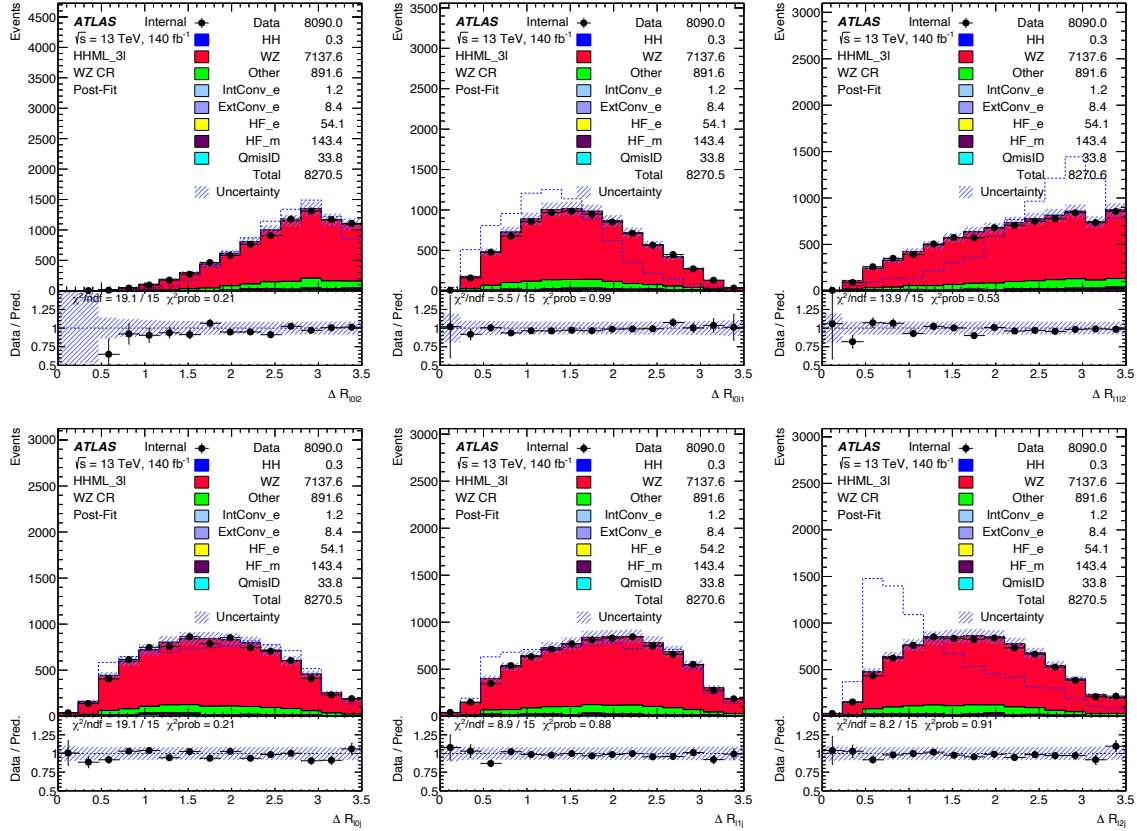


Figure 5-10 The post-fit distribution of distance of lepton pairs and jets, where all the events are required to pass the pre-selection. Scaling factors for External Conversion, HF(electron), and HF(muon) are applied. Additionally, the WZ background is adjusted using a fitted scaling function. Both statistical uncertainties and systematic errors are accounted for.

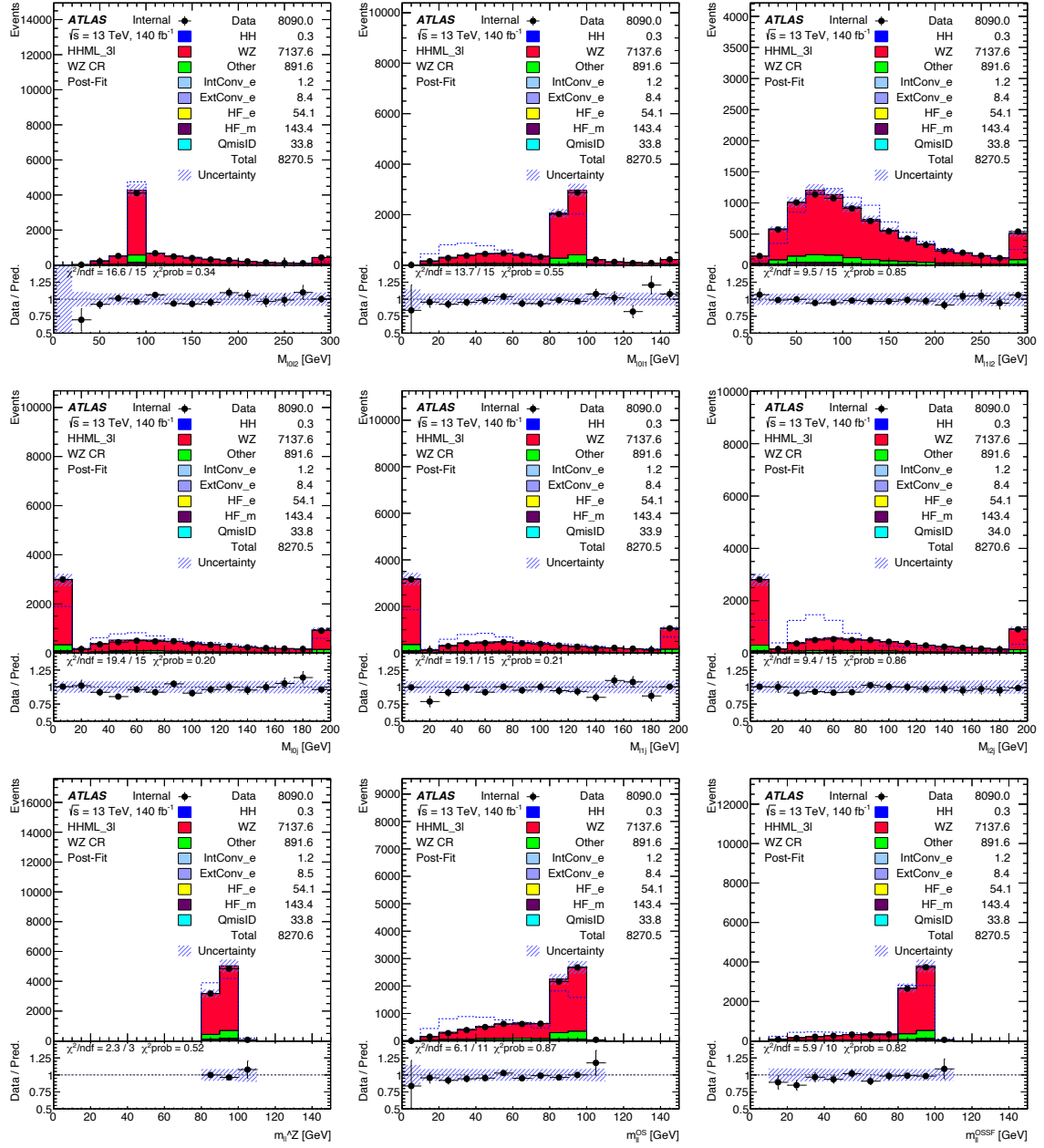


Figure 5-11 The post-fit distribution of invariant mass of lepton pairs and jets, where all the events are required to pass the pre-selection. Scaling factors for External Conversion, HF(electron), and HF(muon) are applied. Additionally, the WZ background is adjusted using a fitted scaling function. Both statistical uncertainties and systematic errors are accounted for.

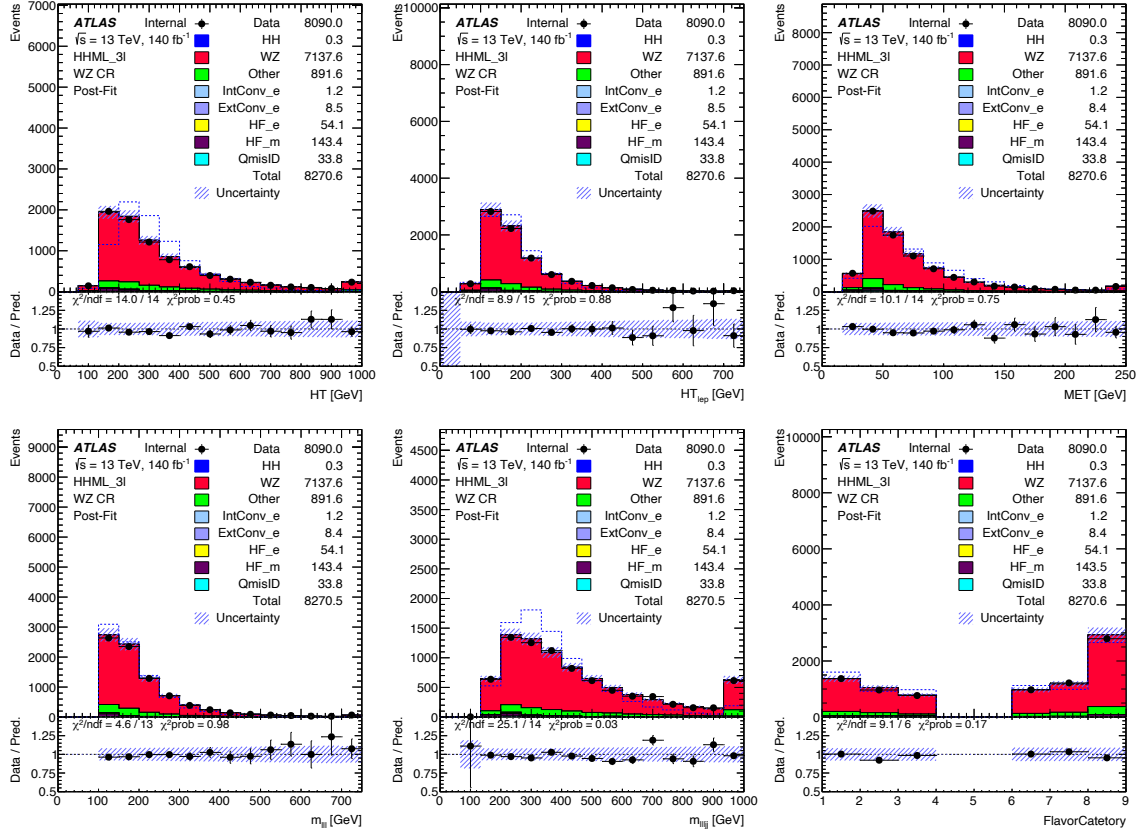


Figure 5-12 The post-fit distribution of the remaining kinematics, where all the events are required to pass the pre-selection. Scaling factors for External Conversion, HF(electron), and HF(muon) are applied. Additionally, the WZ background is adjusted using a fitted scaling function. Both statistical uncertainties and systematic errors are accounted for.

5.4 Systematic Uncertainties

5.4.1 Experimental uncertainties

This subsection outlines the systematic uncertainties inherent in the analysis. These uncertainties stem primarily from the reconstruction and identification of physics objects, including light leptons, jets, and Missing Transverse Energy. Additionally, uncertainties in the integrated luminosity of the dataset are taken into account.

- **Luminosity:** Uncertainty in the integrated luminosity of the combined Run-2 dataset is quantified at 1.7%. This value follows the calibration methodology^[141], which uses x-y beam-separation scans conducted from 2015 to 2018. This luminosity uncertainty is propagated to all Monte Carlo samples but is exempt for the data and fake continuum background.
- **Pileup:** The procedure for pileup reweighting involves contrasting the mean number of interactions per proton-proton collision ($\langle \mu \rangle$) in the data against that in simulated samples. Uncertainties are assessed through the variation of the scaling factor applied to the data.
- **Trigger:** Uncertainties related to electron and muon trigger efficiency are accounted for through the respective trigger scale factors^[142]. In leptonic channels, either the Single Lepton Trigger (SLT) or Double Lepton Trigger (DLT) strategy is employed, and the relevant scale factor is applied. Photon trigger uncertainties are also incorporated.
- **Muons:** The Muon Combined Performance group^[143] provides guidelines for the inclusion of uncertainties concerning muon efficiency, energy scale, resolution, object reconstruction, identification, and isolation. The efficiency uncertainty is disaggregated into both statistical and systematic components, addressing specific conditions such as bad muons, isolation, low transverse momentum muons, and track-to-vertex association (TTVA).
- **Electrons:** Similar to muons, uncertainties for electrons encompass aspects like resolution, scale, and efficiency, as specified by the Egamma Combined Performance group^[144].
- **Jets:** Jets are reconstructed using the anti- k_t algorithm with a radius parameter of $R = 0.4$, based on energy deposits in topological clusters of calorimeter cells. Uncertainties in the Jet Energy Scale (JES) and Jet Energy Resolution (JER) are considered

and derived through a combination of Monte Carlo-based and in situ calibrations^[145]. For these uncertainties, both the CategoryReduction and FullJER schemes are implemented.

- **Flavour Tagging:** Excluding the $b\bar{b} + 4\ell$ channel, a b-jet veto is enforced at a tagging efficiency of 77% to maintain orthogonality with other di-Higgs analyses. Uncertainties originate from the tagging efficiency for jets containing b-hadrons, c-hadrons, light hadrons, or hadronically decaying taus. The associated scale factors are obtained via the BtaggingEfficiencyTool's `getScaleFactor` method^[146]. The Non-Perturbative (NP) reduction scheme used for b-tagging uncertainties is categorized as medium.
- **Missing Transverse Momentum:** Systematic variations are considered with respect to the scale and resolutions (both parallel and perpendicular) of the soft term.

5.4.2 Theory uncertainties

The inclusive cross sections for ggF in Higgs boson pair production^[147] are computed for a Higgs mass $m_H = 125$ GeV, with a central scale setting of $\mu_0 = \mu_R = \mu_F = M_{HH}/2$. Uncertainties to consider include the PDF and α_s (together termed as "PDF + α_s unc"), scale, and top-quark mass (m_{top} , termed as "Scale + m_{top} unc") as recommended by the LHC Higgs Cross Section Working Group^[148]. Uncertainties in percentage are as follows: QCD Scale: $^{+2.1}_{-4.9}$, PDF($+\alpha_s$): $^{+3}_{-3}$, m_{top} : $^{+4}_{-18}$. Cross section uncertainties for VBF in Higgs pair production are in accordance with the recommendations^[148].

The systematic variations stemming from these uncertainties are individually weighted for each event through specialized systematic samples. For background processes, namely $t\bar{t}V$, multi-boson processes (VV , VVV), $V\gamma$, as well as rare decay modes (tZ , WtZ , $t\bar{t}WW$), a comprehensive summary of cross-sections and corresponding treatments for uncertainties, inclusive of those from data, is provided in Table 5-10.

5.4.3 WZ reweighting uncertainties

To rigorously quantify the uncertainties introduced by fitting errors in the reweighting of the WZ sample, we establish an eigenspace representation based on the covariance matrix of the fitting parameters A, B, and C, as detailed in Table 5-11. By transforming these parameters and associated uncertainties into this eigenspace (refer to Table 5-12), we obtain the eigenvalues and eigenvectors' nominal values and uncertainties (denoted as fA, fB, fC). This

Process	Precision order	Cross section central value	Cross section uncertainty	Modelling uncertainty	Normalized to data
MC samples contributing to fake lepton templates					
$t\bar{t}$	NNLO+NNLL	832 pb	-	alternative MC	Yes
s -, t -channel single top	NLO	227 pb	-	-	Yes
Wt single top	NNLO approx	71.7 pb	-	-	Yes
$Z/\gamma^* \rightarrow l^+l^-$	NNLO	0.9751×SHERPA	-	-	
$W \rightarrow \ell\nu$	NNLO	0.9751×SHERPA	-	-	
MC samples of irreducible background processes					
$t\bar{t}W$	NLO	601 fb	-	alternative MC scale variations	Yes
$t\bar{t}t\bar{t}$	NLO	12 fb	20%	alternative MC	No
$t\bar{t}(Z/\gamma^* \rightarrow l^+l^-)$	NLO	839 fb	-	alternative MC scale variations	Yes
$t\bar{t}H$	NLO	507 fb	11%	alternative MC scale variations	No
WH	NLO	1102 fb		scale variations	No
ZH	NLO	601 fb		scale variations	No
$VV, qqVV$	NLO	SHERPA	-	10% (+LF jets), scale variations	Yes (+HF jets)
$t(Z/\gamma^*)$	LO	240 fb	5%	-	No
$t\bar{t}t$	LO	1.6 fb	50%	-	No
$tW(Z/\gamma^*)$	NLO	16 fb	50%	-	No
$t\bar{t}W^+W^-$	NLO	9.9 fb	50%	-	No
VVV	NLO	SHERPA	50%	-	No

Table 5–10 The background sample normalizations and their uncertainties were used in the analysis. The uncertainties on the inclusive cross sections are taken from the ATLAS Physics Modelling Group Twiki.

orthogonal transformation of the parameter space provides a more nuanced understanding, allowing us to evaluate the impact of each fitting parameter in an independent manner.

Upon obtaining the eigenvalues and eigenvectors (notated as fA, fB, fC) within the established eigenspace, these components are varied by a single standard deviation (1σ) to scrutinize the influence of their respective uncertainties. Given that variations within the eigenspace are orthogonal and therefore independent, this ensures that the calculated uncertainties remain uncorrelated.

Subsequent to this variation, these parameters are transformed back to their original space, specifically to the A, B, and C parameters, thereby generating altered fitting functions.

	Correlation Matrix			Covariance Matrix		
	A	B	C	A	B	C
A	1.0000	0.6111	-0.4148	0.0003182	0.0001804	-0.000196
B	0.6111	1.0000	0.4640	0.0001804	0.0002739	0.0002034
C	-0.4148	0.4640	1.0000	-0.000196	0.0002034	0.0007015

Table 5–11 Correlation and Covariance Matrix for Parameters A, B, and C

Eigenvalues		Eigenvectors	
6.1146e-07	0.6217	0.7346	0.2719
4.7741e-04	-0.6885	0.6780	-0.2576
8.1551e-04	0.3736	0.0271	-0.9272

Table 5–12 Eigenvalues and Eigenvectors of the Covariance Matrix for Parameters A, B, and C

Utilizing these modified functions, we proceed to reweight the WZ background and estimate its subsequent contribution to the final state. A comparative analysis between the reweighted WZ background and its nominal counterpart, derived from the initial fitting function, allows us to gauge the uncertainties' repercussions on the reweighting methodology. These findings are graphically represented in Figure 5–13.

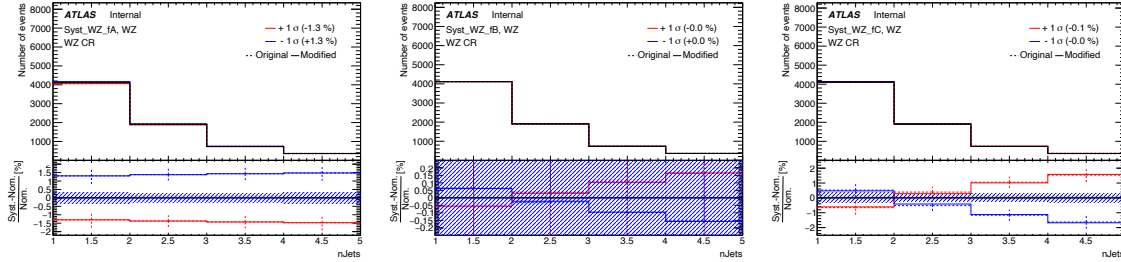


Figure 5–13 The systematics plots for reweighted WZ samples in WZ enriched region.

5.4.4 Uncertainties on data-driven background estimation

The Template Fit method is dependent on Monte Carlo simulations, giving rise to three primary types of systematic uncertainties:

- $t\bar{t}$ modelling uncertainties
- Z +jets modelling uncertainties

- Fakes template uncertainties

For $t\bar{t}$ and Z +jets modelling, we employ standard procedures recommended by the top group, involving variations in radiation and scale choices. It is noteworthy that these systematic uncertainties minimally impact the final results.

To address uncertainties in the fakes templates, the comprehensive definition of a "tight lepton" is subdivided into components that target specific origins of fakes: namely, conversions (ambiguity bin) versus heavy flavors (by loosening the criteria for Tight ID Selection on ℓ_1 and ℓ_2). This approach allows us to isolate selections with high proportions of fakes, which are then compared to data after the subtraction of remaining backgrounds. As a result, systematic uncertainties for each heavy flavor template component (either electron or muon) are obtained. These are then used as a correlated nuisance parameter for all bins in the final fit. Importantly, these shape-related systematics are not considered to be among the most impactful uncertainties on the analysis.

Control regions featuring relaxed identification criteria are examined, and the ratio of (Data – Non-Fake BG)/Fake BG is included as an additional systematic uncertainty, specifically for the heavy-flavor (HF) fakes and Conversion fakes in designated control or signal regions as shown in Table 5–8.

5.5 Statistical Interpretation

5.5.1 Statistical model

The analytical likelihood function is expressed as:

$$\mathcal{L}(\vec{\mu}, \vec{\theta}; \text{data}) = \prod_{c=1}^{N_{\text{cat}}} \mathcal{L}_c(\vec{\mu}, \vec{\theta}; \text{data}) \prod_{k \in \text{NP constraints}} g_k(\theta_k) \quad (5-2)$$

Here, $\vec{\mu}$ and $\vec{\theta}$ symbolize the vectors for the parameters of interest (POIs) and nuisance parameters (NPs), respectively. N_{cat} represents the total number of categories, and \mathcal{L}_c signifies the likelihood for each specific category c . Constraint terms for some of the NPs are represented by g_k . Further elucidation of the likelihood template can be found in Ref. [149].

POIs can encompass diverse parameters like the signal strength, denoted as μ , and coupling variables such as κ_λ and κ_{2V} . The NPs are either unconstrained, i.e., determined solely by data, or constrained through auxiliary measurements. In each category c , the likelihood

is a product of individual Poisson distributions for each bin:

$$\mathcal{L}_c(\vec{\mu}, \vec{\theta}; \text{data}) = \prod_{i=1}^{n_{\text{bin}}} P\left(\sum_s N_{S_s}^c(\vec{\mu}) + \sum_b N_{B_b}^c, n_i\right) \quad (5-3)$$

The Poisson distribution uses n_i as the observed event count for each bin, and $\sum_s N_{S_s}^c(\vec{\mu}) + \sum_b N_{B_b}^c$ as the sum of signal and background yields.

The profile likelihood ratio, $\Lambda(\mu)$, for statistical tests is formulated as:

$$\Lambda(\mu) = \frac{\mathcal{L}(\mu, \hat{\hat{\theta}}(\mu))}{\mathcal{L}(\hat{\mu}, \hat{\theta})} \quad (5-4)$$

Here, the terms $\hat{\hat{\theta}}$ and $\hat{\theta}$ are the profiled values of the NPs that maximize the likelihood conditionally and unconditionally, respectively.

In the regime of large sample sizes, the test statistic $-2 \ln \Lambda(\mu)$ asymptotically follows a χ^2 distribution. The degrees of freedom (d.o.f) of this distribution correspond to the dimensionality of the parameter vector $\vec{\mu}$. This is predicated on the central limit theorem, which states that the sampling distribution of the likelihood will approach a Gaussian distribution as the sample size increases. This Gaussian approximation allows the transformation $-2 \ln \Lambda(\mu)$ to adhere to a χ^2 distribution, facilitating hypothesis testing for the parameters of interest (POIs).

The CL_s method^[150] is employed to establish upper limits at a 95% Confidence Level (CL) on the HH signal strength μ_{HH} and the associated production cross-section. CL_s is a modified frequentist approach for hypothesis testing that avoids the issue of overly-optimistic exclusion limits, a problem encountered in the traditional CL methodology. It does so by normalizing the p -value of the signal hypothesis by the p -value of the background-only hypothesis, thereby incorporating systematic uncertainties in a more conservative manner.

The test statistic \tilde{q}_μ utilized in the CL_s framework is formulated as:

$$\tilde{q}_\mu = \begin{cases} -2 \ln \frac{\mathcal{L}(\mu, \hat{\hat{\theta}}(\mu))}{\mathcal{L}(0, \hat{\hat{\theta}}(0))} & \hat{\mu} < 0, \\ -2 \ln \frac{\mathcal{L}(\mu, \hat{\hat{\theta}}(\mu))}{\mathcal{L}(\hat{\mu}, \hat{\theta})} & 0 \leq \hat{\mu} \leq \mu, \\ 0 & \hat{\mu} > \mu. \end{cases} \quad (5-5)$$

The CL_s values are computed from the distribution of \tilde{q}_μ under the signal-plus-background and background-only hypotheses, which in turn allows one to set data-driven upper limits.

5.5.2 Statistical analysis and Results

The statistical analysis for the 3-lepton channel is carried out using the TrexFitter package [151–152]. We employ a profile-likelihood fit on the Asimov dataset, which is a theoretical dataset that represents expected outcomes using pure MC dataset, to estimate the expected upper limit on the cross-section for SM HH production. This fit utilizes templates, which are constructed from predicted yields of both the signal and the relevant background processes, divided by bins in the input distribution for the 3-lepton channel specifically. For each bin in the input distribution, Monte Carlo statistical uncertainties are incorporated into the fit through an additional Poisson term (γ). The BDTG score distribution in the 3-lepton channel is used as the input distribution for the fit (only score > 0.55 is considered as SR). The BDTG score distribution is shown in Figure 5–14a.

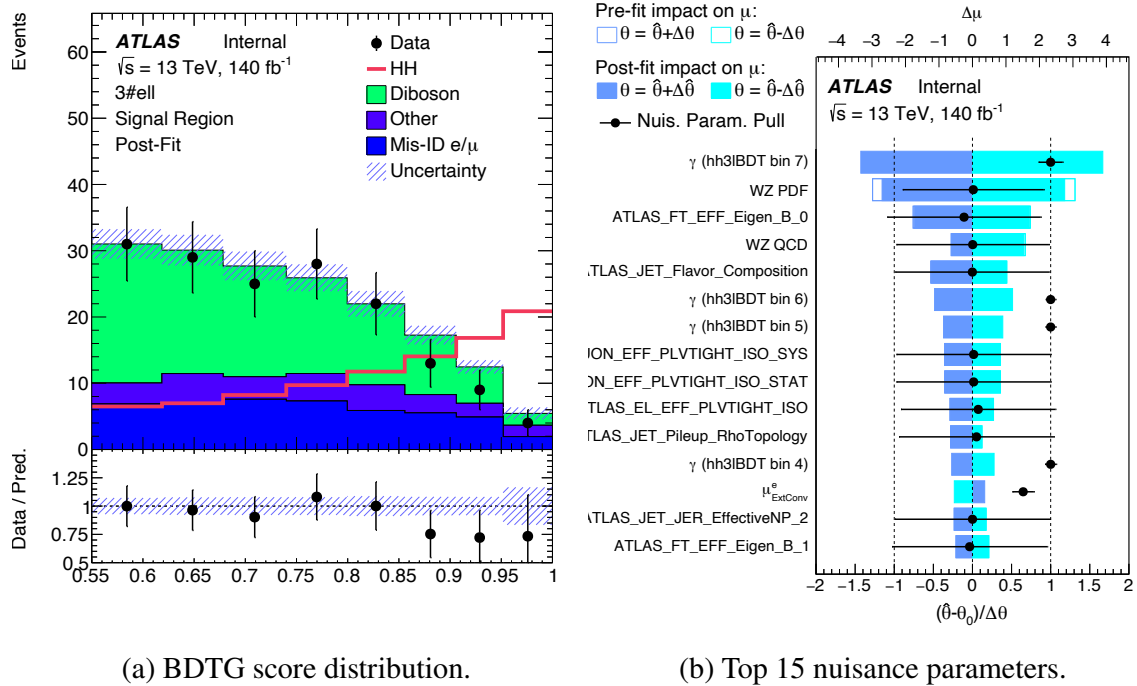


Figure 5–14 Fitting results for 3ℓ channel, including all systematics and data-driven nuisance parameters.

In the statistical analysis, the discriminant distribution serves as the basis for fitting the



	-2σ	-1σ	Expected	$+1\sigma$	$+2\sigma$	Observed
$\sigma_{HH}/\sigma_{HH}^{SM}$ Stats.	12.79	17.16	23.82	34.03	47.68	15.88
$\sigma_{HH}/\sigma_{HH}^{SM}$ Sys.	15.10	20.27	28.13	40.94	58.70	19.27

Table 5–13 Expected Upper limits in 3ℓ channel. First row: Limits with stats only; Second row: Limits with systematics.

signal and background distributions to the observed data. The primary parameter under scrutiny during the fitting procedure is the ratio of the observed signal cross-section to the Standard Model prediction. Data within the signal region are kept blinded for unbiased results.

Subsequent to the fitting, the maximum signal significance is quantified as 0.073, while the upper limit on the $HH \rightarrow 3\ell$ cross-section relative to the SM prediction stands at $23.13^{+10.21}_{-6.66}$ (considering only statistical uncertainties) and $28.09^{+12.81}_{-7.86}$ (inclusive of all uncertainties). A comprehensive summary of these expected upper limits can be found in Table 5–13.

Figures 5–15 and 5–14b depict the correlation matrix of the nuisance parameters and the ranking of the top 15 nuisance parameters, respectively. Regarding the ranked nuisance parameters, a few observations are noteworthy. The highest-ranking source of uncertainty is the statistical uncertainty of the simulation of the background in the last bin of the Signal Region (SR), an expected outcome owing to low statistics in that region. The second-highest perturbation emanates from the WZ background, which is dominant in this context. Finally, the third-ranking source is the b-jet calibration, which plays a crucial role in the estimation of fake rates in the presence of a $t\bar{t}$ background.

5.6 Combination Results

5.6.1 Overview of other channels

Channel	Region	$N_{\text{lep}}^{\Sigma \mathcal{O}_i'}$	$N_{\text{had}}^{\Sigma \mathcal{O}_i'}$	N_{jet}	$N_{b\text{-jet}}$	BDT cut	$m_{\ell\ell\ell}$ [GeV]	$m_{\ell^+\ell^-}$ [GeV]	$m_{\ell^+\ell^+}$ [GeV]	$E_{\text{T}}^{\text{miss}}$ [GeV]	m_{jj} [GeV]
2ℓSS	WZ CR	3^{+1}	0	≥ 2	0	$BDT_{\text{All}} < -0.4, BDT_{V_{\text{jets}}} > -0.8$	$ m_{\ell\ell\ell} - m_Z > 10$	$ m_{\ell^+\ell^-} - m_Z < 10$	$ m_{\ell^+\ell^+} - m_Z > 10$	> 30	> 300
	$W^\pm W^\pm jj$ CR	2^{+2}	0	≥ 2	0	$BDT_{\text{All}} < -0.4, BDT_{V_{\text{jets}}} > -0.8$			$ m_{\ell^+\ell^+} - m_Z > 10$		
	QmisID	$e^\pm e^\pm / e^\pm e^\mp$	0	< 2	0			[78.5, 102.3]	[76.5, 101.3]		
	Conv CR	2^{+2}	0	≥ 2	≥ 1						
	QED CR	2^{+2}	0	≥ 2	≥ 1						
	HF- e CR	$\ell^\pm e^\pm$	0	2,3	1/2						
	HF- μ CR	$\ell^\pm \mu^\pm$	0	2,3	≥ 1						
3ℓ	VR	2^{+2}	0	≥ 2	0	$BDT_{\text{All}} < -0.4$					
	WZ CR	3^{+1}	0	≥ 1	0		$ m_{\ell\ell\ell} - m_Z > 10$	$ m_{\ell\ell} - m_Z < 10$		> 30	
	VR	3^{+1}	0	≥ 1	0	$BDT < 0.55$					
$b\bar{b} + 4\ell$	Conv CR	3^{+1}	0	≥ 1	0		$ m_{\ell\ell\ell} - m_Z < 10$				
	HF- e CR	$\ell^\pm e^\pm e^\mp$	0	≥ 2	≥ 2		$ m_{\ell\ell\ell} - m_Z > 10$				
	HF- μ CR	$\ell^\pm \mu^\pm \mu^\mp$	0	≥ 2	≥ 2		$ m_{\ell\ell\ell} - m_Z > 10$				
	$t\bar{t}$ CR	$\ell^\pm \ell^\mp + e^\pm \mu^\mp$	0	1	≥ 2			$ m_{\ell\ell} - m_Z > 10$			
	$t\bar{t}Z$ CR	$\ell^\pm \ell^\mp + e^\pm \mu^\mp$	0	1	≥ 2			$ m_{\ell\ell} - m_Z < 10$			
$\ell + 2\tau_{\text{had}}$	VV+Higgs CR	4^0	0	1	0						
	Z+jets CR	4^0	0	1	≥ 2			$ m_{\ell\ell} - m_Z < 10$			
	VR	4^0	0	≥ 2	$\geq 1, \leq 3$		$ m_{\ell\ell\ell} - m_{H_{\text{iggs}}} \geq 10$				
	VR	1^{+1}	2^{+2}	≥ 2	0			$ m_{\ell\ell} - m_Z < 10$			
	Z+jets CR	2^0	2^{+2}	≥ 0	0			$ m_{\ell\ell} - m_Z > 10$			
$2\ell + 2\tau_{\text{had}}$	$t\bar{t}$ CR	2^0	2^{+2}	≥ 0	1						
	VR	2^{+2}	2^{+2}	≥ 0	0			$ m_{\ell\ell} - m_Z < 10$			
	Z+jets CR	2^0	2^{+2}	≥ 0	0			$ m_{\ell\ell} - m_Z > 10$			
2ℓSS + τ_{had}	$t\bar{t}$ CR	2^0	2^{+2}	≥ 0	1						
	VV CR	2^{+2}	1^{+1}	≤ 1	0			$ m_{\ell\ell} - m_Z > 10$			
	TF CR	$\ell^\pm \ell^\mp$	1^{+1}	≥ 2	0	$BDTG < -0.2$					
	VR	2^{+2}	1^{+1}	≥ 2	0						
	HF- e CR	$\ell^\pm e^\pm$	1^{+1}	≥ 2	1						
$\gamma\gamma + X$	HF- μ CR	$\ell^\pm \mu^\pm$	1^{+1}	≥ 2	≥ 1						
	Fit background CR	≥ 0	≥ 0	≥ 0	0	$m_{\gamma\gamma}$ in sideband region in all sub-channels, $ m_{\gamma\gamma} - 125 > 5$					

Table 5–14 Selection criteria applied to each of the control and validation regions defined in each channel. The requirements that guarantees orthogonality with respect to the corresponding signal region are highlighted in blue.

Channels	Selections
$2\ell SS$	Two same-sign tight leptons, $p_T \geq 20$ GeV $N_{\text{jets}} \geq 2$ and $N_{\text{b-jet}} = 0$ $m_{\ell\ell} > 12$ GeV BDT > -0.4
$2\ell SS + \tau_{\text{had}}$	Two same-sign tight leptons, $p_T \geq 20$ GeV $m_{\ell\ell} > 12$ GeV $N_{\text{jets}} \geq 2$ and $N_{\text{b-jet}} = 0$ exactly one RNN medium τ_{had} with $p_T \geq 25$ GeV tau with opposite charge to leptons BDTG > -0.2
3ℓ	One loose lepton with leading $p_T \geq 10$ GeV and two tight leptons with $p_T > 15$ GeV total electric charge of ± 1 $N_{\text{jets}} \geq 1$ and $N_{\text{b-jet}} = 0$ $m_{\ell\ell} > 12$ GeV and $ m_{\ell\ell} - 91.2 > 10$ GeV for all SFOS lepton pairs $ m_{\ell\ell\ell} - 91.2 > 10$ GeV BDT > 0.55
$\ell + 2\tau_{\text{had}}$	exactly one loose lepton exactly two RNN medium τ_{had} with opposite-sign $\Delta R_{(\tau_0, \tau_1)} \leq 2$ $N_{\text{jets}} \geq 2$ and $N_{\text{b-jet}} = 0$
$2\ell + 2\tau_{\text{had}}$	exactly two loose leptons with opposite-sign $m_{\ell\ell} > 12$ GeV exactly two RNN medium τ_{had} of opposite charge Z-veto for light lepton pairs $\Delta R_{(\tau_0, \tau_1)} \leq 2$ $N_{\text{jets}} \geq 1$ and $N_{\text{b-jet}} = 0$
$b\bar{b} + 4\ell$	Two leading baseline leptons and at least one subleading tight lepton, $p_T^1 \geq 20$ GeV, $p_T^2 \geq 15$ GeV, $p_T^3 \geq 10$ GeV $\Delta R > 0.02$ to any lepton pairs $m_{\ell\ell} > 5$ GeV for OSSF pairs. $50 \text{ GeV} < m_{\text{leading pair}} < 106 \text{ GeV}$ and $m_{\text{sub-leading pair}} < 115 \text{ GeV}$ $N_{\text{jets}} \geq 2$ and $3 \geq N_{\text{b-jet}} \geq 1$ $115 \text{ GeV} < M_{4\ell} < 135 \text{ GeV}$
$\gamma\gamma + X$	2 tight isolated photons with $E_T > 35$ GeV and $E_T > 25$ GeV $p_T/m_{\gamma\gamma} > 0.35$ (0.25) for the leading (subleading) photon $105 \text{ GeV} < m_{\gamma\gamma} < 160 \text{ GeV}$ b-veto: $N_{\text{b-jet}} = 0$ $p_T^{\gamma\gamma} > 50$ GeV $E_T^{\text{miss}} > 35$ GeV except $\gamma\gamma + 1\mu 0\tau_{\text{had}}$ channel $m_{\ell\ell} > 12$ GeV in $\gamma\gamma + 2\ell$ channel Events are classified in three different categories ($\gamma\gamma + \ell$, $\gamma\gamma + \tau_{\text{had}}$ and $\gamma\gamma + 2\ell$) by means of the number of light lepton and τ_{had} .

Table 5–15 Selection criteria applied to each channel to form the signal regions.

The definitions for the Signal Region, Control Regions, and Validation Regions across all channels featuring multi-lepton final states have been formulated. These regions are vital for both the optimization of the signal sensitivity and the validation of background estimations. Detailed tabulations of these region definitions for each channel have been systematically organized and can be found in Tables 5–15 and 5–14. These tables serve as comprehensive references for the specialized selections employed in each region.

5.6.2 Treatment of the Normalization Factors (NFs)

In the overarching framework of this integrated analysis, the workspaces for each individual channel are aggregated to perform a composite fit, with the parameter μ_{HH} designated as the unified Parameter of Interest (POI). To align the theoretical predictions with the empirical data, normalization factors are employed. These factors are channel-specific but are harmonized across channels when they address the same background source. Detailed information regarding these normalization factors, including their fitted values in both individual channels and the composite fit, is provided in Table 5-16. It is noteworthy that specific normalization factors such as NF_ExtConv_e , μ_{HF-e} , and $\mu_{HF-\mu}$ are only fitted in a combined manner as they are common to multiple channels. Channels like $\ell + 2\tau_{\text{had}}$, $2\ell + 2\tau_{\text{had}}$, and $\gamma\gamma + X$ do not utilize any normalization factors. Numbers in brackets in the $2\ell\text{SS} + \tau_{\text{had}}$ channel denote values obtained from fitting specific Control Regions.

NormFactor	$2\ell\text{SS}$	3ℓ	$2\ell\text{SS} + \tau_{\text{had}}$	$b\bar{b} + 4\ell$	combined
NF_IntConv_e	2.01 ± 0.28	-	-	-	-
NF_ExtConv_e	0.80 ± 0.36	0.66 ± 0.13	-	-	0.79 ± 0.16
μ_{HF-e}	1.18 ± 0.27	1.50 ± 0.50	$1.27 \pm 1.14(0.87)$	-	1.34 ± 0.17
$\mu_{HF-\mu}$	1.57 ± 0.17	1.51 ± 0.23	$0.59 \pm 1.03(0.75)$	-	1.56 ± 0.12
μ_{WZ}	0.82 ± 0.06	-	-	-	-
μ_{VVjj}	1.62 ± 0.13	-	-	-	-
$\mu_{t\bar{t}W}(\text{fake})$	1.24 ± 0.36	-	-	-	-
NF_VV	-	-	$0.98 \pm 0.42(0.94)$	-	-
$\mu_{t\bar{t}}$	-	-	-	1.50 ± 0.28	-
$\mu_{t\bar{t}Z}$	-	-	-	1.27 ± 0.22	-
μ_{VV}	-	-	-	1.12 ± 0.46	-
μ_{Higgs}	-	-	-	1.09 ± 0.42	-
$\mu_{Z+\text{jets}}$	-	-	-	1.01 ± 0.36	-

Table 5-16 Summary table of employed normalization factors, detailing individual and composite fit values. Specific channels without normalization factors are also indicated.

5.6.2.1 Systematics Correlation Scheme

A comprehensive outline of the correlation landscape among various uncertainties is presented in Table 5-16. Luminosity and pile-up re-weighting uncertainties are fully correlated across the board. Owing to channel-specific target objects, experimental uncertainties man-

NPs	2lss	2lss1tau	3l	1l2tau	2l2tau	bb4l	yym	Treatment
Lumi.+PRW	LUMI_Run2 PU_PRW_DATASF							correlated
EGamma	RES_ALL, SCALE_ALL, SCALE_AF2					RES_ALL SCALE_AF2	RES_ALL SCALE_ALL SCALE_AF2	correlated
Photon	-	-	-	-	-	-	EFF_ID EFF_ISO EFF_TRIGGER	-
Lepton	Common ATLAS NPs							correlated
Tau								
Jet+MET								
Flavor								
Theory	HH signal backgrounds					ggHH signal VBF HH signal backgrounds	HH signal Single Higgs	Mostly correlated
Others	QMisID			Fake tau			Background modeling	uncorrelated

Figure 5–16 Correlation scheme of the systematic uncertainties in the analysis.

ifest correlations for common objects between channels. For theoretical uncertainties tied to Di-Higgs signal processes, a full correlation is maintained across all channels, with a notable exception being the $b\bar{b} + 4\ell$ channel. In this channel, signal uncertainties are partitioned distinctly for ggF and VBF HH processes.

In the $\gamma\gamma + X$ channel, only uncertainties related to single Higgs processes are factored into the background modeling. The continuum background in this channel is regulated by data from sidebands and encapsulated within the domain of background modeling uncertainties. For other theoretical uncertainties, correlation is generally applied where relevant, particularly when the definition of "other background" overlaps between channels.

5.6.2.2 Combination Results

The synthesis of 95% Confidence Level upper limits across all multi-lepton sub-channels is enumerated in Table 5–17 and visually represented in Fig. 5–17. These limits are derived using Asimov datasets to separately assess the contributions of statistical uncertainties alone, statistical combined with Monte Carlo uncertainties, and a fully systematic scenario. It is noteworthy that most channels suffer from limited MC statistics, with the $\gamma\gamma + X$ sub-channels standing as an exception.

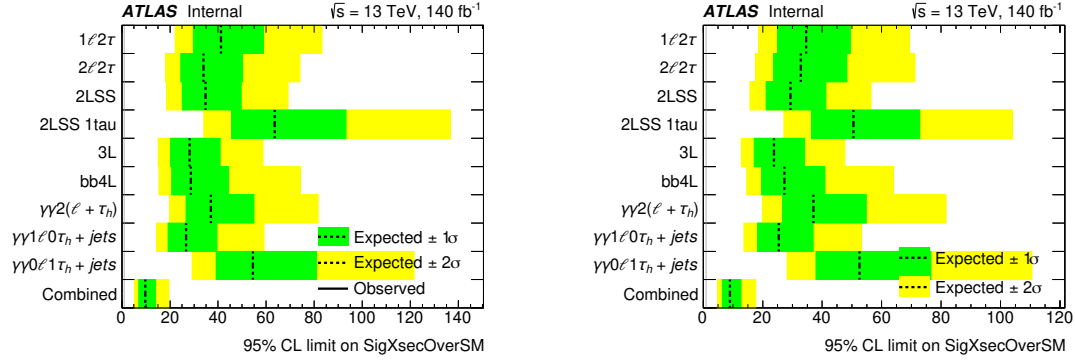


Figure 5–17 Expected individual and combined upper limits in channels, with full systematic uncertainties (left) and statistics only (right).

Channels	Stats. Only	Stats. + MC syst.	Stats.+ full syst.
$2\ell\text{SS}$	$30.70^{43.47}_{22.12}$	$31.62^{44.76}_{22.79}$	$34.81^{49.61}_{25.08}$
3ℓ	$23.82^{34.03}_{17.16}$	$25.58^{37.00}_{18.43}$	$28.13^{40.94}_{20.27}$
$b\bar{b} + 4\ell$	$27.24^{40.90}_{19.63}$	$27.62^{41.76}_{19.90}$	$28.71^{44.41}_{20.68}$
$\ell + 2\tau_{\text{had}}$	$34.64^{49.51}_{24.96}$	$38.31^{54.33}_{27.60}$	$41.21^{58.92}_{29.70}$
$2\ell + 2\tau_{\text{had}}$	$32.82^{48.34}_{23.65}$	$33.46^{49.12}_{24.11}$	$33.99^{50.09}_{24.49}$
$2\ell\text{SS} + \tau_{\text{had}}$	$50.50^{72.83}_{36.39}$	$62.37^{91.18}_{44.94}$	$63.52^{93.27}_{45.77}$
$\gamma\gamma + \ell$	$25.43^{36.95}_{18.32}$	$25.43^{36.95}_{18.32}$	$26.68^{39.53}_{19.23}$
$\gamma\gamma + \tau_{\text{had}}$	$52.58^{76.54}_{37.89}$	$52.50^{76.57}_{37.90}$	$54.50^{80.98}_{39.27}$
$\gamma\gamma + 2\ell$	$37.05^{54.86}_{26.70}$	$37.05^{54.86}_{26.70}$	$38.21^{57.76}_{27.53}$
Combined	$8.93^{12.69}_{6.44}$	$9.29^{13.22}_{6.70}$	$9.74^{13.91}_{7.02}$

Table 5–17 Table of 95% C.L. upper limits on signal strength for multi-lepton channels. Limits are derived using Asimov datasets under varying scenarios of statistical and systematic uncertainties.

Chapter 6 SM Di-Higgs Searches in $b\bar{b}\tau^+\tau^-$ Final States

6.1 Introduction

The search for SM production of Higgs boson pairs (HH) serves as a pivotal probe of the electroweak symmetry breaking mechanism, as mentioned in Section 2.3.2. Among various decay channels, the $b\bar{b}\tau^+\tau^-$ final state stands unique in terms of both signature and utility. This channel consists of two bottom quarks and two τ leptons. It holds the third-highest branching fraction of 7.3%, following $b\bar{b}b\bar{b}$ (34%) and $b\bar{b}WW^*$ (25%). Despite its lower branching fraction, the $b\bar{b}\tau^+\tau^-$ channel offers a cleaner experimental signature compared to the aforementioned channels.

The τ leptons can decay in two distinct modes: leptonically (τ_{lep}) into an electron or a muon, and hadronically (τ_{had}) into typically one (1-prong) or three (3-prong) charged hadrons accompanied by neutral hadrons. Consequently, this analysis considers two sub-channels: $b\bar{b}\tau_{\text{lep}}\tau_{\text{had}}$ and $b\bar{b}\tau_{\text{had}}\tau_{\text{had}}$, with the $b\bar{b}\tau_{\text{lep}}\tau_{\text{lep}}$ events being analyzed separately in $b\bar{b}\ell^+\ell^-$ channel.

The present analysis builds on previous work^[153] which was primarily optimized for the gluon-gluon fusion Standard Model production mode. The legacy analysis set an upper limit on the HH cross-section to 130 (110) fb at 95% CL, corresponding to 4.7 (3.9) times the SM prediction. While the legacy analysis provided important constraints on the κ_λ modifier, with a 95% confidence interval of $[-2.4, 9.2]$, the present analysis aims to improve these results through methodological enhancements and additional categorizations.

This analysis introduces several refinements:

- It is re-optimized specifically for constraining the κ_λ modifier by implementing an event categorization based on the invariant mass of the HH system (m_{HH}) in the ggF region.
- The sensitivity to the κ_{2V} parameter has been enhanced by adding a dedicated vector boson fusion (VBF) category.
- Advanced multivariate analysis (MVA) techniques are utilized for optimal signal-background separation, and the MVA outputs serve as the final discriminants in the fitting procedure.

Table 6–1 Summary of MC samples for signal and background processes.

Process	ME generator	ME QCD order	ME PDF	PS and hadronisation	UE model tune	Cross-section order
Signal						
$gg \rightarrow HH$ (ggF with $\kappa_t = 1, 10$)	POWHEG BOX v2	NLO	PDF4LHC15NLO	PYTHIA 8.244	A14	NNLO FTApprox
$qq \rightarrow qqHH$ (VBF with varied $\kappa_{t,1}, \kappa_{2V}, \kappa_V$)	MADGRAPH5_AMC@NLO 2.7.3	LO	NNPDF3.0NLO	PYTHIA 8.244	A14	N ³ LO(QCD)
Top-quark						
$t\bar{t}$	POWHEG BOX v2	NLO	NNPDF3.0NLO	PYTHIA 8.230	A14	NNLO+NNLL
t -channel	POWHEG BOX v2	NLO	NNPDF3.0NLO	PYTHIA 8.230	A14	NLO
s -channel	POWHEG BOX v2	NLO	NNPDF3.0NLO	PYTHIA 8.230	A14	NLO
Wt	POWHEG BOX v2	NLO	NNPDF3.0NLO	PYTHIA 8.230	A14	NLO
$t\bar{t}Z$	SHERPA 2.2.1	NLO	NNPDF3.0NNLO	SHERPA 2.2.1	Default	NLO
$t\bar{t}W$	SHERPA 2.2.8	NLO	NNPDF3.0NNLO	SHERPA 2.2.8	Default	NLO
Vector boson + jets						
W/Z +jets	SHERPA 2.2.11	NLO (≤ 2 jets) LO (3,4,5 jets)	NNPDF3.0NNLO	SHERPA 2.2.11	Default	NNLO
Diboson						
WW, WZ, ZZ	SHERPA 2.2.1	NLO (≤ 1 jet) LO (2,3 jets)	NNPDF3.0NNLO	SHERPA 2.2.1	Default	NLO
Single Higgs boson						
ggF	POWHEG BOX v2	NNLO	NNPDF3.0NLO	PYTHIA 8.212	AZNLO	N ³ LO(QCD)+NLO(EW)
VBF	POWHEG BOX v2	NLO	NNPDF3.0NLO	PYTHIA 8.212	AZNLO	NNLO(QCD)+NLO(EW)
$qq \rightarrow WH$	POWHEG BOX v2	NLO	NNPDF3.0NLO	PYTHIA 8.212	AZNLO	NNLO(QCD)+NLO(EW)
$qq \rightarrow ZH$	POWHEG BOX v2	NLO	NNPDF3.0NLO	PYTHIA 8.212	AZNLO	NNLO(QCD)+NLO(EW) ^(†)
$gg \rightarrow ZH$	POWHEG BOX v2	NLO	NNPDF3.0NLO	PYTHIA 8.212	AZNLO	NLO+NNL
$t\bar{t}H$	POWHEG BOX v2	NLO	NNPDF3.0NLO	PYTHIA 8.230	A14	NLO

6.2 Data and Monte Carlo samples

The analysis presented in this chapter uses proton-proton collision data, taken at a centre-of-mass energy of $\sqrt{s} = 13$ TeV by the ATLAS experiment from 2015 to 2018. The data corresponds to an integrated luminosity of $\mathcal{L} = 140.1 \pm 1.2 \text{ fb}^{-1}$ [154]. Event selections were based on the ATLAS Good-Run-List (GRL) to ensure the operational integrity of all relevant detector components.

To simulate the SM backgrounds and both SM and BSM HH signal, we utilize Monte Carlo event samples. These samples are processed through the ATLAS detector simulation based on Geant4 [129]. Pile-up effects are incorporated by overlaying minimum-bias events generated via PYTHIA 8.186 [127] with A3 tune [128] and the NNPDF2.3Lo [155] PDFs. The hadronic decays of b and c quarks are modeled by the EVTGEN program [156], except in samples generated with SHERPA [157], where generator-specific models are used.

For all MC samples containing a SM Higgs boson, a mass of 125 GeV is assumed for consistency in both decay branching fractions and cross-section calculations. The cross-sections are calculated with expansions in the strong coupling constant (α_s), unless otherwise specified.

The MC samples are summarized in Table 6-1, which details the generators used for simulating the signal and background processes. The nomenclatures ME, PS, and UE refer to matrix element, parton shower, and underlying event, respectively. Note that for samples with (\dagger), the $qq \rightarrow ZH$ process is normalized to the NNLO (QCD) + NLO (EW) cross-section for the $pp \rightarrow ZH$ process, after the $gg \rightarrow ZH$ contribution is subtracted.

6.2.1 Simulation of Signal Datasets

The HH signal is modeled considering both gluon-gluon fusion (ggF) and vector-boson fusion (VBF) as contributing processes.

6.2.1.1 ggF HH production

Samples¹ for κ_λ values of 1.0 and 10.0 were generated using POWHEG BOX v2 at NLO with finite top-quark mass considerations^[158]. The PDF4LHC15_NLO_30_PDFAS PDF set (code 90400 in LHAPDF^[159]) was employed^[160]. Parton showering and hadronisation were performed via PYTHIA 8.244^[127] using the A14 tune^[161-162] and NNPDF2.3LO PDF set. Figure 6-1 depicts the invariant mass distribution m_{HH} for ggF HH samples in the $\tau_{\text{had}}\tau_{\text{had}}$ channel, highlighting the potential for analysis categorization as elaborated in Section 6.3.4.

To model ggF HH events with varied κ_λ values in the range $\kappa_\lambda \in [-20, 20]$, either of the two base samples can be reweighted using the HH κ_λ reweighting tool², which offers event-specific weightings as a function of the desired κ_λ value and the true m_{HH} .

The SM process normalization is defined by the di-Higgs cross-section in the ggF channel, $\sigma_{\text{ggF}} = 31.05$ fb, as computed at NNLO FTApprox^[163], and then multiplied by the $b\bar{b}\tau^+\tau^-$ branching ratio, leading to a value of 2.2683967 fb.

Alternative ggF samples³ for $\kappa_\lambda = 1.0, 10.0$ were also generated using the POWHEG BOX v2 at NLO and were interfaced with HERWIG 7^[164] to examine parton showering uncertainties.

6.2.1.2 VBF HH production

VBF signal samples were synthesized at leading order (LO) utilizing the MADGRAPH5_AMC@NLO 2.7. framework, in combination with the NNPDF3.0NLO PDF model^[126]. The parton showers and subsequent hadronization steps were conducted through PYTHIA 8.244 with the A14 config-

¹ <https://its.cern.ch/jira/browse/ATLMCPROD-8884>

² [kLambdaReweightTool](#)

³ <https://its.cern.ch/jira/browse/ATLMCPROD-9170>

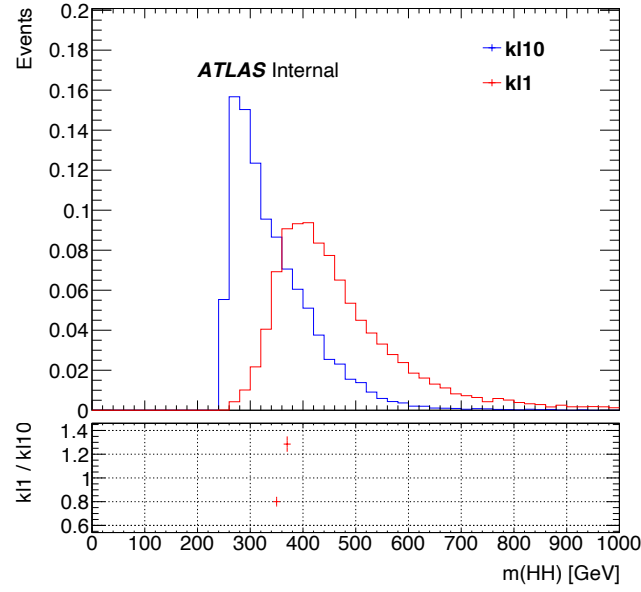


Figure 6–1 Invariant mass (m_{HH}) distribution at the parton level for the ggF HH signal in the $\tau_{had}\tau_{had}$ channel, with overlaid κ_{λ} values of 1.0 and 10.0.

uration and NNPDF2.3Lo PDF set. Various coupling modulators κ_{λ} , κ_{2V} , and κ_V were employed, as cataloged in Table 6–2. A linear blend of six reference points in the $(\kappa_{\lambda}, \kappa_{2V}, \kappa_V)$ space allows for more refined granularity in κ_{2V} values.

Table 6–2 Considered κ_{λ} , κ_{2V} , and κ_V coupling modifiers for VBF HH simulations.

κ_{λ}	κ_{2V}	κ_V
1	1	1
1	0	1
1	0.5	1
1	1.5	1
1	2	1
1	3	1
0	1	1
2	1	1
10	1	1
1	1	0.5
1	1	1.5
0	0	1
-5	1	0.5

Figures 6–2 display representative parton-level distributions of these samples, featuring key observables and their relation to the coupling parameters [166].

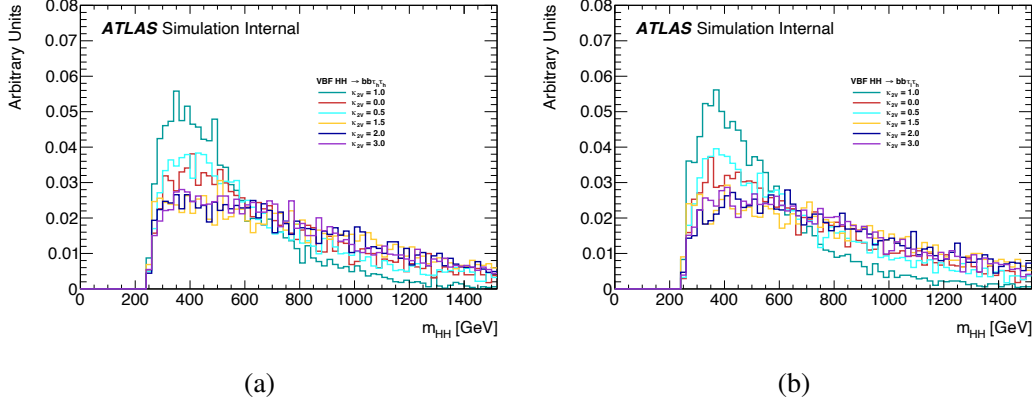


Figure 6–2 Inclusive distributions of VBF HH samples for varying κ_{2V} at parton-level, presented for the $\tau_{\text{had}}\tau_{\text{had}}$ and $\tau_{\text{lep}}\tau_{\text{had}}$ channels. Couplings are adjusted as outlined in Table 6–2.

The SM normalization is determined by the VBF HH cross-section $\sigma_{\text{VBF}} = 1.726 \text{ fb}$, calculated at N³LO in QCD, and the $b\bar{b}\tau^+\tau^-$ branching ratio, resulting in a final value of $\sigma_{\text{VBF}} \times \mathcal{B}(b\bar{b}\tau^+\tau^-) = 0.126 \text{ fb}$. BSM normalization follows a quadratic function of κ_{2V} [148].

For systematic variations in parton shower, alternate VBF HH samples were produced at specific coupling values, as denoted in Table 6–3, using the MADGRAPH5_AMC@NLO 2.7.3 and NNPDF3.0NLO models, interfaced to HERWIG 7 [164].

Table 6–3 Coupling modifier values for generating alternative VBF HH samples.

κ_λ	κ_{2V}	κ_V
1	1	1
1	0	1
10	1	1

6.2.2 Background Simulation Samples

Top Quark Processes The simulation of both top-antitop ($t\bar{t}$) and individual top quark productions in Wt , s , and t -channels are generated through the POWHEG BOX v2 generator [167–169]. The PDF utilized is NNPDF30NLO [170]. Post-generation event dynamics, including parton showers and hadronization, are conducted with PYTHIA 8 version 8.230 [171].

The tuning parameter set used is A14^[162,172]. The decays of bottom and charm hadrons are handled via EvtGen v1.6.0^[166].

Vector Boson + Jets (V +jets) These events, containing either W or Z bosons accompanied by jets, are generated through the SHERPA 2.2.11^[157]. A mixed NLO and LO framework for matrix elements is used, with NLO matrix elements considering up to two additional partons and LO matrix elements accounting for up to five additional partons. These are computed through Comix^[173] and OPENLOOPS^[174-176].

Diboson Processes Diboson events, characterized by one boson decaying hadronically and the other leptonically, are modeled using SHERPA version 2.2.1^[157]. PDFs are based on the NNPDF3.0NNLO set^[126].

Top-Quark and Vector Boson Associated Production (ttV) Simulations are executed using SHERPA v2.2.1 for ttZ and SHERPA v2.2.8 for ttW , both employing multileg NLO merging techniques. PDFs are based on NNPDF3.0NNLO^[126].

SM Single Higgs Production This analysis incorporates SM Higgs boson as a part of the background and is elaborated below:

- ttH : Produced via POWHEG BOX, it employs NNPDF30NLO for PDFs and PYTHIA 8 v8.230 for parton showers^[171].
- ZH : Utilizes POWHEG BOX v2 and considers both $qqZH$ and $ggZH$ channels. PDFs are NNPDF3.0NNLO^[126].
- WH : Generated using POWHEG BOX v2 with PDFs from NNPDF3.0NNLO^[126].
- $ggF H \rightarrow \tau^+\tau^-$: Simulated through POWHEG BOX v2 with NNPDF3.0NNLO PDFs^[126].
- $VBF H \rightarrow \tau^+\tau^-$: Produced via POWHEG BOX v2, using NNPDF3.0NNLO^[126] for PDFs.

6.3 Event selection

The analysis procedure is divided into two sub-channels according to the di- τ decay mode. A schematic representation of this approach is provided in Figure 6-3. The first sub-channel, denoted as $b\bar{b}\tau_{\text{had}}\tau_{\text{had}}$, focuses on events featuring two oppositely charged $\tau_{\text{had-vis}}$ along with two b -jets. The second, termed $b\bar{b}\tau_{\text{lep}}\tau_{\text{had}}$, targets events with one lepton (electron or muon), one oppositely charged $\tau_{\text{had-vis}}$, and two b -jets. For both sub-channels, the two b -jets are required to pass a working point with 77% efficiency.

The schematic in Figure 6-3 illustrates the sequence of triggers and event selection criteria for the two sub-channels. It also depicts the BDT framework that establishes the Signal Regions (SR) orthogonality between ggF and VBF categories. Further, the ggF SR is partitioned by an invariant mass threshold of 350 GeV to enhance sensitivity to the parameter κ_λ .

Event classification into ggF and VBF SRs is achieved through specialized BDTs. The ggF SRs are further divided into low- and high-mass regions using an invariant mass cut-off of 350 GeV for the HH system.

A Control Region (CR), designated as Z+HF CR, is established to calibrate the Z+HF background normalization. This CR utilizes $b\bar{b}\ell\ell$ triggers and focuses on the $m_{\ell\ell}$ shape as the parameter of interest, consistent with the schematic representation.

Both sub-channels are required to pass a common set of object selection criteria as in Section 6.3.1. Detailed trigger configurations for these sub-channels are elaborated in Section 6.3.2. Subsequent sections will elucidate the updated definition of the Z+HF CR phase space relative to the prior analysis [177].

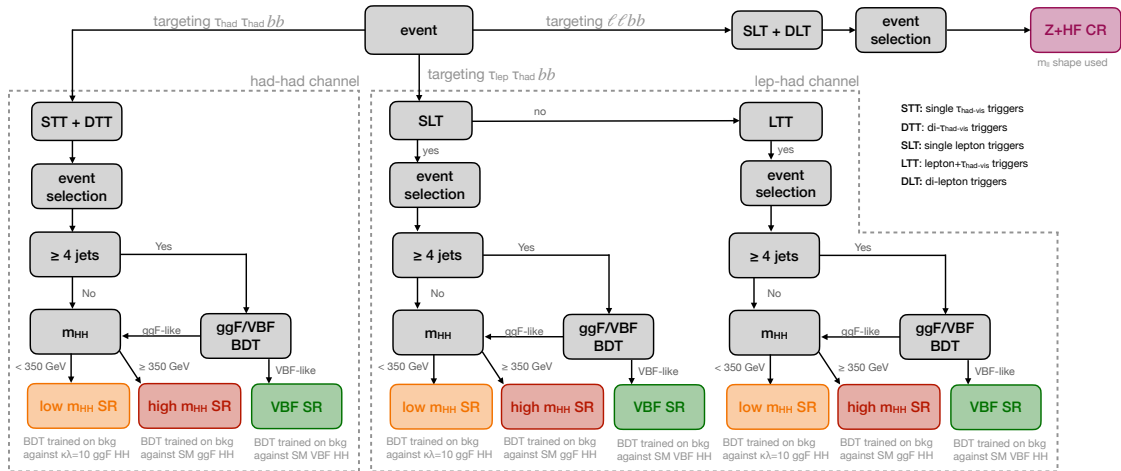


Figure 6-3 Schematic representation of the analysis strategy.

An overview of the event selection procedures is provided in Table 6-4. This table disaggregates the event criteria according to the different triggers that are employed for selection. For events requiring pairs of reconstructed objects of identical nature, the table specifies distinct p_T thresholds for both leading and sub-leading objects. These are indicated outside and

$\tau_{\text{had}}\tau_{\text{had}}$ category		$\tau_{\text{lep}}\tau_{\text{had}}$ categories	
STT	DTT	SLT	LTT
e/μ selection			
No loose e/μ		Exactly one loose e/μ	
		e (μ) must be tight (medium and have $ \eta < 2.5$)	
		$p_{\text{T}}^e > 25, 27$ GeV	$18 \text{ GeV} < p_{\text{T}}^e < \text{SLT cut}$
		$p_{\text{T}}^\mu > 21, 27$ GeV	$15 \text{ GeV} < p_{\text{T}}^\mu < \text{SLT cut}$
$\tau_{\text{had-vis}}$ selection			
Two loose $\tau_{\text{had-vis}}$		One loose $\tau_{\text{had-vis}}$	
		$ \eta < 2.3$	
$p_{\text{T}} > 100, 140, 180$ (25) GeV	$p_{\text{T}} > 40$ (30) GeV	$p_{\text{T}} > 30$ GeV	
Jet selection			
≥ 2 jets with $ \eta < 2.5$			
Leading jet $p_{\text{T}} > 45$ GeV	Trigger dependent	Leading jet $p_{\text{T}} > 45$ GeV	Trigger dependent
Event-level selection			
Trigger requirements passed			
Collision vertex reconstructed			
$m_{\tau\tau}^{\text{MMC}} > 60$ GeV			
Opposite-sign electric charges of $e/\mu/\tau_{\text{had-vis}}$ and $\tau_{\text{had-vis}}$			
Exactly two b -tagged jets			
$m_{bb} < 150$ GeV			

Table 6–4 Summary of the event selections, shown separately for events that are selected by different triggers.

inside parentheses, respectively. In cases where the selection constraints are influenced by the year of data acquisition, multiple acceptable parameter values are enumerated and separated by commas. Notably, the jet selection criteria under the LTT and DTT triggers are an exception and adhere to a more intricate set of guidelines, as detailed in Section 6.3. It is essential to note that the listed trigger p_{T} thresholds are imposed on offline physics objects that have been appropriately matched to their corresponding trigger entities. For the scope of this study, the event selection will be exclusively focused on the $\tau_{\text{had}}\tau_{\text{had}}$ channel.

6.3.1 Object Reconstruction

6.3.1.1 Electrons

Electron candidates in the ATLAS experiment undergo a multi-criteria reconstruction and identification process, as summarized below [178]:

- **Identification Criteria:**
 - Track properties: Imposed requirements on measured track attributes.
 - Calorimetric clustering: Conditions on energy deposit cluster shape.
 - Track-to-cluster matching: Quality metrics for association.
 - Track quality: Additional hit requirements.
- **Likelihood Technique:** Utilizes a *loose* working point to achieve 95% electron identification efficiency.
- **Kinematic Requirements:**
 - $p_T > 7 \text{ GeV}$
 - $|\eta| < 2.47$ (excluding $1.37 < |\eta| < 1.52$)
- **Isolation Criteria:**
 - *fixed cut loose* working point.
 - p_T -dependent upper bounds on track momenta and topo-clusters.
- **Trigger Specifics:**
 - LTT involvement necessitates *tight* isolation working point.
 - Trigger scale factors only available for *tight* isolation electrons.

6.3.1.2 Muons

Muon candidates undergo specific reconstruction and identification procedures, as outlined below^[179]:

- **Track Reconstruction:**
 - Inner Detector (ID): Independent track reconstruction.
 - Muon Spectrometer (MS): Independent track reconstruction.
 - Minimum hit requirements: Enforced in both ID and MS.
 - Combined fit: Utilizes both ID and MS for momentum refinement.
- **Kinematic Criteria:**
 - $p_T > 7 \text{ GeV}$
 - $|\eta| < 2.7$
- **Identification:**
 - Working Point: Required to pass *loose* identification criteria.
- **Isolation:**
 - Criteria: Required to pass PflowLoose_VarRadIso^[180].

- Inversion: Performed for background control region establishment.

6.3.1.3 hadronic- τ Leptons

- **Reconstruction**^[181]:
 - Seeding: Jets formed via anti- k_t algorithm, $\Delta R = 0.4$.
 - BDT Classification: Sorts tracks into core and isolation tracks within $\Delta R = 0.4$ of $\tau_{\text{had-vis}}$ axis.
 - Prongs: Defined by the number of core (charged) tracks.
- **Identification**^[112]:
 - RNN Classifier: Utilized for discrimination against jet-like signatures.
 - Algorithms: Specific for 1-prong and 3-prong $\tau_{\text{had-vis}}$.
 - Working Points: Efficiency = 85% for 1-prong, 75% for 3-prong.
- **Selection Criteria:**
 - $p_T > 20$ GeV
 - $|\eta| < 2.5$ and veto region $1.37 < |\eta| < 1.52$
 - Tracks: One or three.
 - Charge: Unit charge.
 - Working Point: *loose* with 85% efficiency for 1-prong and 75% for 3-prong.
- **Additional Rejection:** Against electrons.
 - BDT: Utilizing track and shower shape information.
 - Efficiency: Approximately 95% for true $\tau_{\text{had-vis}}$.
- **Anti- τ_{had} Definition**^[177,182]:
 - Fail RNN loose τ_{had} -ID with an RNN score > 0.01 .
 - Defined by the Fake-Tau-Task-Force, used for background estimation.
 - Efficiency: Approximately 99% for true- τ_{had} in $\gamma^* \rightarrow \tau\tau$ events.
- **Anti- τ_{had} Selection**^[182]:
 - Selected in events where the number of offline τ_{had} passing the $\tau_{\text{had-ID}}$ is less than the channel-specific requirement (e.g., one for the $\tau_{\text{lep}}\tau_{\text{had}}$ channel, two for the $\tau_{\text{had}}\tau_{\text{had}}$ channel).
 - Requirement: Ensures total number of selected τ_{had} (loose and anti- τ_{had}) corresponds to the required multiplicity.
 - Trigger-Level Matching: For channels with $\tau_{\text{had-ID}}$ at the trigger level, only matched

anti- τ_{had} are considered.

- Random Selection: Employed when multiple anti- τ_{had} satisfy criteria and a τ_{had} trigger is not used.

6.3.1.4 Jets

Jets are reconstructed using the anti- k_t algorithm^[183] with a distance parameter $R = 0.4$, and further refined using the Particle-Flow (PF) algorithm^[184]. Jet cleaning is performed to mitigate the effects of non-collision backgrounds (NCB) and calorimeter noise, utilizing the jet cleaning algorithm based on certain working points^[185]. The jet-vertex-tagger (JVT) algorithm is applied for pile-up suppression, specifically with a JVT threshold that varies based on p_T of the jet^[161].

Calibrations for the Jet Energy Scale (JES) and Jet Energy Resolution (JER) are meticulously conducted, adhering to the protocols established in the previously cited work^[184]. Additional corrections for pile-up and underlying event effects are also applied^[186].

6.3.1.5 b -jet Identification and Calibration

b -jets are identified using a deep learning-based algorithm, the DL1r tagger^[187-188]. The tagger utilizes jet kinematics, impact parameters, and the presence of displaced vertices to discriminate between b -jets and lighter jets. It takes inputs from a recurrent neural network for impact parameter scoring (RNNIP)^[189].

The analysis utilizes pseudo-continuous b -tagging, applying multiple working points corresponding to 77%, 70%, and 60% b -tagging efficiencies, following internal documentation^[182]. These working points are used for multiple discriminant analysis (MDA) optimizations.

Shape comparison plots of the DL1r quantiles of the sub-leading b -tagged jet are shown in Figure 6-4a for the SM ggF, ggF ($\kappa_\lambda = 10.0$) and SM VBF signals, along with the sum of the backgrounds. Figure 6-4b shows the same variable for each background component.

The b -jet energy scale (bJES) and b -jet energy resolution (bJER) are specifically calibrated based on Ref.^[182]. Scale factors (SF) for b -tagging efficiencies are obtained from the CDI file 2020-21-13TeV-MC16-CDI-2021-04-16_v1.root^[187].

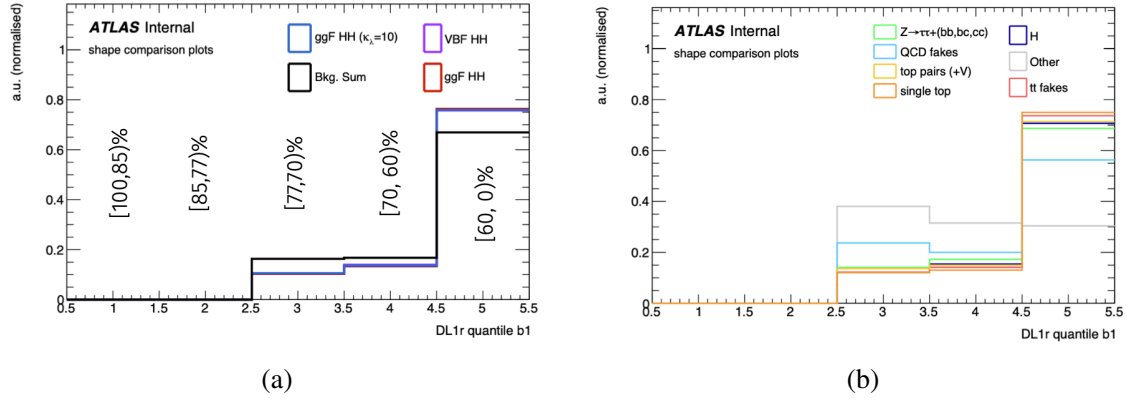


Figure 6–4 Sub-leading b -jet DL1r quantiles. Figure (a) shows the SM ggF, ggF ($\kappa_\lambda = 10.0$) and SM VBF signals, along with the sum of the backgrounds. Figure (b) shows the same variable for each background component.

6.3.1.6 Missing Transverse Momentum (E_T^{miss})

The E_T^{miss} is determined as the negative of the accumulated transverse momentum vectors of calibrated leptons, τ -leptons decaying via hadronic channels, and jets. Additionally, a ‘soft term’ is included, computed as the vector sum of the transverse momenta (p_T) of tracks that are linked to the primary vertex but are not connected to any recognized lepton or jet [190].

6.3.1.7 Overlap Removal

Pair	Condition	Action	Notes
$e_1 - e_2$	Shared track	Reject e_1 if $p_{T1} < p_{T2}$	
$\tau_{\text{had-vis}} - e$	$\Delta R_y < 0.2$	Reject $\tau_{\text{had-vis}}$	e must pass DFCommonElectronsLHLoose
$\tau_{\text{had-vis}} - \mu$	$\Delta R_y < 0.2$	Reject $\tau_{\text{had-vis}}$	Case 1: $p_{T,\tau} > 50 \text{ GeV}$, $p_{T,\mu} > 2 \text{ GeV}$ and combined μ Case 2: $p_{T,\tau} \leq 50 \text{ GeV}$, $p_{T,\mu} > 2 \text{ GeV}$
$\mu - e$	Calo-muon	Reject μ	Shared ID track
$e - \mu$	–	Reject e	Shared ID track
jet - e	$\Delta R_y < 0.2$	Reject jet	
e - jet	$\Delta R_y < 0.4$	Reject e	
jet - μ	$N_{\text{track}} < 3$ or $\Delta R_y < 0.2$	Reject jet	$p_{T,\text{track}} > 500 \text{ MeV}$
μ - jet	$\Delta R_y < 0.4$	Reject μ	
jet - $\tau_{\text{had-vis}}$	$\Delta R_y < 0.2$	Reject jet	Analysis-specific
anti- $\tau_{\text{had-vis}}$ - jet	$\Delta R_y < 0.2$	Reject anti- τ	Only if jet is b -tagged
jet - anti- $\tau_{\text{had-vis}}$	$\Delta R_y < 0.2$	Reject jet	

Table 6–5 Summary of overlap-removal procedures with the standard working point.

After event reconstruction, an overlap-removal algorithm is utilized to address instances

where a single physical object is identified as multiple particle types in the ATLAS detector. The algorithm measures the angular separation between two reconstructed objects using the metric $\Delta R_y = \sqrt{\Delta y^2 + \Delta \phi^2}$.

For most particle combinations, a standard toolkit called AssociationUtils is employed with a default working point^[191]. However, the overlap between reconstructed $\tau_{\text{had, vis}}$ and jets follows a unique, analysis-specific procedure. Specialized overlap-removal algorithms are also applied to $\tau_{\text{had, vis}}$, anti- $\tau_{\text{had, vis}}$, and jets, adhering to a predefined priority sequence ($\tau_{\text{had, vis}} > \text{anti-}\tau_{\text{had, vis}} > \text{jets}$). The summary of the overlap removal steps and the standard working point is presented in Table 6-5.

6.3.2 Trigger Selection

6.3.2.1 $\tau_{\text{had}}\tau_{\text{had}}$

The trigger logic for the $\tau_{\text{had}}\tau_{\text{had}}$ sub-channel comprises two types: single- $\tau_{\text{had-vis}}$ triggers (STTs) and di- $\tau_{\text{had-vis}}$ triggers (DTTs). STTs require at least one $\tau_{\text{had-vis}}$ at the High-Level Trigger (HLT) with a p_T threshold varying between 80 GeV and 160 GeV, dependent on the data collection epoch. DTTs necessitate at least a $\tau_{\text{had-vis}}$ pair at the HLT with a minimum p_T of 35 GeV and 25 GeV for the leading and sub-leading $\tau_{\text{had-vis}}$, respectively.

From 2016 onward, additional criteria were enforced at the Level-1 (L1) trigger to mitigate DTT rate inflation. For the 2016 dataset, an extra jet with $E_T > 25$ GeV was required. The 2017 and 2018 periods used additional jet requirements based on offline jet presence, with specific energy and spatial constraints.

To enhance trigger modelling, offline $\tau_{\text{had-vis}}$ objects are constrained to be spatially near the HLT $\tau_{\text{had-vis}}$ objects within $\Delta R = 0.2$ and also meet additional p_T requirements. Events satisfying both STTs and DTTs are processed using the STT offline constraints.

For a comprehensive list of triggers, refer to Table 6-6. Additional specifications can be found in internal documentation^[182] and the previous analysis iteration^[177].

6.3.3 $\tau_{\text{had}}\tau_{\text{had}}$ Event Selection

In addition to the trigger selection delineated in Section 6.3.2, supplementary selection criteria are imposed to isolate the signal region in the $\tau_{\text{had}}\tau_{\text{had}}$ sub-channel. In this context,

¹ ATL-COM-PHYS-2020-766

Period	Trigger
Single-$\tau_{\text{had-vis}}$ triggers (STT)	
15 – 16 A	HLT_tau80_medium1_tracktwo_L1TAU60
16 B – 16 D3	HLT_tau125_medium1_tracktwo
16 D4 – 17 B4	HLT_tau160_medium1_tracktwo
17 B5 – 17 end	HLT_tau160_medium1_tracktwo_L1TAU100
18 –	HLT_tau160_medium1_tracktwoEF_L1TAU100
18 K –	HLT_tau160_mediumRNN_tracktwoMVA_L1TAU100
Di-$\tau_{\text{had-vis}}$ triggers (DTT)	
15	HLT_tau35_medium1_tracktwo_tau25_medium1_tracktwo_L1TAU20IM_2TAU12IM
16 – 17 B4	HLT_tau35_medium1_tracktwo_tau25_medium1_tracktwo
17	HLT_tau35_medium1_tracktwo_tau25_medium1_tracktwo_L1TAU20IM_2TAU12IM_4J12
17 B5 – 17 end	HLT_tau35_medium1_tracktwo_tau25_medium1_tracktwo_L1DR-TAU20ITAU12I-J25
18 –	HLT_tau35_medium1_tracktwoEF_tau25_medium1_tracktwoEF_L1TAU20IM_2TAU12IM_4J12.0ETA23
18 –	HLT_tau35_medium1_tracktwoEF_tau25_medium1_tracktwoEF_L1DR-TAU20ITAU12I-J25
18 K –	HLT_tau35_mediumRNN_tracktwoMVA_tau25_mediumRNN_tracktwoMVA_L1TAU20IM_2TAU12IM_4J12.0ETA23
18 K –	HLT_tau35_mediumRNN_tracktwoMVA_tau25_mediumRNN_tracktwoMVA_L1DR-TAU20ITAU12I-J25

Table 6–6 Data-taking triggers for the $\tau_{\text{had}}\tau_{\text{had}}$ channel.

each event is mandated to encompass exactly two τ -leptons that satisfy the *loose* identification prerequisites. These τ -leptons must exhibit opposite-sign charges. Moreover, the event must contain a minimum of two jets, out of which exactly two must be b -tagged, adhering to the DL1r 77% working point.

Events presenting any surplus leptons, whether they be electrons or muons, are subjected to vetoing. Furthermore, the leading and sub-leading b -tagged jets within the event are compelled to display a transverse momentum (p_T) greater than 45 GeV and 20 GeV, respectively.

The invariant mass of the τ -lepton pair, denoted as $m_{\tau\tau}^{\text{MMC}}$, is ascertained via the Missing Mass Calculator (MMC) [192]. This computation employs the four-momenta of the visible hadronic decays of the τ -leptons ($\tau_{\text{had-vis}}$) as well as the missing transverse momentum ($\mathbf{p}_T^{\text{miss}}$). The MMC operates under the assumption that the missing transverse momentum originates exclusively from the neutrinos resulting from the τ -lepton decays.

For the purpose of mitigating background interference from low-mass Drell-Yan events, a condition is set such that $m_{\tau\tau}^{\text{MMC}}$ must exceed 60 GeV.

The confluence of these event selection steps culminates in the $\tau_{\text{had}}\tau_{\text{had}}$ signal region, summarized in Table 6–4. The corresponding cutflow tables for the Standard Model ggF HH and VBF HH signals in the $\tau_{\text{had}}\tau_{\text{had}}$ sub-channel are provided in Table 6–7 and Table 6–8.

Description	Number of events		Efficiency [%]		Relative Efficiency [%]	
	STT	DTT	STT	DTT	STT	DTT
HH	4314.87		x			x
$HH \rightarrow b\bar{b}\tau\tau$	315.23		x			x
$HH \rightarrow b\bar{b}\tau_{\text{had}}\tau_{\text{had}}$	132.32		100.00		100.00	
Generator filter	102.78		77.68		77.68	
Derivation skimming	88.28		66.72		85.89	
Object preselection	40.44		30.56		45.81	
Trigger selection (online+offline)	17.30		13.08		42.79	
Trigger category	1.95	15.35	1.48	11.60	11.29	88.71
Random τ selection	1.93	15.31	1.46	11.57	99.03	99.78
Object selection ($n_\tau = 2$, further requirements on jets and tau-jet OLR)	1.86	14.12	1.40	10.67	95.92	92.19
Pileup Correction	1.91	14.40	1.44	10.88	x	x
2 Loose τ (one Loose τ already required in derivation)	1.37	11.64	1.04	8.80	71.95	80.84
Subleading τ $p_T > 25$ GeV	1.21	11.64	0.91	8.80	87.74	x
MMC > 60 GeV	1.15	11.40	0.87	8.62	95.40	97.98
At least one jet with $p_T > 45$ GeV	1.15	11.17	0.87	8.44	99.63	97.95
DTT offline jet cuts	1.15	9.95	0.87	7.52	x	89.05
Scale Factors	1.16	10.48	0.87	7.92	x	x
Opposite charge sign	1.14	10.34	0.86	7.82	98.14	98.71
Both jets are b-tagged	0.57	4.83	0.43	3.65	49.86	46.74
ggF low m_{HH} SR	0.004	0.583	<0.01	0.44	0.71	12.07
ggF high m_{HH} SR	0.504	3.874	0.38	2.93	89.36	80.21
VBF SR	0.056	0.373	0.04	0.28	9.93	7.72

Table 6-7 SM ggF HH signal cutflow (POWHEG + PYTHIA 8) in the $\tau_{\text{had}}\tau_{\text{had}}$ sub-channel.

Description	Number of events			Efficiency [%]			Relative Efficiency [%]		
	STT	DTT	STT	DTT	STT	DTT	STT	DTT	DTT
HH	239.85		x					x	
$HH \rightarrow b\bar{b}\tau\tau$	17.52		x					x	
$HH \rightarrow b\bar{b}\tau_{\text{had}}\tau_{\text{had}}$	7.36		100.00					100.00	
Generator filter	5.00		67.99					67.99	
Derivation skimming	4.24		57.61					84.73	
Object preselection	1.89		25.69					44.59	
Trigger selection (online+offline)	0.74		10.11					39.36	
Trigger category	0.06	0.69	0.79	9.32	7.82			92.18	
Random τ selection	0.06	0.68	0.78	9.28	98.64			99.55	
Object selection ($n_\tau = 2$, further requirements on jets and tau-jet OLR)	0.05	0.59	0.72	7.99	92.33			86.07	
Pileup Correction	0.05	0.60	0.74	8.13	x			x	
2 Loose τ s (one Loose τ already required in derivation)	0.04	0.48	0.56	6.54	74.81			80.37	
Subleading τ $p_T > 25$ GeV	0.04	0.48	0.49	6.54	88.41			x	
MMC > 60 GeV	0.03	0.47	0.47	6.37	95.60			97.52	
At least one jet with $p_T > 45$ GeV	0.03	0.45	0.46	6.07	98.65			95.26	
DTT offline jet cuts	0.03	0.35	0.46	4.80	x			78.99	
Scale Factors	0.03	0.37	0.47	5.03	x			x	
Opposite charge sign	0.03	0.36	0.46	4.94	97.86			98.19	
Both jets are b-tagged	0.01	0.15	0.20	2.07	42.67			41.98	
ggF low m_{HH} SR	<0.001	0.008	<0.01	0.11	0.46			5.40	
ggF high m_{HH} SR	0.004	0.041	0.06	0.57	30.35			27.59	
VBF SR	0.010	0.102	0.14	1.38	69.20			67.00	

Table 6-8 SM VBF HH signal cutflow (PowHEG + Pythia 8) in the $\tau_{\text{had}}\tau_{\text{had}}$ sub-channel.

6.3.4 Event Categorization

In a substantial improvement from the full Run 2 analysis, the current work introduces a refined categorization scheme for events, visualized in Figure 6-5. This new framework divides each sub-channel into three distinct signal regions, adding an extra layer of granularity to our understanding of these events.

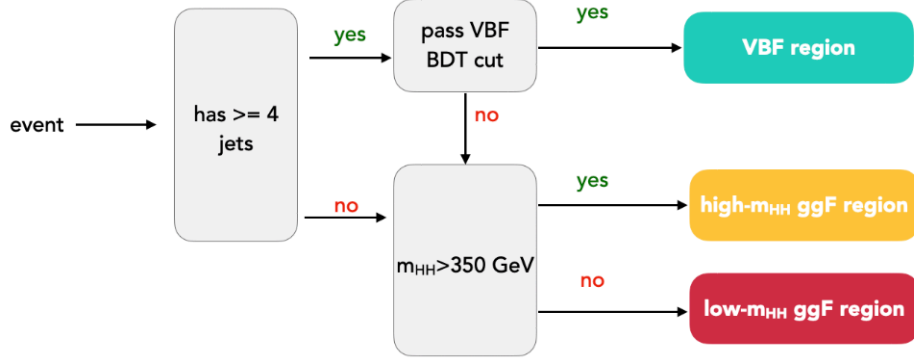


Figure 6-5 Event categorisation into low- m_{HH} ggF, high- m_{HH} ggF, and VBF signal regions.

For events with at least four jets, a specialized BDT classifier is deployed to optimally distinguish between ggF and VBF production modes. Events passing a particular working point for this BDT, as specified for example in the $\tau_{\text{had}}\tau_{\text{had}}$ channel in Section 6.5.2, are tagged as VBF-like and are allocated to a dedicated VBF signal region.

Conversely, events featuring fewer than four jets or failing the BDT threshold are considered ggF-like. Within this category, additional granularity is achieved by classifying these events based on the invariant mass of the di-Higgs system (m_{HH}). Specifically, a low-mass ggF signal region is established with an upper m_{HH} bound of 350 GeV. This low-mass categorization aims to probe BSM scenarios, particularly those characterized by non-standard κ_λ values.

Events surpassing this 350 GeV limit are designated to a high-mass ggF signal region, thereby focusing on SM-like HH events. The selection of the 350 GeV threshold aims to maintain a balance between constraining κ_λ rigorously and retaining a large enough sample size in the low-mass region.

In a final layer of categorization, separate BDT classifiers are trained for each signal region using different HH signal hypotheses to achieve optimal separation from background

events. A detailed discussion of these multivariate analytical methods, including the list of input variables and hyperparameter optimization, is presented in Section 6.5. The adoption of this intricate categorization scheme is motivated and supported by a series of MVA training studies and fit analyses, comprehensively discussed in Sections 6.8.4.

6.3.5 Z+HF control region

The SHERPA Monte Carlo (MC) simulation is recognized to inadequately model the cross-section of Z boson production when in concert with heavy flavour (b, c) jets. Therefore, data-driven normalization is implemented within a designated control region, in alignment with the protocol established in the prior analytical cycle, as described in the internal note [182] and the preceding analysis round [177]. Given that jet production is decoupled from the Z boson's decay channel, a high-purity sample featuring $Z \rightarrow \mu\mu/ee$ coupled with heavy flavour jets is chosen. This sample is orthogonal to the selection criteria for signal regions and is used in the simultaneous fit to obtain data-based Z+HF normalization. The criteria delineating the Z+HF control region have been updated for this phase of the analysis, expounded in Section 6.3.5.1.

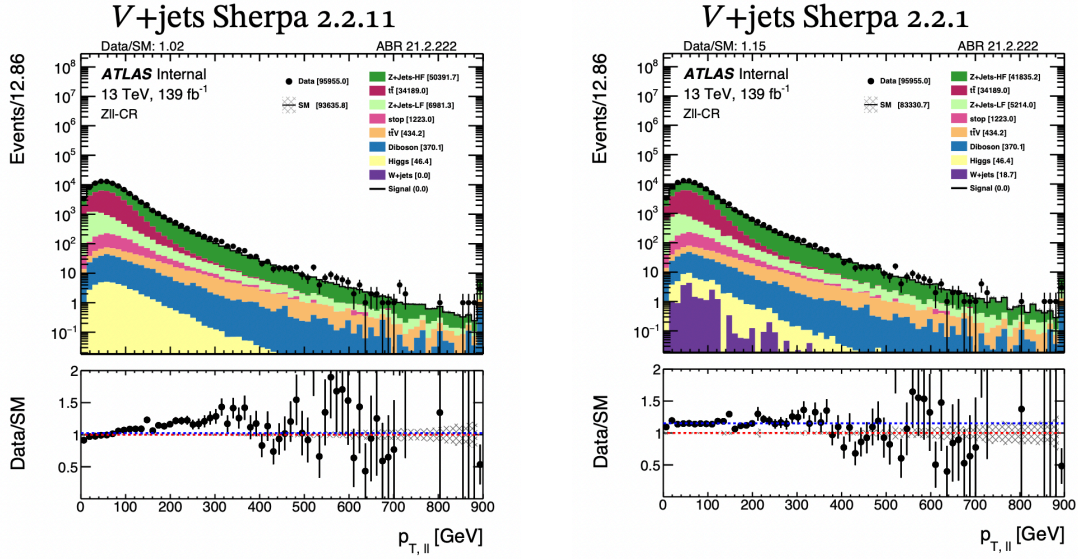
6.3.5.1 Redefinition of the Z+HF control region phase space

The cross-section for Z -boson production in conjunction with heavy-flavor jets (b, c) is often inaccurately predicted by the SHERPA MC. Therefore, normalization to data is performed in a designated control region from the previous analysis cycle [177]. Utilizing $Z \rightarrow \mu\mu/ee +$ heavy-flavor jets ensures a high-purity, orthogonal sample to the signal regions, allowing for data-driven Z+HF normalization.

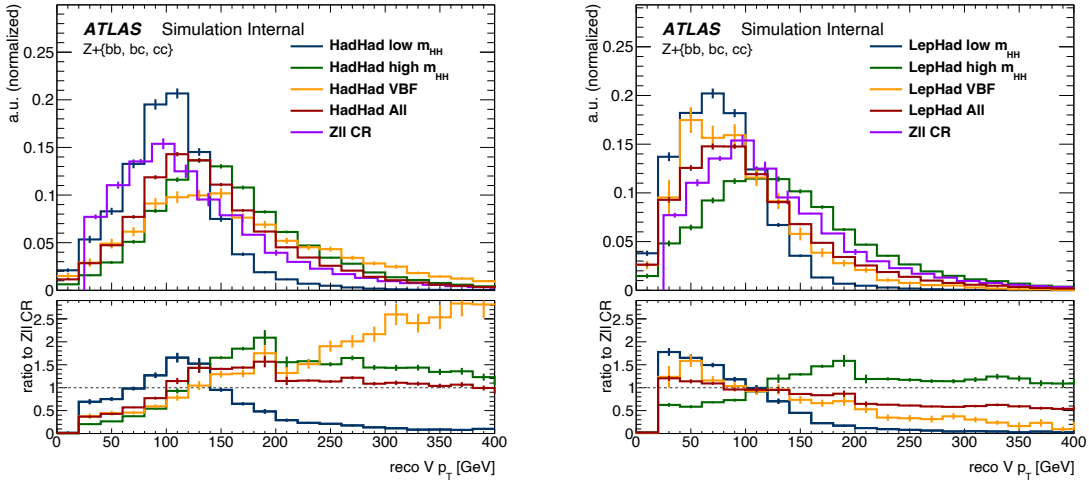
To mitigate phase-space extrapolation uncertainties between the SR and CR, adjustments have been made to the CR criteria. Event selection in the revamped control region is determined as follows:

- $b\bar{b}\ell\ell$ trigger selection using single-lepton and di-lepton triggers.
- Exactly two opposite-sign charged muons or electrons.
- Two b -tagged jets with DL1r tagger and 77% working point.
- $75 \text{ GeV} < m_{\ell\ell} < 110 \text{ GeV}$.
- $m_{bb} < 40 \text{ GeV}$ or $m_{bb} > 210 \text{ GeV}$.

¹ [ATL-COM-PHYS-2020-766](#)

Figure 6-6 Data/MC comparison in the prior $Z + HF$ control region.

- Leading b -jet $p_T > 45$ GeV.
- Lepton $p_T > 40$ GeV.

Figure 6-7 Comparison of $V p_T$ shapes between the SRs and the Z CR.

These refinements have brought the $V p_T$ distributions of the SR and CR into closer alignment, as shown in Figure 6-7. Subsequent analysis indicates a normalization factor for $Z+HF$ of 1.20 ± 0.05 , closely aligning with the 1.3 factor from prior analysis rounds. The impact of these changes on the systematic uncertainties and signal strength will be further elaborated.

6.3.5.2 Initial Normalization Coefficients

Equations 6-2 and 6-3 present the calculation for the pre-fit normalization constants μ_{Z+HF} . These constants are obtained for the Z+HF ($Z + (bb, bc, cc)$) terms within the Z+HF control region, computed via the ratio depicted in Equation 6-1¹.

$$\mu_{Z+HF} = \frac{\text{data} - (\text{sum of backgrounds} + Z(ee, \mu\mu) + HF + Z(\tau\tau) + HF)}{Z(ee, \mu\mu) + HF + Z(\tau\tau) + HF}. \quad (6-1)$$

The normalization constants are extracted using Equation 6-1 and are specifically detailed in Equations 6-2 and 6-3 for Sherpa 2.2.1 and Sherpa 2.2.11 configurations, respectively.

$$\mu_{Z+HF}^{\text{SHERPA2.2.1}} = \frac{(21458 - 18566.0578 + 9970.59 + 1.210)}{(9970.59 + 1.210)} \approx 1.29 \quad (6-2)$$

$$\mu_{Z+HF}^{\text{SHERPA2.2.11}} = \frac{(21458 - 18596.707 + 10837.434 + 1.309)}{(10837.434 + 1.309)} \approx 1.26 \quad (6-3)$$

For context, the Sherpa 2.2.11 normalization factor derived from the original Z+HF control region, unadjusted for the new cuts, stands at 1.05. The modification in the control region criteria brings the normalization factors of Sherpa 2.2.1 and Sherpa 2.2.11 into closer concordance.

6.3.5.3 Projection to Signal Regions

To account for the observed discrepancies in the V transverse momentum ($V p_T$) between the data and MC simulations, a specialized shape uncertainty is formulated. The uncertainty is quantified by the complete difference between the experimental data and the baseline MC estimations in varying bins of the reconstructed $V p_T$. This is documented in Figure 6-8.

Subsequently, this shape uncertainty is propagated to the Sherpa 2.2.11 predictions for Z+HF within the three signal regions, in relation to the true-level $p_T(\tau\tau)$. This variable is the closest analog to the reconstructed $V p_T$ assessed in the control region.

¹ The equation serves as an approximation attributing to the Z+HF background any data/MC discrepancies. In the full scope of the analysis, the mass distribution fit in the CR will normalize $t\bar{t}$ to data, encapsulating only excesses that align with the Z process.

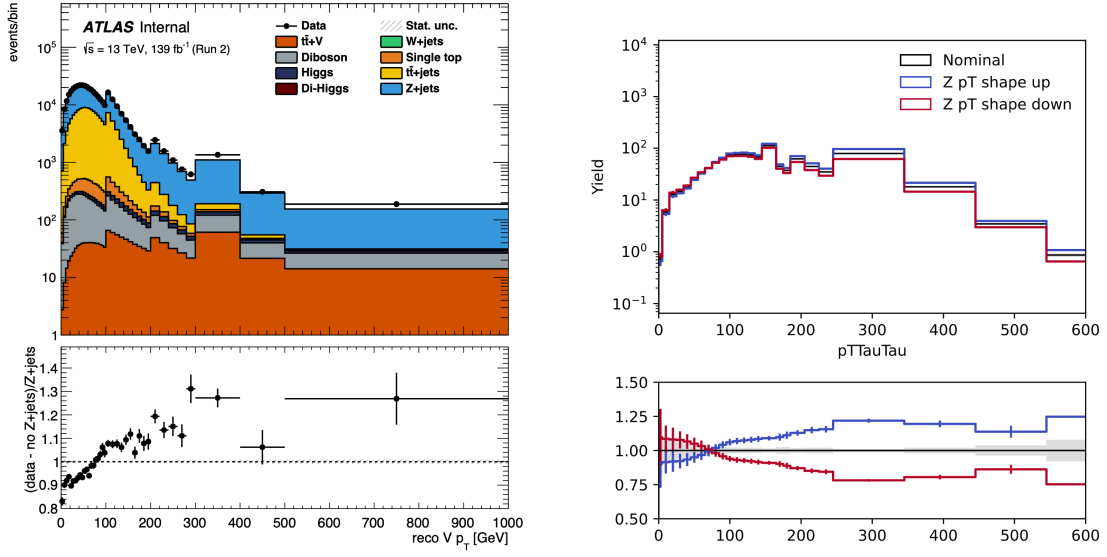


Figure 6–8 (a) Quantification of the V p_T shape uncertainty, representing the full discrepancy between data and nominal MC forecast in the Z CR. (b) The subsequent discrete parameterization of the shape uncertainty.

6.4 Background Modelling

Background estimation in our analysis utilizes a combination of simulation and data-driven techniques. Simulated event samples, as outlined in Section 6.2.2, provide the foundation for modeling most background processes. For fake- τ_{had} backgrounds, data-driven methods are employed differently across channels.

In the $\tau_{\text{lep}}\tau_{\text{had}}$ channel, an inclusive fake-factor method handles fake- τ_{had} contributions from $t\bar{t}$ and multi-jet processes. Conversely, in the $\tau_{\text{had}}\tau_{\text{had}}$ channel, we deploy a two-pronged approach: multi-jet backgrounds rely on a data-driven fake-factor method in Section 6.4.1, while $t\bar{t}$ backgrounds utilize scale-factors extracted from data to correct MC predictions in Section 6.4.2.

The separation of estimation methods for multi-jet and $t\bar{t}$ in $\tau_{\text{had}}\tau_{\text{had}}$ is necessitated by distinct fake- τ_{had} features and trigger selections in Section 6.3.2. Given the statistical limitations of the Run 2 dataset and the minor impact of fake- τ_{had} backgrounds on sensitivity, this segregated approach is justified.

Furthermore, templates for $t\bar{t}$ with true- τ_{had} and $Z + \text{HF}$ are MC-based but their normalizations are data-driven and integrated into the final fit model. Minor backgrounds arising from misidentified electrons or muons are treated in simulation and aligned with true- τ_{had} $t\bar{t}$

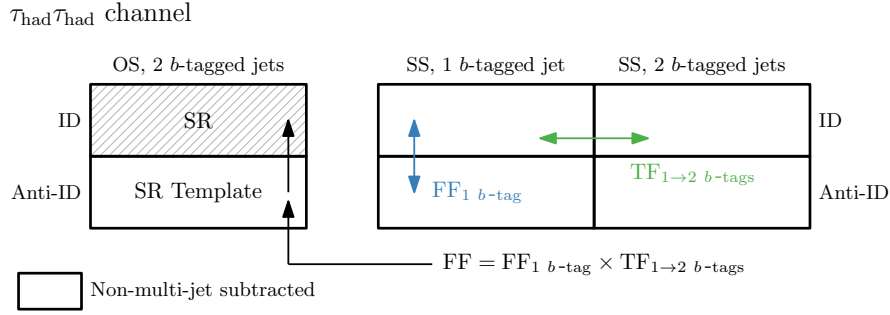


Figure 6–9 Schematic illustration of the application of the fake-factor method for estimating multi-jet backgrounds featuring fake- $\tau_{had-vis}$ in the $\tau_{had}\tau_{had}$ channel. In all control regions, non-multi-jet backgrounds are simulated and subsequently deducted from the observed data, as denoted by 'Subtracted Non-Multi-Jet Backgrounds' in the legend.

events^[177,182].

6.4.1 Multijet with fake- τ backgrounds in the $\tau_{had}\tau_{had}$ channel

In the $\tau_{had}\tau_{had}$ channel, the estimation of the multi-jet background employs a data-driven fake-factor approach, consistent with the methodology applied in preceding analyses of the $b\bar{b}\tau_{had}\tau_{had}$ ^[177,193]. The fake factors (FFs) used in the prior analysis^[177] are retained. The Monte Carlo settings' transition from SHERPA 2.2.1 to SHERPA 2.2.11 for the V +jets samples does not alter the multi-jet background calculations. The leading $\tau_{had} p_T$ distributions for each category in the 1-tag SS and 1-tag OS regions show that the new samples do not affect the estimation strategy. The different regions used for the multijet estimation are schematically depicted in Figure 6–9.

FFs are obtained in a control region with two $\tau_{had-vis}$ having same-sign charges, as a ratio of events with two loose τ_{had} to those with one loose and one anti- τ_{had} . FFs are computed separately for 1- and 3-prong τ_{had} , for STT and DTT trigger categories, and for the 0-, 1-, and 2-b-tag regions. Additionally, FFs are year-specific to consider changing τ_{had} identification criteria and trigger selections. Due to low statistics, the 1-b-tag FFs are used in the 2-b-tag region with appropriate transfer factors for corrections.

$$FF_i(p_T \tau_{had}^i, \eta \tau_{had}^i, N_{prong} \tau_{had}^i, \dots) = \frac{N_{data}(\text{loose } \tau_{had}^i) - N_{non-multijet MC}(\text{loose } \tau_{had}^i)}{N_{data}(\text{anti-}\tau_{had}^i) - N_{non-multijet MC}(\text{anti-}\tau_{had}^i)} \quad (6-4)$$

Two types of FFs, labeled as FF_0 and FF_1 , are then averaged. Their statistical compat-

ibility has been validated, and they are averaged with respect to their statistical significance in a given p_T bin.

$$FF_{\text{avg}}(p_T \tau_{\text{had}}, \eta \tau_{\text{had}}, N_{\text{prong}} \tau_{\text{had}}, \dots) = \frac{N_{\text{data}}(\text{loose } \tau_{\text{had}}) - N_{\text{non-multijet MC}}(\text{loose } \tau_{\text{had}})}{N_{\text{data}}(\text{anti-}\tau_{\text{had}}) - N_{\text{non-multijet MC}}(\text{anti-}\tau_{\text{had}})} \quad (6-5)$$

The final fake factors for $\tau_{\text{had}}\tau_{\text{had}}$ channel are shown in Figure 6-10.

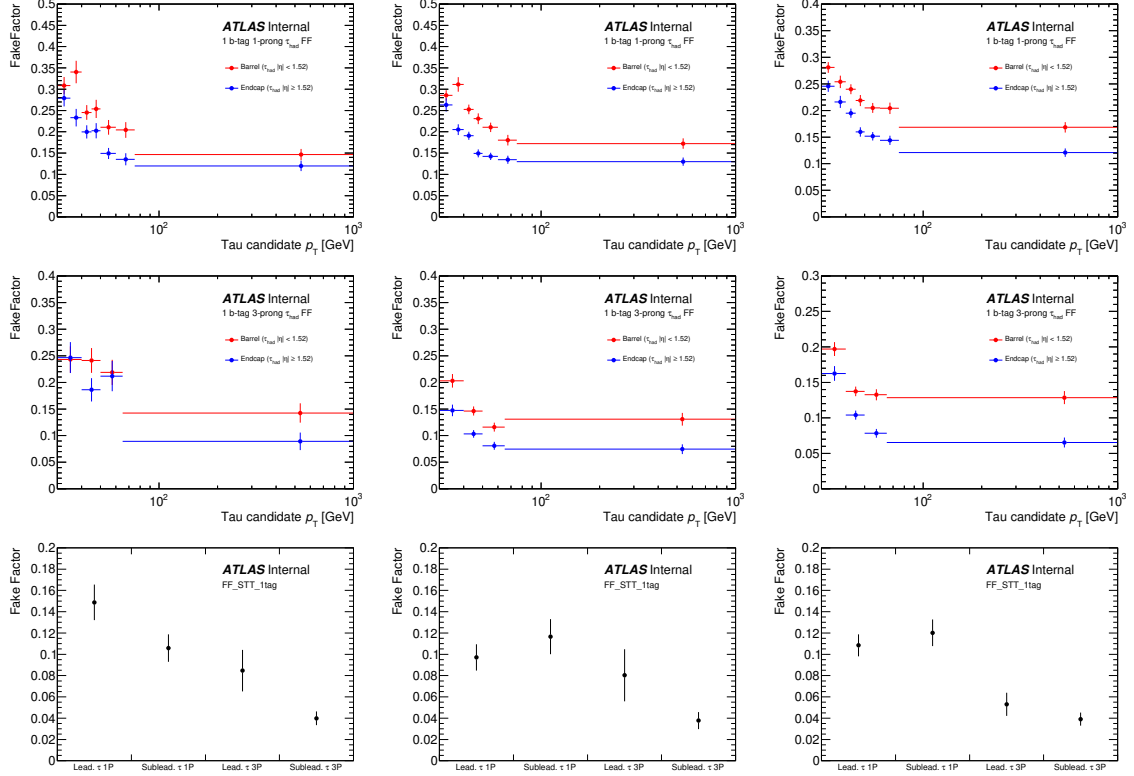


Figure 6-10 Fake factors for 1-prong DTT (top), 3-prong DTT (middle), and STT (bottom) for the data-taking periods 15-16 (left), 17 (centre), and 18 (right) for the di-Higgs $\tau_{\text{had}}\tau_{\text{had}}$ channel.

6.4.2 $t\bar{t}$ with fake- τ_{had} in the $\tau_{\text{had}}\tau_{\text{had}}$ channel with scale-factor method

The background events attributed to $t\bar{t}$ production that contain fake- $\tau_{\text{had-vis}}$ in the $\tau_{\text{had}}\tau_{\text{had}}$ channel are quantified through simulation. However, for enhanced accuracy, the misidentification efficiencies of fake- $\tau_{\text{had-vis}}$ are modified by data-derived SFs. A graphical overview of this methodology is portrayed in Figure 6-11.

The SFs are a function of the fake- $\tau_{\text{had-vis}}$ transverse momentum (p_T), segregated for 1-prong and 3-prong decay modes. A profile-likelihood fit to the transverse mass (m_T^W) dis-

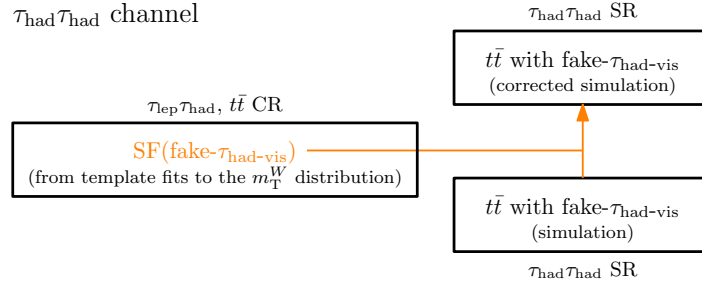


Figure 6-11 Illustrative summary of the data-corrected scale-factor technique employed for evaluating $t\bar{t}$ background containing fake- $\tau_{\text{had-vis}}$ in the $\tau_{\text{had}}\tau_{\text{had}}$ channel.

tribution effectively calibrates the SFs. Separate fitting processes are carried out for distinct trigger categories.

The numerical behavior of SFs varies with p_T : for 1-prong fake- $\tau_{\text{had-vis}}$, SFs are approximately 1 for p_T below 40 GeV and diminish to around 0.6 for p_T exceeding 70 GeV. For the 3-prong mode, the SFs are typically about 20% greater than their 1-prong counterparts.

To evaluate the $t\bar{t}$ background in the $\tau_{\text{had}}\tau_{\text{had}}$ SR, the simulation is scaled by the appropriate SFs for each fake- $\tau_{\text{had-vis}}$ in the event. Various uncertainties, including detector response and theoretical modeling, are accounted for during the likelihood fit for SF extraction.

The resulting covariance matrix, encompassing both statistical and systematic uncertainties, is diagonalized to produce independent nuisance parameters (NPs), which are subsequently propagated into the final signal extraction fit.

For the estimation of fake- $\tau_{\text{had-vis}}$ background from multi-jet processes, a considerable fraction of $t\bar{t}$ events containing at least one fake- $\tau_{\text{had-vis}}$ must be removed from the data in the opposite-sign 2- b -tagged-jet anti-identification (anti-ID) region to accurately gauge the multi-jet influence. The modelling of $t\bar{t}$ events in this region is corrected via data-derived SFs, obtained using a methodology similar to the one described.

6.5 Multivariate signal extraction

6.5.1 General MVA and optimisation strategy

The discriminant employed for isolating the signal is derived from a multivariate algorithm, as elaborated in Section 5.5.1. Distinct from the complete Run 2 data analysis cycle, Boosted Decision Trees (BDTs) are now utilized uniformly for both sub-channels in all cate-

gories, as specified in Section 6.3. An expanded set of predictor variables has been examined, and optimal hyperparameters have been selected to enhance the model's efficacy. Uniform training protocols are applied to both $\tau_{\text{had}}\tau_{\text{had}}$ and $\tau_{\text{lep}}\tau_{\text{had}}$ scenarios, utilizing a standardized training infrastructure [194] and based on the TMVA toolkit [95].

The training procedures have been specifically designed for various channels: $\tau_{\text{had}}\tau_{\text{had}}$, $\tau_{\text{lep}}\tau_{\text{had}}$ SLT, and $\tau_{\text{lep}}\tau_{\text{had}}$ LTT, as detailed in their respective sections. However, the focus of the ensuing discussion will be solely on the $\tau_{\text{had}}\tau_{\text{had}}$ channel.

6.5.1.1 Partitioning Technique for Model Validation

The architectural layout of the MVA approach necessitates a dependable and impartial forecast of the anticipated analytical sensitivity. This constraint dictates that the same events cannot be employed for both the calibration of the BDT (covering its hyperparameters and predictor variables) and the formulation of the histogram schematics for the resultant BDT scores.

A straightforward methodology fulfilling this stipulation is to subdivide the obtainable ensemble of simulated events into three equally-sized subsets. In this specific adaptation, the approach is executed based on the event identification number.

Model	Fold 0	Fold 1	Fold 2
	event_number %3 = 0	event_number %3 = 1	event_number %3 = 2
BDT 0	Training	Validation	Testing
BDT 1	Testing	Training	Validation
BDT 2	Validation	Testing	Training

Table 6–9 Demarcation of the simulated event pools used for the learning, fine-tuning, and scrutiny of the BDT algorithms.

Consequently, a trio of distinct BDT models are developed, each exploiting an individual subset of the available simulated data (referred to as Training folds) as outlined in Table 6–9. A consistent set of hyperparameters and predictor variables is applied across all trainings. These are ascertained through the maximization of BDT efficacy on the Validation folds, which remain unseen during the training phase.

The synthetic events encapsulated in the Testing folds contribute to the formation of the histogram fit blueprints. Intrinsically, these events are excluded from the BDT training steps,

thereby safeguarding an impartial forecast of the forthcoming analytical sensitivity.

6.5.1.2 Hyperparameter Tuning Strategy

The performance of the BDT is highly sensitive to specific training hyperparameters employed within TMVA. Two primary hyperparameters warrant special attention: the number of ensemble trees (NTrees) and the maximum depth of each individual tree (MaxDepth).

To optimize these hyperparameters effectively, a comprehensive grid search is undertaken. The search is implemented following the partitioning mechanism detailed in Section 6.5.1.1. Subsequently, the score distribution of the BDT output is analyzed, both for the signal and the aggregated backgrounds, utilizing the events within the validation subsets. (The bin structure is determined using the same algorithm that defines the binning for the likelihood fitting, as discussed in Section 6.7.2.) For performance assessment, the metric of binned signal significance is employed, given by

$$Z = \sqrt{\sum_{i \in \text{bins}} 2 \left((s_i + b_i) \log \left(1 + \frac{s_i}{b_i} \right) - s_i \right)}, \quad (6-6)$$

where s_i and b_i denote the yields of signal and background events in the i^{th} bin, respectively.

A defined hyperparameter space is explored, varying according to the specific analysis region and BDT variant. Bayesian optimization techniques are employed to favor hyperparameter configurations that yield elevated binned significance metrics.

The optimal hyperparameter set is identified from the ensemble of configurations evaluated during the tuning process, and utilized in the training, validation, and test phases.

6.5.1.3 Optimization of Feature Selection

For the $b\bar{b}\tau\tau$ system, many variables can help distinguish between different outcomes. However, using too many variables can make the model complex and less reliable. So, even though it's not a strict requirement, it's simpler and more effective to choose a limited but useful set of variables.

The feature selection procedure operates as follows:

- A set of "core" variables is invariably included. The specific constituents of this core set are BDT-dependent and will be detailed subsequently.

- Using a greedy algorithm, further variables are incrementally chosen from the remaining list based on their ability to enhance the binned signal significance, as quantified by Eq. 6-6, evaluated over the validation partitions.
- If adding a new variable doesn't improve the performance based on the validation data, then the variable that has the smallest negative impact on performance is included instead.
- The process terminates after N_p consecutive steps without a significant boost in significance.

Such a heuristic optimization strategy is prone to statistical noise, potentially distorting the variable selection. To mitigate this, the binned significance Z is calculated using a coarser binning scheme than that applied in the likelihood fitting procedure, as elaborated upon in a later section.

6.5.2 $\tau_{\text{had}}\tau_{\text{had}}$ MVAs

In total, four sets of BDTs are utilized in the $\tau_{\text{had}}\tau_{\text{had}}$ channel, described below.

6.5.2.1 BDT for ggF and VBF Classification

The purpose of the ggF/VBF distinction BDT is to segregate SM ggF HH events from SM VBF HH events (see Section 6.3.4 for details). The BDT employs only VBF preselected events in both its training and application phases. VBF preselected events are characterized as those having a minimum of two jets that are distinct from the $H \rightarrow b\bar{b}$ jets. Approximately 50% of ggF HH events and 80% of VBF HH events meet this VBF preselection criterion. The BDT is calibrated such that events resembling ggF have scores approaching 1.0, whereas events similar to VBF have scores nearing -1.0. A specific score threshold (or working point) is chosen to delineate events into the VBF category. The methodology for input variable selection and hyperparameter tuning for BDT training is elaborated upon in the following sections.

Input Variable Selection The performance trajectory of the BDT in ggF/VBF classification is visualized in Figure 6-12. The significance is calculated in accord with the binning methodology outlined in Section 6.7.2, albeit without imposing a minimum threshold on the number of background events per bin. Here, $z_s = z_b = 7$.

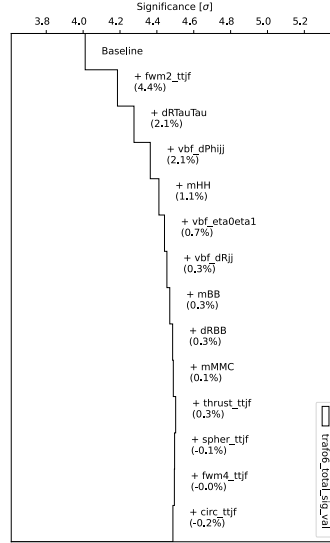


Figure 6-12 Performance progression of the ggF/VBF classification BDT as supplementary variables are incrementally appended to the baseline variables, which consist of m_{jj} and $\Delta\eta_{jj}$.

As a foundation, two variables, m_{jj} and $\Delta\eta_{jj}$, are selected. Ultimately, the seven most impactful variables are employed as BDT inputs. These include a Fox-Wolfram moment^[195], m_{HH} , $\Delta R_{\tau\tau}$, along with additional VBF-specific variables. A comprehensive listing of these input variables is provided in Table 6-10. Their respective distributions for the ggF and VBF HH signal events are illustrated in Figure 6-13.

Variable	Description
m_{HH}	Invariant mass of the HH system, reconstructed from the τ -lepton pair (using the MMC) and b -tagged jet pair
$\Delta R_{\tau\tau}$	The ΔR between the two visible τ decay products
$\text{VBF } \eta_0 \times \eta_1$	Product of the pseudorapidities of the leading and sub-leading VBF jets
$\Delta\eta_{jj}^{\text{VBF}}$	The $\Delta\eta$ between the two VBF jets
$\Delta\phi_{jj}^{\text{VBF}}$	The $\Delta\phi$ between the two VBF jets
m_{jj}^{VBF}	Invariant mass of the VBF jet system
$\text{fwm2}(\tau\tau jj)$	2 nd order Fox-Wolfram moment, taking into account the τ -lepton pair and central and forward jets

Table 6-10 Input variables used for the ggF/VBF BDT training in the $\tau_{\text{had}}\tau_{\text{had}}$ channel.

Hyperparameter Tuning In accordance with the method described in Section 6.5.1.2, we focus our optimization efforts on the principal hyperparameters NTrees and MaxDepth. Figure 6-14 illustrates how the binned significance, evaluated on the validation folds, varies with changes in these hyperparameters. Optimal parameter settings are identified by maximizing

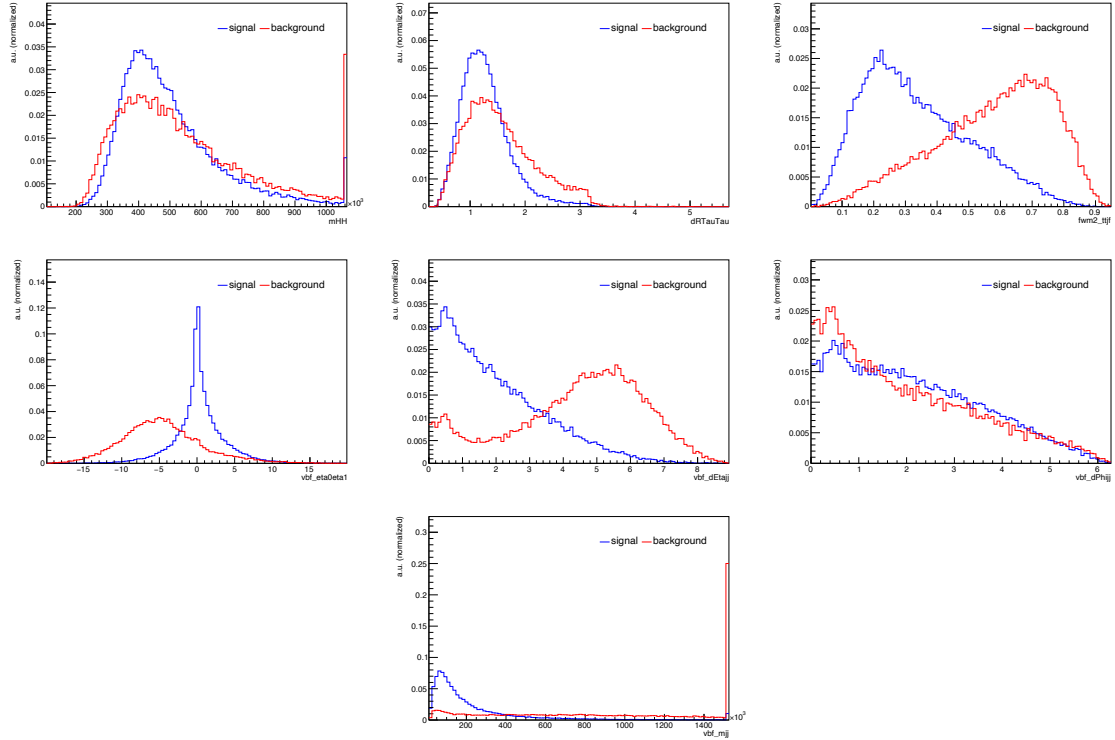


Figure 6–13 Histograms of input variables for the ggF/VBF BDT in the $\tau_{\text{had}}\tau_{\text{had}}$ channel, illustrating the distinction between ggF HH events (signal in blue) and VBF HH events (background in red).

this performance metric.

For the other hyperparameters, a marginal impact on the BDT’s performance is observed. Thus, they are assigned default values. A comprehensive enumeration of these hyperparameter choices is provided in Table [6–11](#).

Hyperparameter	Selected Value
NTrees	109
MaxDepth	6
MinNodeSize	1%
BoostType	GradBoost
IgnoreNegWeightsInTraining	True

Table 6–11 Chosen hyperparameters for the ggF/VBF BDT training in the $\tau_{\text{had}}\tau_{\text{had}}$ channel.

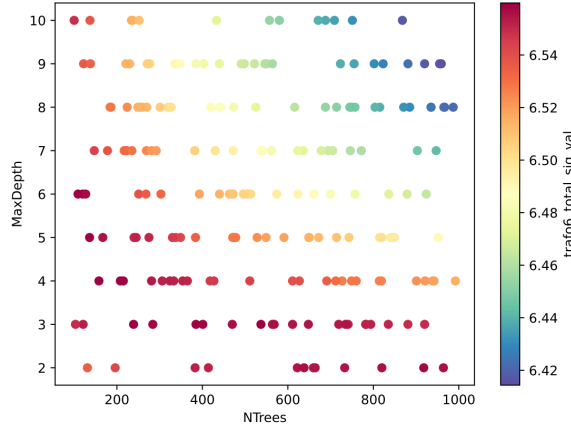


Figure 6-14 Variation of binned significance, as assessed on the validation partitions, with respect to the ensemble's tree count (NTrees) and each tree's maximum depth (MaxDepth).

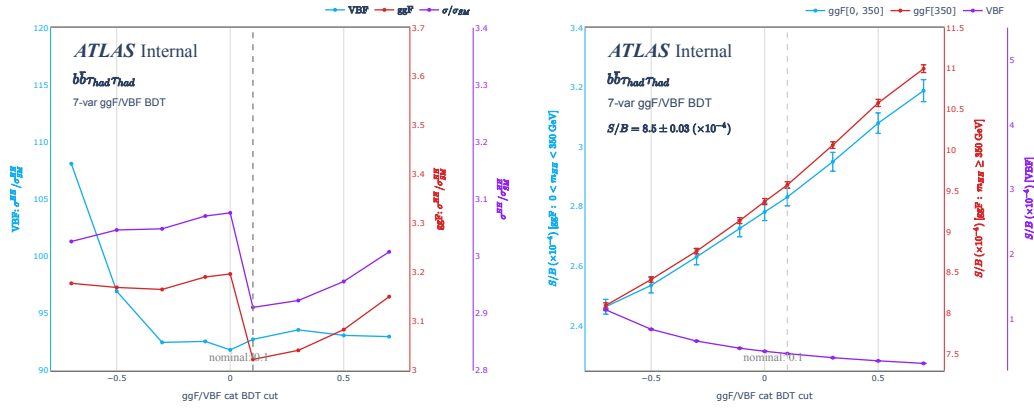


Figure 6-15 Dependence of HH signal strengths on the ggF vs VBF BDT cut value for the refined set of variables (left). The right figure shows the aggregate signal-to-background ratio also as a function of the cut value. A vertical dashed line marks the chosen cut value of 0.1.

Determination of Optimal Cut Threshold The SRs for ggF and VBF are demarcated by applying a threshold cut on the ggF/VBF classification BDT output. To identify the optimal cut threshold, we evaluate the analysis sensitivity across multiple potential cut values. Figure 6-15 illustrates the influence of the cut value on the ggF, VBF, and inclusive HH signal strengths (left), along with the overall signal-to-background ratio (right). These are computed via a likelihood fit incorporating the three analysis categories as well as the Z CR.

It should be noted that the discriminant scores used for this initial evaluation are derived from a provisional BDT training, prior to the application of the hyperparameter and input

variable optimization procedures outlined in earlier sections. Various tests have confirmed that subsequent retraining does not materially alter the resulting significance.

Based on these evaluations, a cut value of 0.1 is selected for optimal sensitivity to both ggF and VBF HH signals. Additional analyses are conducted to compare the sensitivity of this optimized method with a more basic strategy that employs only the baseline variables m_{jj} and $\Delta\eta_{jj}$.

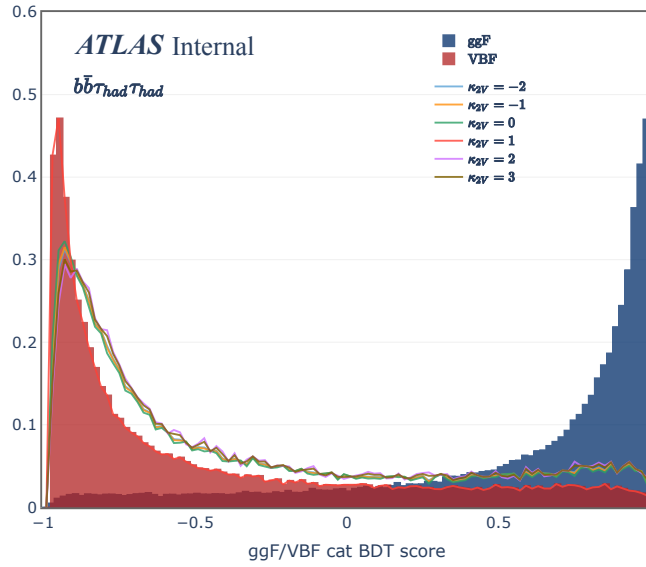


Figure 6–16 Distribution of ggF/VBF BDT scores for various VBF processes under signal region preselection conditions.

Score Distribution Analysis Figure 6–16 illustrates the score distributions for multiple VBF processes under the preselection criteria in the signal region, utilizing the seven-variable ggF/VBF BDT setup. The histograms filled in blue and red correspond to SM ggF and VBF HH events, respectively. Variations in κ_{2V} are represented by histograms in different colors. The robustness of the seven-variable ggF/VBF BDT in segregating ggF HH events from κ_{2V} fluctuations is thereby demonstrated. The absence of a significant systematic trend in the non-SM VBF samples underscores the stable categorization performance of the BDT for VBF events.

6.5.2.2 SR-Specific BDTs

Within each of the three SRs, specialized BDTs are constructed to distinguish HH signal from the aggregate of all SM backgrounds.

For the low- m_{HH} region, the BDT is trained utilizing ggF events with $\kappa_\lambda = 10$. Conversely, the high- m_{HH} region BDT employs the ggF SM signal sample for training. In both scenarios, training sets are restricted to events that meet the full SR criteria, including the previously applied ggF/VBF BDT cut.

The BDT aimed at the VBF region employs SM VBF HH signal events for its training. Importantly, events from both VBF and ggF SRs contribute to the training dataset to optimize statistical power. This approach has been verified to substantially enhance the VBF sensitivity when compared to training solely on VBF SR events.

Each BDT's hyperparameters and input variables are individually optimized for their respective regions. The resulting BDT scores are subsequently employed in a profile likelihood fit to derive the ultimate findings, elaborated in Section 6.8.

Hyperparameter Tuning for Signal Region BDTs The approach to hyperparameter optimization is akin to the methodology described in Section 6.5.2.1. The key hyperparameters NTrees and MaxDepth are specifically fine-tuned. The target for optimization is the binned validation significance, computed in accordance with the binning schema detailed in Section 6.7.2. The constraints for this are a minimum of 1.0 background events per bin, an upper limit on the MC background prediction's statistical uncertainty of 20%, and the use of $z_s = 10$ and $z_b = 5$.

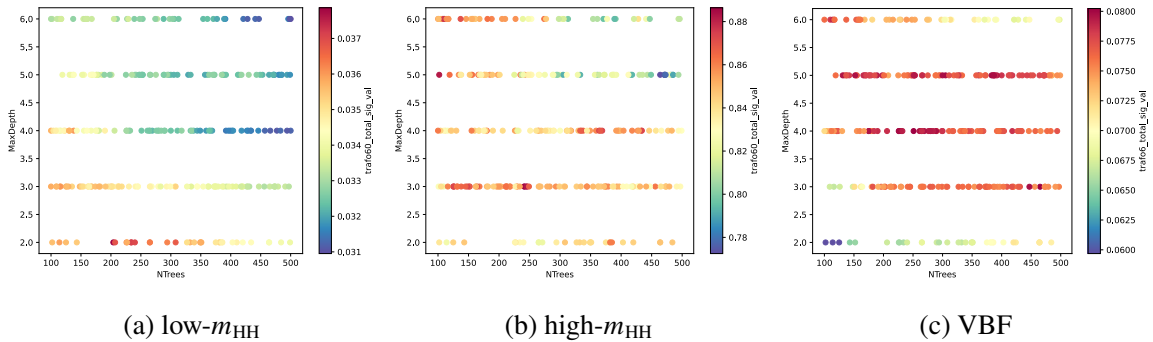


Figure 6–17 Impact of the NTrees and MaxDepth hyperparameters on the validation significance for the respective BDT training sets in the $\tau_{\text{had}}\tau_{\text{had}}$ channel.

Hyperparameter	low- m_{HH} ggF SR	high- m_{HH} ggF SR	VBF SR
NTrees	204	241	465
MaxDepth	2	3	3
MinNodeSize	1%	1%	1%
BoostType	Grad	Grad	Grad
Shrinkage	0.2	0.2	0.2
IgnoreNegWeightsInTraining	True	True	True

Table 6–12 Training hyperparameters chosen for the BDTs used in the three $\tau_{\text{had}}\tau_{\text{had}}$ analysis categories.

Figure 6–17 provides a visualization of how NTrees and MaxDepth affect this metric across the three distinct BDT sets. Optimal hyperparameters were chosen based on their ability to maximize the validation significance. The chosen parameters are cataloged in Table 6–12.

Optimization of Input Variables In line with the iterative optimization strategy delineated in Section 6.5.1.3, we begin with a set of five foundational variables: m_{jj} , m_{bb} , $m_{\tau\tau}^{\text{MMC}}$, ΔR_{bb} , and $\Delta R_{\tau\tau}$. Due to statistical constraints imposed by the limited size of the background MC datasets, we utilize a validation significance metric that employs a coarser binning, ensuring a minimum of 5.0 expected background events per bin. This is visualized alongside a finer binning strategy in Figures 6–18.

Especially in the high- m_{HH} regime, noticeable statistical fluctuations are apparent in the early optimization phases when employing the finer binning. These instabilities stabilize as more variables are incorporated. Ultimately, the top N predictors are chosen for the final model, where N is determined by the point at which performance stabilization is achieved in both binnings under investigation.

The finalized input sets for the individual BDTs are cataloged in Table 6–13, Table 6–14 and Table 6–15.

The subsequent illustrations present a characteristic ensemble of pre-fit MVA predictor variables for each signal region in the $\tau_{\text{had}}\tau_{\text{had}}$ channel. In these graphical representations, background adjustments are performed using scaling coefficients derived from a comprehen-

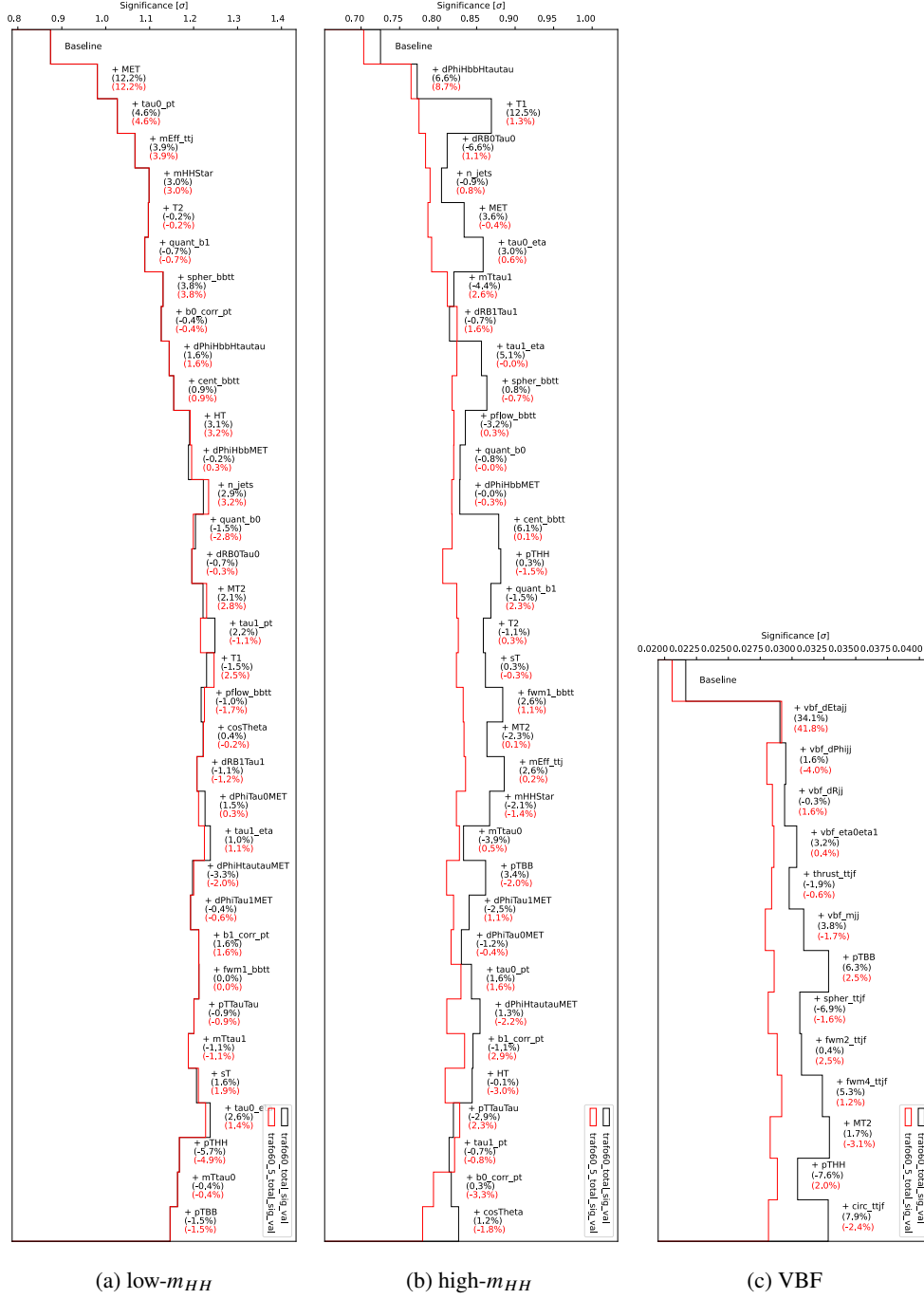


Figure 6–18 Trajectory of the validation significance as additional predictor variables are incorporated. The baseline set consists of m_{jj} , m_{bb} , $m_{\tau\tau}^{\text{MMC}}$, ΔR_{bb} , and $\Delta R_{\tau\tau}$. Red curves (trafo60_5_total_sig_val) represent binned significance with at least 5.0 expected background events per bin, whereas black curves (trafo60_total_sig_val) require only a minimum of 1.0 expected background events per bin.

Variable	Description
m_{HH}	Invariant mass of the HH system, reconstructed from the τ -lepton pair (using the MMC) and b -tagged jet pair
m_{bb}	Invariant mass of the b -tagged jet pair system
$m_{\tau\tau}^{MMC}$	Invariant mass of the τ -lepton pair system, calculated using the MMC
ΔR_{bb}	The ΔR between the two b -tagged jets
$\Delta R_{\tau\tau}$	The ΔR between the two $\tau_{had-vis}$
n_jets	Number of jets in the event
H_T	Total hadronic transverse energy in the event, perpendicular to the beamline
T_2	Topness, as defined in Ref. ^{Kim:2018xf} assuming $\sigma_t = 15$ GeV and $\sigma_W = 5$ GeV
E_T^{miss}	The missing transverse momentum of the event
M_{T2}	Stranverse mass, as defined in Ref. ^{Lester_1999}
$p_T(\tau_0)$	Transverse momentum of the leading $\tau_{had-vis}$
$p_T(\tau_1)$	Transverse momentum of the sub-leading $\tau_{had-vis}$
$p_T(b_0)$	Transverse momentum of the leading b -tagged jet
$\Delta\phi(bb, E_T^{miss})$	The $\Delta\phi$ between the b -tagged jet pair system and missing transverse energy
$\Delta\phi(bb, \tau\tau)$	The $\Delta\phi$ between the b -tagged jet pair and τ -lepton pair systems
quant b_0	b -tagging quantile of leading b -tagged jet
quant b_1	b -tagging quantile of sub-leading b -tagged jet
m_{HH}^*	Reduced 4-object invariant mass, defined as $m_{HH}^* = m_{HH} - m_{bb} - m_{\tau\tau}^{MMC} + 250$ GeV
$\Delta R(b_0, \tau_0)$	The ΔR between the leading b -tagged jet and $\tau_{had-vis}$
cent($bb\tau\tau$)	Centrality, taking into account only the HH decay products
$m_{eff}(\tau\tau j)$	Effective mass, taking into account the τ -lepton pair and central jets
spher($bb\tau\tau$)	Sphericity, taking into account only the HH decay products
$\eta(\tau_0)$	Pseudorapidity of the leading $\tau_{had-vis}$
$\eta(\tau_1)$	Pseudorapidity of the sub-leading $\tau_{had-vis}$

Table 6–13 Input variables used for the low- m_{HH} ggF BDT training in the $\tau_{had}\tau_{had}$ channel.

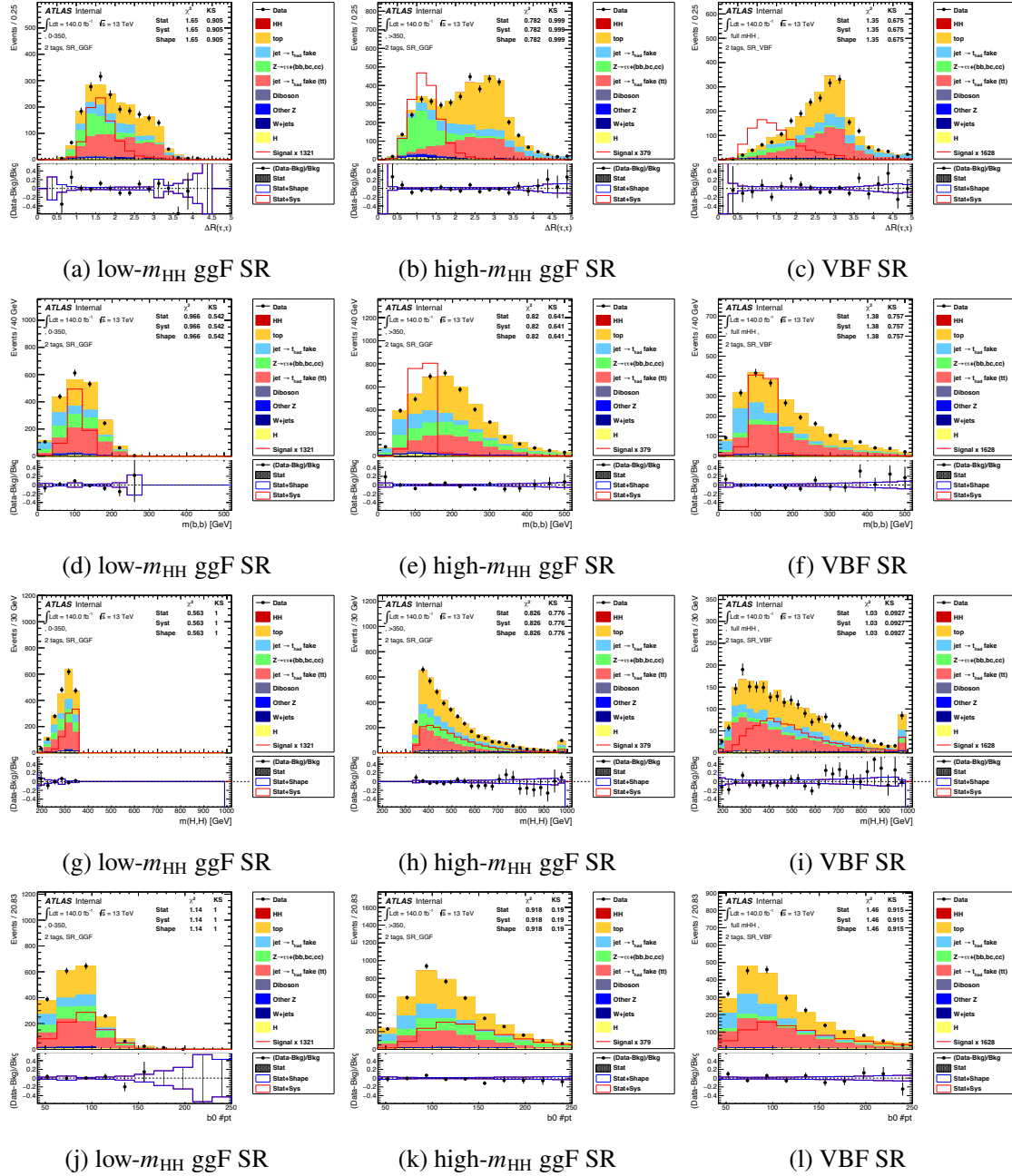
sive fit to empirical data. Figure 6–19 delineates the distribution of essential variables across the triad of signal regions. Concurrently, Figure 6–20 introduces novel variables specifically tailored for the discrimination of signal from background through BDT in each designated region. Lastly, Figure 6–21 showcases the BDT employed for the stratification between ggF and VBF signal domains, restricting the analysis to events featuring a minimum of four jets.

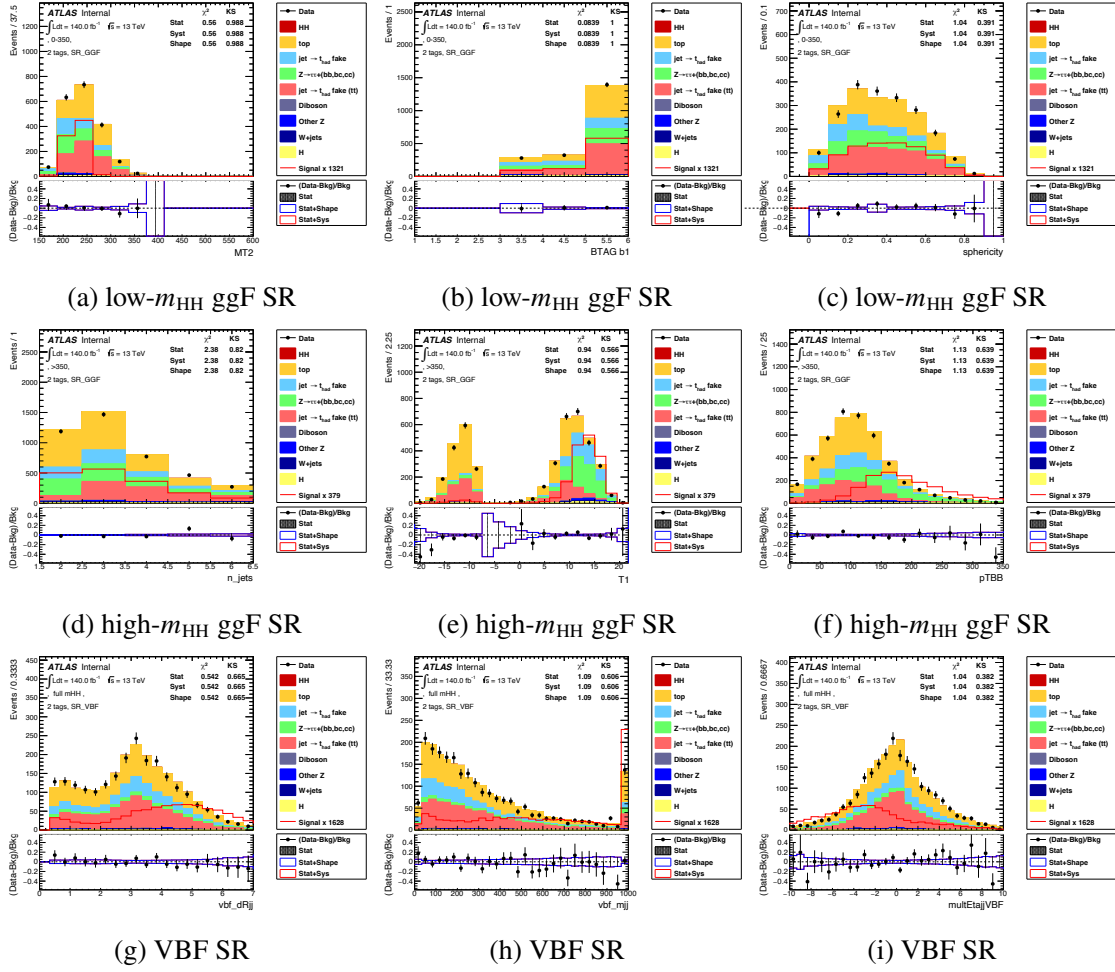
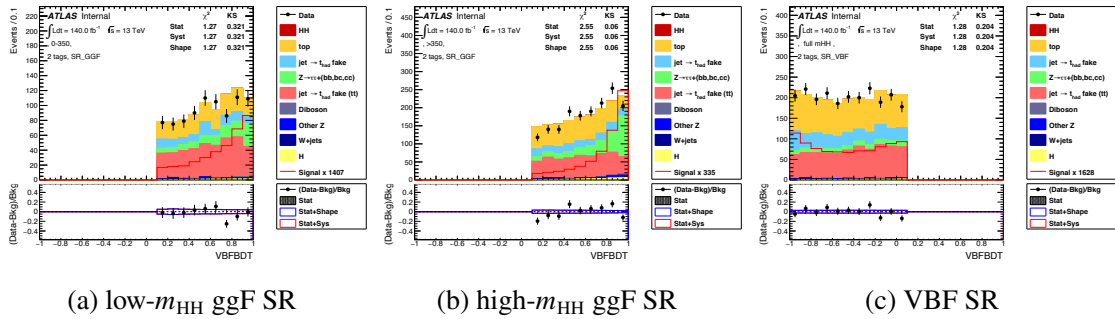
Variable	Description
m_{HH}	Invariant mass of the HH system, reconstructed from the τ -lepton pair (using the MMC) and b -tagged jet pair
m_{bb}	Invariant mass of the b -tagged jet pair system
$m_{\tau\tau}^{\text{MMC}}$	Invariant mass of the τ -lepton pair system, calculated using the MMC
ΔR_{bb}	The ΔR between the two b -tagged jets
$\Delta R_{\tau\tau}$	The ΔR between the two $\tau_{\text{had-vis}}$
n_jets	Number of jets in the event
T_1	Topness, as defined in Ref. Kim:2018cxf assuming $\sigma_t = 5$ GeV and $\sigma_W = 5$ GeV.
E_T^{miss}	The missing transverse momentum of the event
$p_T(HH)$	Transverse momentum of the HH system
$m_T(\tau_1)$	Transverse mass of the sub-leading $\tau_{\text{had-vis}}$
$\Delta\phi(bb, E_T^{\text{miss}})$	The $\Delta\phi$ between the b -tagged jet pair system and missing transverse energy
$\Delta\phi(bb, \tau\tau)$	The $\Delta\phi$ between the b -tagged jet pair and τ -lepton pair systems
quant b_0	b -tagging quantile of leading b -tagged jet
quant b_1	b -tagging quantile of sub-leading b -tagged jet
$\Delta R(b_0, \tau_0)$	The ΔR between the leading b -tagged jet and $\tau_{\text{had-vis}}$
$\Delta R(b_1, \tau_1)$	The ΔR between the sub-leading b -tagged jet and $\tau_{\text{had-vis}}$
cent($bb\tau\tau$)	Centrality, taking into account only the HH decay products
spher($bb\tau\tau$)	Sphericity, taking into account only the HH decay products
pflow($bb\tau\tau$)	Planar flow, taking into account only the HH decay products
$\eta(\tau_0)$	Pseudorapidity of the leading $\tau_{\text{had-vis}}$
$\eta(\tau_1)$	Pseudorapidity of the sub-leading $\tau_{\text{had-vis}}$

Table 6–14 Input variables used for the high- m_{HH} ggF BDT training in the $\tau_{\text{had}}\tau_{\text{had}}$ channel.

Variable	Description
m_{HH}	Invariant mass of the HH system, reconstructed from the τ -lepton pair (using the MMC) and b -tagged jet pair
m_{bb}	Invariant mass of the b -tagged jet pair system
$m_{\tau\tau}^{\text{MMC}}$	Invariant mass of the τ -lepton pair system, calculated using the MMC
ΔR_{bb}	The ΔR between the two b -tagged jets
$\Delta R_{\tau\tau}$	The ΔR between the two visible τ decay products
VBF $\eta_0 \times \eta_1$	Product of the pseudorapidities of the leading and sub-leading VBF jets
$\Delta\eta_{jj}^{\text{VBF}}$	The $\Delta\eta$ between the two VBF jets
$\Delta\phi_{jj}^{\text{VBF}}$	The $\Delta\phi$ between the two VBF jets
$\Delta R_{jj}^{\text{VBF}}$	The ΔR between the two VBF jets
m_{jj}^{VBF}	Invariant mass of the VBF jet system
thrust($\tau\tau jj$)	Thrust, taking into account the τ -lepton pair and central and forward jets
circ($\tau\tau jj$)	Circularity, taking into account the τ -lepton pair and central and forward jets
$\eta(\tau_0)$	Pseudorapidity of the leading $\tau_{\text{had-vis}}$
$\eta(\tau_1)$	Pseudorapidity of the sub-leading $\tau_{\text{had-vis}}$

Table 6–15 Input variables used for the VBF BDT training in the $\tau_{\text{had}}\tau_{\text{had}}$ channel.

Figure 6-19 Representative set of pre-fit MVA input variable distributions in the $\tau_{had}\tau_{had}$ SRs.

Figure 6–20 Representative set of pre-fit MVA input variable distributions in the $\tau_{had}\tau_{had}$ SRs.Figure 6–21 Categorisation BDT variable distributions in the $\tau_{had}\tau_{had}$ SRs.

BDT Score Distribution Components Figure 6-23 displays the constituent background yields in the bins most indicative of the signal, based on the binning scheme employed within the likelihood fitting procedure. Comprehensive enumerations of prefit background yields across all three SRs are itemized in Tables 6-16, 6-17 and 6-18.

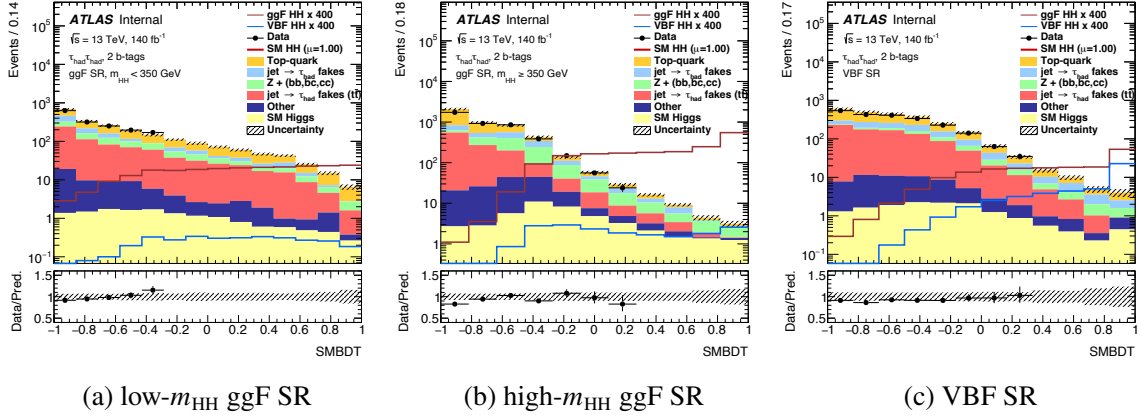


Figure 6-22 Pre-fit BDT score distributions in the $\tau_{had}\tau_{had}$ signal regions.

In specific scenarios, such as for the QCD fake background in the most signal-like bin within the high- m_{HH} SR, a prefit background projection may yield a negative value accompanied by significant statistical uncertainty. These negative yields pose no issue; they are adjusted to zero during the generation of the fitting workspace, with the corresponding uncertainties accurately integrated into the constraint term for the Beeston-Barlow nuisance parameter (NP) specific to that bin.

Figure 6-22 illustrates the comparison between the data and model predictions for prefit BDT scores within the $\tau_{had}\tau_{had}$ SRs. These regions are presently subject to blinding in the

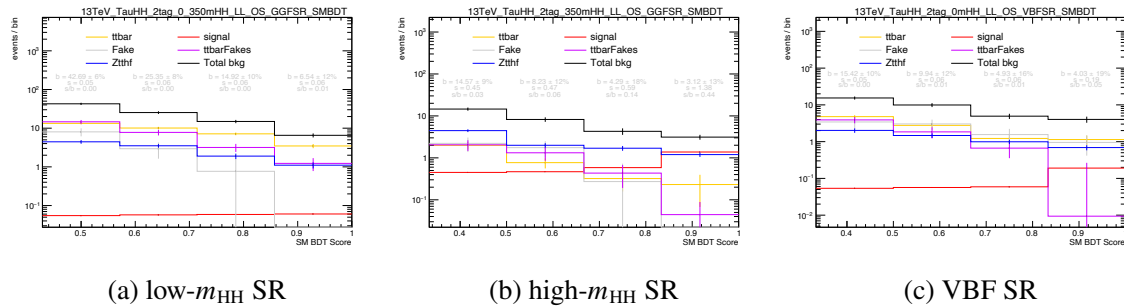


Figure 6-23 Prefit yields of the main background components, the total signal, as well as the total background in the most signal-like BDT bins in the $\tau_{had}\tau_{had}$ SRs.

Sample	Highest bin	2nd-highest bin	3rd-highest bin	4th-highest bin
Fake	0.000 ± 0.268	0.272 ± 0.456	1.753 ± 0.741	2.215 ± 0.838
ggFHtautau	0.438 ± 0.093	0.338 ± 0.090	0.324 ± 0.082	0.370 ± 0.090
ttbar	0.231 ± 0.164	0.321 ± 0.163	0.769 ± 0.209	1.987 ± 0.389
ttH	0.246 ± 0.022	0.303 ± 0.024	0.369 ± 0.027	0.457 ± 0.030
ttZ	0.012 ± 0.010	0.059 ± 0.012	0.064 ± 0.014	0.095 ± 0.020
ttW	0.011 ± 0.007	0.002 ± 0.002	0.010 ± 0.006	0.018 ± 0.008
VBFHtautau	0.019 ± 0.008	0.036 ± 0.009	0.031 ± 0.009	0.048 ± 0.011
WHtautau	0.000 ± 0.000	0.000 ± 0.000	0.015 ± 0.015	0.012 ± 0.012
qqZHtautau	0.303 ± 0.043	0.330 ± 0.043	0.305 ± 0.041	0.539 ± 0.056
WHbb	0.002 ± 0.001	0.002 ± 0.001	0.002 ± 0.001	0.001 ± 0.001
ggZHbb	0.031 ± 0.004	0.045 ± 0.004	0.061 ± 0.005	0.129 ± 0.008
qqZHbb	0.079 ± 0.004	0.091 ± 0.005	0.138 ± 0.006	0.242 ± 0.008
ggZHtautau	0.126 ± 0.023	0.120 ± 0.022	0.150 ± 0.025	0.185 ± 0.028
W	0.000 ± 0.000	0.000 ± 0.000	0.000 ± 0.000	0.000 ± 0.040
Wtt	0.000 ± 0.000	0.000 ± 0.444	0.097 ± 0.097	0.295 ± 0.222
ttbarFakes	0.044 ± 0.044	0.433 ± 0.241	1.321 ± 0.470	2.047 ± 0.585
Zhf	0.000 ± 0.000	0.012 ± 0.012	0.000 ± 0.023	0.021 ± 0.021
Zlf	0.000 ± 0.000	0.000 ± 0.000	0.000 ± 0.000	0.000 ± 0.000
Ztthf	1.197 ± 0.146	1.698 ± 0.223	1.995 ± 0.247	4.461 ± 0.341
Zttlf	0.024 ± 0.016	0.009 ± 0.036	0.412 ± 0.283	0.166 ± 0.058
stop	0.267 ± 0.190	0.192 ± 0.150	0.405 ± 0.238	0.914 ± 0.470
diboson	0.092 ± 0.064	0.028 ± 0.029	0.009 ± 0.065	0.367 ± 0.148
signal	1.379 ± 0.010	0.585 ± 0.006	0.467 ± 0.006	0.450 ± 0.006
bkg	3.124 ± 0.417	4.292 ± 0.759	8.233 ± 1.018	14.569 ± 1.274

Table 6–16 Prefit yields of the individual background components and the total ggF+VBF HH signal (labelled signal) in the four most signal-like BDT bins, shown for the $\tau_{\text{had}}\tau_{\text{had}}$ high- m_{HH} region.

most sensitive bins, as elaborated in Section 6.7.3.

Sample	Highest bin	2nd-highest bin	3rd-highest bin	4th-highest bin
Fake	0.000 ± 0.364	0.767 ± 0.858	2.945 ± 1.319	8.037 ± 1.881
ggFHtautau	0.009 ± 0.007	0.117 ± 0.057	0.046 ± 0.033	0.112 ± 0.052
ttbar	3.472 ± 0.430	7.141 ± 0.568	10.091 ± 0.723	13.307 ± 0.773
ttH	0.146 ± 0.017	0.177 ± 0.018	0.196 ± 0.019	0.213 ± 0.020
ttZ	0.004 ± 0.005	0.025 ± 0.010	0.041 ± 0.024	0.052 ± 0.018
ttW	0.000 ± 0.005	0.022 ± 0.009	0.010 ± 0.007	0.032 ± 0.010
VBFHtautau	0.000 ± 0.000	0.006 ± 0.003	0.014 ± 0.006	0.010 ± 0.005
WHtautau	0.000 ± 0.000	0.010 ± 0.008	0.000 ± 0.000	0.000 ± 0.000
qqZHtautau	0.061 ± 0.019	0.052 ± 0.017	0.139 ± 0.028	0.106 ± 0.025
WHbb	0.000 ± 0.000	0.001 ± 0.001	0.000 ± 0.000	0.010 ± 0.006
ggZHbb	0.005 ± 0.001	0.011 ± 0.002	0.011 ± 0.002	0.015 ± 0.002
qqZHbb	0.031 ± 0.006	0.061 ± 0.009	0.068 ± 0.009	0.093 ± 0.011
ggZHtautau	0.012 ± 0.007	0.008 ± 0.005	0.012 ± 0.007	0.027 ± 0.011
W	0.000 ± 0.000	0.000 ± 0.000	0.000 ± 0.000	0.000 ± 0.000
Wtt	0.000 ± 0.000	0.517 ± 0.517	0.104 ± 0.104	0.049 ± 0.049
ttbarFakes	1.230 ± 0.451	3.176 ± 0.748	7.782 ± 1.284	14.618 ± 1.690
Zhf	0.009 ± 0.009	0.000 ± 0.011	0.000 ± 0.000	0.000 ± 0.000
Zlf	0.000 ± 0.000	0.000 ± 0.000	0.000 ± 0.000	0.000 ± 0.000
Ztthf	1.105 ± 0.195	1.896 ± 0.306	3.510 ± 0.374	4.443 ± 0.487
Zttlf	0.028 ± 0.019	0.281 ± 0.169	0.124 ± 0.065	0.152 ± 0.075
stop	0.346 ± 0.206	0.563 ± 0.282	0.101 ± 0.101	1.301 ± 0.436
diboson	0.081 ± 0.044	0.092 ± 0.081	0.157 ± 0.065	0.113 ± 0.066
signal	0.061 ± 0.002	0.059 ± 0.002	0.057 ± 0.002	0.055 ± 0.002
bkg	6.540 ± 0.777	14.922 ± 1.448	25.352 ± 2.021	42.689 ± 2.727

Table 6–17 Prefit yields of the individual background components and the total ggF+VBF HH signal (labelled signal) in the four most signal-like BDT bins, shown for the $\tau_{\text{had}}\tau_{\text{had}}$ low- m_{HH} region.

Sample	Highest bin	2nd-highest bin	3rd-highest bin	4th-highest bin
Fake	0.952 ± 0.535	1.556 ± 0.668	3.030 ± 0.935	3.430 ± 1.135
ggFHtautau	0.171 ± 0.064	0.064 ± 0.031	0.123 ± 0.054	0.182 ± 0.060
ttbar	1.140 ± 0.323	1.222 ± 0.220	2.773 ± 0.364	4.789 ± 0.460
ttH	0.124 ± 0.016	0.094 ± 0.014	0.154 ± 0.017	0.228 ± 0.021
ttZ	0.014 ± 0.007	0.022 ± 0.012	0.049 ± 0.016	0.103 ± 0.016
ttW	0.002 ± 0.002	0.000 ± 0.000	0.015 ± 0.016	0.038 ± 0.018
VBFHtautau	0.037 ± 0.009	0.016 ± 0.006	0.025 ± 0.008	0.047 ± 0.011
WHtautau	0.014 ± 0.014	0.000 ± 0.000	0.000 ± 0.000	0.000 ± 0.000
qqZHtautau	0.015 ± 0.009	0.000 ± 0.000	0.022 ± 0.011	0.018 ± 0.010
ggZHbb	0.017 ± 0.003	0.016 ± 0.003	0.028 ± 0.003	0.036 ± 0.004
qqZHbb	0.009 ± 0.002	0.010 ± 0.002	0.010 ± 0.002	0.021 ± 0.003
ggZHtautau	0.056 ± 0.016	0.027 ± 0.010	0.026 ± 0.010	0.020 ± 0.009
W	0.000 ± 0.017	0.000 ± 0.000	0.000 ± 0.000	0.000 ± 0.000
Wtt	0.083 ± 0.071	0.000 ± 0.000	0.175 ± 0.175	0.052 ± 0.160
WHbb	0.000 ± 0.000	0.001 ± 0.001	0.000 ± 0.000	0.000 ± 0.000
ttbarFakes	0.009 ± 0.256	0.666 ± 0.311	1.843 ± 0.614	3.902 ± 0.752
Zhf	0.000 ± 0.000	0.000 ± 0.000	0.000 ± 0.000	0.000 ± 0.000
Zlf	0.000 ± 0.000	0.000 ± 0.000	0.000 ± 0.000	0.000 ± 0.000
Zthf	0.690 ± 0.110	0.992 ± 0.134	1.469 ± 0.214	2.021 ± 0.285
Ztlf	0.161 ± 0.075	0.003 ± 0.018	0.167 ± 0.079	0.150 ± 0.073
stop	0.342 ± 0.243	0.141 ± 0.141	0.000 ± 0.000	0.305 ± 0.216
diboson	0.189 ± 0.189	0.102 ± 0.075	0.024 ± 0.024	0.076 ± 0.043
signal	0.191 ± 0.003	0.059 ± 0.002	0.057 ± 0.002	0.054 ± 0.002
bkg	4.025 ± 0.761	4.931 ± 0.798	9.935 ± 1.213	15.418 ± 1.494

Table 6–18 Prefit yields of the individual background components and the total ggF+VBF HH signal (labelled signal) in the four most signal-like BDT bins, shown for the $\tau_{\text{had}}\tau_{\text{had}}$ VBF region.

6.5.2.3 ggF and VBF Classification: MVA versus Cut-Based

To systematically assess the benefits of utilizing a BDT for differentiating ggF and VBF HH processes in contrast to a basic cut-based methodology, the BDT in question is retrained. This retraining also involves a hyperparameter optimization and is restricted to two parameters, m_{jj}^{VBF} and $\Delta\eta_{jj}^{\text{VBF}}$, thereby mimicking the cut-based method. This is juxtaposed with a 7-var BDT and a legacy 15-var BDT, which included variables unsuitable for VBF HH characterization and was consequently supplanted.

Figure 6-24 exhibits a comparative analysis of the 2-var and 7-var ggF/VBF configurations, focusing on HH signal strengths and signal-to-background ratios¹. The evaluations span across all three signal regions and vary with BDT thresholds. The low- m_{HH} and high- m_{HH} regions are color-coded in blue and red, respectively, and the VBF region is denoted in purple. A nominal BDT threshold of 0.1 is indicated by a dashed grey line. It is observed that the 2-var BDT yields superior signal-to-background ratio in the VBF region at the nominal point, while the 7-var BDT performs more effectively in the ggF regions.

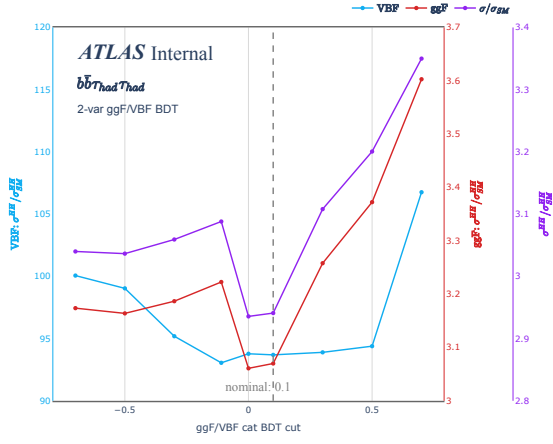
Table 6-19 presents a comparative summary of the 15-var BDT, implemented at the stage of EB request, against the 2-var and 7-var BDTs, discussing the ultimate evaluation metrics (95% CL upper boundaries as well as κ_λ and κ_{2V} intervals).

	95% CL Upper Limits on Signal Strength			95% CL Intervals	
	μ_{HH}	μ_{ggF}^{2D}	μ_{VBF}^{2D}	κ_λ	κ_{2V}
15-var BDT	2.92	3.04	90	11.19	2.85
2-var BDT	3.08 (5%)	3.22 (6%)	93.05 (3%)	11.29 (0.9%)	2.91(2%)
7-var BDT	2.90 (-0.7%)	3.01 (-1%)	93.56 (4%)	11.27 (0.7%)	2.92 (2%)

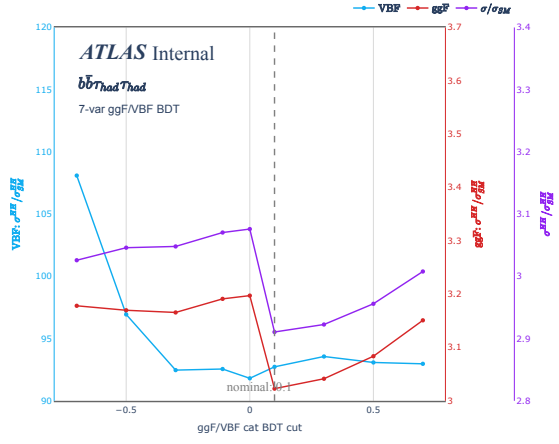
Table 6-19 Comparison of BDT configurations for ggF/VBF in relation to the ultimate fit outcomes. These limits are derived from a fit that incorporates solely floating normalizations and MC statistical uncertainties. A consistent BDT threshold of 0.1 is employed across all scenarios. The percentage enhancement relative to the 15-var BDT outcome is indicated in parentheses.

Eliminating variables with low sensitivity to the VBF HH process yields minimal impact on the BDT's effectiveness. Notably, a performance enhancement is evident when contrasting the 2-var ggF/VBF BDT with its 7-var counterpart. Consequently, the 7-var BDT is chosen

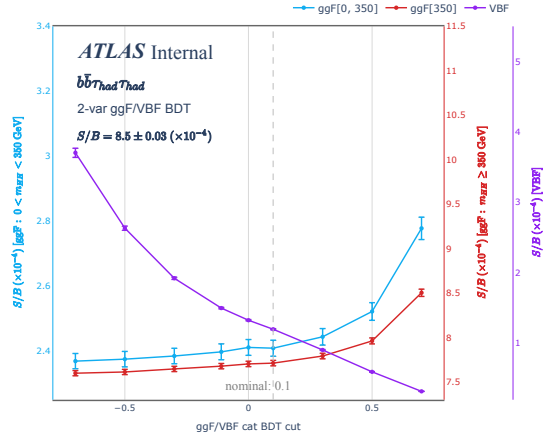
¹ The ggF HH process is viewed as the signal in ggF SRs, while the VBF HH is for the VBF SR.



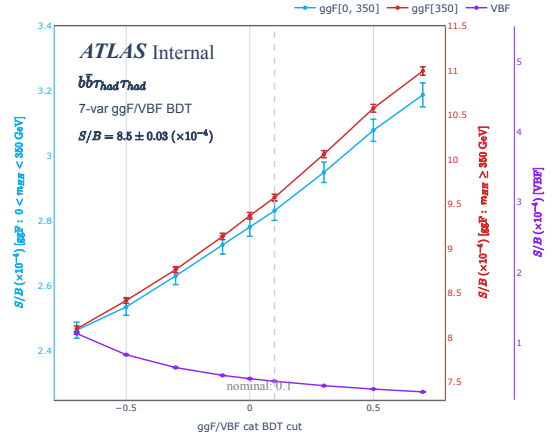
(a) Sensitivity: 2-var



(b) Sensitivity: 7-var



(c) Inclusive S/B: 2-var



(d) Inclusive S/B: 7-var

Figure 6–24 Top row: Sensitivity as a function of the cut on the ggF vs VBF classification BDT for different variable sets. Bottom row: Inclusive S/B as a function of the cut on the ggF vs VBF classification BDT for different variable sets.

for classification tasks.

6.6 Systematic uncertainties

The dominant uncertainty in our analysis arises from the limited dataset. Nonetheless, systematic uncertainties affecting both signal and background estimates cannot be overlooked. For details on detector-response-based uncertainties in object selection and reconstruction, readers are referred to our previous study^[177].

We apply the Beeston-Barlow method in a simplified form to model statistical uncertainties in background predictions^[196]. A luminosity uncertainty of 0.8% is applied, derived from LUCID-2 measurements^[154,197].

For processes reliant on MC simulations, various sources of theoretical uncertainties are studied. The BDT shape variations are handled through a specific rebinning algorithm, emphasizing statistically significant variations. Details of these procedures and criteria are elaborated in Section 6.5.

Uncertainties related to $t\bar{t}$ production involve comparisons between default and alternative MC configurations. For instance, uncertainties originating from hard-scattering and parton shower mechanisms are scrutinized through different generator setups. Contributions from scales, PDF, and α_s are also studied. For the Wt process, uncertainties related to the interference with $t\bar{t}$ are evaluated by comparing the diagram removal and subtraction schemes. These are parameterized based on the BDT output.

For the Z +HF process, hard-scatter and parton-shower uncertainties are similarly quantified using alternative MC setups. Scale and PDF variations are also considered. Effects of higher-order corrections are examined and deemed negligible.

For the Standard Model ggF HH signal, the parton shower-related uncertainties are extracted by contrasting the default sample with a HERWIG7-modelled sample. Uncertainties related to κ_λ reweighting are also assessed. These uncertainties have a direct bearing on the categories selected for analysis.

For VBF HH , the study involves comparisons with HERWIG7 models and variations in PDF and QCD scales.

For single-top processes, interference effects are assessed through diagram removal and subtraction methods. Uncertainties are parameterized based on BDT output scores.

Cross-section and decay branching ratio uncertainties are implemented according to the LHC Higgs Cross Section Working Group^[148]. Additionally, uncertainties specific to the

modeling of b or c jets in the absence of genuine heavy-flavor quarks are applied to relevant single-Higgs processes. The uncertainties from parton-shower models and NLO matching are also accounted for. Furthermore, PDF and scale uncertainties are evaluated using standard techniques. For the $t\bar{t}H$ process, additional uncertainties related to the modeling of initial and final state radiation are also assessed.

Systematic uncertainties for minor backgrounds, such as single-top s - and t -channels, Z +light-flavour jets, W +jets, and di-boson processes, are mainly constrained to acceptance uncertainties affecting only the normalisation. For the s - and t -channels of single-top production, an acceptance uncertainty of 20% is levied based on results from the SM $VHbb$ analysis^{ATLAS-CONF-2020-006}. An acceptance uncertainty of 23% is assigned to the Z +light-flavour jets background, consistent with previous analyses. In the W +jets background, different uncertainties are assigned for the two channels: 37% for the $\tau_{\text{lep}}\tau_{\text{had}}$ channel and 50% for the $\tau_{\text{had}}\tau_{\text{had}}$ channel to account for the fake- τ contribution. Acceptance uncertainties for di-boson processes are delineated as 25% for WW , 26% for WZ , and 20% for ZZ . For the irreducible ZZ background, additional studies reveal that scale uncertainties negligibly impact acceptance and shape within each analysis category. Apart from acceptance uncertainties, cross-section uncertainties are also applied to all minor backgrounds. However, their magnitude is comparatively smaller and thus less impactful.

Data-driven estimates for backgrounds involving objects mimicking hadronic τ leptons contribute to the analysis selection. These are collectively termed "Fake" in the $\tau_{\text{lep}}\tau_{\text{had}}$ channel and further subdivided into "Fake" and "ttbarFake" in the $\tau_{\text{had}}\tau_{\text{had}}$ channel. The estimation techniques closely align with prior work^[182]. Specifically, the τ fake factors are parameterized based on variables such as transverse momentum and prong-ness. Since the regions under the current analysis are finer sub-categories of those used previously, we uphold the validity of the existing fake factors. Given this foundation, the systematic uncertainties for Fake- τ_{had} backgrounds are modeled consistently with the prior analysis for both the $\tau_{\text{lep}}\tau_{\text{had}}$ and $\tau_{\text{had}}\tau_{\text{had}}$ channels. The sources and impact of these uncertainties follow the same framework as earlier work, with special attention given to instances where the current methodology diverges.

The methodology for evaluating uncertainties on the HH signal, encompassing cross-section, acceptance, and shape, is principally inherited from the previous round of analysis.

Alternative MC samples are used to probe the sensitivity to parton shower variations. Internal weights present in the nominal samples facilitate the assessment of PDF and scale variations. Parton Shower uncertainties are evaluated by contrasting nominal samples showered with PYTHIA8 against alternatives with HERWIG7. Internal alternative weights in the nominal samples are utilized for assessing uncertainties arising from PDF and scale variations. The PDF4LHC recommendations are followed for the combination of PDF and α_s uncertainties.

6.7 Statistical interpretation

The statistical interpretation of the $HH \rightarrow b\bar{b}\tau^+\tau^-$ analysis is framed within a simultaneous binned maximum-likelihood fit. This fit targets the MVA output distributions across all considered event categories, both $\tau_{\text{had}}\tau_{\text{had}}$ and $\tau_{\text{lep}}\tau_{\text{had}}$, delineated in Sections 6.3.4 and 6.5. Additionally, the fit incorporates the m_{ll} distribution in the Z+HF CR. The details of mathematical framework for statistical inference can be found in Section 5.5.1.

6.7.1 Fit step

The binned profile likelihood fit is conducted across all MVA score categories and additionally incorporates the m_{ll} distribution in the Z+HF CR.

For the SM fits, the POI is the Higgs boson pair (HH) signal strength, denoted by μ_{HH} . This POI is normalized to the sum of ggF and VBF cross-sections, i.e., $31.05 + 1.726$ fb, multiplied by the branching ratio. Separate fits introducing individual POIs μ_{ggF} and μ_{VBF} are also executed, each having an individual normalization constant.

The top quark pair ($t\bar{t}$) and Z+HF jets backgrounds are allowed to freely float during the fit, with their normalization being determined empirically. Normalization uncertainties between the SR and CR are applied as outlined in Section 6.6.

In the scans of likelihood as functions of the couplings κ_λ and κ_{2V} , we prepare 3 ggF and 6 VBF templates as elaborated in Section 6.2.1. These scans modify the workspaces to introduce new POIs for κ_λ and κ_{2V} . Linear combinations of these templates are used to generate signal distributions for arbitrary κ_λ and κ_{2V} values.

All systematic uncertainties discussed in Section 6.6 are incorporated as NPs in the profile likelihood fitting procedure. Each NP exerts its influence on either the shape or the normalization of the fit templates. While shape uncertainties are encapsulated using alternate

histograms, normalization uncertainties are modeled using either flat or Gaussian distributions.

- Across all fit regions, experimental, cross-section, and acceptance uncertainties are fully correlated.
- Correlations also extend to floating normalisations for $t\bar{t}$ and Z+HF.
- Exceptions include certain uncorrelated shape uncertainties, particularly for Z+HF in control regions.
- Data-driven background uncertainties remain uncorrelated.

Preprocessing steps for NPs include symmetrisation, smoothing, and pruning, in that order.

- Symmetrisation is applied to one-sided and same-sided systematic variations to rectify under-constraint issues.
- Smoothing is selectively applied to 4-vector-based CP variations using iterative rebinning algorithms, aimed at reducing likelihood minimization instabilities.
- Pruning is employed to remove inconsequential systematics, based on specific criteria such as less than 0.5% variation in yield or shape, among others.

Additionally, MC statistical uncertainties are introduced as NPs using Poissonian priors, identified by the SR and bin number.

6.7.2 Binning

In the analysis, an initial BDT score histogram is constructed with 2090 non-uniform bins. The range from -1 to 0.990 uses a 10^{-3} bin width, and the range from 0.990 to 1 employs a 10^{-4} width. The rebinning algorithm, termed Trafo60, is used uniformly across both $\tau_{\text{lep}}\tau_{\text{had}}$ and $\tau_{\text{had}}\tau_{\text{had}}$ channels. The algorithm starts with the most signal-like bins and iteratively merges them according to criteria described by the function:

$$Z(I[k, l]) = z_s \frac{n_s(I[k, l])}{N_s} + z_b \frac{n_b(I[k, l])}{N_b}, \quad (6-7)$$

Parameters $(z_s, z_b) = (10, 5)$ are employed in all analysis regions to maintain sensitivity. Iterations continue until MC statistical uncertainty on the sum of background events in each bin falls below 20% and the number of expected background events in each bin exceeds 3.

6.7.3 Blinding strategy

The analysis is conducted under blinded conditions to mitigate the risk of bias. Specifically, the observed point of interests (POIs) are hidden. For all channels and analysis categories, pre-fit MVA score distributions are blinded in the region that includes 85% of the total signal. The fitting exercise uses the complete signal region and relies on pre-fit Asimov data.

6.8 Results

The fitting scheme, delineated in Section 5.5.1, is subject to multiple levels of validation. The validation encompasses not only the global fit across all analytical domains but also channel-specific fits for both $\tau_{\text{had}}\tau_{\text{had}}$ and $\tau_{\text{lep}}\tau_{\text{had}}$ modes. For the validation exercises, fits are executed on both Asimov datasets as well as actual experimental data. When conducting the fit on the latter, the signal strength corresponding to the signal hypothesis is constrained to zero.

Furthermore, during the data fitting stage, specific NPs, particularly those pertaining to the signal as well as those background NPs exhibiting high correlation with the signal, are omitted from the results display.

6.8.1 Fits

6.8.1.1 CR-Only Fit

In the analysis, a crucial step is the validation of the Z+HF background model in the CR. The default fit configuration includes floating normalisation factors for Z+HF and $t\bar{t}$ processes. No explicit normalisation uncertainties from modelling are considered.

Figure 6-25 illustrates the variations in the nuisance parameters (NPs) obtained from fitting the CR data. Notably, only a limited set of NPs are either pulled or constrained in the fit. Of particular significance is the constraining effect on the egamma energy resolution, which is a carry-over from the previous iteration of the analysis. Additionally, constraints on the Z+HF generator NP are imposed, owing to its substantial impact on the m_{ll} distribution.

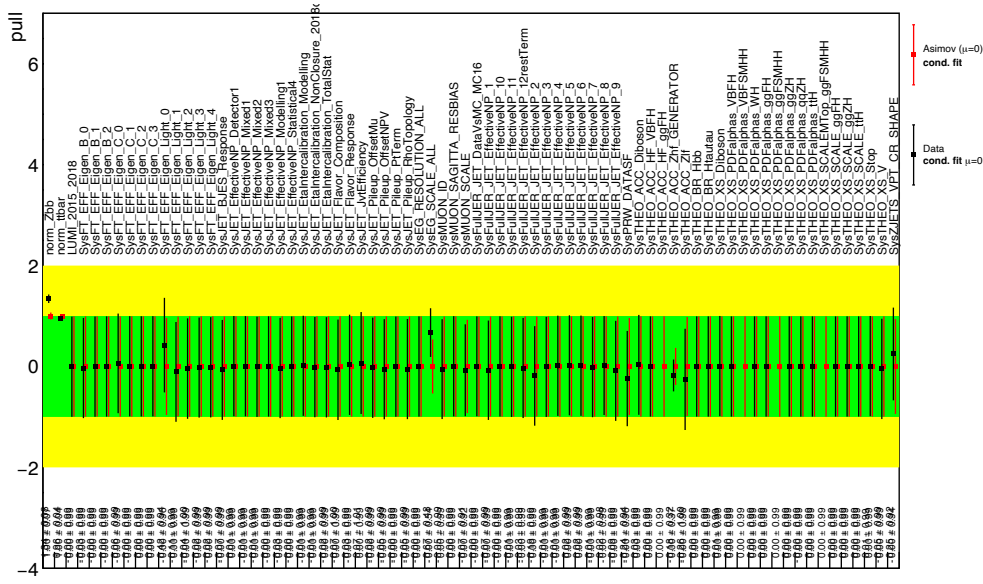


Figure 6-25 Post-fit values of the NPs included in the fit of the di-lepton invariant mass distribution in the CR.

The fitted normalisation factors are as follows:

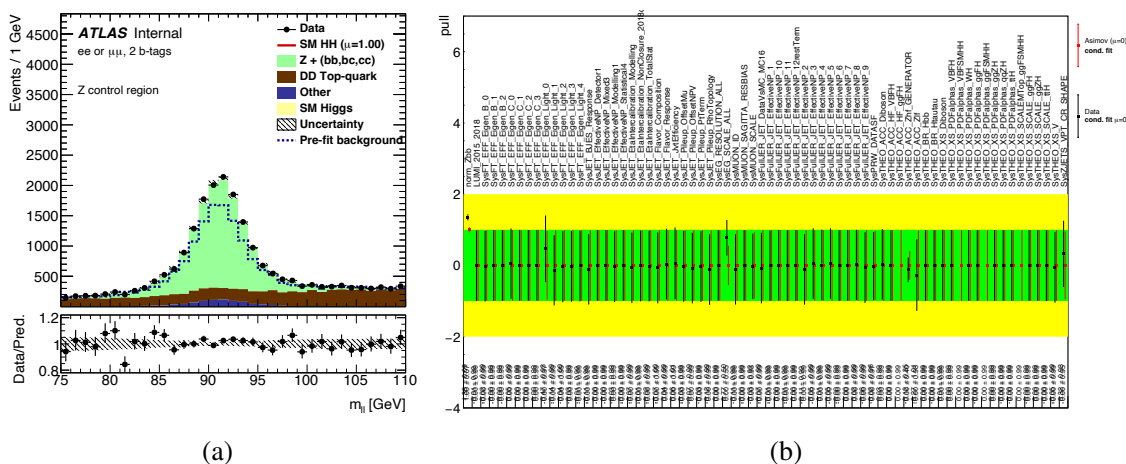
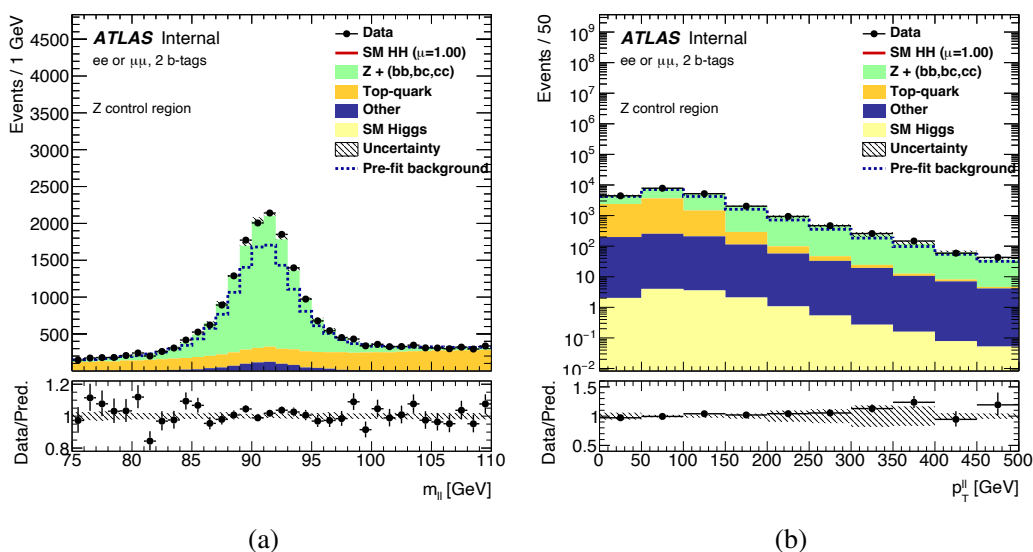
$$\text{NF}_{Z+\text{HF}} = 1.33 \pm 0.09,$$

$$\text{NF}_{t\bar{t}} = 0.96 \pm 0.04.$$

A correlation of +72% between these factors is mainly driven by the FTag systematics. The post-fit distributions in m_{ll} and p_T^{ll} are shown in Figure 6-26.

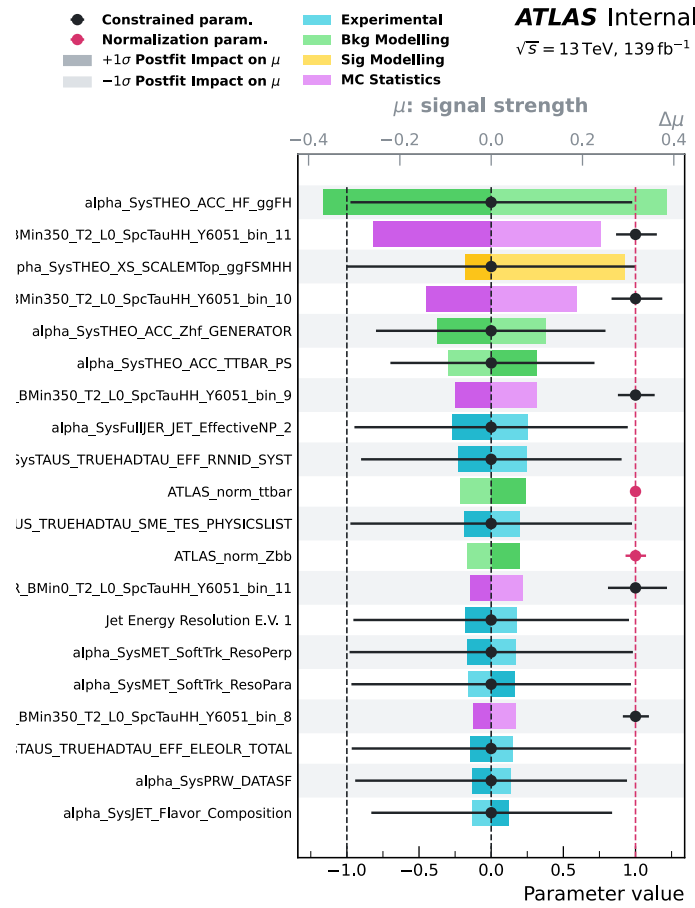
6.8.2 Data-driven $t\bar{t}$ Modelling

As a cross-check to minimize reliance on simulations, a data-driven approach for the $t\bar{t}$ background is performed. A dedicated CR, the $e\mu$ CR, is defined Section 6.3.5.1. The normalisation factor for Z+HF in this setup is 1.35 ± 0.09 , in agreement with the default setup. The post-fit results are presented in Figure 6-27.



6.8.3 $\tau_{\text{had}}\tau_{\text{had}}$ Fitting Results

Figure 6–28 depicts the ranking of the NPs based on the fit to the Asimov dataset.

Figure 6–28 Nuisance parameter ranking in the $\tau_{\text{had}}\tau_{\text{had}}$ fit using the Asimov dataset.

The predominant uncertainties affecting the determination of signal strength are:

1. Uncertainty on the single Higgs plus heavy flavour production.
2. Scale uncertainty on the HH cross-section.
3. Monte Carlo statistical uncertainties, particularly in the high BDT bins of the high m_{HH} region.

It is worth mentioning that the expected data statistical uncertainty on the combined signal strength in all 3 SRs is estimated to be 1.15, which is significantly larger than all these contributions.

Figure 6–29 portrays the correlations among the highly correlated¹ nuisance parameters as derived from the $\tau_{\text{had}}\tau_{\text{had}}$ fit to both the Asimov dataset and the actual data. It is important to

¹ Here, 'highly correlated' refers to NPs having a correlation greater than 25% with at least one other NP.

note that the correlations concerning Monte Carlo (MC) statistical uncertainties are deliberately excluded from this representation. An analogous degree of NP correlation is noticeable between the two fit configurations, further solidifying the robustness of the model.

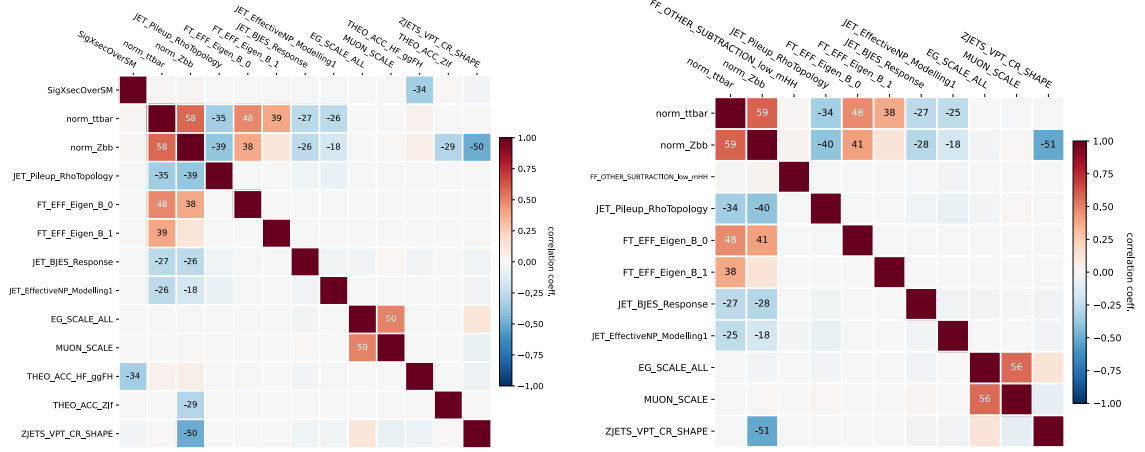
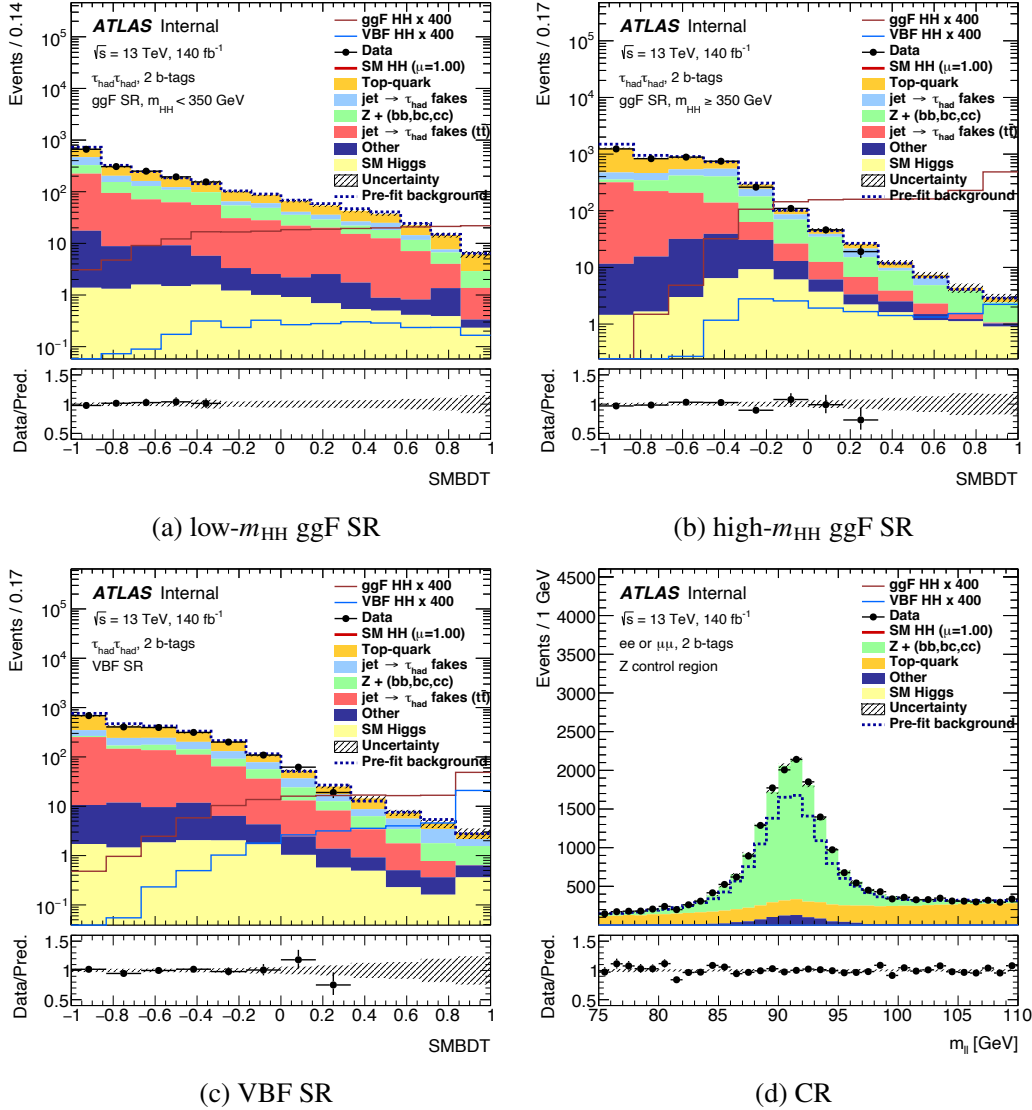


Figure 6–29 Correlations among NPs in the $\tau_{\text{had}}\tau_{\text{had}}$ SM fit to the Asimov dataset (left) and real data (right). MC statistical uncertainties are purposefully omitted.

Finally, blinded post-fit distributions of the fitted variables in the 4 regions are shown in Figure 6–30. The choice of the binning is discussed in Section 6.7.2.

Figure 6-30 Post-fit BDT score distributions in the $\tau_{had}\tau_{had}$ signal regions.

6.8.4 Limits and scans

6.8.4.1 $\tau_{had}\tau_{had}$

Figure 6-20 presents the estimated 95% CL upper limits on the HH signal strength, further subdivided into ggF and VBF production modes. These limits are derived from both one-dimensional and two-dimensional fits of μ_{ggF} and μ_{VBF} , where the other parameter is allowed to float when assessing one¹. These assessments are conducted within the context

¹ When evaluating the limit on μ_{ggF} , the normalisation factor for μ_{VBF} is not constrained, and vice versa.

of the $\tau_{\text{had}}\tau_{\text{had}}$ decay channel, with calculations carried out under a background-only hypothesis. Subsequently, the two rightmost columns present the 95% CL expected intervals for the κ_λ and κ_{2V} coupling constants. These intervals are extracted based on the negative log-likelihoods (NLLs), computed as functions of κ_λ and κ_{2V} . It is pertinent to note that the NLL evaluations are performed under the standard model HH production assumption.

	95% CL Upper Limits on Signal Strength					95% CL Intervals	
	μ_{HH}	$\mu_{\text{ggF}}^{\text{1D}}$	$\mu_{\text{VBF}}^{\text{1D}}$	$\mu_{\text{ggF}}^{\text{2D}}$	$\mu_{\text{VBF}}^{\text{2D}}$	κ_λ	κ_{2V}
Baseline w/o syst.	3.46	3.52	219	12.5	778	[-2.79, 9.58]	[-0.58, 2.71]
Baseline w/ syst.	4.2	4.25	260	18.0	1086	[-3.36, 10.3]	[-0.63, 2.76]
Updated w/o syst.	2.95	2.98	90	3.07	93	[-2.35, 8.94]	[-0.37, 2.51]
Updated w/ syst.	3.55	3.60	86	3.66	88	[-2.74, 9.40]	[-0.34, 2.51]

Table 6–20 Summarized 95% CL expected upper boundaries on HH signal strength and intervals for κ_λ and κ_{2V} , categorized by production mode in the $\tau_{\text{had}}\tau_{\text{had}}$ channel. All estimations with and without systematic uncertainties are included.

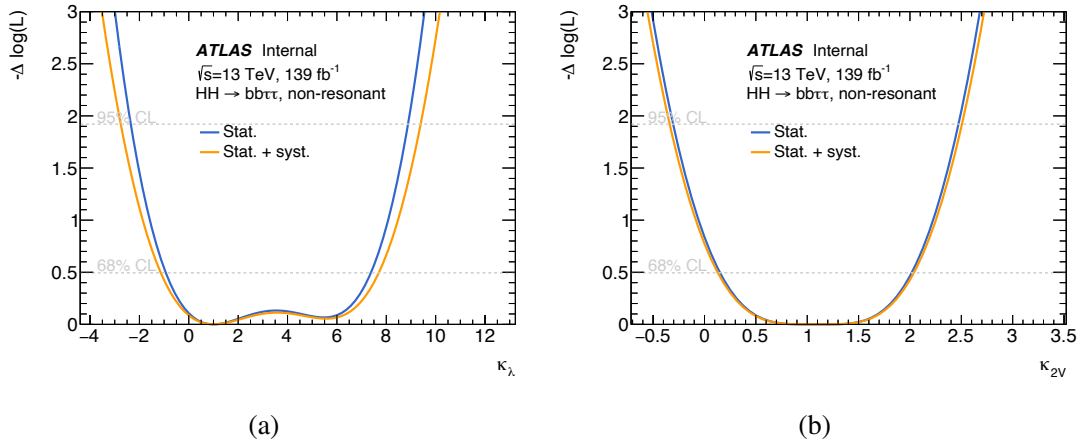


Figure 6–31 Negative logarithm of the likelihood ratio comparing different κ_λ (a) and κ_{2V} (b) hypotheses to an Asimov dataset constructed under the SM hypothesis in the $\tau_{\text{had}}\tau_{\text{had}}$ channel.

Pre-fit Asimov dataset-based limits are depicted both with and without the inclusion of systematic uncertainties for all relevant figures of merit. A comparative assessment is performed between the limits obtained from the baseline and updated analysis categories.

Likelihood scans are conducted across all three individual analysis categories, as well as for an aggregated case that incorporates all categories. Figure 6–31 displays the likelihood

scans for the coupling constants κ_λ and κ_{2V} . When evaluating the likelihood for a specific parameter, either κ_λ or κ_{2V} , all other coupling constants that influence both single-Higgs and di-Higgs production are maintained at their Standard Model values.

6.8.4.2 Combined $\tau_{\text{had}}\tau_{\text{had}}$ and $\tau_{\text{lep}}\tau_{\text{had}}$

Tables 6–21 combine the consolidated anticipated upper constraints on signal strength and the confidence intervals for κ_λ and κ_{2V} parameters, as obtained from both the updated and baseline analyses. The baseline data are generated using a pre-fit Asimov dataset, serving as a robust benchmark for comparative evaluation. Moreover, the table includes metrics of relative enhancement over the baseline results.

For the $\tau_{\text{had}}\tau_{\text{had}}$ decay channel specifically, the composite analysis yields a 16% enhancement in the upper limit on HH production. Furthermore, the specialized region dedicated to VBF production facilitates the concurrent establishment of upper constraints on both VBF and ggF mechanisms.

	95% CL Upper Limits on Signal Strength					95% CL Intervals	
	μ_{HH}	$\mu_{\text{ggF}}^{\text{1D}}$	$\mu_{\text{VBF}}^{\text{1D}}$	$\mu_{\text{ggF}}^{\text{2D}}$	$\mu_{\text{VBF}}^{\text{2D}}$	κ_λ	κ_{2V}
Baseline w/o syst.	2.84	2.89	189	9.24	572	[-2.35, 9.19]	[-0.42, 2.55]
Baseline w/ syst.	3.61	3.68	241	13.2	772	[-2.97, 10.1]	[-0.50, 2.63]
Legacy w/o syst.	2.41	2.44	61	2.49	62	[-1.97, 8.58]	[-0.14, 2.32]
Legacy w/ syst.	2.98	3.01	63	3.05	64	[-2.40, 9.11]	[-0.17, 2.34]
Rel. improvement w/o syst.	15%	16%	68%	73%	89%	8.6%	17.2%
Rel. improvement w/ syst.	17%	18%	74%	77%	92%	11.9%	19.8%

Table 6–21 Expected 95% CL limits on HH signal strength and intervals for κ_λ and κ_{2V} from the combined fit. The statistics are reported both with and without systematic uncertainties.

In Figure 6–32, panels (a) and (b) depict the NLL scans against κ_λ and κ_{2V} , respectively. These scans employ a fit to the SM-based Asimov dataset and consider both the aggregated scenario as well as the isolated $\tau_{\text{had}}\tau_{\text{had}}$ and $\tau_{\text{lep}}\tau_{\text{had}}$ channels.

The graphical data reinforce the $\tau_{\text{had}}\tau_{\text{had}}$ channel as the main contributor to the analytic rigor. The inclusion of the $\tau_{\text{lep}}\tau_{\text{had}}$ channel has a more pronounced impact on the κ_{2V} interval than on the κ_λ interval.

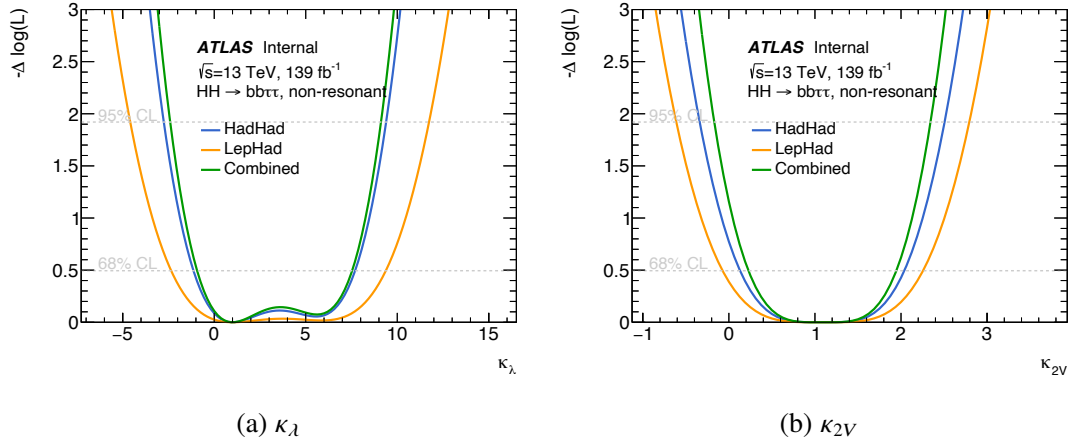


Figure 6–32 Negative log-likelihood ratios assessing various κ_λ and κ_{2V} scenarios, in reference to an Asimov dataset created under the SM framework. Analyses incorporate both individual channels and their amalgamation. Solid lines intersecting dashed horizontal lines indicate 68% and 95% confidence levels.

Chapter 7 Constraining the Higgs boson self-coupling from single- and double-Higgs production

7.1 Introduction

Following the discovery of the Higgs boson by the ATLAS and CMS collaborations^[198–199], the Large Hadron Collider (LHC)^[200] has been tasked with the accurate measurement of its properties. This is done to confirm their alignment with the predictions of the Standard Model (SM)^[201–204] or to reveal new physics phenomena. In the SM, the Higgs boson plays a crucial role in electroweak symmetry breaking^[205–209]. This not only furnishes elementary particles with mass but also maintains perturbative unitarity. The trilinear Higgs boson self-coupling, λ_{HHH} , is dictated by the Higgs boson mass m_H ^[210] and the Fermi constant G_F ^[211].

This work focuses on combining the three most sensitive double-Higgs decay channels: $b\bar{b}\gamma\gamma$, $b\bar{b}\tau^+\tau^-$, and $b\bar{b}b\bar{b}$ ^[177, 212–213]. The data used for this analysis was collected by ATLAS from 2015–2018, corresponding to an integrated luminosity of 126–139 fb⁻¹ at $\sqrt{s} = 13$ TeV. The coupling modifier κ_λ is utilized to report results, where $\kappa_\lambda = \lambda_{HHH}/\lambda_{HHH}^{\text{SM}}$.

The trilinear self-coupling also affects single-Higgs production via substantial next-to-leading-order (NLO) electroweak corrections^[214–219]. Further constraints on κ_λ are drawn from combining recent ATLAS single-Higgs measurements^[220] with the aforementioned double-Higgs results. This combination enables κ_λ testing without specific assumptions regarding other SM Higgs interactions.

Previous ATLAS combinations on partial Run 2 data have set an upper limit on SM HH production to be 6.9 (expected 10) times the SM prediction at a 95% CL^[221]. The permitted range for κ_λ was found to be $-5.0 \leq \kappa_\lambda \leq 12.0$. The CMS collaboration has also published similar constraints using its complete Run 2 data, up to 138 fb⁻¹^[222].

7.2 Theoretical framework

The κ framework offers a methodology for scrutinizing the Standard Model (SM) in the Higgs sector, particularly in relation to single and double-Higgs production^[223–224]. In this framework, the couplings of the Higgs boson to other SM particles at leading order (LO) are

scaled by factors denoted as κ_m , defined as the ratio of the coupling between the particle m and the Higgs boson to its SM value. These scaling factors serve as a simplified yardstick for comparing experimental results to SM predictions. The framework principally focuses on four coupling modifiers for single-Higgs interactions: κ_t , κ_b , κ_τ , and κ_V . A departure of κ from unity indicates the presence of Beyond Standard Model (BSM) physics^[223].

Double-Higgs production serves as a direct probe into the Higgs boson self-coupling. In the SM, the primary mechanism for double-Higgs production is gluon–gluon fusion, contributing to over 90% of the $pp \rightarrow HH$ cross-section^[225]. The process is sensitive to two main coupling modifiers: κ_λ , and κ_t , which scale different amplitudes in the process, as shown in Figure 2–5. Deviations from the SM predictions can be parameterized in terms of these coupling modifiers^[224, 226–228].

The $pp \rightarrow HH$ process allows for sensitivity to the relative sign of κ_λ and the top-quark couplings, mainly because of the destructive interference between amplitudes. The second most abundant process, VBF, in Figure 2–6, is parameterized using a combination of the κ_λ , κ_V , and κ_{2V} coupling modifiers^[166].

While single-Higgs processes are generally not sensitive to the Higgs boson self-coupling at leading order (LO), the complete next-to-leading order (NLO) electroweak (EW) corrections incorporate λ_{HHH} through Higgs boson self-energy loops and additional diagrams, offering indirect constraints on κ_λ ^[214–215]. Concurrently, the Simplified Template Cross-Section (STXS) framework offers a refined methodology for analyzing single-Higgs processes. It employs fiducial phase space regions defined by kinematic variables, enabling the identification of localized deviations from Standard Model predictions^[229]. This facilitates mapping back to constraints on κ_m parameters, enriching the utility of the κ framework. The STXS approach categorizes bins by production mode, decay channel, and additional criteria such as jet multiplicity and transverse momentum, thereby offering a more detailed understanding of Higgs properties^[230–231].

Any significant deviation in the measured κ_m from unity, or discrepancies in the cross-sections of double-Higgs production processes from SM predictions, would be indicative of new physics. Such deviations would warrant further investigation, possibly heralding the discovery of particles or interactions not accounted for in the SM.

The κ framework serves as a valuable tool for exploring the Higgs sector. By employ-

ing coupling modifiers, it simplifies the analysis of both single and double-Higgs processes. While the framework has its limitations, such as the absence of considerations for new particles in loop-level diagrams, it remains a robust methodology for initial explorations into BSM physics in the Higgs sector.

7.3 Individual channel measurements

This study incorporates both single-Higgs and di-Higgs channels, leveraging the full Run 2 dataset acquired by the ATLAS experiment in pp collisions at 13 TeV during the 2015–2018 data-taking window^[232–234]. Depending on the trigger selection, the available integrated luminosity spans 126 to 139 fb^{−1}. Event selection employs a two-level trigger system^[235].

For data reconstruction, analysis, and detector operations, an extensive software framework is utilized^[236]. Although the current focus is on di-Higgs channels, single-Higgs analyses also contribute significantly to the study. A concise summary of each input analysis contributing to this combination is presented in Table 7–1. These analyses categorize selected events into distinct kinematic and topological regions. For a comprehensive understanding of the individual analyses, readers are referred to the respective references listed in Table 7–1.

Table 7–1 Summary of datasets for each contributing analysis channel, with their corresponding integrated luminosities in fb^{−1}. Detailed descriptions of each channel can be found in the last column’s references.

Analysis channel	Integrated luminosity [fb ^{−1}]	Ref.
$HH \rightarrow b\bar{b}\gamma\gamma$	139	[212]
$HH \rightarrow b\bar{b}\tau^+\tau^-$	139	[177]
$HH \rightarrow b\bar{b}b\bar{b}$	126	[213]
$H \rightarrow \gamma\gamma$	139	[237]
$H \rightarrow ZZ^* \rightarrow 4\ell$	139	[238]
$H \rightarrow \tau^+\tau^-$	139	[239]
$H \rightarrow WW^* \rightarrow e\nu\mu\nu$ (ggF, VBF)	139	[240]
$H \rightarrow b\bar{b}$ (VH)	139	[241]
$H \rightarrow b\bar{b}$ (VBF)	126	[242]
$H \rightarrow b\bar{b}$ ($t\bar{t}H$)	139	[243]

7.4 Statistical Methodology and Analysis Combination

The statistical methodology adheres to established procedures outlined in the previous works^[244–245]. We define a global likelihood function, $L(\vec{\alpha}, \vec{\theta})$, where $\vec{\alpha}$ constitutes the model’s parameters of interest (POI) and $\vec{\theta}$ encompasses nuisance parameters, inclusive of systematic uncertainties. These nuisance parameters are constrained by control regions or sidebands in the data.

The global likelihood is a multiplicative aggregation of individual analysis likelihoods, which themselves are products of likelihoods computed across distinct analysis categories. Results are presented through the profile-likelihood-ratio test statistic, $\Lambda(\vec{\alpha}, \vec{\theta})$. Confidence intervals at 68% and 95% CL are extracted utilizing asymptotic approximations^[246]. Upper limits on the cross-section are specifically derived via the CL_s method^[247].

For hypothesis testing, Asimov datasets are generated^[246], locking nuisance parameters to data-derived values and fixing POIs to predefined hypothesis values.

Statistical independence is assumed for combining likelihoods. Event overlaps among individual analyses, previously established as negligible^[220], are verified to be below 0.1% for newly combined di-Higgs studies.

The origins and correlations of systematic uncertainties are elaborated in the cited references of Table 7–1. Additional cross-correlations among di-Higgs and single-Higgs systematic factors have been scrutinized and integrated as warranted. Data-condition related uncertainties, such as those tied to pile-up and luminosity, are deemed fully correlated. Methodological differences in experimental uncertainties led to the treatment of some as uncorrelated.

A sensitivity study was undertaken to assess the impact of correlation assumptions on the derived exclusion limits. The discrepancy between correlated and uncorrelated treatments is found to be less than 2%.

For di-Higgs analyses, dominant uncertainties arise from data-based background estimations, largely uncorrelated with those in single-Higgs analyses. Altering correlation assumptions yields a marginal influence, with the exception being the $pp \rightarrow HH$ cross-section theoretical uncertainties, where correlation relaxes signal strength constraints by 7%.

7.5 Di-Higgs Combined Results

7.5.1 Global signal strength

In this work^[248], we combine the analyses focusing on the decay channels $b\bar{b}b\bar{b}$, $b\bar{b}\tau^+\tau^-$, and $b\bar{b}\gamma\gamma$ as cited in Table 7-1. The aim is to extract constraints on the signal strength parameter μ_{HH} , defined as the observed over expected double-Higgs production cross-section, with particular emphasis on the ggF and VBF mechanisms. The standard model (SM) prediction for this cross-section is 32.7 fb^[225].

The aggregate analysis furnishes an observed 95% confidence level (CL) upper bound of $\mu_{HH} = 2.4$. In the SM context, the expected 95% CL upper limits are calculated to be 2.9 and 4.0, assuming no signal and the presence of an SM-compatible signal, respectively. These results are visually represented in Figure 7-1. A best-fit signal strength value of $\mu_{HH} = -0.7 \pm 1.3$ was attained, commensurate with the SM prediction, yielding a p -value of 0.2.

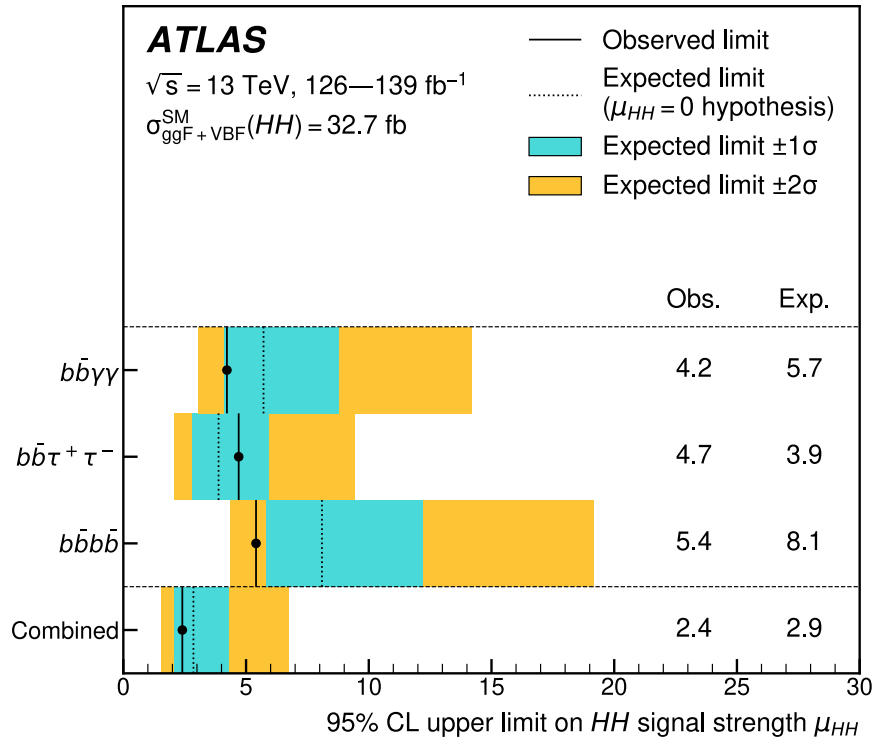


Figure 7-1 Illustration of the observed and expected 95% CL upper bounds on the signal strength μ_{HH} for the considered decay channels and their statistical amalgamation. The SM prediction assumes $m_H = 125.09$ GeV.

Further, a stringent 95% CL upper limit on the total double-Higgs production (ggF and

VBF only) cross-section of 73 fb was established, in contrast to an expected limit of 85 fb under the no-signal hypothesis.

7.5.2 Constraints on Higgs self-coupling

The analysis that combines different decay channels gives the constraints on the self-coupling κ_λ and the quartic coupling κ_{2V} of the Higgs boson.

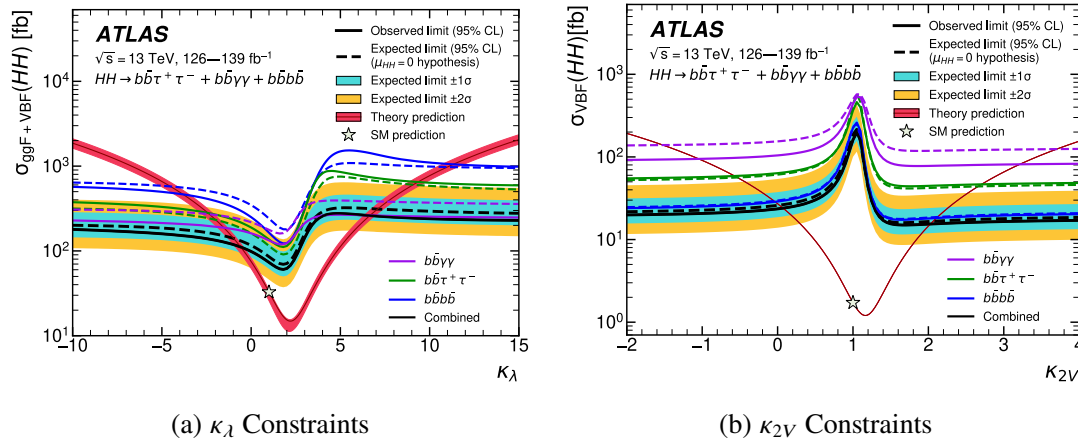


Figure 7–2 95% CL constraints on κ_λ and κ_{2V} from the combined analysis. The red lines indicate the theory constraints, while the solid lines represent observed limits.

For the Higgs boson self-coupling κ_λ , the 95% confidence level observed constraints are $-0.6 < \kappa_\lambda < 6.6$. Under the assumption of the Standard Model, the expected constraints are $-2.1 < \kappa_\lambda < 7.8$. These limits offer significant insights into the non-linear structure of the Higgs potential and serve as a crucial test for the Standard Model.

For the quartic coupling constant κ_{2V} , which relates to the $HHVV$ interactions, the observed limits at a 95% confidence level are $0.1 < \kappa_{2V} < 2.0$. The expected limits are $0.0 < \kappa_{2V} < 2.1$ under the Standard Model hypothesis. These constraints are significant for understanding the quartic interactions involving the Higgs boson.

The observed and expected limits are depicted in Figure 7–2, with the subfigures for κ_λ and κ_{2V} shown in Figure 7–2a and Figure 7–2b, respectively.

7.6 Single- and Di-Higgs Combined Results

In this study, the combined single-Higgs and double-Higgs analyses offer enhanced constraints on the coupling modifier κ_λ , as detailed in Table 7-1. Leveraging statistical methodologies delineated in Section 7.2, multiple fitting procedures are conducted under varying assumptions on the coupling modifiers.

Figure 7-3 presents a thorough investigation into the test statistic $-2 \ln \Lambda$, plotted against the Higgs self-coupling modifier κ_λ . Two distinct scenarios are examined: observed data and projected or Asimov data. Figure 7-3a depicts the observed $-2 \ln \Lambda$ values for both single-Higgs and double-Higgs analyses, color-coded in blue and red respectively. Their combined results are shown in black. In addition, a general model allowing for free-floating κ_t , κ_b , κ_V , and κ_τ is represented by the green curve. Figure 7-3b mirrors this structure but uses the expected or Asimov data. This figure serves as a cornerstone for the constraint evaluation on κ_λ , facilitating an intercomparison among various scenarios and assumptions.

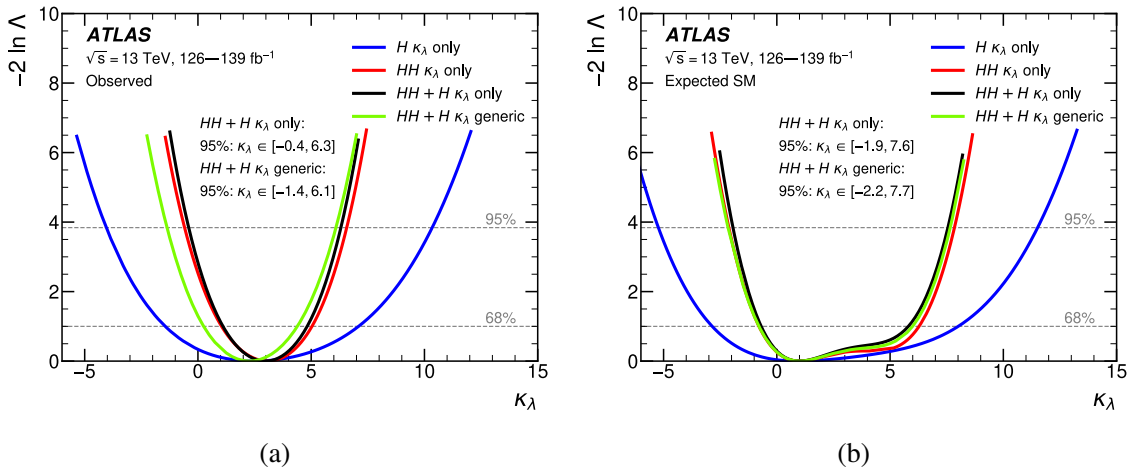


Figure 7-3 Observed (a) and projected (b) test statistics in terms of κ_λ .

One of the advantages of integrating the single-Higgs analyses into the overall fit is the additional flexibility it provides in relaxing certain coupling assumptions without substantially compromising the robustness of our constraints. Specifically, the assumption on the Higgs boson to top-quark coupling modifier, κ_t , can be considerably relaxed. Thanks to the robust boundaries set by single-Higgs measurements, the constraints on κ_λ are hardly affected when the value of κ_t is allowed to float freely, a claim substantiated by the data presented in Table 7-2.

Against this backdrop, Figure 7-4 serves as a critical asset for understanding the relationship between κ_λ and κ_t . The figure comprises two sub-figures: Figure 7-4a employs observed data, and Figure 7-4b is constructed using expected, or Asimov, data. Both sub-figures feature 68% and 95% confidence level contours, marked by solid and dashed lines respectively. In Figure 7-4a, constraints solely based on single-Higgs analyses are denoted by blue contours, whereas those emerging from double-Higgs analyses are depicted in red. The black contours represent the synthesized outcome of both these analyses. Importantly, red contours are restricted to κ_t values below 1.2. Figure 7-4b adopts a similar coloring scheme but relies on Asimov data to form its contours.

Overall, the figures demonstrate that when κ_t is allowed to float, the combined single- and double-Higgs analyses still manage to provide nearly as stringent constraints on κ_λ as when κ_t is fixed, affirming the efficacy of the integrated analytical approach.

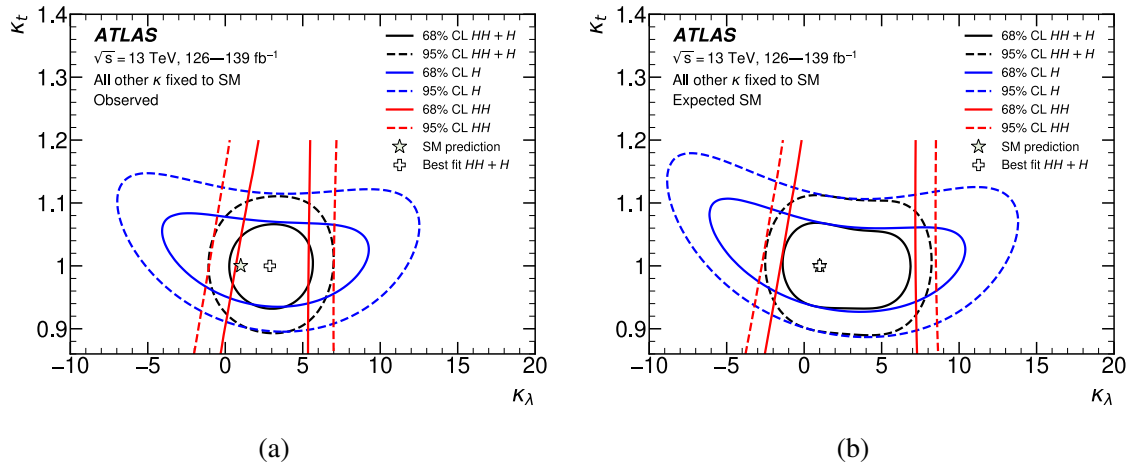


Figure 7-4 Constraints in the κ_λ - κ_t parameter space.

Finally, Table 7-2 provides a rigorous, multi-faceted summary of the constraints on the coupling modifier κ_λ . The table covers scenarios ranging from isolated double-Higgs (HH) and single-Higgs (H) combinations to increasingly inclusive fits where additional coupling modifiers are allowed to float. The most generic model is the least restrictive, allowing κ_λ , κ_t , κ_b , κ_τ , and κ_V to float, while fixing κ_{2V} to unity due to the absence of a comprehensive parameterization for single-Higgs NLO EW corrections as a function of this modifier. In this most generic fit, we observe an exclusion of $-1.4 < \kappa_\lambda < 6.1$ at the 95% confidence level, closely aligned with the expected exclusion of $-2.2 < \kappa_\lambda < 7.7$. These findings cor-

roborate that all other coupling modifiers agree with the Standard Model predictions within uncertainties. Notably, the sensitivity of the results to κ_{2V} is minor; a separate check revealed that allowing κ_{2V} to float only weakens the observed constraints on κ_λ by less than 5%. This manifests the robustness of our analytical framework even when extended to accommodate more free parameters.

Combination assumption	Obs. 95% CL	Exp. 95% CL	Obs. value $^{+1\sigma}_{-1\sigma}$
HH combination	$-0.6 < \kappa_\lambda < 6.6$	$-2.1 < \kappa_\lambda < 7.8$	$\kappa_\lambda = 3.1^{+1.9}_{-2.0}$
Single- H combination	$-4.0 < \kappa_\lambda < 10.3$	$-5.2 < \kappa_\lambda < 11.5$	$\kappa_\lambda = 2.5^{+4.6}_{-3.9}$
$HH+H$ combination	$-0.4 < \kappa_\lambda < 6.3$	$-1.9 < \kappa_\lambda < 7.6$	$\kappa_\lambda = 3.0^{+1.8}_{-1.9}$
$HH+H$ combination, κ_t floating	$-0.4 < \kappa_\lambda < 6.3$	$-1.9 < \kappa_\lambda < 7.6$	$\kappa_\lambda = 3.0^{+1.8}_{-1.9}$
$HH+H$ combination, κ_t , κ_b , κ_τ , and κ_V floating	$-1.4 < \kappa_\lambda < 6.1$	$-2.2 < \kappa_\lambda < 7.7$	$\kappa_\lambda = 2.3^{+2.1}_{-2.0}$

Table 7–2 Comprehensive summary of κ_λ constraints.

Chapter 8 Search for Long-Lived Particle with the Future Lepton Collider

8.1 Introduction

As introduced in Section 2.4, LLPs can be a potential probe for new physics beyond the Standard Model.

8.1.1 Methods and Subsystems for LLP Detection in Collider Experiments

Collider-based searches for LLPs can be broadly classified into direct and indirect detection methods. In direct detection, the LLP interacts directly with the detector subsystems, whereas indirect detection involves the reconstruction of the LLP's decay into SM particles. A typical collider detector consists of several main subsystems: the inner detector (ID), electromagnetic calorimeter (ECAL), and hadronic calorimeter (HCAL), along with specialized systems for muon tracking (Muon Spectrometer). These subsystems work in tandem to measure various particle properties such as charge, momentum, and energy. It is crucial to note that while these subsystems are optimized for detecting SM particles, they also provide avenues for LLP detection.

8.1.2 Challenges and Considerations in LLP Detection

LLP detection poses unique challenges compared to SM particles. First, the efficiency of LLP detection decreases as the displacement of the LLP from the interaction point increases. Second, traditional tracking algorithms may not adequately capture LLPs, leading to missed or irregular tracks. Nonetheless, the versatility of collider detectors, when adjusted for these specific challenges, makes them powerful tools for LLP searches. In particular, careful consideration must be given to the differences in reconstruction techniques for prompt and displaced particles.

While LLPs may themselves escape detection due to their long lifetimes, they often yield displaced vertices upon decay, creating anomalous tracks in the inner detector or atypical energy deposits in calorimeters. In the case of LLP decays in the muon system, specialized tracks distinct from typical muon signatures may emerge. These atypical features, col-

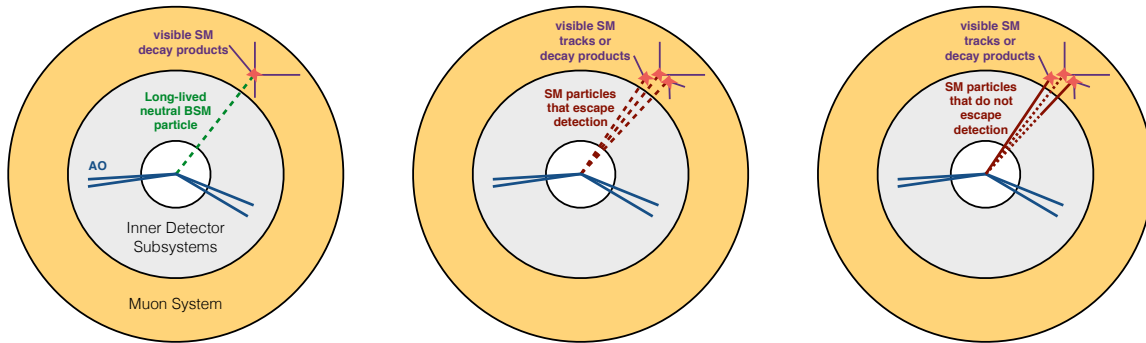


Figure 8-1 The schematic representation of LLPs' decaying process in the detector.

lectively termed as Associated Objects (AOs), serve as key markers for LLP identification. However, LLP searches are complicated by a variety of Standard Model backgrounds. For instance, punch-through jets could mimic the energy deposit pattern of an LLP in calorimeters. Similarly, bremsstrahlung from high-energy muons can create misleading signatures. Furthermore, some heavy flavor hadrons have lifetimes that could lead to displaced vertices, thus contributing to the background. These backgrounds necessitate rigorous data analysis techniques to discern genuine LLP signatures. A schematic representation of LLPs' decaying process in the detector is shown in Figure 8-1.

8.1.3 Signatures of Neutral Long-Lived Particles

The focus of this study is solely on neutral LLPs. Given their neutral charge, these particles do not exhibit some of the signals commonly associated with charged LLPs, such as anomalous tracks in the inner detector or in the muon system. Instead, neutral LLPs are typically identified through their decay products. The following paragraphs describe the various signatures of neutral LLPs in collider experiments.

8.1.3.1 Time-Delayed Detector Responses

A neutral LLP traversing the detector at reduced velocity compared to SM particles exhibits time-delayed signals in various subsystems, such as calorimeters and Muon Spectrometers (MS). This delayed arrival serves as a unique identifying feature. Precise timing resolutions on the order of 1 ns, along with the detector's dimensions, allow for accurate speed measurements. These measurements, in combination with momentum data, facilitate mass determination for the neutral LLP. Unlike SM particles with identical momenta (almost at

the speed of light), heavy, neutral LLPs take an extended period to traverse from the point of production to the detection subsystems. The timing disparity^[249], Δt , can be quantified as

$$\Delta t = t_{\text{hit}} - \frac{L_{\text{SM}}}{c}, \quad (8-1)$$

where t_{hit} is the timestamp of the detector hit, L_{SM} represents the distance from the primary vertex to the point of detection, and c is the speed of light. For neutral LLPs, Δt exhibits a distribution shifted significantly towards positive values, whereas for SM particles, it clusters around zero.

8.1.3.2 Non-Prompt Track Signatures

Tracks originating from neutral LLP decays often deviate considerably from the beam spot, typically characterized by the transverse impact parameter d_0 . Accounting for detector uncertainties, a large d_0/σ_{d_0} ratio is indicative of a displaced track. Due to data and computational resource constraints, tracks with large d_0 or z_0 values are not typically reconstructed by default algorithms. Specialized reconstruction methods have emerged to address these challenges.

8.1.3.3 Identifying Displaced Vertices

When multiple tracks from a neutral LLP decay are detected, they often converge at a displaced vertex (DV). The DV's position and its covariance matrix can be determined through vertex-fitting algorithms. This vertex distance is generally more accurate than d_0 , and various kinematic variables can further distinguish it from background. As analysis techniques mature, rejection of background vertices near dense material becomes increasingly effective.

8.1.3.4 Signatures in Calorimeters

While the Inner Detector (ID) is usually limited to small spatial measurements, calorimeters extend the search to larger distances. Longitudinal shower shapes and energy deposition ratios between the Electromagnetic Calorimeter (ECAL) and Hadronic Calorimeter (HCAL) can offer insights into neutral LLP decays occurring within the calorimeter volume. These features are notably distinct from standard SM jets and thus serve as valuable markers for neutral LLPs.

8.1.3.5 Composite Detection Methods

While individual signatures are informative, their combined use can enhance the sensitivity and robustness of neutral LLP searches. Correlations between different subsystems provide multiple, uncorrelated handles for background rejection. It's crucial to note that the standard reconstruction methods may introduce biases and additional systematic uncertainties when applied to displaced objects.

8.1.3.6 LLP Detection at LHC and Future Lepton Colliders

There are many existing studies on LLPs performed using data from the ATLAS^[250] and CMS^[251] experiments at the LHC. However, it's crucial to note that the sensitivity of these experiments to LLPs is currently suboptimal. A primary limiting factor lies in the high level of QCD background, colloquially referred to as *dirty backgrounds*. These pervasive backgrounds impose a ceiling on the precision of exclusion limits set by these experiments. Moreover, the detector designs for ATLAS and CMS were not originally optimized to efficiently search for LLP signatures. The constraints are more profound when one considers the increasing luminosity of the LHC, exacerbating the challenge of identifying relatively weak signals from LLPs amid an overwhelming amount of SM background noise.

In contrast, future lepton colliders such as the FCC-ee^[252] and the CEPC^[253-254] present more promising avenues for LLP detection. These colliders are expected to offer a substantially cleaner environment with reduced QCD background, thus allowing for more stringent exclusion limits for LLPs. The well-defined initial state and fewer sources of systematic uncertainty enable these colliders to be highly effective in identifying the subtle signals associated with LLPs. Furthermore, the lower center-of-mass energy of these colliders allows for the production of LLPs with lower masses, which are challenging to detect at the LHC.

Despite the abundance of theoretical models proposing various LLPs, focusing on final states presents a strategic approach to exploring LLPs in future lepton colliders. This focus is underpinned by the distinct signature of LLPs, setting them apart from SM particles. Typical final states in this context would contain one or two visible LLPs accompanied by easily-tagged SM particles, such as the Z-boson. One such production mechanism involves a resonance or scalar particle, exemplified by the Higgs boson. Lepton colliders offer a high occurrence rate for the $e^+e^- \rightarrow ZH$ process, serving as a natural avenue for LLP production

via the $H \rightarrow XX$ decay channel, where X is the neutral LLP. Therefore, this study will concentrate on the physics process denoted as $e^+e^- \rightarrow ZH \rightarrow Z_{\text{products}} + XX$, where X could either decay into invisible particles or SM jets/leptons. However, it should be noted that the methodology employed is extensible to any model yielding similar final states.

To this end, this study will be primarily anchored in simulations and data from the CEPC. Leveraging the CEPC's advantageous features, such as its lower systematic uncertainties and cleaner background, we aim to provide a comprehensive analysis of LLP detection mechanisms and their underlying implications in a lepton-collider setting.

8.2 Event Generation and Simulation at CEPC

8.2.1 Overview of CEPC

The CEPC^[253-254] is engineered to function both as a Higgs boson factory with a center-of-mass energy (\sqrt{s}) of 240 GeV and as a Z boson factory at $\sqrt{s} = 91.2$ GeV. Additionally, it is capable of conducting threshold scans for W boson production around $\sqrt{s} = 160$ GeV. Table 8-1 outlines the likely operational modes and the projected yields of H, W, and Z bosons.

Operation mode	Z factory	WW threshold	Higgs factory
\sqrt{s} (GeV)	91.2	160	240
Run time (year)	2	1	7
Instantaneous luminosity ($10^{34} \text{ cm}^{-2} \text{ s}^{-1}$)	16 – 32	10	3
Integrated luminosity (ab^{-1})	8 – 16	2.6	5.6
Higgs boson yield	-	-	10^6
W boson yield	-	10^7	10^8
Z boson yield	$10^{11} - 10^{12}$	10^8	10^8

Table 8-1 Projected Operational Modes of CEPC and Corresponding Yields of Higgs, W, and Z Bosons; calculations Based on Two Interaction Points and Integrated Luminosity

During its seven-year tenure as a Higgs factory, the CEPC aims to generate roughly 1 million Higgs bosons at two interaction points. Concurrently, the collider is expected to yield nearly 100 million W bosons and approximately 1 billion Z bosons. Such large data sets serve dual purposes: detector calibration and precision measurements in electroweak

theory.

When operating around the W boson threshold of $\sqrt{s} = 160$ GeV, the CEPC is projected to produce about 10^7 W bosons within one year. In the Z boson factory mode, estimates suggest a production rate ranging from 10^{11} to 10^{12} Z bosons. These abundant samples facilitate highly precise measurements of a range of electroweak parameters.

8.2.1.1 Preliminary Detector Design

The primary aim of the CEPC experiments is an exhaustive study of Higgs boson properties. Consequently, detectors must exhibit high performance in identifying and reconstructing key physical entities such as charged leptons, photons, jets, and missing variables (energy and momentum). Flavor tagging of jets arising from b, c, or light quarks is particularly essential for isolating hadronic decay channels of the Higgs boson.

Tracking system	
Vertex detector	6 pixel layers
Silicon tracker	3 barrel layers, 6 forward disks on each side
Time projection chamber	220 radial readouts
Calorimetry	
ECAL	W/Si, $24X_0$, 5×5 mm ² cell with 30 layers
HCAL	Fe/RPC, 6λ , 10×10 mm ² cell with 40 layers
Performance	
Track momentum resolution	$\Delta(1/p_T) \sim 2 \times 10^{-5} (1/\text{GeV})$
Impact parameter resolution	$5\mu\text{m} \oplus 10\mu\text{m} / [(p/\text{GeV})(\sin\theta)^{3/2}]$
ECAL energy resolution	$\Delta E/E \sim 16\% / \sqrt{E/\text{GeV}} \oplus 1\%$
HCAL energy resolution	$\Delta E/E \sim 60\% / \sqrt{E/\text{GeV}} \oplus 1\%$

Table 8–2 Fundamental Specifications and Efficacy Metrics of the CEPC Detector System.

Inspired by the International Large Detector (ILD)^[255], the preliminary detector model for the CEPC is fundamentally aligned with a particle flow paradigm. This strategy is rooted in the principle of optimally employing individual sub-detectors to reconstruct visible final-state particles. The particle flow^[256–258] approach thus provides a unified interpretation of a complete event and is especially beneficial for tagging complex objects like τ leptons and

jets.

To achieve these goals, the CEPC features a low-material tracking system and high-granularity calorimetry, encapsulated within a 3.5 Tesla magnetic field. Key components include Silicon-based vertex and tracking detectors, a Time Projection Chamber (TPC), and advanced calorimeters. The geometric configurations and performance metrics for the CEPC detector are summarized in Table 8-2.

8.2.2 Event generation and simulation

Event generation and the ensuing simulation processes employ a gamut of specialized software tools tailored to accurately model both the SM signal and background events. Specifically, Whizard^[259] is utilized for generating a comprehensive dataset comprising Higgs boson signals alongside SM background events. Post-generation, these events are subjected to simulation and reconstruction via MokkaC^[260], which serves as the CEPC's official simulation software and is constructed upon the framework initially designed for ILC studies^[255].

Due to computational limitations, background event samples are occasionally subjected to pre-selection based on lax generator-level criteria or are alternatively processed using accelerated simulation tools. For a more granular simulation and reconstruction, Geant4^[52-53] is applied to all Higgs boson signal samples and a subset of leading background samples. The remaining background samples employ a dedicated fast simulation tool where various parameters such as detector acceptance, efficiency, and intrinsic resolution are suitably parameterized.

Table 8-3 enumerates the expected event yields for various processes at an integrated luminosity of 5.6 ab^{-1} . It should be noted that interference effects can manifest between the same final states originating from different processes subsequent to the decay of W or Z bosons (see the main text for details). The cross-section calculations for most processes are carried out using the Whizard program^[259]. For the Bhabha process specifically, cross-section values are computed using the BABAYAGA event generator^[261], with constraints imposed on the final-state particles ($|\cos \theta| < 0.99$) and any resulting photons (if present) to have $E_\gamma > 0.1 \text{ GeV}$ and $|\cos \theta_{e\pm\gamma}| < 0.99$.

Process	Cross section	Events in 5.6 ab ⁻¹
Higgs boson production, cross section in fb		
$e^+e^- \rightarrow ZH$	204.7	1.15×10^6
$e^+e^- \rightarrow \nu_e \bar{\nu}_e H$	6.85	3.84×10^4
$e^+e^- \rightarrow e^+e^- H$	0.63	3.53×10^3
Total	212.1	1.19×10^6
Background processes, cross section in pb		
$e^+e^- \rightarrow e^+e^- (\gamma)$ (Bhabha)	850	4.5×10^9
$e^+e^- \rightarrow q\bar{q}(\gamma)$	50.2	2.8×10^8
$e^+e^- \rightarrow \mu^+\mu^-(\gamma)$ [or $\tau^+\tau^-(\gamma)$]	4.40	2.5×10^7
$e^+e^- \rightarrow WW$	15.4	8.6×10^7
$e^+e^- \rightarrow ZZ$	1.03	5.8×10^6
$e^+e^- \rightarrow e^+e^- Z$	4.73	2.7×10^7
$e^+e^- \rightarrow e^+\nu W^-/e^-\bar{\nu}W^+$	5.14	2.9×10^7

Table 8–3 Cross-Section of Higgs and Background Processes at CEPC

8.2.3 LLP Signal Production

The primary mechanism for LLP signal production in this study is the Higgsstrahlung process $e^+e^- \rightarrow ZH$, where the Z boson is allowed to decay inclusively—that is, into any of its possible decay modes. Subsequently, the Higgs boson decays into a pair of LLPs $H \rightarrow X_1 X_2$. The specific channel under investigation assumes that X_1 decays into a pair of quarks ($X_1 \rightarrow qq$) while X_2 may either decay invisibly or similarly into quarks ($X_2 \rightarrow qq$). Figure 8-2 presents Feynman diagrams of two specific final state configurations, viz., $X_1 \rightarrow qq$, $X_2 \rightarrow$ invisible and $X_1 \rightarrow qq$, $X_2 \rightarrow qq$.

To simulate these processes, we utilize MADGRAPH5_AMC@NLO3.0^[262] for event generation. Signal samples are generated for three distinct mass points of X_1 and X_2 which are 1 GeV, 10 GeV, 50 GeV, and for five distinct lifetimes of 10^{-3} , 10^{-1} , 1, 10, 100 ns. At each point in this parameter space, a total of 10^6 events are generated for statistical robustness.

Signal acceptance is dictated in the generator level by the unique characteristics of LLPs, which decay according to exponential laws. Given the limitations of the CEPC detector, which has a maximum detection range of approximately 6 meters, special attention must be paid to the LLPs that decay within this confinement. To model this behavior accurately, LLPs are generated with intrinsic lifetimes and then Lorentz-boosted based on their respec-

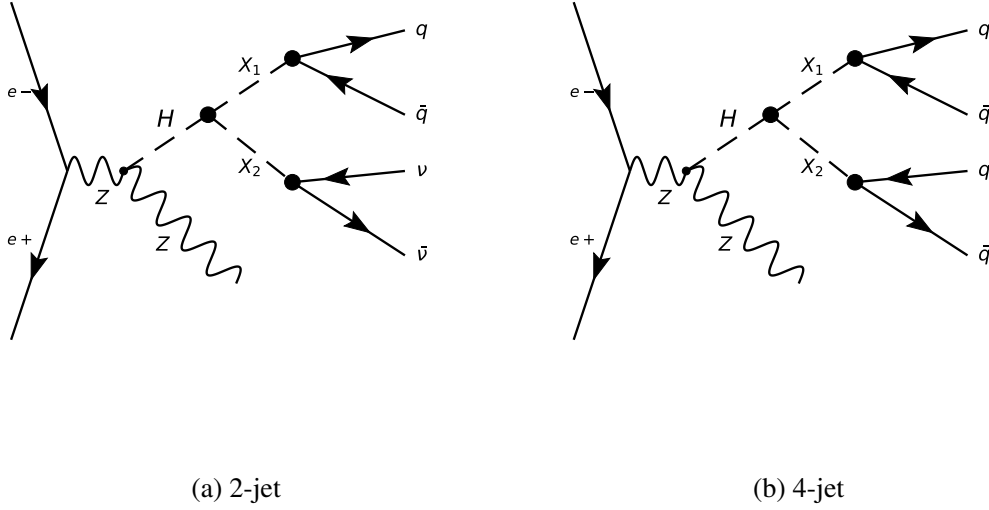


Figure 8–2 Feynman diagrams illustrating LLP production via the Higgsstrahlung process.

tive masses and momenta. Subsequently, we apply stringent selection criteria to only include those LLPs whose decay vertices fall within the physical boundaries of the CEPC detector. These selected events are then tabulated for further analysis, as shown in Table 8–4.

Mass (GeV)	Lifetime (ns)				
	0.001	0.1	1	10	100
50	1.0	1.0	1.0	0.993	0.404
10	1.0	1.0	0.998	0.468	0.062
1	1.0	1.0	0.488	0.065	0.007

Table 8–4 Signal Acceptance for Different Mass and Lifetime Parameters

8.3 Analysis Strategy

The cornerstone of the analysis strategy in this study is the application of machine learning techniques to directly analyze raw detector information. This approach deviates substantially from conventional LLPs studies that primarily focus on analyzing reconstructed object-level data. The motivation behind this unique methodology arises from the complexities associated with the LLP signal topology. In different ranges of the LLP decay vertex,

whether it is within the tracking detector, calorimeter, or muon spectrometer, the signal characteristics and corresponding Standard Model background processes can vary significantly. Traditional methods would necessitate categorizing multiple channels based on the LLP decay length, and potentially developing new reconstruction algorithms for each sub-category, thus complicating the analysis pipeline.

In contrast, our approach aims to streamline the analysis by directly using raw detector hits as input to classify LLP events from SM background events. This eliminates the need for segregating the dataset into multiple sub-channels and simplifies the overall analysis procedures. We utilize two machine learning algorithms, Convolutional Neural Networks (CNN) and Graph Neural Networks (GNN), in parallel for cross-validation. Both algorithms receive identical inputs and produce comparable outputs, enabling a more robust assessment of performance. Raw detector hits are first transformed into either image-like or graph-like structures, which are then fed into the neural networks to generate a five-class score. This preliminary classification is further refined using XGBoost^[263], which takes the predicted score probabilities to categorize the possible event classes. A final discriminant variable is computed, serving as the basis for the final statistical fitting of the data.

The analysis strategy is organized as followed. Section 8.3.2 introduces an image-based deep learning methodology using CNN. This section focuses on how event data is transformed into image format and details the configuration of the CNN model. Section 8.3.3 explores the use of GNN for event classification. In this part, the procedure to construct event graphs from raw calorimeter and tracker hits is elaborated, followed by the GNN network configuration. In Section 8.3.4, we employ XGBoost, to fine-tune the event selection process. Lastly, Section 8.3.5 offers an efficiency comparison between the CNN and GNN methods. The efficacy of each approach is evaluated post-application of XGBoost, providing an integrated perspective on the overall performance.

8.3.1 General Training Configuration

The training configuration primarily focuses on two aspects: background process determination and signal categorization, coupled with an evaluation strategy that ensures minimal bias and optimal resource utilization.

8.3.1.1 Background Processes:

The distinct decay signature of LLPs allows for minimal interference with Standard Model background processes. Nonetheless, some jet configurations could potentially resemble the LLP signal, as shown in Figure 8-1. As a result, we identify the $e^+e^- \rightarrow qq$ process, which exhibits the highest branching ratio for jet-related final states, as our primary background. This category is labeled the *2-fermion* background, and it now includes the SM ZH Higgs process when it results in 2-fermion final states.

In addition, we also consider other hadronic backgrounds featuring Z bosons in the final state as secondary background sources. These include $e^+e^- \rightarrow WW, ZZ \rightarrow \text{jets}$, known as the *4-fermion* backgrounds. The SM ZH Higgs process is also accounted for in this category when it leads to 4-fermion final states.

8.3.1.2 Signal Categorization:

Our analysis strategy centers on a refined method of classifying signals, moving away from the traditional emphasis on the types of particles in the final state. Rather than categorizing events based on the number of jets in the final state (i.e., 2-jet or 4-jet), the analysis centers on the number of detectable Long-Lived Particles (DLLPs), referred to as 0/1/2 – DLLP categories. This shift in focus allows us to account for a multitude of scenarios influenced by both the geometric constraints of the CEPC detector and the kinematic variables of the LLPs.

For example, in scenarios where X_1 decays outside the detection range while X_2 decays into an invisible state, the event falls into the 0 – DLLP category, implying zero detectable LLPs. Conversely, if X_1 decays within the detection range and X_2 either decays outside or into an invisible state, the event belongs to the 1 – DLLP category. Finally, events where both X_1 and X_2 decay within the detection range and yield visible decay products, specifically into jets, are classified under the 2 – DLLP category.

These categories form the basis for subsequent machine learning model training, using LLP kinematics and detector geometry. To establish a reliable model, the fraction of detectable LLPs in 2-jet and 4-jet final states is carefully estimated. This quantification is accomplished through truth-level information extracted from MC simulations. This MC-derived fraction serves as an essential template during the final statistical fitting procedures,

ensuring that our machine learning models are grounded in physically meaningful categorizations.

8.3.1.3 Training Schema

Given the five designated categories (0/1/2 – DLLP for the signal and 2-fermion and 4-fermion for the background), the preprocessed data serve as the input to various machine learning algorithms. Each algorithm produces a five-score array, where each score corresponds to a particular category.

Due to computational constraints and the exceedingly large number of background samples (10^8), we employ a subset of the available data for training. Specifically, only 10% of the total background samples are used. These background samples are sourced from the official CEPC MC production, while the signal samples are generated in-house.

To mitigate the introduction of biases and to ensure statistical rigor, a k-fold cross-validation strategy is adopted. The k-fold distribution is 3-fold for CNN, 5-fold for GNN, and 6-fold for XGBoost. This maintains orthogonality between the training, testing, and application datasets.

For the final evaluation stage, an unbiased application of the trained models is performed on the complete dataset, which includes both the 10% subset used for training and the remaining 90%. This comprehensive evaluation ensures maximum statistical efficiency while leveraging the limited computational resources effectively.

8.3.2 Image-based Deep Learning Analysis (CNN)

8.3.2.1 Event Image Construction

We initially embarked on an investigation that uses CNN to analyze events recorded by the CEPC detector. In this methodology, each captured event is converted into a two-dimensional, two-channel image with dimensions $R \times \phi = 200 \times 200$ pixels. Here, R signifies the radial distance from the interaction point to the position of a digital hit (digi), while ϕ denotes the azimuthal angle of the digi. Each event's raw digital hits are mapped into this coordinate system to construct the image.

The two channels serve distinct purposes: the E-channel is responsible for capturing energy deposition, and the T-channel records time differences defined in Equation 8-1. Specifically, the E-channel aggregates the energy of all digital hits contained within each pixel. In

contrast, the T-channel computes the maximum time difference $\Delta t = t_{\text{digi}} - \frac{R_{\text{digi}}}{c}$ among raw hits with an energy deposition greater than 0.1 GeV, aiming to filter out electronic noise.

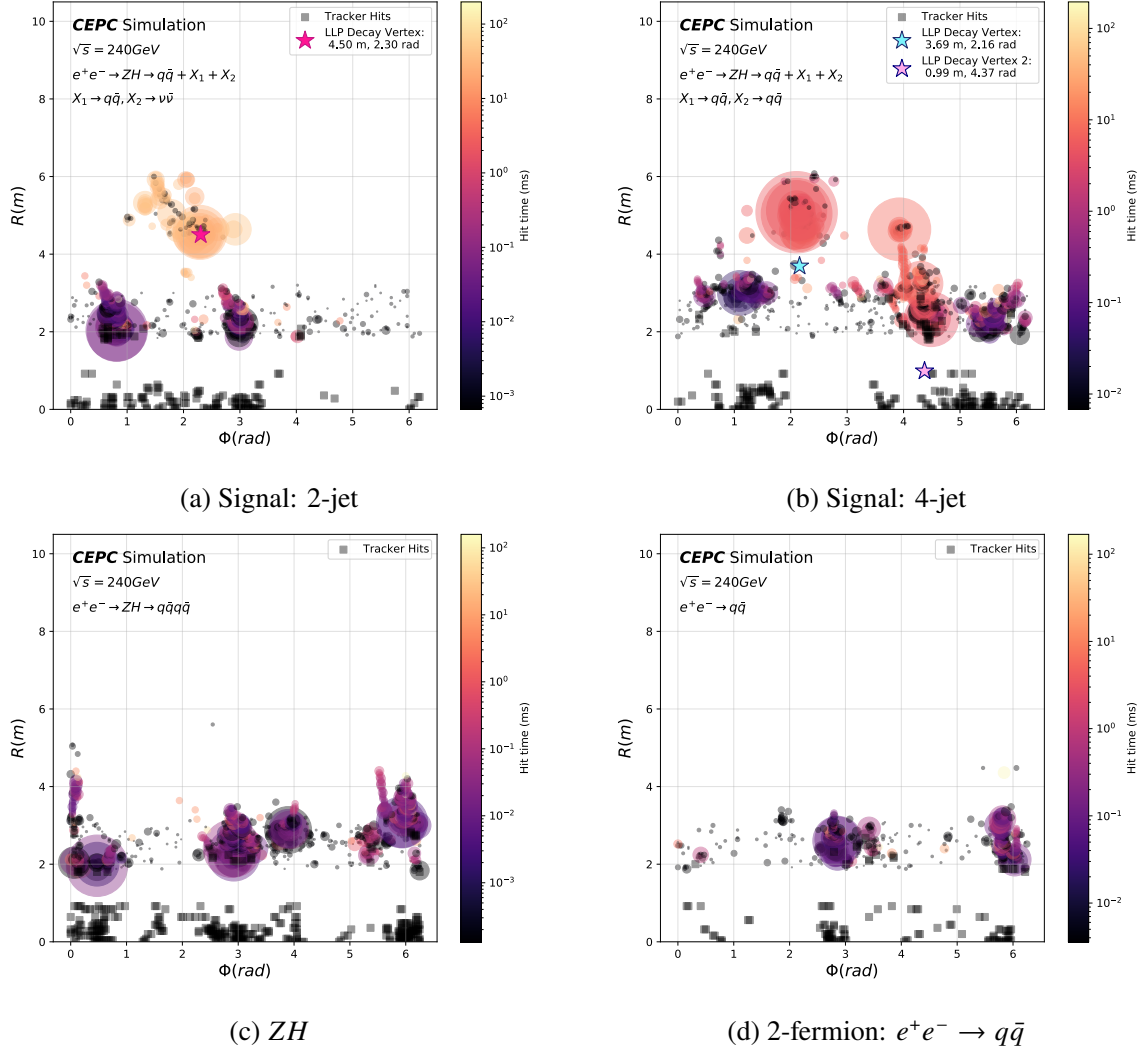


Figure 8-3 Illustration of image built from raw detector hits for four different processes.

In Figure 8-3, four representative images are showcased, illustrating both signal and background events pertinent to two-jet and four-jet final states. In these images, three types of graphical symbols are employed for clarity: a star symbol marks the decay vertex of the LLP, serving as a reference point for the event topology, while circular symbols represent the hits as detected by the calorimeter and the muon spectrometer and square markers are the tracker hits. The size of each circle is proportional to the energy deposition, with a larger circle indicating a greater amount of deposited energy. The color intensity of both the squares

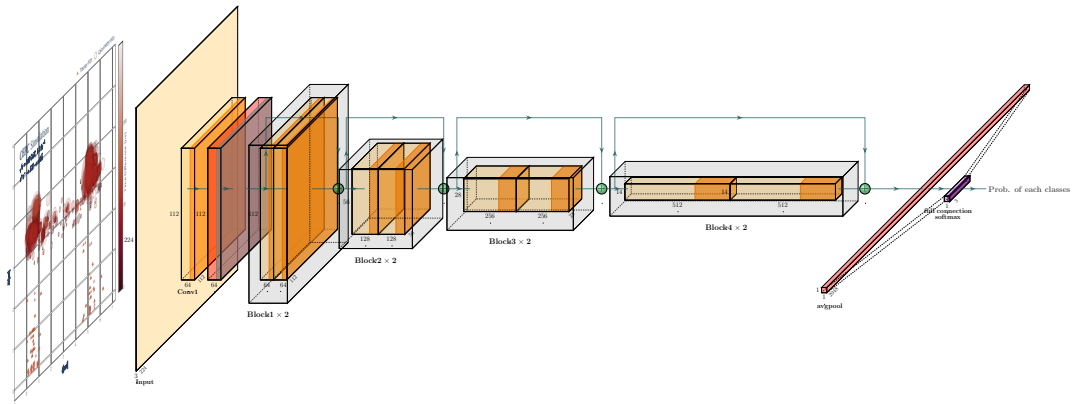


Figure 8-4 Illustration of the architecture of ResNet-18 based neural network.

and circles signifies the time of arrival, with darker hues corresponding to earlier times. This pixel-based representation proves effective in discriminating between signal and background events. Specifically, background events generally lack a displaced vertex and tend to show larger energy depositions in the inner detectors, distinguishing them from signal events.

8.3.2.2 Network Configuration

The choice of the appropriate CNN model for our analysis is far from trivial, particularly due to the unique LLP signatures and their displaced vertices. To this end, we employ a well-known CNN model, ResNet^[264], originally developed for the ImageNet Large Scale Visual Recognition Challenge (ILSVRC) in 2015. The architecture of the ResNet-18 model is detailed in Figure 8-4. ResNet offers the advantage of scalability and efficiency; it can be configured to operate both as a shallow network for simpler tasks and as a deep network for more complex tasks. This flexibility minimizes the need for extensive model modifications tailored to specific tasks.

The learning rate is a crucial hyperparameter that necessitates careful tuning. For our LLP-specific tasks across all mass and lifetime regimes, we have observed rapid model convergence with a relatively low number of epochs (≈ 15). This suggests that the learning rate can be kept relatively constant, although a task-specific learning rate schedule may further optimize the training process.

The network's raw output is further processed using the softmax function to generate a

five-class prediction array, mathematically represented as follows:

$$\text{Softmax}(\text{Score}) = \frac{e^{\text{Score}_i}}{\sum_j e^{\text{Score}_j}}$$

For this multi-class classification problem, we employ the cross-entropy loss function, defined as:

$$\mathcal{L} = - \sum_i y_i \log(p_i)$$

Where y_i is the true label and p_i is the predicted probability for class i .

8.3.3 Graph-based Deep Learning Analysis (GNN)

8.3.3.1 Event Graph Construction

To extend the predictive power and feature representation capabilities of our model, we employ Graph Neural Networks (GNNs). These are particularly useful for capturing the complex topological structures inherent in high-energy particle collision events.

Node Types and Edge Construction: In a single collision event, we represent the raw calorimeter and tracker hits as a heterogeneous graph, comprising two types of nodes: one for calorimeter hits, referred to as *calorimeter-type nodes*, and the other for tracker hits, referred to as *tracker-type nodes*. Within each type, all nodes are fully connected, meaning that every node is directly connected to every other node of the same type.

Calorimeter-Type Node Formation: For calorimeter-type nodes, a clustering algorithm is employed. The most energetic calorimeter hit is identified within the event, and it serves as a seed for the clustering process. This seed clusters together all neighboring hits that are within a pre-defined radial distance $R = 50$ mm. To control the quality of clustering, we enforce two specific criteria:

- Minimum number of neighboring hits in the cluster, $N_{\text{neighbor}} \geq 3$.
- Minimum number of total hits for forming a valid cluster, $N_{\text{cluster}} \geq 10$.

Momentum Assignment to Calorimeter-Type Nodes: Following the clustering, each calorimeter-type node is assigned a four-momentum p^μ . This momentum is defined as being parallel to the node's position vector, with a magnitude determined by the energy of the calorimeter hit.

Tracker-Type Node Formation: Tracker hits are organized into spatial blocks based on their $R - \phi$ coordinates. Given computational considerations, the division is designed into 5×6 blocks. Within each block, tracker hits are aggregated into a tracker-type node, with the node's features being the average spatial position and the summed hit count within the block.

Feature Translation: Both calorimeter and tracker features are then transformed into a unified graph-based representation, creating a feature-rich event-level description. The specific definitions of the node and edge features are meticulously cataloged in Table 8-5.

Features	Variable	Definition
calorimeter type node i	$ x_i^\mu $	the space-time interval
	$ p_i^\mu $	the invariant mass
	N_i	the number of hits
	η_i	$\frac{1}{2} \ln \frac{1+\frac{p_z}{p}}{1-\frac{p_z}{p}}$
	ϕ_i	$\arctan \frac{p_y}{p_x}$
	R_i	$\sqrt{\eta^2 + \phi^2}$
calorimeter type edge between node i and j	$x_i^\mu x_{j\mu}, p_i^\mu p_{j\mu}, x_i^\mu p_{j\mu}, p_i^\mu x_{j\mu}$ $ x_i^\mu - x_j^\mu , p_i^\mu - p_j^\mu , \eta_i - \eta_j, \phi_i - \phi_j, R_i - R_j$	
tracker type node i	$ r $	euclidean distance
	N_i	the number of hits
	η_i	$\frac{1}{2} \ln \frac{1+\frac{z}{r}}{1-\frac{z}{r}}$
	ϕ_i	$\arctan \frac{y}{x}$
	R_i	$\sqrt{\eta^2 + \phi^2}$
tracker type edge between node i and j	$ r_i - r_j , r_i r_j, \eta_i - \eta_j, \phi_i - \phi_j, R_i - R_j$	

Table 8-5 Node and edge features defined in the heterogenous graph.

8.3.3.2 Network Configuration

To use the topological features of LLP events, we utilize a sophisticated GNN-based heterogeneous architecture, as illustrated in Figure 8-5.

Initial node and edge features are embedded into a high-dimensional latent space. These embeddings serve as inputs to the Heterogeneous Detector Information Block (HDIB), which orchestrates message passing between calorimeter and tracker nodes.

The HDIB comprises two Detector Information Blocks (DIBs) and two Multilayer Per-

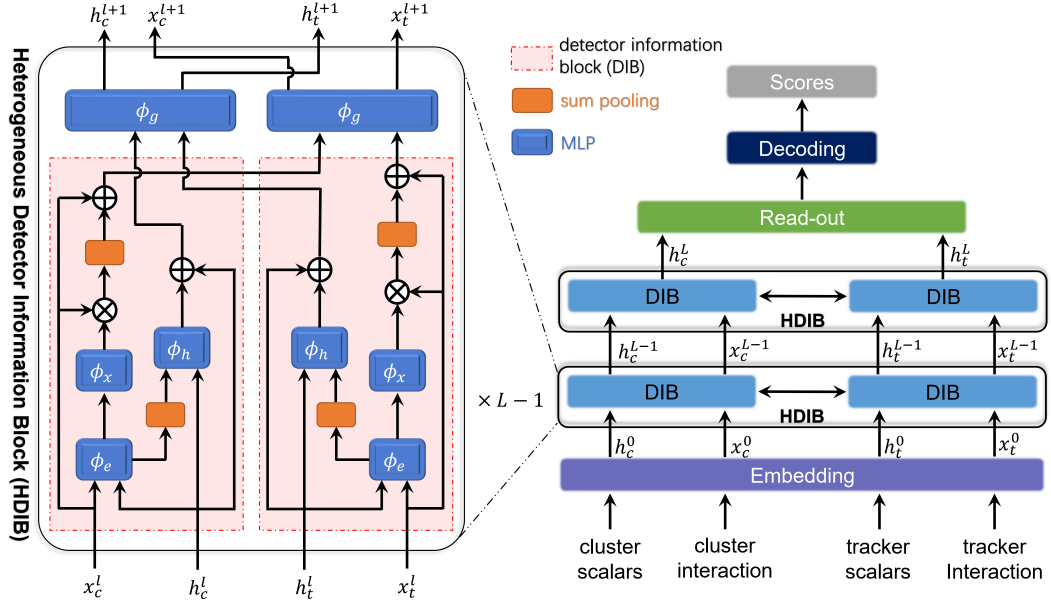


Figure 8-5 Illustration of the architecture of the GNN-based neural network.

ceptors (MLPs), designated as ϕ_g . Each DIB focuses on processing the node and edge embeddings of either tracker or calorimeter hits. Inspired by LorentzNet^[263], we have extended the DIB architecture to accommodate heterogeneous graphs.

The DIB outputs serve as the latent spaces for the node features h^l and edge features x^l at each layer l . These are computed separately for tracker and calorimeter nodes as h_t^l and h_c^l , respectively.

Since tracker and calorimeter nodes are not directly connected in the heterogeneous graph, their latent spaces are concatenated and processed through a MLP ϕ_g . The outputs of ϕ_g are reshaped to obtain the updated latent spaces h^{l+1} and x^{l+1} . This scheme facilitates the adaptive exchange of information between tracker and calorimeter nodes.

Following L layers of HDIBs, the final node embeddings h^L are aggregated and fed into the decode layer to yield classification scores.

Training Configuration:

- **Hardware:** The model is trained on a cluster with 8 NVIDIA Tesla V100S PCIE 32 GB GPUs.
- **Batch Size:** Each GPU processes a batch size of 256 graphs.
- **Learning Rate:** An initial learning rate of 10^{-4} is employed.

- **Dropout Rate:** A dropout rate of 0.1 is applied to mitigate overfitting.
- **Optimizer:** Adam optimizer is used without weight decay.
- **Epochs:** The network is trained for a total of 30 epochs, with validation performed at the end of each epoch.
- **Model Selection:** The model exhibiting the minimum validation loss is chosen for application to the final test dataset.

8.3.4 Event selection with XGBoost

Due to the complexity of the feature space, particularly with five predicted class scores from the neural networks (CNN and GNN), direct rectangular cuts prove to be inefficient for event categorization. Thus, we opt to employ the gradient boosting framework XGBoost to refine the event selection process. The XGBoost model takes the five class-predicted scores as input features and outputs a final discriminant value.

The XGBoost model is trained on three distinct signal categories, namely 0-DLLP, 1-DLLP, and 2-DLLP. The aim is to optimize the discriminant cut for each category such that the background contribution becomes negligible. Subsequently, the cut efficiency within each category essentially represents the signal efficiency in the absence of background contamination.

In order to assess the signal efficiency tailored to distinct final states, such as the 2-jet and 4-jet scenarios, the output from the XGBoost model is divided into regions. These regions are predicated upon the number of Detectable Long-Lived Particles (DLLPs) present, and are denoted as $nDLLP_0$, $nDLLP_1$, and $nDLLP_2$.

For systematic representation, we introduce an efficiency matrix, $\mathbf{E} \in \mathbb{R}^{2 \times 3}$, where the rows correspond to the 2-jet and 4-jet final states, and the columns correspond to the aforementioned $nDLLP$ regions. Mathematically, the matrix is defined as:

$$\mathbf{E} = \begin{pmatrix} E_{00} & E_{01} & E_{02} \\ E_{10} & E_{11} & E_{12} \end{pmatrix}, \quad (8-2)$$

where E_{ij} denotes the efficiency for the i -th final state in the j -th $nDLLP$ region.

The elements of \mathbf{E} are subsequently utilized in the computation of the expected signal yields, Y_{ij} , defined as:

$$Y_{ij} = E_{ij} \times \text{Acceptance}, \quad (8-3)$$

Where acceptance can be obtained in Table 8-4. These expected yields serve as critical parameters in the subsequent stages of statistical fitting.

8.3.5 Efficiency comparison between CNN and GNN

To provide an aggregate assessment of the efficiency of CNN and GNN in classifying events, the signal efficiencies were weighted across all sub-channels, namely the 2-jet and 4-jet categories. The results are compiled in a table that details these efficiencies under various scenarios, taking into account both the mass and lifetime parameters of the LLPs.

Approach	Efficiency	Lifetime [ns]				
	Mass [GeV]	0.001	0.1	1	10	100
CNN	1	0.82	0.90	0.79	0.74	0.77
	10	0.80	0.89	0.90	0.89	0.84
	50	0.88	0.96	0.99	0.98	0.93
GNN	1	0.83	0.89	0.80	0.80	0.79
	10	0.77	0.86	0.92	0.86	0.84
	50	0.88	0.92	0.97	0.97	0.93

Table 8-6 Signal efficiencies for different assumptions of LLPs' mass and lifetime obtained with CNN-based and GNN-based approaches.

From Table 8-6, it is evident that both CNN and GNN manifest high signal efficiencies, with the majority of the data points exceeding an 80% efficiency threshold. This robust performance is consistent across different LLP mass and lifetime considerations. Specifically, for low mass (1 GeV) scenarios, both CNN and GNN achieve efficiencies in the approximate range of 0.80 – 0.83, and similar behavior is observed for medium (10 GeV) and high (50 GeV) mass LLPs.

It is noteworthy that the efficiencies obtained from both CNN and GNN methods are remarkably consistent, thereby reinforcing the robustness of these deep learning architectures in handling complex classification tasks. The product of acceptance and efficiency, which serves as both a critical metric for the performance evaluation and the final input for statistical interpretation, is further illustrated in Figure 8-6.

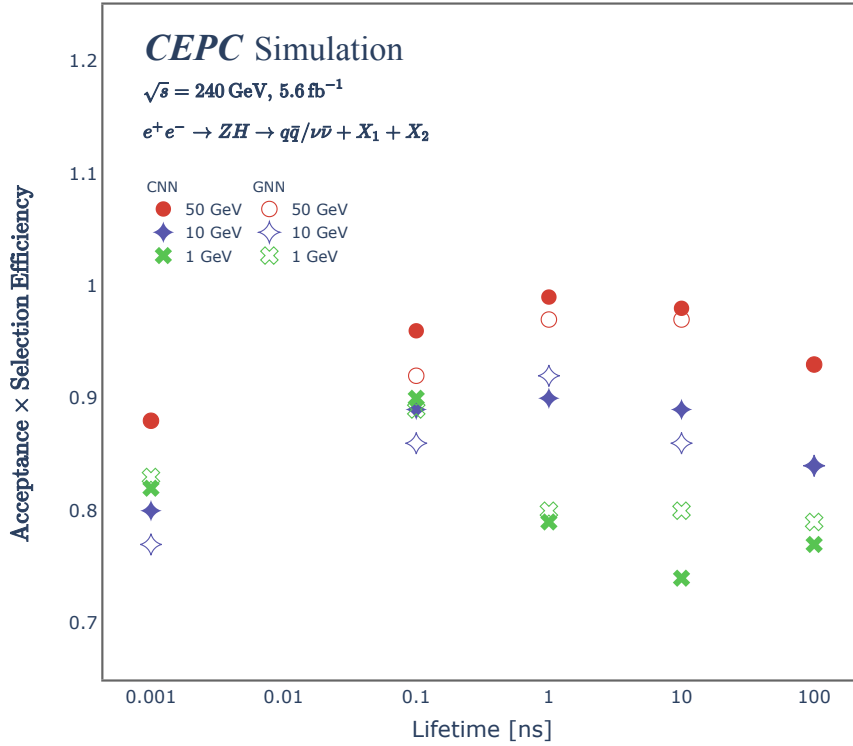


Figure 8–6 The product of signal efficiencies and acceptance for different assumptions of LLPs' mass and lifetime obtained with CNN-based (solid) and GNN-based (dot) approaches.

8.4 Results

Contrary to the CL_s approach commonly employed in di-Higgs search studies, the present analysis does not permit the use of approximate estimations for exclusion limits. This limitation is imposed by the specific condition of having zero background events. To circumvent this, we employ a statistical toy model to compute the upper limits. This model generates pseudo-experiments based on the predicted signal and observed data, allowing for a more robust estimation of the exclusion limits.

Several sources of systematic uncertainties are taken into account. The uncertainty originating from the total number of Higgs bosons is estimated at 1.0%^[26d]. The ML-related uncertainty mainly encompasses network initialization. To assess this uncertainty, we change the random seed during the training and evaluate the corresponding signal efficiency using XGBoost. We obtain 50 different signal efficiencies with different random seeds. The uncertainty is then estimated as half of the difference between the maximum and minimum values and is about 1.7%. Overall, the combined systematic uncertainties are quadratically summed

to be 2.0%.

To estimate the sensitivity of the study, we assume a null hypothesis for LLPs signals and obtain 95% Confidence Level upper limits on the branching ratio $\mathcal{B}(H \rightarrow \text{LLPs})$ for the process $e^+e^- \rightarrow ZH (Z \rightarrow \text{inclusive}, H \rightarrow X_1 + X_2)$. The analyzed samples have a 5.6 ab^{-1} luminosity and about 10^6 Higgs bosons.

For the two LLPs signal types, we have considered the following scenarios:

- Type I and Type II signal yields have a fixed ratio. We define a parameter $\epsilon_V := \frac{BR(X \rightarrow \nu \bar{\nu})}{BR(X \rightarrow q \bar{q})}$ as the ratio and set it with a fixed value of 0.2. A one-dimensional 95% Confidence Level upper limit on $\mathcal{B}(H \rightarrow \text{LLPs})$ is derived and shown in Figure 8-7a.
- Type I and Type II signal yields has a floating ratio and We allow ϵ_V to be between 10^{-6} and 100. A one-dimensional 95% Confidence Level upper limit on $\mathcal{B}(H \rightarrow \text{LLPs})$ is derived and shown in Figure 8-7b.
- Type I and Type II signal yields has a floating ratio and two-dimensional 95% Confidence Level upper limits on $\mathcal{B}_{2\text{-jet}}$ and $\mathcal{B}_{4\text{-jet}}$ are derived. A bivariate statistical fit is performed to derive the upper limits and results are shown in Figure 8-8. More detailed results on 2-D upper limits are shown in Figure 8-9.

Both 1-D and 2-D exclusion limits are summarized in Table 8-7.

Scenario	$\mathcal{B} (\times 10^{-6})$	Lifetime [ns]				
	Mass [GeV]	0.001	0.1	1	10	100
Fixed	1	7	6	19	117	3394
	10	10	7	8	18	99
	50	6	4	5	5	13
Floated	1	11	8	12	74	2395
	10	12	10	5	11	65
	50	8	10	7	8	9

Table 8-7 The 95% C.L. exclusion limit on $BR(h \rightarrow X_1 X_2)$ for all signal channels: fixed and floated ϵ_V , based on CNN's efficiency.

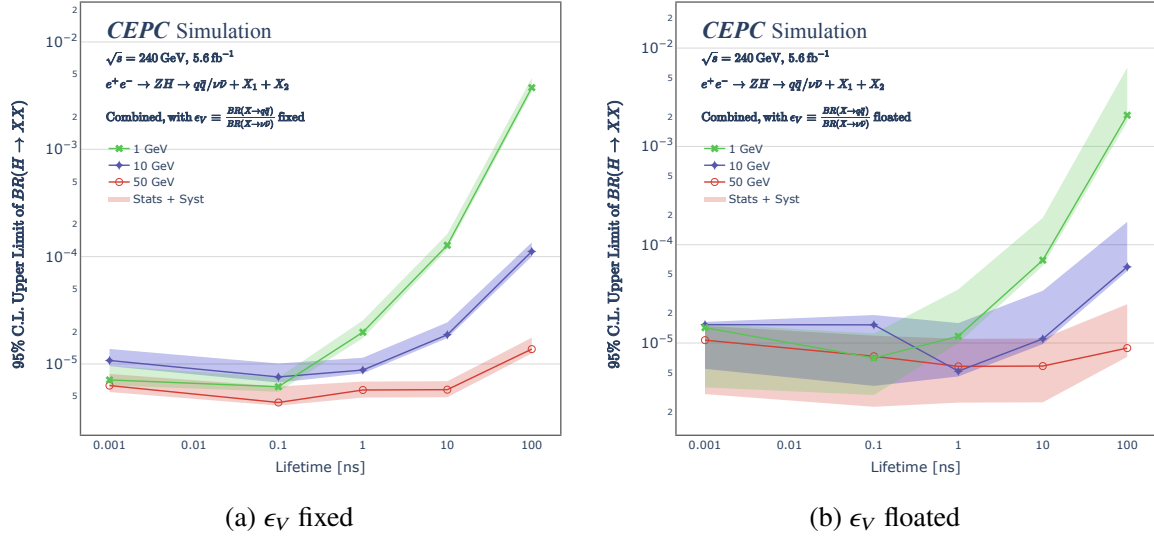


Figure 8-7 The 95% C.L. upper limit on $BR(h \rightarrow X_1 X_2)$ for the process $e^+e^- \rightarrow Zh$ with the condition of ϵ_V fixed (left) and ϵ_V floated (right), where $\epsilon_V := \frac{BR(X \rightarrow \nu \bar{\nu})}{BR(X \rightarrow q \bar{q})}$. Different colored lines indicate different LLPs masses. Shaded area indicate statistical and systematic uncertainties combined.

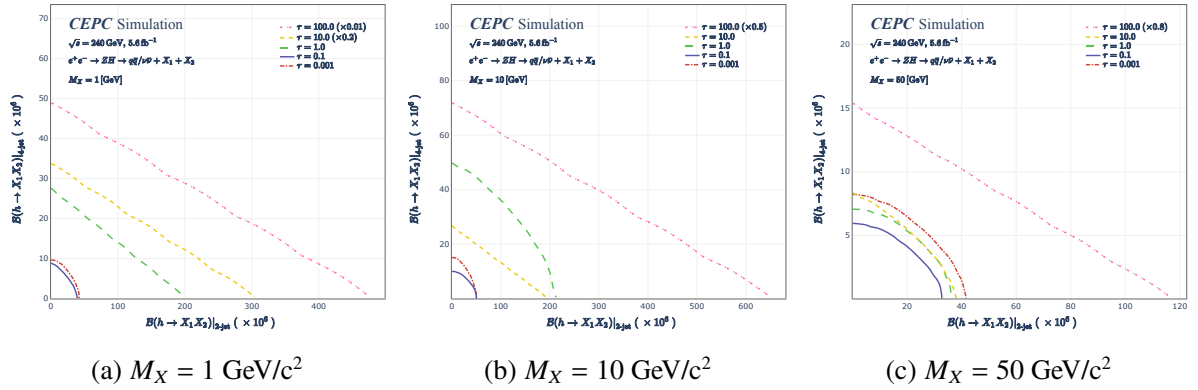


Figure 8-8 The 95% C.L. 2-D upper limit on $(\mathcal{B}_{2\text{-jet}}, \mathcal{B}_{4\text{-jet}})$ for the process $e^+e^- \rightarrow Zh$ for three LLPs masses 50 GeV (left), 10 GeV (middle), 1 GeV (right). Different colored lines indicate different LLPs lifetimes. The uncertainties on the limits are omitted and a few limits are scaled by a factor for better visibility.

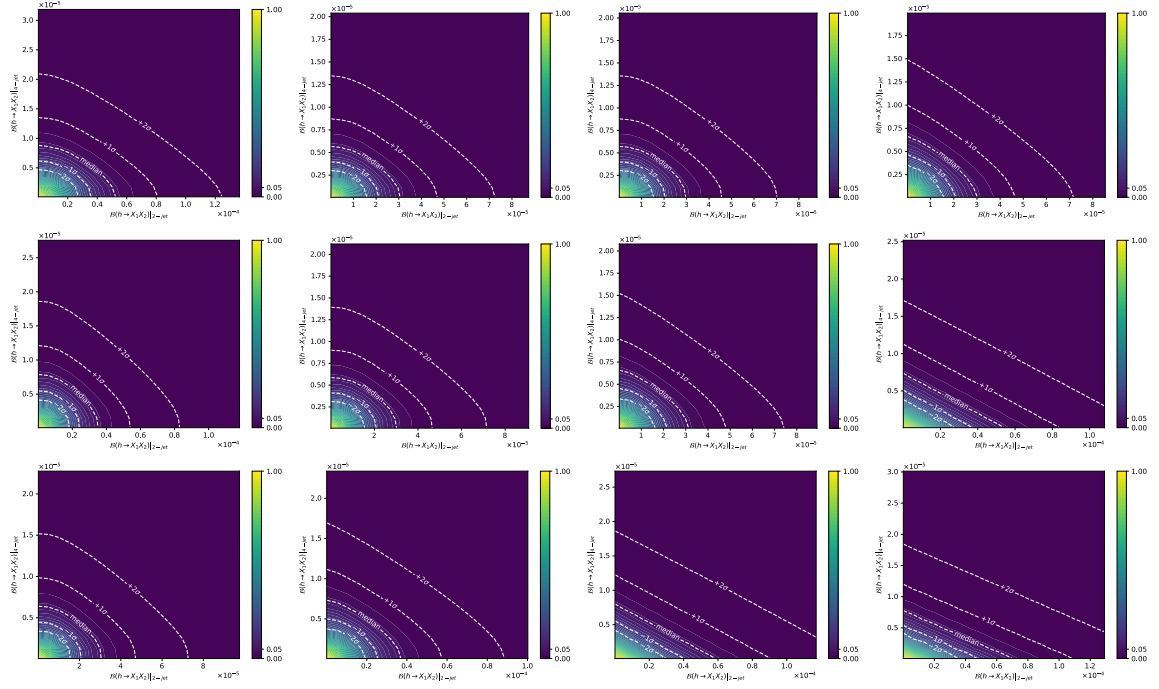


Figure 8-9 The 2D fitting for $(\mathcal{B}_{2\text{-jet}}, \mathcal{B}_{4\text{-jet}})$. From top to bottom, the mass is 50, 10, 1 GeV/c^2 ; From left to right, the lifetime is 0.0001, 0.1, 1.0, 10 ns.

8.5 Discussion and Summary

8.5.1 Comparison with Hadron Colliders: ATLAS and CMS

We evaluate the effectiveness of our ML-based approach for LLPs detection at future lepton colliders by comparing our results with results at hadron colliders with the ATLAS experiment^[250] and CMS experiment^[251] as well as future HL-LHC experiments^[267]. The comparison is based on four primary metrics: signal acceptance, selection efficiency, analysis strategy and signal yields:

- **Signal Acceptance:** Both ATLAS and CMS results have limited signal acceptance, typically a few percent, as they focus on LLPs decaying in the muon detector. In contrast, our ML-based approach covers the entire detector, resulting in 100% signal acceptance except for LLPs with long lifetime (> 1 ns) and low mass (< 1 GeV).
- **Selection Efficiency:** For hadron colliders, LLPs events typically trigger on displaced decays and/or large missing transverse energy. The LLPs trigger efficiency at the ATLAS experiment is estimated to be between 10^{-3} and 0.3^[250]. Besides trigger efficiency, there are additional efficiencies involved such as displaced vertex/object re-

construction efficiencies which are typically in the order of a few percent. In contrast, LLPs event selection at lepton colliders can adapt to a triggerless approach owing to the clean environment. ML-based approach can be applied directly with low-level detector information without any event-level reconstruction. As a result, our ML-based approach with lepton colliders can achieve an overall selection efficiency as high as 99%, an improvement of several orders in magnitude when comparing with LHC or HL-LHC efficiencies.

- **Analysis Strategy:** Traditionally, analyses of LLPs conducted elsewhere have employed a selection-based method, which involves categorizing events into multiple subsets with different decay modes and orthogonal signal types. These analyses necessitate manual re-tuning and re-optimization for each subset and different LLPs mass and lifetime configurations. In contrast, our ML-based approach eliminates the need for manual categorization and optimization. Deep neural networks can be retrained automatically for each LLPs mass and lifetime, resulting in higher efficiencies compared to the selection-based method.
- **Signal Yields and Upper Limits Comparison:** LHC and HL-LHC can produce a significantly larger number of Higgs bosons compared to lepton colliders. Despite this, higher signal acceptance and selection efficiencies in our ML-based approach compensate for the relatively low number of Higgs bosons. We achieve upper limits as low as 4×10^{-6} on $\mathcal{B}(H \rightarrow \text{LLPs})$ with 1×10^6 Higgs bosons. This upper limit is approximately three orders of magnitude better than the 10^{-3} limit observed at the ATLAS and CMS experiments with 10^7 Higgs bosons and it is comparable to the projected HL-LHC limit with about 10^8 expected Higgs bosons.

Besides comparing with hadron colliders, we have also compared our result with a preliminary study^[268] on the ILC sensitivity^[269] with a traditional selection-based method. The ILC sensitivity study searches for long-lived dark photons produced in Higgstrahlung events via the Higgs portal. We have compared our result with the hadronic decay dark photo result since the event signature is similar. We have seen that the signal acceptance factors are similar between ILC and CEPC detectors but the signal efficiencies differ significantly. The signal efficiencies in the ILC study range from 0.1% to 10%, which is at least an order of magnitude lower than ours. The upper limits on $\mathcal{B}(H \rightarrow \text{LLPs})$ in the ILC study are derived

under the assumption of 100% truth-level signal efficiency. Only after making this assumption, two results show similar sensitivities in the low lifetime region ($< 1 \text{ ns}$) of LLPs. In the long lifetime region, for example, for a 1 GeV LLP with a lifetime of a few nanoseconds, our result yields an upper limit of about 10^{-5} which is an order of magnitude better than the ILC's upper limit of 10^{-4} .

In summary, we have developed a ML-based approach for LLP searches that outperforms traditional selection-based methods on almost all fronts. Moreover, our ML-based approach can be easily applied to other future lepton collider experiments, including the ILC, FCC^[270], and CLIC^[271].

Chapter 9 Summary and Future prospects

As we reach the concluding chapter of this dissertation, it is both timely and essential to circle back to the fundamental questions and theoretical frameworks that have informed these diverse yet interconnected endeavors. The Standard Model (SM) of particle physics provides the backbone for understanding the elemental building blocks and interactions that shape our universe. While this framework has been corroborated by a multitude of experimental findings, it nonetheless presents outstanding questions that beckon further scrutiny. Notably, the Higgs sector remains a significant arena for exploration, both to corroborate the SM and to potentially unearth phenomena that lie Beyond the Standard Model.

A parameter of particular interest within this sector is the Higgs boson's self-coupling which holds far-reaching implications for the stability of our universe. The observation and measurement of this unique interaction is a central goal of elementary particle physics research. Understanding it requires not just the identification and study of individual Higgs bosons but also the complex interactions in di-Higgs events. Moreover, this serves as a possible gateway to explore yet unidentified particles and interactions, opening up new horizons for physics beyond our current understanding.

In this dissertation, the first analysis is based on a luminosity of 140 fb^{-1} of proton-proton collision data at $\sqrt{s} = 13 \text{ TeV}$, collected by the ATLAS detector during Run 2 of the LHC. The focus of this work is on the SM Higgs pair (HH) production in 3-lepton final states, predominantly produced via gluon-gluon fusion (ggF) with Vector Boson Fusion (VBF) as an additional signal yield. The primary background, WZ , known for mismodelling in high jet multiplicities, is reweighted using a fitting function. The secondary background arises from fake leptons, estimated via the Template Fit method. Three normalization factors were extracted from multiple control regions to quantify the fake lepton backgrounds. A multivariate analysis strategy employing Gradient Boosted Decision Trees was utilized to optimize the signal and background discrimination. To make full use of the available Monte Carlo statistics, a 3-fold training method was implemented to improve the smoothness of the Receiver Operating Characteristic (ROC) curve. Detailed hyperparameter tuning was performed for model optimization. Our 3-lepton channel has attained a maximum signal significance of 0.073, with an upper limit of $23.13^{+10.21}_{-6.66}$ on the $HH \rightarrow 3\ell$ cross-section relative to the SM.

When including all uncertainties, the limit stands at $28.09^{+12.81}_{-7.86}$. This represents a 9.4-fold improvement in the upper limit compared to the prior analysis in the $HH \rightarrow WW^*WW^* \rightarrow 3\ell$ channel. In the combined multilepton results, the expected upper limit is $8.93^{+12.69}_{-6.44}$ statistically and $9.74^{+13.91}_{-7.02}$ including all systematic uncertainties. Notably, this 3-lepton channel offers the most robust results among pure leptonic channels and is very close to the leading $\gamma\gamma + 1\ell$ channel. I have been responsible for the entire 3-lepton analysis strategy, acted as the internal note editor, and represented our multilepton group in several editorial board meetings and unblinding request approval talks. Upon the completion of the ATLAS internal review, this analysis is poised to make a significant contribution to HH searches.

The second analysis of the dissertation is the $HH \rightarrow b\bar{b}\tau^+\tau^-$ analysis, which builds upon previous work with 140 fb^{-1} of Full Run 2 data and aims to refine methodological approaches, primarily in the context of the κ_λ and κ_{2V} modifiers. Contrary to the legacy analysis, which was primarily optimized for the gluon-gluon fusion SM production mode, the present study employs advanced Multivariate Analysis techniques for optimal signal-background separation. These techniques are focused on an event categorization based on the invariant mass of the HH system (m_{HH}) in the ggF region and also incorporate a dedicated VBF category to improve sensitivity to the κ_{2V} parameter. The utilization of MVA outputs as final discriminants in the fit has led to notable improvements over the legacy data. Specifically, we have achieved a 17% improvement in the baseline with systematics for μ_{HH} and an 11.9% (19.8%) improvement in the 95% confidence interval for κ_λ (κ_{2V}). Within the $HH \rightarrow b\bar{b}\tau^+\tau^-$ working group, my research has been centered around the application and optimization of BDTs for the separation of ggF and VBF regions and signal-background separation in each signal region. This involved detailed study and optimization of BDT hyperparameters and input variables, exerting a direct influence on the final analysis results.

The $HH+H$ combination analysis serves as a study that amalgamates the primary double-Higgs analyses ($HH \rightarrow b\bar{b}b\bar{b}$, $HH \rightarrow b\bar{b}\gamma\gamma$, $HH \rightarrow b\bar{b}\tau^+\tau^-$) with the single-Higgs workspace. This integrated approach is specifically designed to furnish rigorous constraints on the coupling modifiers, chiefly κ_λ and κ_{2V} . In the most generalized fit that allows multiple coupling modifiers, κ_t , κ_b , κ_τ , and κ_V , to vary freely, we report a 95% confidence level interval of $-1.4 < \kappa_\lambda < 6.1$, closely mirroring the expected bounds of $-2.2 < \kappa_\lambda < 7.7$. The robustness of these constraints is underscored by a negligible sensitivity to variations in κ_{2V} ,

which affect the observed κ_λ bounds by less than 5%. This serves to affirm the agreement of all other coupling modifiers with the SM within the associated uncertainties. My specific role in this undertaking involved the consolidation of the double-Higgs workspaces, facilitating their subsequent integration into the single-Higgs analysis.

Within the scope of ATLAS experiments, the research began with an exploration into the $HH \rightarrow$ multilepton channel. This served as an entry point for engaging with a full-chain analysis, encompassing every phase from production to final results. Subsequently, the research focus shifted to the $HH \rightarrow b\bar{b}\tau^+\tau^-$ channel, which offered an extensive environment for delving into the nuances of BDTs. Detailed investigations into BDT behaviors were conducted, leading to a comprehensive understanding of their effects on the analysis. Lastly, the research culminated in a combined HH+H study. This phase provided a broader framework for understanding di-Higgs phenomena, particularly illuminating the interplay between single-Higgs and double-Higgs processes as well as the roles of various κ modifiers. This structured research trajectory has thus facilitated not only specific channel-based insights but also a more integrative view of di-Higgs physics.

In a natural progression from exploring the complex landscape of di-Higgs interactions, the research embarks on an expedition into realms beyond the SM, specifically addressing the Higgs decays into Long-Lived Particles (LLPs). Utilizing a novel analytical framework, designed for the forthcoming future Lepton Colliders, the study uses the power of convolutional neural networks (CNNs) and graph neural networks (GNNs) directly on raw detector data. These machine-learning models have not only yielded consistent results but have also simplified the analytical landscape. Remarkably, this approach has achieved an expected upper limit of approximately 4×10^{-6} , significantly outperforming the 1×10^{-3} limits set by hadron colliders such as ATLAS and CMS. Furthermore, when compared with lepton colliders like the International Linear Collider (ILC), this methodology outperforms by nearly an order of magnitude in expected exclusion limits for LLPs with lifetimes larger than 1 ns.

Both the $HH \rightarrow$ multilepton and $HH \rightarrow b\bar{b}\tau^+\tau^-$ analyses currently face statistical limitations as their primary constraint. The anticipated doubling of data statistics in ATLAS Run 3 will improve the sensitivity to these channels. Concurrent advancements in algorithms and detector technologies, such as the recently introduced PromptLeptonVeto (PLV) reducing fake lepton backgrounds, signify promising avenues for further refinement. While

the $HH \rightarrow$ multilepton benefits from reduced fake lepton backgrounds, the $HH \rightarrow b\bar{b}\tau^+\tau^-$ stands to gain from enhanced b-jet and tau-lepton tagging technologies. These developments collectively herald a more robust and precise di-Higgs measurement in future ATLAS runs.

The principal bottleneck in expanding the LLP study to a more general-purpose collider analysis is computational power. The application of advanced machine learning algorithms like CNNs and GNNs directly on raw collider data requires significant computational resources. Specifically, the memory requirements for handling large datasets present a limiting factor. Future work will focus on acquiring more computational power and exploring algorithmic modifications to accommodate large-scale data without sacrificing the integrity of the analysis. This expansion in computational capacity will not only benefit LLP studies but also potentially revolutionize broader applications within Beyond the Standard Model physics.

Through simulation-based analysis in the DarkSHINE experiments, the study effectively suppresses background noise, resulting in an expected background yield of 0.015 for 3×10^{14} electrons on target (EOT). Upper limits on the kinetic mixing parameter ϵ^2 have been established over varying EOT scenarios, offering competitive constraints relative to existing experiments. As future steps, the project aims to validate the extrapolation method further and improve the statistical power (up to 10^{16} EOT), potentially refining the exclusion limits for various dark photon models.

In summary, this dissertation describes the di-Higgs searches at the LHC in multiple channels, especially in multi-lepton and $b\bar{b}\tau^+\tau^-$ channels. With the combination of three major di-Higgs channels ($b\bar{b}b\bar{b}$, $b\bar{b}\gamma\gamma$, and $b\bar{b}\tau^+\tau^-$) and all single Higgs channels, constraints on the Higgs self-coupling parameter κ_λ at 95% confidence level interval give $-1.4 < \kappa_\lambda < 6.1$ with the most generalized assumption. The dissertation also searches for new phenomena during Higgs rare decay, where a Higgs particle decays to a pair of LLPs resulting in multiple jets in the final state. This study gives the expected upper limit of 4×10^{-6} for the branching ratio of $H \rightarrow$ LLPs with a LLP mass of 50 GeV and 1 ns lifetime, which is one of the best exclusion limits with an estimated statistics of 10^6 Higgs. Furthermore, the dissertation sets expected exclusion limits parameterized in dark photon mass and kinetic mixing coefficient (ϵ) via the proposed DarkSHINE fixed-target experiment. The expected ϵ^2 exclusion upper limit can reach 1.3×10^{-14} for a dark photon mass of 1 MeV, exceeding all

known experimental results by several orders of magnitude. Together, these detailed studies search for new physics on various fronts in experimental particle physics and enhance our understanding of the SM.

Bibliography

- [1] FEYNMAN R P. Space-Time Approach to Quantum Electrodynamics[J/OL]. Phys. Rev., 1949, 76: 769-789. <https://link.aps.org/doi/10.1103/PhysRev.76.769>. DOI: [10.1103/PhysRev.76.769](https://doi.org/10.1103/PhysRev.76.769).
- [2] SCHWINGER J. Quantum Electrodynamics. I. A Covariant Formulation[J/OL]. Phys. Rev., 1948, 74: 1439-1461. <https://link.aps.org/doi/10.1103/PhysRev.74.1439>. DOI: [10.1103/PhysRev.74.1439](https://doi.org/10.1103/PhysRev.74.1439).
- [3] GELL-MANN M. THE EIGHTFOLD WAY: A THEORY OF STRONG INTERACTION SYMMETRY[J/OL]. 1961. <https://www.osti.gov/biblio/4008239>. DOI: [10.2172/4008239](https://doi.org/10.2172/4008239).
- [4] GELL-MANN M. A schematic model of baryons and mesons[J/OL]. Physics Letters, 1964, 8(3): 214-215. <https://www.sciencedirect.com/science/article/pii/S0031916364920013>. DOI: [https://doi.org/10.1016/S0031-9163\(64\)92001-3](https://doi.org/10.1016/S0031-9163(64)92001-3).
- [5] FRITZSCH H, GELL-MANN M, LEUTWYLER H. Advantages of the color octet gluon picture[J/OL]. Physics Letters B, 1973, 47(4): 365-368. <https://www.sciencedirect.com/science/article/pii/0370269373906254>. DOI: [https://doi.org/10.1016/0370-2693\(73\)90625-4](https://doi.org/10.1016/0370-2693(73)90625-4).
- [6] GLASHOW S L. Partial-symmetries of weak interactions[J/OL]. Nuclear Physics, 1961, 22(4): 579-588. <https://www.sciencedirect.com/science/article/pii/0029558261904692>. DOI: [https://doi.org/10.1016/0029-5582\(61\)90469-2](https://doi.org/10.1016/0029-5582(61)90469-2).
- [7] SALAM A. Weak and electromagnetic interactions[M/OL]//Selected Papers of Abdus Salam: 244-254. eprint: https://www.worldscientific.com/doi/pdf/10.1142/9789812795915_0034. https://www.worldscientific.com/doi/abs/10.1142/9789812795915_0034. DOI: [10.1142/9789812795915_0034](https://doi.org/10.1142/9789812795915_0034).
- [8] WEINBERG S. A Model of Leptons[J]. prl, 1967, 19(21): 1264-1266. DOI: [10.1103/PhysRevLett.19.1264](https://doi.org/10.1103/PhysRevLett.19.1264).
- [9] COLLABORATION T A. Observation of a new particle in the search for the Standard Model Higgs boson with the ATLAS detector at the LHC[J/OL]. Physics Letters B, 2012, 716(1): 1-29. <https://doi.org/10.1016/j.physletb.2012.08.020>. DOI: [10.1016/j.physletb.2012.08.020](https://doi.org/10.1016/j.physletb.2012.08.020).

- [10] YUKAWA H. On the Interaction of Elementary Particles I[J]. Proc. Phys. Math. Soc. Jap., 1935, 17: 48-57. DOI: [10.1143/PTPS.1.1](https://doi.org/10.1143/PTPS.1.1).
- [11] PESKIN M, SCHROEDER D. An Introduction to Quantum Field Theory[M/OL]. Avalon Publishing, 1995. <https://books.google.fr/books?id=i35LALN0GosC>.
- [12] WOITHE J, WIENER G J, der VEKEN F F V. Let's have a coffee with the Standard Model of particle physics![J/OL]. Physics Education, 2017, 52(3): 034001. <https://dx.doi.org/10.1088/1361-6552/aa5b25>. DOI: [10.1088/1361-6552/aa5b25](https://doi.org/10.1088/1361-6552/aa5b25).
- [13] DI LELLA L, RUBBIA C. The Discovery of the W and Z Particles[J]. Adv. Ser. Direct. High Energy Phys., 2015, 23: 137-163. DOI: [10.1142/9789814644150_0006](https://doi.org/10.1142/9789814644150_0006).
- [14] KLEIN M, YOSHIDA R. Collider Physics at HERA[J]. Prog. Part. Nucl. Phys., 2008, 61: 343-393. arXiv: [0805.3334 \[hep-ex\]](https://arxiv.org/abs/0805.3334). DOI: [10.1016/j.ppnp.2008.05.002](https://doi.org/10.1016/j.ppnp.2008.05.002).
- [15] MYERS S. The LEP collider, from design to approval and commissioning[J]. 1991. DOI: [10.5170/CERN-1991-008](https://doi.org/10.5170/CERN-1991-008).
- [16] HOLMES S, MOORE R S, SHILTSEV V. Overview of the Tevatron collider complex: goals, operations and performance[J/OL]. Journal of Instrumentation, 2011, 6(08): T08001. <https://dx.doi.org/10.1088/1748-0221/6/08/T08001>. DOI: [10.1088/1748-0221/6/08/T08001](https://doi.org/10.1088/1748-0221/6/08/T08001).
- [17] ABRAMOWICZ H, ABT I, ADAMCZYK L, et al. Combination of measurements of inclusive deep inelastic $e^{\pm}p$ scattering cross sections and QCD analysis of HERA data[J/OL]. The European Physical Journal C, 2015, 75(12): 580. <https://doi.org/10.1140/epjc/s10052-015-3710-4>. DOI: [10.1140/epjc/s10052-015-3710-4](https://doi.org/10.1140/epjc/s10052-015-3710-4).
- [18] ENGLERT F, BROUT R. Broken Symmetry and the Mass of Gauge Vector Mesons [J/OL]. Phys. Rev. Lett., 1964, 13: 321-323. <https://link.aps.org/doi/10.1103/PhysRevLett.13.321>. DOI: [10.1103/PhysRevLett.13.321](https://doi.org/10.1103/PhysRevLett.13.321).
- [19] HIGGS P W. Broken Symmetries and the Masses of Gauge Bosons[J/OL]. Phys. Rev. Lett., 1964, 13: 508-509. <https://link.aps.org/doi/10.1103/PhysRevLett.13.508>. DOI: [10.1103/PhysRevLett.13.508](https://doi.org/10.1103/PhysRevLett.13.508).
- [20] CERN. CERN Yellow Reports: Monographs, Vol 2 (2017): Handbook of LHC Higgs cross sections: 4. Deciphering the nature of the Higgs sector[EB/OL]. CERN. 2017. <https://e-publishing.cern.ch/index.php/CYRM/issue/view/32>.

- [21] GROUP T L H W. The LHC Higgs Working Group[EB/OL]. 2023 [2023-06-16]. <https://twiki.cern.ch/twiki/bin/view/LHCPhysics/LHCHWG?redirectedfrom=LHCPhysics.LHCHXSWG>.
- [22] DAWSON S, DITTMAIER S, SPIRA M. Neutral Higgs-boson pair production at hadron colliders: QCD corrections[J/OL]. Phys. Rev. D, 1998, 58: 115012. <https://link.aps.org/doi/10.1103/PhysRevD.58.115012>. DOI: [10.1103/PhysRevD.58.115012](https://doi.org/10.1103/PhysRevD.58.115012).
- [23] De FLORIAN D, MAZZITELLI J. Higgs Boson Pair Production at Next-to-Next-to-Leading Order in QCD[J/OL]. Phys. Rev. Lett., 2013, 111: 201801. <https://link.aps.org/doi/10.1103/PhysRevLett.111.201801>. DOI: [10.1103/PhysRevLett.111.201801](https://doi.org/10.1103/PhysRevLett.111.201801).
- [24] BAGLIO J, CAMPANARIO F, GLAUS S, et al. Gluon fusion into Higgs pairs at NLO QCD and the top mass scheme[J/OL]. The European Physical Journal C, 2019, 79(6). <https://doi.org/10.1140/epjc/s10052-019-6973-3>. DOI: [10.1140/epjc/s10052-019-6973-3](https://doi.org/10.1140/epjc/s10052-019-6973-3).
- [25] CEPEDA M, GORI S, ILTEN P, et al. Higgs Physics at the HL-LHC and HE-LHC [Z]. 2019. arXiv: [1902.00134](https://arxiv.org/abs/1902.00134) [hep-ph].
- [26] COLLABORATION D. A search for heavy stable and long-lived squarks and sleptons in e^+e^- collisions at energies from 130 to 183 GeV[J]. Physics Letters B, 1998, 444(3): 491-502.
- [27] COLLABORATION C. Search for heavy, long-lived neutralinos that decay to photons at CDF II using photon timing[J/OL]. Phys. Rev. D, 2008, 78: 032015. <https://link.aps.org/doi/10.1103/PhysRevD.78.032015>. DOI: [10.1103/PhysRevD.78.032015](https://doi.org/10.1103/PhysRevD.78.032015).
- [28] STRASSLER M J, ZUREK K M. Echoes of a hidden valley at hadron colliders [J/OL]. Physics Letters B, 2007, 651(5-6): 374-379. <https://doi.org/10.1016/j.physletb.2007.06.055>. DOI: [10.1016/j.physletb.2007.06.055](https://doi.org/10.1016/j.physletb.2007.06.055).
- [29] ARKANI-HAMED N, DIMOPOULOS S. Supersymmetric unification without low energy supersymmetry and signatures for fine-tuning at the LHC[J/OL]. Journal of High Energy Physics, 2005, 2005(06): 073-073. <https://doi.org/10.1088/1126-6708/2005/06/073>. DOI: [10.1088/1126-6708/2005/06/073](https://doi.org/10.1088/1126-6708/2005/06/073).
- [30] ABDULLAHI A M, ALZÁ S P B, BATELL B, et al. The present and future status

- of heavy neutral leptons[J/OL]. Journal of Physics G: Nuclear and Particle Physics, 2023, 50(2): 020501. <https://doi.org/10.1088/1361-6471/ac98f9>. DOI: 10.1088/1361-6471/ac98f9.
- [31] EVANS L R. The Large Hadron Collider Project[J/OL]. 1997. <https://cds.cern.ch/record/313675>.
- [32] BRÜNING O, BURKHARDT H, MYERS S. The Large Hadron Collider[J/OL]. Prog. Part. Nucl. Phys., 2012, 67: 705-734. <https://cds.cern.ch/record/1443022>. DOI: 10.1016/j.ppnp.2012.03.001.
- [33] COLLABORATION A. ATLAS Experiment at CERN[EB/OL]. 2023. <https://atlas.cern/>.
- [34] CERN. CERN[EB/OL]. 2023. <https://home.cern/>.
- [35] LOPIENSKA E. The CERN accelerator complex, layout in 2022. Complexe des accélérateurs du CERN en janvier 2022[J/OL]. 2022. <https://cds.cern.ch/record/2800984>.
- [36] COLLABORATION A. Public ATLAS Luminosity Results for Run-2 of the LHC [EB/OL]. 2023. <https://twiki.cern.ch/twiki/bin/view/AtlasPublic/LuminosityPublicResultsRun2>.
- [37] COLLABORATION A. Luminosity determination in pp collisions at $\sqrt{s} = 13$ TeV using the ATLAS detector at the LHC[Z]. 2022. arXiv: 2212.09379 [hep-ex].
- [38] ATLAS: technical proposal for a general-purpose pp experiment at the Large Hadron Collider at CERN[M/OL]. Geneva: CERN, 1994. <https://cds.cern.ch/record/290968>. DOI: 10.17181/CERN.NR4P.BG9K.
- [39] ATLAS detector and physics performance: Technical Design Report, 1[M/OL]. Geneva: CERN, 1999. <https://cds.cern.ch/record/391176>.
- [40] PEQUENAO J. Computer generated image of the whole ATLAS detector[Z/OL]. 2008. <https://cds.cern.ch/record/1095924>.
- [41] ATLAS inner detector: Technical Design Report, 1[M/OL]. Geneva: CERN, 1997. <https://cds.cern.ch/record/331063>.
- [42] PEQUENAO J. Computer generated image of the ATLAS inner detector[Z/OL]. 2008. <https://cds.cern.ch/record/1095926>.
- [43] ATLAS calorimeter performance: Technical Design Report[M/OL]. Geneva:

- CERN, 1996. <https://cds.cern.ch/record/331059>.
- [44] PEQUENAO J. Computer Generated image of the ATLAS calorimeter[Z/OL]. 2008. <https://cds.cern.ch/record/1095927>.
- [45] ATLAS muon spectrometer: Technical Design Report[M/OL]. Geneva: CERN, 1997. <https://cds.cern.ch/record/331068>.
- [46] PEQUENAO J. Computer generated image of the ATLAS Muons subsystem[Z/OL]. 2008. <https://cds.cern.ch/record/1095929>.
- [47] COLLABORATION T A. The ATLAS Experiment at the CERN Large Hadron Collider[J/OL]. Journal of Instrumentation, 2008, 3(08): S08003. <https://dx.doi.org/10.1088/1748-0221/3/08/S08003>. DOI: [10.1088/1748-0221/3/08/S08003](https://doi.org/10.1088/1748-0221/3/08/S08003).
- [48] RODRIGUEZ VERA A M, ANTUNES PEQUENAO J. ATLAS Detector Magnet System[Z/OL]. 2021. <https://cds.cern.ch/record/2770604>.
- [49] ELSING M, SCHOERNER-SADENIUS T. Configuration of the ATLAS Trigger System[Z]. 2003. arXiv: [physics/0306046](https://arxiv.org/abs/physics/0306046) [[physics.ins-det](https://arxiv.org/abs/physics/0306046)].
- [50] COLLABORATION T A. The ATLAS Data Acquisition and High Level Trigger system[J/OL]. JINST, 2016, 11(06): P06008. <https://cds.cern.ch/record/2255808>. DOI: [10.1088/1748-0221/11/06/P06008](https://doi.org/10.1088/1748-0221/11/06/P06008).
- [51] CERN. AthenaCore Package Documentation[EB/OL]. <http://atlas-computing.web.cern.ch/atlas-computing/packages/athenaCore/athenaCore.php>.
- [52] AGOSTINELLI S, ALLISON J, AMAKO K, et al. Geant4—a simulation toolkit [J/OL]. Nuclear Instruments and Methods in Physics Research Section A: Accelerators, Spectrometers, Detectors and Associated Equipment, 2003, 506(3): 250-303. <https://www.sciencedirect.com/science/article/pii/S0168900203013688>. DOI: [https://doi.org/10.1016/S0168-9002\(03\)01368-8](https://doi.org/10.1016/S0168-9002(03)01368-8).
- [53] ALLISON J, AMAKO K, APOSTOLAKIS J, et al. Geant4 developments and applications[J]. IEEE Transactions on Nuclear Science, 2006, 53(1): 270-278. DOI: [10.1109/TNS.2006.869826](https://doi.org/10.1109/TNS.2006.869826).
- [54] The ATLAS Collaboration. The ATLAS Simulation Infrastructure[J/OL]. The European Physical Journal C, 2010, 70(3): 823-874. <https://doi.org/10.1140/epjc%2Fs10052-010-1429-9>. DOI: [10.1140/epjc/s10052-010-1429-9](https://doi.org/10.1140/epjc/s10052-010-1429-9).
- [55] BUCKLEY A, ILTEN P, KONSTANTINOV D, et al. The HepMC3 event record li-

- brary for Monte Carlo event generators[J/OL]. Computer Physics Communications, 2021, 260: 107310. <https://doi.org/10.1016%2Fj.cpc.2020.107310>. DOI: [10.1016/j.cpc.2020.107310](https://doi.org/10.1016/j.cpc.2020.107310).
- [56] BOS K, BROOK N, DUELLMANN D, et al. LHC computing Grid: Technical Design Report. Version 1.06 (20 Jun 2005)[M/OL]. Geneva: CERN, 2005. <https://cds.cern.ch/record/840543>.
- [57] BRANCO M, CAMERON D, GAIDIOZ B, et al. Managing ATLAS data on a petabyte-scale with DQ2[J/OL]. J. Phys.: Conf. Ser., 2008, 119: 062017. <https://cds.cern.ch/record/1177372>. DOI: [10.1088/1742-6596/119/6/062017](https://doi.org/10.1088/1742-6596/119/6/062017).
- [58] CORCELLA G, KNOWLES I G, MARCHESINI G, et al. HERWIG 6: an event generator for hadron emission reactions with interfering gluons (including supersymmetric processes)[J/OL]. Journal of High Energy Physics, 2001, 2001(01): 010-010. <https://doi.org/10.1088%2F1126-6708%2F2001%2F01%2F010>. DOI: [10.1088/1126-6708/2001/01/010](https://doi.org/10.1088/1126-6708/2001/01/010).
- [59] BÄHR M, GIESEKE S, GIGG M A, et al. HERWIG physics and manual[J/OL]. The European Physical Journal C, 2008, 58(4): 639-707. <https://doi.org/10.1140%2Fepjc%2Fs10052-008-0798-9>. DOI: [10.1140/epjc/s10052-008-0798-9](https://doi.org/10.1140/epjc/s10052-008-0798-9).
- [60] SJÖSTRAND T, MRENN A S, SKANDS P. PYTHIA 6.4 physics and manual [J/OL]. Journal of High Energy Physics, 2006, 2006(05): 026-026. <https://doi.org/10.1088%2F1126-6708%2F2006%2F05%2F026>. DOI: [10.1088/1126-6708/2006/05/026](https://doi.org/10.1088/1126-6708/2006/05/026).
- [61] SJÖSTRAND T, ASK S, CHRISTIANSEN J R, et al. An introduction to PYTHIA 8.2[J/OL]. Computer Physics Communications, 2015, 191: 159-177. <https://doi.org/10.1016%2Fj.cpc.2015.01.024>. DOI: [10.1016/j.cpc.2015.01.024](https://doi.org/10.1016/j.cpc.2015.01.024).
- [62] GLEISBERG T, HÖCHE S, KRAUSS F, et al. Event generation with SHERPA 1.1 [J/OL]. Journal of High Energy Physics, 2009, 2009(02): 007-007. <https://doi.org/10.1088%2F1126-6708%2F2009%2F02%2F007>. DOI: [10.1088/1126-6708/2009/02/007](https://doi.org/10.1088/1126-6708/2009/02/007).
- [63] GROUP P D. Quantum Chromodynamics[R/OL]. Lawrence Berkeley National Laboratory. 2021. <https://pdg.lbl.gov/2021/reviews/rpp2021-rev-qcd.pdf>.
- [64] BIERLICH C, CHAKRABORTY S, DESAI N, et al. A comprehensive guide to the

- physics and usage of PYTHIA 8.3[Z]. 2022. arXiv: [2203.11601 \[hep-ph\]](#).
- [65] DOBBS M A, FRIXIONE S, LAENEN E, et al. Les Houches Guidebook to Monte Carlo Generators for Hadron Collider Physics[Z]. 2004. arXiv: [hep-ph/0403045 \[hep-ph\]](#).
- [66] LANGE D J. The EvtGen particle decay simulation package[J/OL]. Nuclear Instruments and Methods in Physics Research Section A: Accelerators, Spectrometers, Detectors and Associated Equipment, 2001, 462(1): 152-155. <https://www.sciencedirect.com/science/article/pii/S0168900201000894>. DOI: [https://doi.org/10.1016/S0168-9002\(01\)00089-4](https://doi.org/10.1016/S0168-9002(01)00089-4).
- [67] FRIXIONE S, NASON P, WEBBER B R. Matching NLO QCD and parton showers in heavy flavour production[J/OL]. Journal of High Energy Physics, 2003, 2003(08): 007. <https://dx.doi.org/10.1088/1126-6708/2003/08/007>. DOI: [10.1088/1126-6708/2003/08/007](https://doi.org/10.1088/1126-6708/2003/08/007).
- [68] BOURILKOV D, GROUP R C, WHALLEY M R. LHAPDF: PDF Use from the Tevatron to the LHC[Z]. 2006. arXiv: [hep-ph/0605240 \[hep-ph\]](#).
- [69] PLOTHOW-BESCH H. PDFLIB: a library of all available parton density functions of the nucleon, the pion and the photon and the corresponding α_s calculations[J/OL]. Comput. Phys. Commun., 1993, 75: 396-416. <https://cds.cern.ch/record/239783>. DOI: [10.1016/0010-4655\(93\)90051-D](https://doi.org/10.1016/0010-4655(93)90051-D).
- [70] TUNG W K, LAI H L, PUMPLIN J, et al. Global QCD Analysis and Collider Phenomenology-CTEQ[Z]. 2007. arXiv: [0707.0275 \[hep-ph\]](#).
- [71] An NLO QCD analysis of inclusive cross-section and jet-production data from the ZEUS experiment[J/OL]. The European Physical Journal C, 2005, 42(1): 1-16. <https://doi.org/10.1140%2Fepjc%2Fs2005-02293-x>. DOI: [10.1140/epjc/s2005-02293-x](https://doi.org/10.1140/epjc/s2005-02293-x).
- [72] GROUP T Q W, ALBROW M, BEGEL M, et al. Tevatron-for-LHC Report of the QCD Working Group[Z]. 2006. arXiv: [hep-ph/0610012 \[hep-ph\]](#).
- [73] ATLAS PIXEL C. Pixel Offline Analysis for EndcapA Cosmic Data[R/OL]. for The ATLAS Pixel Collaboration. Geneva: CERN, 2007. <https://cds.cern.ch/record/1074907>.
- [74] KITTELMANN T H. Slepton spin determination and simulation of the transition radiation tracker at the ATLAS experiment[D/OL]. 2007. <https://cds.cern.ch/record/1074907>.

- d/2224292].
- [75] GADOMSKI S. Model of the SCT detectors and electronics for the ATLAS simulation using Geant4[R/OL]. revised version number 1 submitted on 2001-06-18 18:53:11. Geneva: CERN, 2001. <https://cds.cern.ch/record/684197>.
- [76] LAMPL W, LAPLACE S, LECHOWSKI M, et al. Digitization of LAr calorimeter for CSC simulations[R/OL]. This is the calo CSC note calo-5. Geneva: CERN, 2007. <https://cds.cern.ch/record/1057879>.
- [77] REBUZZI D, ASSAMAGAN K A, DI SIMONE A, et al. Geant4 Muon Digitization in the ATHENA Framework[R/OL]. Geneva: CERN, 2007. <https://cds.cern.ch/record/1010495>.
- [78] BARBERIO E, BOUDREAU J, BUTLER B, et al. The Geant4-Based ATLAS Fast Electromagnetic Shower Simulation[R/OL]. Geneva: CERN, 2008. <https://cds.cern.ch/record/1064665>. DOI: [10.1142/9789812819093_0133](https://doi.org/10.1142/9789812819093_0133).
- [79] BARBERIO E, BOUDREAU J, BUTLER B, et al. Fast shower simulation in the ATLAS calorimeter[J/OL]. J. Phys.: Conf. Ser., 2008, 119: 032008. <https://cds.cern.ch/record/1176890>. DOI: [10.1088/1742-6596/119/3/032008](https://doi.org/10.1088/1742-6596/119/3/032008).
- [80] GROUP U H. ATLFAST[EB/OL]. <http://www.hep.ucl.ac.uk/atlas/atlfast/>.
- [81] RICHTER-WAS E, FROIDEVAUX D, POGGIOLI L. ATLFAST 2.0 a fast simulation package for ATLAS[R/OL]. Geneva: CERN, 1998. <https://cds.cern.ch/record/683751>.
- [82] MECHNICH J. FATRAS - the ATLAS Fast Track Simulation project[R/OL]. Geneva: CERN, 2011. <https://cds.cern.ch/record/1321871>.
- [83] AABOUD M, AAD G, ABBOTT B, et al. Performance of the ATLAS track reconstruction algorithms in dense environments in LHC Run 2[J]. The European Physical Journal C, 2017, 77(10): 673.
- [84] CORNELISSEN T, ELSING M, GAVRILENKO I, et al. The new ATLAS track reconstruction (NEWT)[J/OL]. Journal of Physics: Conference Series, 2008, 119(3): 032014. <https://dx.doi.org/10.1088/1742-6596/119/3/032014>. DOI: [10.1088/1742-6596/119/3/032014](https://doi.org/10.1088/1742-6596/119/3/032014).
- [85] PEI Y, BISWAS S, FUSSELL D S, et al. An Elementary Introduction to Kalman Filtering[Z]. 2019. arXiv: [1710.04055](https://arxiv.org/abs/1710.04055) [eess.SY].

- [86] FRUEHWIRTH R. Application of Kalman filtering to track and vertex fitting[Z]. 1987. DOI: [10.1016/0168-9002\(87\)90887-4](https://doi.org/10.1016/0168-9002(87)90887-4).
- [87] COLLABORATION T A. A neural network clustering algorithm for the ATLAS silicon pixel detector[J/OL]. Journal of Instrumentation, 2014, 9(09): P09009-P09009. <https://doi.org/10.1088/1748-0221/9/09/p09009>. DOI: [10.1088/1748-0221/9/09/p09009](https://doi.org/10.1088/1748-0221/9/09/p09009).
- [88] Electron and photon reconstruction and performance in ATLAS using a dynamical, topological cell clustering-based approach[R/OL]. Geneva: CERN, 2017. <https://cds.cern.ch/record/2298955>.
- [89] COLLABORATION T A. Electron efficiency measurements with the ATLAS detector using 2012 LHC proton–proton collision data[J/OL]. The European Physical Journal C, 2017, 77(3). <https://doi.org/10.1140/epjc/s10052-017-4756-2>. DOI: [10.1140/epjc/s10052-017-4756-2](https://doi.org/10.1140/epjc/s10052-017-4756-2).
- [90] COLLABORATION T A. Measurement of the photon identification efficiencies with the ATLAS detector using LHC Run-1 data[J/OL]. The European Physical Journal C, 2016, 76(12). <https://doi.org/10.1140/epjc/s10052-016-4507-9>. DOI: [10.1140/epjc/s10052-016-4507-9](https://doi.org/10.1140/epjc/s10052-016-4507-9).
- [91] COLLABORATION T A. Electron reconstruction and identification in the ATLAS experiment using the 2015 and 2016 LHC proton–proton collision data at $\sqrt{s} = 13$ TeV[J/OL]. The European Physical Journal C, 2019, 79(8): 639. <https://doi.org/10.1140/epjc/s10052-019-7140-6>. DOI: [10.1140/epjc/s10052-019-7140-6](https://doi.org/10.1140/epjc/s10052-019-7140-6).
- [92] COLLABORATION T A. Topological cell clustering in the ATLAS calorimeters and its performance in LHC Run 1[J/OL]. The European Physical Journal C, 2017, 77(7). <https://doi.org/10.1140/epjc/s10052-017-5004-5>. DOI: [10.1140/epjc/s10052-017-5004-5](https://doi.org/10.1140/epjc/s10052-017-5004-5).
- [93] HE F. High Precision Electron and Muon Reconstruction Performance with ATLAS at LHC Run-2[R/OL]. Geneva: CERN, 2022. <https://cds.cern.ch/record/2841383>. DOI: [10.22323/1.414.0675](https://cds.cern.ch/record/2841383).
- [94] COLLABORATION T A. Electron reconstruction and identification in the ATLAS experiment using the 2015 and 2016 LHC data[J/OL]. The European Physical Journal C, 2019, 79(8). <https://doi.org/10.1140/epjc/s10052-019-7140-6>. DOI: [10.1140/epjc/s10052-019-7140-6](https://doi.org/10.1140/epjc/s10052-019-7140-6).

- 10.1140/epjc/s10052-019-7140-6.
- [95] HOECKER A, SPECKMAYER P, STELZER J, et al. TMVA - Toolkit for Multivariate Data Analysis[Z]. 2009. arXiv: [physics/0703039](https://arxiv.org/abs/physics/0703039) [[physics.data-an](https://arxiv.org/archive/physics)].
- [96] COLLABORATION A. EGAM-2022-02[EB/OL]. CERN. 2022. <https://atlas.web.cern.ch/Atlas/GROUPS/PHYSICS/PLOTS/EGAM-2022-02/>.
- [97] COLLABORATION T A. Electron and photon performance measurements with the ATLAS detector using the 2015 – 2017 LHC proton-proton collision data[J/OL]. Journal of Instrumentation, 2019, 14(12): P12006-P12006. <https://doi.org/10.1088/1748-0221/14/12/p12006>. DOI: [10.1088/1748-0221/14/12/p12006](https://doi.org/10.1088/1748-0221/14/12/p12006).
- [98] COLLABORATION A. EGAM-2021-01[EB/OL]. CERN. 2021. <http://atlas.web.cern.ch/Atlas/GROUPS/PHYSICS/PAPERS/EGAM-2021-01/>.
- [99] ZHANG Y, LI L, BERNARDI G. Improvement of photon ID against electron fakes of the ATLAS experiment[R/OL]. Geneva: CERN, 2022. <https://cds.cern.ch/record/2808007>.
- [100] GUO F, FANG Y, LOU X. Topo-cluster variable performance study with Radiative Z events in 13TeV ATLAS data[R/OL]. Geneva: CERN, 2021. <https://cds.cern.ch/record/2774734>.
- [101] SJÖSTRAND T, MRENNA S, SKANDS P. A brief introduction to PYTHIA 8.1[J/OL]. Computer Physics Communications, 2008, 178(11): 852-867. <https://doi.org/10.1016/j.cpc.2008.01.036>. DOI: [10.1016/j.cpc.2008.01.036](https://doi.org/10.1016/j.cpc.2008.01.036).
- [102] ALIOLI S, NASON P, OLEARI C, et al. A general framework for implementing NLO calculations in shower Monte Carlo programs: the POWHEG BOX[J/OL]. Journal of High Energy Physics, 2010, 2010(6). [https://doi.org/10.1007/jhep06\(2010\)043](https://doi.org/10.1007/jhep06(2010)043). DOI: [10.1007/jhep06\(2010\)043](https://doi.org/10.1007/jhep06(2010)043).
- [103] CORNELISSEN T, ELSING M, FLEISCHMANN S, et al. Concepts, Design and Implementation of the ATLAS New Tracking (NEWT)[R/OL]. Geneva: CERN, 2007. <https://cds.cern.ch/record/1020106>.
- [104] Performance of the ATLAS Silicon Pattern Recognition Algorithm in Data and Simulation at $\sqrt{s} = 7$ TeV[R/OL]. Geneva: CERN, 2010. <https://cds.cern.ch/record/1281363>.

- [105] ILLINGWORTH J, KITTLER J. A survey of the hough transform[J/OL]. Computer Vision, Graphics, and Image Processing, 1988, 44(1): 87-116. <https://www.sciencedirect.com/science/article/pii/S0734189X88800331>. DOI: [https://doi.org/10.1016/S0734-189X\(88\)80033-1](https://doi.org/10.1016/S0734-189X(88)80033-1).
- [106] COLLABORATION T A. Muon reconstruction performance of the ATLAS detector in proton–proton collision data at $\sqrt{s} = 13$ TeV[J/OL]. The European Physical Journal C, 2016, 76(5). <https://doi.org/10.1140/epjc/s10052-016-4120-y>. DOI: [10.1140/epjc/s10052-016-4120-y](https://doi.org/10.1140/epjc/s10052-016-4120-y).
- [107] COLLABORATION T A. MUON-2018-03[EB/OL]. 2018. <https://atlas.web.cern.ch/Atlas/GROUPS/PHYSICS/PAPERS/MUON-2018-03/>.
- [108] CACCIARI M, SALAM G P, SOYEZ G. The anti- k_T jet clustering algorithm[J/OL]. Journal of High Energy Physics, 2008, 2008(04): 063-063. <https://doi.org/10.1088/1126-6708/2008/04/063>. DOI: [10.1088/1126-6708/2008/04/063](https://doi.org/10.1088/1126-6708/2008/04/063).
- [109] COLLABORATION T A. Identification and energy calibration of hadronically decaying tau leptons with the ATLAS experiment in pp collisions at $\sqrt{s} = 8$ TeV[J/OL]. The European Physical Journal C, 2015, 75(7). <https://doi.org/10.1140/epjc/s10052-015-3500-z>. DOI: [10.1140/epjc/s10052-015-3500-z](https://doi.org/10.1140/epjc/s10052-015-3500-z).
- [110] Measurement of the tau lepton reconstruction and identification performance in the ATLAS experiment using pp collisions at $\sqrt{s} = 13$ TeV[R/OL]. Geneva: CERN, 2017. <https://cds.cern.ch/record/2261772>.
- [111] Reconstruction, Energy Calibration, and Identification of Hadronically Decaying Tau Leptons in the ATLAS Experiment for Run-2 of the LHC[R/OL]. Geneva: CERN, 2015. <https://cds.cern.ch/record/2064383>.
- [112] COLLABORATION T A. Identification of hadronic tau lepton decays using neural networks in the ATLAS experiment[EB/OL]. CERN. 2019. <https://atlas.web.cern.ch/Atlas/GROUPS/PHYSICS/PUBNOTES/ATL-PHYS-PUB-2019-033/>.
- [113] Jet global sequential corrections with the ATLAS detector in proton-proton collisions at $\sqrt{s} = 8$ TeV[R/OL]. Geneva: CERN, 2015. <https://cds.cern.ch/record/2001682>.
- [114] Data-driven determination of the energy scale and resolution of jets reconstructed in the ATLAS calorimeters using dijet and multijet events at $\sqrt{s} = 8$ TeV[R/OL]. Geneva: CERN, 2015. <https://cds.cern.ch/record/2008678>.

- [115] COLLABORATION T A. Jet reconstruction and performance using particle flow with the ATLAS Detector. Jet reconstruction and performance using particle flow with the ATLAS Detector[J/OL]. Eur. Phys. J. C, 2017, 77(7): 466. arXiv: [1703.10485](#). <https://cds.cern.ch/record/2257597>. DOI: [10.1140/epjc/s10052-017-5031-2](https://doi.org/10.1140/epjc/s10052-017-5031-2).
- [116] CACCIARI M, SALAM G P, SOYEZ G. The catchment area of jets[J/OL]. Journal of High Energy Physics, 2008, 2008(04): 005-005. <https://doi.org/10.1088/1126-6708/2008/04/005>. DOI: [10.1088/1126-6708/2008/04/005](https://doi.org/10.1088/1126-6708/2008/04/005).
- [117] CACCIARI M, SALAM G P. Pileup subtraction using jet areas[J/OL]. Physics Letters B, 2008, 659(1-2): 119-126. <https://doi.org/10.1016/j.physletb.2007.09.077>. DOI: [10.1016/j.physletb.2007.09.077](https://doi.org/10.1016/j.physletb.2007.09.077).
- [118] Monte Carlo Calibration and Combination of In-situ Measurements of Jet Energy Scale, Jet Energy Resolution and Jet Mass in ATLAS[R/OL]. Geneva: CERN, 2015. <https://cds.cern.ch/record/2044941>.
- [119] Optimisation of the ATLAS *b*-tagging performance for the 2016 LHC Run[R/OL]. Geneva: CERN, 2016. <https://cds.cern.ch/record/2160731>.
- [120] COLLABORATION A. Performance of *b*-jet identification in the ATLAS experiment[J/OL]. Journal of Instrumentation, 2016, 11(04): P04008. <https://dx.doi.org/10.1088/1748-0221/11/04/P04008>. DOI: [10.1088/1748-0221/11/04/P04008](https://doi.org/10.1088/1748-0221/11/04/P04008).
- [121] GRAVES A. Supervised Sequence Labelling with Recurrent Neural Networks: vol. 385[M]. 2012. DOI: [10.1007/978-3-642-24797-2](https://doi.org/10.1007/978-3-642-24797-2).
- [122] COLLABORATION T A. Identification of Jets Containing *b*-Hadrons with Recurrent Neural Networks at the ATLAS Experiment[R/OL]. CERN. 2017. <https://atlas.web.cern.ch/Atlas/GROUPS/PHYSICS/PUBNOTES/ATL-PHYS-PUB-2017-003/>.
- [123] COLLABORATION T A. Performance of missing transverse momentum reconstruction with the ATLAS detector using proton–proton collisions at $\sqrt{s} = 13$ TeV[J/OL]. The European Physical Journal C, 2018, 78(11): 903. <https://doi.org/10.1140/epjc/s10052-018-6288-9>. DOI: [10.1140/epjc/s10052-018-6288-9](https://doi.org/10.1140/epjc/s10052-018-6288-9).
- [124] ATLAS Collaboration. ATLAS data quality operations and performance for 2015–2018 data-taking[J]. JINST, 2020, 15: P04003. arXiv: [1911.04632](#) [[physics.ins-det](#)]. DOI: [10.1088/1748-0221/15/04/P04003](https://doi.org/10.1088/1748-0221/15/04/P04003).

- [125] PileupReweighting. <https://twiki.cern.ch/twiki/bin/viewauth/AtlasProtected/ExtendedPileupReweighting>.
- [126] BALL R D, et al. Parton distributions for the LHC run II[J]. JHEP, 2015, 04: 040. arXiv: [1410.8849 \[hep-ph\]](https://arxiv.org/abs/1410.8849). DOI: [10.1007/JHEP04\(2015\)040](https://doi.org/10.1007/JHEP04(2015)040).
- [127] SJÖSTRAND T, MRENNA S, SKANDS P. A brief introduction to PYTHIA 8.1[J]. Comput. Phys. Commun., 2008, 178: 852-867. arXiv: [0710.3820 \[hep-ph\]](https://arxiv.org/abs/0710.3820). DOI: [10.1016/j.cpc.2008.01.036](https://doi.org/10.1016/j.cpc.2008.01.036).
- [128] ATLAS Collaboration. The Pythia 8 A3 tune description of ATLAS minimum bias and inelastic measurements incorporating the Donnachie–Landshoff diffractive model. ATL-PHYS-PUB-2016-017. 2016. <https://cds.cern.ch/record/2206965>.
- [129] GEANT4 Collaboration, AGOSTINELLI S, et al. GEANT4 – a simulation toolkit[J]. Nucl. Instrum. Meth. A, 2003, 506: 250. DOI: [10.1016/S0168-9002\(03\)01368-8](https://doi.org/10.1016/S0168-9002(03)01368-8).
- [130] LAI S, LI X, LI L, et al. Search for Higgs pair production decaying to WWWW with the final state of three leptons, missing energy and at least two jets in 36.1 fb⁻¹ proton-proton data at $\sqrt{s} = 13$ TeV[R/OL]. Geneva: CERN, 2016. <https://cds.cern.ch/record/2229725>.
- [131] ATLAS Collaboration. Vertex Reconstruction Performance of the ATLAS Detector at $\sqrt{s} = 13$ TeV. ATL-PHYS-PUB-2015-026. 2015. <https://cds.cern.ch/record/2037717>.
- [132] VAZQUEZ SCHROEDER T, POLIFKA R, POVEDA TORRES X, et al. Search for the Associated Production of a Higgs Boson and a Top Quark Pair in multilepton final states in 80 fb⁻¹ pp Collisions at $\sqrt{s} = 13$ TeV with the ATLAS Detector[R/OL]. Geneva: CERN, 2018. <https://cds.cern.ch/record/2314122>.
- [133] TriggerEfficiency. <https://twiki.cern.ch/twiki/bin/viewauth/Atlas/TrigGlobalEfficiencyCorrectionTool>.
- [134] OSPANOV R, ROBERTS R T, WYATT T R. Tagging non-prompt electrons and muons[R/OL]. Geneva: CERN, 2016. <https://cds.cern.ch/record/2220954>.
- [135] COLLABORATION A. ATLAS flavour-tagging algorithms for the LHC Run 2 pp collision dataset[J]. The European Physical Journal C, 2023, 83(7): 681.
- [136] COLLABORATION A. ATLAS Flavor-Tagging Calibration Results with 139 fb [EB/OL]. 2019. <http://atlas.web.cern.ch/Atlas/GROUPS/PHYSICS/PLOTS/F>

- TAG-2019-004/.
- [137] COLLABORATION A. Expected performance of the 2019 ATLAS b-taggers [EB/OL]. 2019. <http://atlas.web.cern.ch/Atlas/GROUPS/PHYSICS/PLOTS/F> TAG-2019-005/.
- [138] Overlap Removal. https://twiki.cern.ch/twiki/bin/view/AtlasProtected/TopRecoObjTwikiModel#Overlap_Removal.
- [139] AGARAS M N. Search for vector-like leptons coupling to first and second generation Standard Model leptons in multilepton final states[R/OL]. Geneva: CERN, 2022. <https://cds.cern.ch/record/2845251>.
- [140] BRUN R, RADEMAKERS F. ROOT: An object oriented data analysis framework[J]. Nucl. Instrum. Meth. A, 1997, 389: 81-86. DOI: [10.1016/S0168-9002\(97\)00048-X](https://doi.org/10.1016/S0168-9002(97)00048-X).
- [141] ATLAS Collaboration. Luminosity determination in pp collisions at $\sqrt{s} = 13$ TeV using the ATLAS detector at the LHC. ATLAS-CONF-2019-021. 2019. <https://cds.cern.ch/record/2677054>.
- [142] trigger recommendations. <https://twiki.cern.ch/twiki/bin/view/Atlas/TriggerRecommendationsForAnalysisGroupsFullRun2>.
- [143] Muon CP group. <https://twiki.cern.ch/twiki/bin/view/AtlasProtected/MCPAnalysisWinterMC16>.
- [144] Egamma-CP. <https://twiki.cern.ch/twiki/bin/view/AtlasProtected/LatestRecommendationsElectronIDRun2>.
- [145] ATLAS Collaboration. Jet energy scale measurements and their systematic uncertainties in proton–proton collisions at $\sqrt{s} = 13$ TeV with the ATLAS detector[J]. Phys. Rev. D, 2017, 96: 072002. arXiv: [1703.09665 \[hep-ex\]](https://arxiv.org/abs/1703.09665). DOI: [10.1103/PhysRevD.96.072002](https://doi.org/10.1103/PhysRevD.96.072002).
- [146] Btagging Calibration. https://twiki.cern.ch/twiki/bin/view/AtlasProtected/BTagging_Calibration_December2020CDI.
- [147] GRAZZINI M, HEINRICH G, JONES S, et al. Higgs boson pair production at NNLO with top quark mass effects[J/OL]. Journal of High Energy Physics, 2018, 2018(5): 59. [https://doi.org/10.1007/JHEP05\(2018\)059](https://doi.org/10.1007/JHEP05(2018)059). DOI: [10.1007/JHEP05\(2018\)059](https://doi.org/10.1007/JHEP05(2018)059).
- [148] LHC Higgs Cross Section HH Sub-group[EB/OL]. <https://twiki.cern.ch/twiki/bin/view/LHCPhysics/LHCHWGGHH?redirectedfrom=LHCPhysics.LHCHXSWGHH>.

- [149] CRANMER K, LEWIS G, MONETA L, et al. HistFactory: A tool for creating statistical models for use with RooFit and RooStats. New York, 2012. <https://cds.cern.ch/record/1456844>.
- [150] READ A L. Presentation of search results: the CLs technique[J]. Journal of Physics G: Nuclear and Particle Physics, 2002, 28(10): 2693.
- [151] TRexFitter framework documentatio. <https://trexfitter-docs.web.cern.ch/trexfitter-docs/>.
- [152] TRexFitter framework gitlab project.
- [153] COLLABORATION T A. Search for resonant and non-resonant Higgs boson pair production in the $b\bar{b}\tau^+\tau^-$ decay channel using 13 TeV pp collision data from the ATLAS detector[J]. Journal of High Energy Physics, 2023, 2023(7): 40.
- [154] ATLAS Collaboration. Luminosity determination in pp collisions at $\sqrt{s} = 13$ TeV using the ATLAS detector at the LHC[J]. 2022. arXiv: [2212.09379 \[hep-ex\]](https://arxiv.org/abs/2212.09379).
- [155] BALL R D, et al. Parton distributions with LHC data[J]. Nucl. Phys. B, 2013, 867: 244. arXiv: [1207.1303 \[hep-ph\]](https://arxiv.org/abs/1207.1303). DOI: [10.1016/j.nuclphysb.2012.10.003](https://doi.org/10.1016/j.nuclphysb.2012.10.003).
- [156] LANGE D J. The EvtGen particle decay simulation package[J]. Nucl. Instrum. Meth. A, 2001, 462: 152. DOI: [10.1016/S0168-9002\(01\)00089-4](https://doi.org/10.1016/S0168-9002(01)00089-4).
- [157] BOTHMANN E, et al. Event generation with Sherpa 2.2[J]. SciPost Phys., 2019, 7(3): 034. arXiv: [1905.09127 \[hep-ph\]](https://arxiv.org/abs/1905.09127). DOI: [10.21468/SciPostPhys.7.3.034](https://doi.org/10.21468/SciPostPhys.7.3.034).
- [158] ALIOLI S, NASON P, OLEARI C, et al. A general framework for implementing NLO calculations in shower Monte Carlo programs: the POWHEG BOX[J]. JHEP, 2010, 06: 043. arXiv: [1002.2581 \[hep-ph\]](https://arxiv.org/abs/1002.2581). DOI: [10.1007/JHEP06\(2010\)043](https://doi.org/10.1007/JHEP06(2010)043).
- [159] BUCKLEY A, FERRANDO J, LLOYD S, et al. LHAPDF6: parton density access in the LHC precision era[J]. Eur. Phys. J. C, 2015, 75: 132. arXiv: [1412.7420 \[hep-ph\]](https://arxiv.org/abs/1412.7420). DOI: [10.1140/epjc/s10052-015-3318-8](https://doi.org/10.1140/epjc/s10052-015-3318-8).
- [160] BUTTERWORTH J, et al. PDF4LHC recommendations for LHC Run II[J]. J. Phys. G, 2016, 43: 023001. arXiv: [1510.03865 \[hep-ph\]](https://arxiv.org/abs/1510.03865). DOI: [10.1088/0954-3899/43/2/023001](https://doi.org/10.1088/0954-3899/43/2/023001).
- [161] ATLAS Collaboration. ATLAS Pythia 8 tunes to 7 TeV data. ATL-PHYS-PUB-2014-021. 2014. <https://cds.cern.ch/record/1966419>.
- [162] ATLAS Collaboration. Summary of ATLAS Pythia 8 tunes. ATL-PHYS-PUB-2012-

003. 2012. <https://cds.cern.ch/record/1474107>.
- [163] GRAZZINI M, HEINRICH G, JONES S, et al. Higgs boson pair production at NNLO with top quark mass effects[J]. JHEP, 2018, 05: 059. arXiv: [1803.02463 \[hep-ph\]](https://arxiv.org/abs/1803.02463). DOI: [10.1007/JHEP05\(2018\)059](https://doi.org/10.1007/JHEP05(2018)059).
- [164] BÄHR M, et al. Herwig++ physics and manual[J]. Eur. Phys. J. C, 2008, 58: 639. arXiv: [0803.0883 \[hep-ph\]](https://arxiv.org/abs/0803.0883). DOI: [10.1140/epjc/s10052-008-0798-9](https://doi.org/10.1140/epjc/s10052-008-0798-9).
- [165] ALWALL J, FREDERIX R, FRIXIONE S, et al. The automated computation of tree-level and next-to-leading order differential cross sections, and their matching to parton shower simulations[J]. JHEP, 2014, 07: 079. arXiv: [1405.0301 \[hep-ph\]](https://arxiv.org/abs/1405.0301). DOI: [10.1007/JHEP07\(2014\)079](https://doi.org/10.1007/JHEP07(2014)079).
- [166] BISHARA F, CONTINO R, ROJO J. Higgs pair production in vector-boson fusion at the LHC and beyond[J]. Eur. Phys. J. C, 2017, 77(7): 481. arXiv: [1611.03860 \[hep-ph\]](https://arxiv.org/abs/1611.03860). DOI: [10.1140/epjc/s10052-017-5037-9](https://doi.org/10.1140/epjc/s10052-017-5037-9).
- [167] P. Nason. A New method for combining NLO QCD with shower Monte Carlo algorithms[J]. JHEP, 2004, 11: 040. arXiv: [hep-ph/0409146 \[hep-ph\]](https://arxiv.org/abs/hep-ph/0409146). DOI: [10.1088/1126-6708/2004/11/040](https://doi.org/10.1088/1126-6708/2004/11/040).
- [168] S. Frixione, P. Nason and C. Oleari. Matching NLO QCD computations with parton shower simulations: the POWHEG method[J]. JHEP, 2007, 11: 070. arXiv: [0709.2092 \[hep-ph\]](https://arxiv.org/abs/0709.2092). DOI: [10.1088/1126-6708/2007/11/070](https://doi.org/10.1088/1126-6708/2007/11/070).
- [169] ALIOLI S, NASON P, OLEARI C, et al. A general framework for implementing NLO calculations in shower Monte Carlo programs: the POWHEG BOX[J]. JHEP, 2010, 06: 043. arXiv: [1002.2581 \[hep-ph\]](https://arxiv.org/abs/1002.2581). DOI: [10.1007/JHEP06\(2010\)043](https://doi.org/10.1007/JHEP06(2010)043).
- [170] NNPDF Collaboration. Parton distributions for the LHC Run II[J]. 2014. arXiv: [1410.8849 \[hep-ph\]](https://arxiv.org/abs/1410.8849).
- [171] SJOSTRAND T, et al. An Introduction to PYTHIA 8.2[J]. Comput.Phys.Commun., 2015, 191: 159-177. arXiv: [1410.3012 \[hep-ph\]](https://arxiv.org/abs/1410.3012).
- [172] ATLAS Collaboration. ATLAS Pythia 8 tunes to 7 TeV data. ATL-PHYS-PUB-2014-021. 2014. <https://cds.cern.ch/record/1966419>.
- [173] GLEISBERG T, HÖCHE S. Comix, a new matrix element generator[J]. JHEP, 2008, 12: 039. arXiv: [0808.3674 \[hep-ph\]](https://arxiv.org/abs/0808.3674). DOI: [10.1088/1126-6708/2008/12/039](https://doi.org/10.1088/1126-6708/2008/12/039).
- [174] BUCCIONI F, LANG J N, LINDERT J M, et al. OpenLoops 2[J]. Eur. Phys. J. C,

- 2019, 79(10): 866. arXiv: [1907.13071 \[hep-ph\]](#). DOI: [10.1140/epjc/s10052-019-7306-2](#).
- [175] CASCIOLI F, MAIERHÖFER P, POZZORINI S. Scattering Amplitudes with Open Loops[J]. Phys. Rev. Lett., 2012, 108: 111601. arXiv: [1111.5206 \[hep-ph\]](#). DOI: [10.1103/PhysRevLett.108.111601](#).
- [176] DENNER A, DITTMAIER S, HOFER L. COLLIER: A fortran-based complex one-loop library in extended regularizations[J]. Comput. Phys. Commun., 2017, 212: 220-238. arXiv: [1604.06792 \[hep-ph\]](#). DOI: [10.1016/j.cpc.2016.10.013](#).
- [177] ATLAS Collaboration. Search for resonant and non-resonant Higgs boson pair production in the $b\bar{b}\tau^+\tau^-$ decay channel using 13 TeV pp collision data from the ATLAS detector[J]. 2022. arXiv: [2209.10910 \[hep-ex\]](#).
- [178] ATLAS Collaboration. Electron reconstruction and identification efficiency measurements with the ATLAS detector using the 2011 LHC proton-proton collision data[J]. Eur. Phys. J. C, 2014, 74: 2941. arXiv: [1404.2240 \[hep-ex\]](#). DOI: [10.1140/epjc/s10052-014-2941-0](#).
- [179] ATLAS Collaboration. Muon reconstruction performance of the ATLAS detector in proton-proton collision data at $\sqrt{s} = 13$ TeV[J]. Eur. Phys. J. C, 2016, 76: 292. arXiv: [1603.05598 \[hep-ex\]](#). DOI: [10.1140/epjc/s10052-016-4120-y](#).
- [180] ATLAS Collaboration. Recommended Isolation Working Points[J/OL]. https://twiki.cern.ch/twiki/bin/viewauth/AtlasProtected/RecommendedIsolationWPs#Muon_working_points.
- [181] AAD G, et al. Identification and energy calibration of hadronically decaying tau leptons with the ATLAS experiment in pp collisions at $\sqrt{s}=8$ TeV[J]. Eur. Phys. J., 2015, C75(7): 303. arXiv: [1412.7086 \[hep-ex\]](#). DOI: [10.1140/epjc/s10052-015-3500-z](#).
- [182] BETTI A, BEVAN A J, BOKAN P, et al. Searches for Higgs boson pair production in the $b\bar{b}\tau^+\tau^-$ final state with 139 fb $^{-1}$ of pp collision data with the ATLAS detector [R/OL]. Geneva: CERN, 2020. <https://cds.cern.ch/record/2743097>.
- [183] CACCIARI M, SALAM G P, SOYEZ G. The anti- k_t jet clustering algorithm[J]. JHEP, 2008, 04: 063. arXiv: [0802.1189 \[hep-ph\]](#). DOI: [10.1088/1126-6708/2008/04/063](#).

- [184] AABOUD M, et al. Jet reconstruction and performance using particle flow with the ATLAS Detector[J]. Eur. Phys. J., 2017, C77(7):466. arXiv: [1703.10485 \[hep-ex\]](#). DOI: [10.1140/epjc/s10052-017-5031-2](#).
- [185] ATLAS Collaboration. 2015 start-up trigger menu and initial performance assessment of the ATLAS trigger using Run-2 data. ATL-DAQ-PUB-2016-001. 2016. <https://cds.cern.ch/record/2136007>.
- [186] ATLAS Collaboration. Jet Calibration and Systematic Uncertainties for Jets Reconstructed in the ATLAS Detector at $\sqrt{s} = 13$ TeV. ATL-PHYS-PUB-2015-015. 2015. <https://cds.cern.ch/record/2037613>.
- [187] ATLAS Collaboration. ATLAS b -jet identification performance and efficiency measurement with $t\bar{t}$ events in pp collisions at $\sqrt{s} = 13$ TeV[J]. Eur. Phys. J. C, 2019, 79: 970. arXiv: [1907.05120 \[hep-ex\]](#). DOI: [10.1140/epjc/s10052-019-7450-8](#).
- [188] ATLAS Collaboration. Optimisation and performance studies of the ATLAS b -tagging algorithms for the 2017-18 LHC run. ATL-PHYS-PUB-2017-013. 2017. <https://cds.cern.ch/record/2273281>.
- [189] ATLAS Collaboration. Identification of Jets Containing b -Hadrons with Recurrent Neural Networks at the ATLAS Experiment. ATL-PHYS-PUB-2017-003. 2017. <https://cds.cern.ch/record/2255226>.
- [190] AABOUD M, et al. Performance of missing transverse momentum reconstruction with the ATLAS detector using proton-proton collisions at $\sqrt{s} = 13$ TeV[J]. Eur. Phys. J., 2018, C78(11):903. arXiv: [1802.08168 \[hep-ex\]](#). DOI: [10.1140/epjc/s10052-018-6288-9](#).
- [191] ATLAS Collaboration. Recommended Overlap Removal Working Points[J/OL]. https://indico.cern.ch/event/631313/contributions/2683959/attachments/1518878/2373377/Farrell_ORTools_ftaghbb.pdf.
- [192] ELAGIN A, MURAT P, PRANKO A, et al. A New Mass Reconstruction Technique for Resonances Decaying to di-tau[J]. Nucl. Instrum. Meth. A, 2011, 654:481-489. arXiv: [1012.4686 \[hep-ex\]](#). DOI: [10.1016/j.nima.2011.07.009](#).
- [193] ATLAS Collaboration. A search for resonant and non-resonant Higgs boson pair production in the $b\bar{b}\tau^+\tau^-$ decay channel in pp collisions at $\sqrt{s} = 13$ TeV with the ATLAS detector[J]. Phys. Rev. Lett., 2018, 121:191801. arXiv: [1808.00336](#)

- [hep-ex]. DOI: [10.1103/PhysRevLett.121.191801](https://doi.org/10.1103/PhysRevLett.121.191801).
- [194] Bbtautau ML Toolkit. HBBHtautau ML Toolkit[Z]. <https://gitlab.cern.ch/bmoser/hbbhatautau/mltoolkit>. CERN GitLab repository. 2023.
- [195] BERNACIAK C, BUSCHMANN M S A, BUTTER A, et al. Fox-Wolfram moments in Higgs physics[J/OL]. Physical Review D, 2013, 87(7). <https://doi.org/10.1103/PhysRevD.87.073014>. DOI: [10.1103/physrevd.87.073014](https://doi.org/10.1103/physrevd.87.073014).
- [196] BARLOW R, BEESTON C. Fitting using finite Monte Carlo samples[J]. Computer Physics Communications, 1993, 77(2): 219-228.
- [197] G. Avoni et al. The new LUCID-2 detector for luminosity measurement and monitoring in ATLAS[J]. JINST, 2018, 13(07): P07017. DOI: [10.1088/1748-0221/13/07/P07017](https://doi.org/10.1088/1748-0221/13/07/P07017).
- [198] ATLAS Collaboration. Observation of a new particle in the search for the Standard Model Higgs boson with the ATLAS detector at the LHC[J]. Phys. Lett. B, 2012, 716: 1. arXiv: [1207.7214](https://arxiv.org/abs/1207.7214) [hep-ex]. DOI: [10.1016/j.physletb.2012.08.020](https://doi.org/10.1016/j.physletb.2012.08.020).
- [199] CMS Collaboration. Observation of a new boson at a mass of 125 GeV with the CMS experiment at the LHC[J]. Phys. Lett. B, 2012, 716: 30. arXiv: [1207.7235](https://arxiv.org/abs/1207.7235) [hep-ex]. DOI: [10.1016/j.physletb.2012.08.021](https://doi.org/10.1016/j.physletb.2012.08.021).
- [200] L. Evans and P. Bryant. LHC Machine[J]. JINST, 2008, 3: S08001. DOI: [10.1088/1748-0221/3/08/S08001](https://doi.org/10.1088/1748-0221/3/08/S08001).
- [201] GLASHOW S L. Partial-symmetries of weak interactions[J]. Nucl. Phys., 1961, 22: 579-588. DOI: [10.1016/0029-5582\(61\)90469-2](https://doi.org/10.1016/0029-5582(61)90469-2).
- [202] SALAM A. Weak and Electromagnetic Interactions[J]. Conf. Proc. C, 1968, 680519: Proceedings of the eighth Nobel symposium. DOI: [10.1142/9789812795915_0034](https://doi.org/10.1142/9789812795915_0034).
- [203] WEINBERG S. A Model of Leptons[J]. Phys. Rev. Lett., 1967, 19: 1264-1266. DOI: [10.1103/PhysRevLett.19.1264](https://doi.org/10.1103/PhysRevLett.19.1264).
- [204] 'T HOOFT G, VELTMAN M J G. Regularization and Renormalization of Gauge Fields[J]. Nucl. Phys. B, 1972, 44: 189-213. DOI: [10.1016/0550-3213\(72\)90279-9](https://doi.org/10.1016/0550-3213(72)90279-9).
- [205] ENGLERT F, BROUT R. Broken Symmetry and the Mass of Gauge Vector Mesons [J]. Phys. Rev. Lett., 1964, 13: 321-323. DOI: [10.1103/PhysRevLett.13.321](https://doi.org/10.1103/PhysRevLett.13.321).
- [206] HIGGS P W. Broken symmetries, massless particles and gauge fields[J]. Phys. Lett., 1964, 12: 132-133. DOI: [10.1016/0031-9163\(64\)91136-9](https://doi.org/10.1016/0031-9163(64)91136-9).

- [207] HIGGS P W. Broken Symmetries and the Masses of Gauge Bosons[J]. Phys. Rev. Lett., 1964, 13: 508-509. DOI: [10.1103/PhysRevLett.13.508](https://doi.org/10.1103/PhysRevLett.13.508).
- [208] HIGGS P W. Spontaneous Symmetry Breakdown without Massless Bosons[J]. Phys. Rev., 1966, 145: 1156-1163. DOI: [10.1103/PhysRev.145.1156](https://doi.org/10.1103/PhysRev.145.1156).
- [209] GURALNIK G S, HAGEN C R, KIBBLE T W B. Global Conservation Laws and Massless Particles[J]. Phys. Rev. Lett., 1964, 13: 585. DOI: [10.1103/PhysRevLett.13.585](https://doi.org/10.1103/PhysRevLett.13.585).
- [210] ATLAS and CMS Collaborations. Combined Measurement of the Higgs Boson Mass in pp Collisions at $\sqrt{s} = 7$ and 8 TeV with the ATLAS and CMS Experiments[J]. Phys. Rev. Lett., 2015, 114: 191803. arXiv: [1503.07589 \[hep-ex\]](https://arxiv.org/abs/1503.07589). DOI: [10.1103/PhysRevLett.114.191803](https://doi.org/10.1103/PhysRevLett.114.191803).
- [211] Particle Data Group, WORKMAN R L, et al. Review of Particle Physics[J]. PTEP, 2022, 2022: 083C01. DOI: [10.1093/ptep/ptac097](https://doi.org/10.1093/ptep/ptac097).
- [212] ATLAS Collaboration. Search for Higgs boson pair production in the two bottom quarks plus two photons final state in pp collisions at $\sqrt{s} = 13$ TeV with the ATLAS detector[J]. Phys. Rev. D, 2021, 106: 052001. arXiv: [2112.11876 \[hep-ex\]](https://arxiv.org/abs/2112.11876). DOI: [10.1103/PhysRevD.106.052001](https://doi.org/10.1103/PhysRevD.106.052001).
- [213] ATLAS Collaboration. Search for non-resonant pair production of Higgs bosons in the $b\bar{b}b\bar{b}$ final state in pp collisions at $\sqrt{s} = 13$ TeV with the ATLAS detector. 2023. arXiv: [2301.03212 \[hep-ex\]](https://arxiv.org/abs/2301.03212).
- [214] DEGRASSI G, GIARDINO P P, MALTONI F, et al. Probing the Higgs self coupling via single Higgs production at the LHC[J]. JHEP, 2016, 12: 080. arXiv: [1607.04251 \[hep-ph\]](https://arxiv.org/abs/1607.04251). DOI: [10.1007/JHEP12\(2016\)080](https://doi.org/10.1007/JHEP12(2016)080).
- [215] MALTONI F, PAGANI D, SHIVAJI A, et al. Trilinear Higgs coupling determination via single-Higgs differential measurements at the LHC[J]. Eur. Phys. J. C, 2017, 77(12): 887. arXiv: [1709.08649 \[hep-ph\]](https://arxiv.org/abs/1709.08649). DOI: [10.1140/epjc/s10052-017-5410-8](https://doi.org/10.1140/epjc/s10052-017-5410-8).
- [216] DI VITA S, GROJEAN C, PANICO G, et al. A global view on the Higgs self-coupling [J]. JHEP, 2017, 09: 069. arXiv: [1704.01953 \[hep-ph\]](https://arxiv.org/abs/1704.01953). DOI: [10.1007/JHEP09\(2017\)069](https://doi.org/10.1007/JHEP09(2017)069).
- [217] GORBAHN M, HAISCH U. Indirect probes of the trilinear Higgs coupling: $gg \rightarrow h$

- and $h \rightarrow \gamma\gamma$ [J]. JHEP, 2016, 10: 094. arXiv: [1607.03773 \[hep-ph\]](#). DOI: [10.1007/JHEP10\(2016\)094](#).
- [218] BIZON W, GORBAHN M, HAISCH U, et al. Constraints on the trilinear Higgs coupling from vector boson fusion and associated Higgs production at the LHC[J]. JHEP, 2017, 07: 083. arXiv: [1610.05771 \[hep-ph\]](#). DOI: [10.1007/JHEP07\(2017\)083](#).
- [219] MCCULLOUGH M. An Indirect Model-Dependent Probe of the Higgs Self-Coupling[J]. Phys. Rev. D, 2014, 90(1): 015001. arXiv: [1312.3322 \[hep-ph\]](#). DOI: [10.1103/PhysRevD.90.015001](#).
- [220] ATLAS Collaboration. A detailed map of Higgs boson interactions by the ATLAS experiment ten years after the discovery[J]. Nature, 2022, 607: 52. arXiv: [2207.00092 \[hep-ex\]](#). DOI: [10.1038/s41586-022-04893-w](#).
- [221] ATLAS Collaboration. Combination of searches for Higgs boson pairs in pp collisions at $\sqrt{s} = 13$ TeV with the ATLAS detector[J]. Phys. Lett. B, 2020, 800: 135103. arXiv: [1906.02025 \[hep-ex\]](#). DOI: [10.1016/j.physletb.2019.135103](#).
- [222] CMS Collaboration. A portrait of the Higgs boson by the CMS experiment ten years after the discovery[J]. Nature, 2022, 607: 60. arXiv: [2207.00043 \[hep-ex\]](#). DOI: [10.1038/s41586-022-04892-x](#).
- [223] LHC Higgs Cross Section Working Group, HEINEMEYER S, et al. Handbook of LHC Higgs Cross Sections: 3. Higgs Properties[J]. CERN-2013-004, CERN, Geneva, 2013. arXiv: [1307.1347 \[hep-ph\]](#). DOI: [10.5170/CERN-2013-004](#).
- [224] LHC Higgs Cross Section Working Group, de FLORIAN D, et al. Handbook of LHC Higgs Cross Sections: 4. Deciphering the Nature of the Higgs Sector[J]. CERN-2017-002-M, 2017. arXiv: [1610.07922 \[hep-ph\]](#). DOI: [10.23731/CYRM-2017-002](#).
- [225] DI MICCO B, et al. Higgs boson potential at colliders: Status and perspectives[J]. Reviews in Physics, 2020, 5: 100045. arXiv: [1910.00012](#). DOI: [https://doi.org/10.1016/j.revip.2020.100045](#).
- [226] DAWSON S, DITTMAIER S, SPIRA M. Neutral Higgs boson pair production at hadron colliders: QCD corrections[J]. Phys. Rev. D, 1998, 58: 115012. arXiv: [hep-ph/9805244 \[hep-ph\]](#). DOI: [10.1103/PhysRevD.58.115012](#).
- [227] BOROWKA S, GREINER N, HEINRICH G, et al. Higgs Boson Pair Production

- in Gluon Fusion at Next-to-Leading Order with Full Top-Quark Mass Dependence [J]. Phys. Rev. Lett., 2016, 117(1): 012001. arXiv: [1604.06447 \[hep-ph\]](#). DOI: [10.1103/PhysRevLett.117.012001](#).
- [228] BAGLIO J, CAMPANARIO F, GLAUS S, et al. Gluon fusion into Higgs pairs at NLO QCD and the top mass scheme[J]. Eur. Phys. J. C, 2019, 79(6): 459. arXiv: [1811.05692 \[hep-ph\]](#). DOI: [10.1140/epjc/s10052-019-6973-3](#).
- [229] ANDERSEN J R, et al. Les Houches 2015: Physics at TeV Colliders Standard Model Working Group Report[C]//9th Les Houches Workshop on Physics at TeV Colliders (PhysTeV 2015) Les Houches, France, June 1-19, 2015. 2016. arXiv: [1605.04692 \[hep-ph\]](#).
- [230] ATLAS Collaboration. Constraint of the Higgs boson self-coupling from Higgs boson differential production and decay measurements[R/OL]. ATL-PHYS-PUB-2019-009. Geneva: CERN, 2019. <https://cds.cern.ch/record/2667570>.
- [231] LHC Higgs Cross Section Working Group. Modelling of the single-Higgs simplified template cross-sections (STXS 1.2) for the determination of the Higgs boson trilinear self-coupling[R/OL]. LHCHWG-2022-002. Geneva: CERN, 2022. <https://cds.cern.ch/record/2803606>.
- [232] ATLAS Collaboration. The ATLAS Experiment at the CERN Large Hadron Collider [J]. JINST, 2008, 3: S08003. DOI: [10.1088/1748-0221/3/08/S08003](#).
- [233] ATLAS Collaboration. ATLAS Insertable B-Layer Technical Design Report. 2010. <https://cds.cern.ch/record/1291633>.
- [234] ABBOTT B, et al. Production and integration of the ATLAS Insertable B-Layer[J]. JINST, 2018, 13(05): T05008. arXiv: [1803.00844 \[physics.ins-det\]](#). DOI: [10.1088/1748-0221/13/05/t05008](#).
- [235] ATLAS Collaboration. Performance of the ATLAS trigger system in 2015[J]. Eur. Phys. J. C, 2017, 77: 317. arXiv: [1611.09661 \[hep-ex\]](#). DOI: [10.1140/epjc/s10052-017-4852-3](#).
- [236] ATLAS Collaboration. The ATLAS Collaboration Software and Firmware. ATL-SOFT-PUB-2021-001. 2021. <https://cds.cern.ch/record/2767187>.
- [237] ATLAS Collaboration. Measurement of the properties of Higgs boson production at $\sqrt{s} = 13$ TeV in the $H \rightarrow \gamma\gamma$ channel using 139 fb^{-1} of pp collision data with the

- ATLAS experiment[J]. 2022. arXiv: [2207.00348 \[hep-ex\]](#).
- [238] ATLAS Collaboration. Higgs boson production cross-section measurements and their EFT interpretation in the 4ℓ decay channel at $\sqrt{s} = 13$ TeV with the ATLAS detector[J]. Eur. Phys. J. C, 2020, 80: 957. arXiv: [2004.03447 \[hep-ex\]](#). DOI: [10.1140/epjc/s10052-020-8227-9](#).
Erratum: Eur. Phys. J. C, 2021, 81: 29. DOI: [10.1140/epjc/s10052-020-08644-x](#).
- [239] ATLAS Collaboration. Measurements of Higgs boson production cross-sections in the $H \rightarrow \tau^+\tau^-$ decay channel in pp collisions at $\sqrt{s} = 13$ TeV with the ATLAS detector[J]. JHEP, 2022, 08: 175. arXiv: [2201.08269 \[hep-ex\]](#). DOI: [10.1007/JHEP08\(2022\)175](#).
- [240] ATLAS Collaboration. Measurements of Higgs boson production by gluon–gluon fusion and vector-boson fusion using $H \rightarrow WW^* \rightarrow e\nu\mu\nu$ decays in pp collisions at $\sqrt{s} = 13$ TeV with the ATLAS detector[J]. 2022. arXiv: [2207.00338 \[hep-ex\]](#).
- [241] ATLAS Collaboration. Measurements of WH and ZH production in the $H \rightarrow b\bar{b}$ decay channel in pp collisions at 13 TeV with the ATLAS detector[J]. Eur. Phys. J. C, 2021, 81: 178. arXiv: [2007.02873 \[hep-ex\]](#). DOI: [10.1140/epjc/s10052-020-08677-2](#).
- [242] ATLAS Collaboration. Measurements of Higgs Bosons Decaying to Bottom Quarks from Vector Boson Fusion Production with the ATLAS Experiment at $\sqrt{s} = 13$ TeV [J]. Eur. Phys. J. C, 2020, 81: 537. arXiv: [2011.08280 \[hep-ex\]](#). DOI: [10.1140/epjc/s10052-021-09192-8](#).
- [243] ATLAS Collaboration. Measurement of Higgs boson decay into b -quarks in associated production with a top-quark pair in pp collisions at $\sqrt{s} = 13$ TeV with the ATLAS detector[J]. JHEP, 2021, 06: 097. arXiv: [2111.06712 \[hep-ex\]](#). DOI: [10.1007/JHEP06\(2022\)097](#).
- [244] ATLAS and CMS Collaborations. Measurements of the Higgs boson production and decay rates and constraints on its couplings from a combined ATLAS and CMS analysis of the LHC pp collision data at $\sqrt{s} = 7$ and 8 TeV[J]. JHEP, 2016, 08: 045. arXiv: [1606.02266 \[hep-ex\]](#). DOI: [10.1007/JHEP08\(2016\)045](#).
- [245] ATLAS Collaboration. Combined measurements of Higgs boson production and decay using up to 80 fb^{-1} of proton–proton collision data at $\sqrt{s} = 13$ TeV collected

- with the ATLAS experiment[J]. Phys. Rev. D, 2020, 101: 012002. arXiv: [1909.02845 \[hep-ex\]](#). DOI: [10.1103/PhysRevD.101.012002](#).
- [246] COWAN G, CRANMER K, GROSS E, et al. Asymptotic formulae for likelihood-based tests of new physics[J]. Eur. Phys. J. C, 2011, 71: 1554. arXiv: [1007.1727 \[physics.data-an\]](#). DOI: [10.1140/epjc/s10052-011-1554-0](#).
- [247] READ A L. Presentation of search results: the CL_s technique[J]. J. Phys. G, 2002, 28: 2693-2704. DOI: [10.1088/0954-3899/28/10/313](#).
- [248] AAD G, et al. Constraints on the Higgs boson self-coupling from single- and double-Higgs production with the ATLAS detector using pp collisions at $s=13$ TeV[J]. Phys. Lett. B, 2023, 843: 137745. arXiv: [2211.01216 \[hep-ex\]](#). DOI: [10.1016/j.physletb.2023.137745](#).
- [249] LIU J, LIU Z, WANG L T. Enhancing Long-Lived Particles Searches at the LHC with Precision Timing Information[J/OL]. Physical Review Letters, 2019, 122(13). <https://doi.org/10.1103/PhysRevLett.122.131801>. DOI: [10.1103/PhysRevLett.122.131801](#).
- [250] Search for events with a pair of displaced vertices from long-lived neutral particles decaying into hadronic jets in the ATLAS muon spectrometer in pp collisions at $\sqrt{s} = 13$ TeV[J/OL]. Phys. Rev. D, 2022, 106: 032005. <https://link.aps.org/doi/10.1103/PhysRevD.106.032005>. DOI: [10.1103/PhysRevD.106.032005](#).
- [251] Search for long-lived particles decaying in the CMS muon detectors in proton-proton collisions at $\sqrt{s} = 13$ TeV[R/OL]. Geneva: CERN, 2023. <https://cds.cern.ch/record/2864874>.
- [252] AGAPOV I, BENEDIKT M, BLONDEL A, et al. Future Circular Lepton Collider FCC-ee: Overview and Status[Z]. 2022. arXiv: [2203.08310 \[physics.acc-ph\]](#).
- [253] GROUP T C S. CEPC Conceptual Design Report: Volume 1 - Accelerator[Z]. 2018. arXiv: [1809.00285 \[physics.acc-ph\]](#).
- [254] GROUP T C S. CEPC Conceptual Design Report: Volume 2 - Physics & Detector [Z]. 2018. arXiv: [1811.10545 \[hep-ex\]](#).
- [255] GROUP T I C. The International Large Detector: Letter of Intent[Z]. 2010. arXiv: [1006.3396 \[hep-ex\]](#).
- [256] THOMSON M. Particle flow calorimetry and the PandoraPFA algorithm[J/OL]. Nu-

- clear Instruments and Methods in Physics Research Section A: Accelerators, Spectrometers, Detectors and Associated Equipment, 2009, 611(1): 25-40. <https://doi.org/10.1016/j.nima.2009.09.009>. DOI: [10.1016/j.nima.2009.09.009](https://doi.org/10.1016/j.nima.2009.09.009).
- [257] RUAN M. Arbor, a new approach of the Particle Flow Algorithm[Z]. 2014. arXiv: [1403.4784](https://arxiv.org/abs/1403.4784) [[physics.ins-det](https://arxiv.org/abs/1403.4784)].
- [258] Particle-Flow Event Reconstruction in CMS and Performance for Jets, Taus, and MET[R/OL]. Geneva: CERN, 2009. <http://cds.cern.ch/record/1194487>.
- [259] KILIAN W, OHL T, REUTER J. WHIZARD—simulating multi-particle processes at LHC and ILC[J/OL]. The European Physical Journal C, 2011, 71(9). <https://doi.org/10.1140/epjc/s10052-011-1742-y>. DOI: [10.1140/epjc/s10052-011-1742-y](https://doi.org/10.1140/epjc/s10052-011-1742-y).
- [260] MORA DE FREITAS P, VIDEAU H. Detector simulation with MOKKA / GEANT4: Present and future[C]// International Workshop on Linear Colliders (LCWS 2002). 2002: 623-627.
- [261] CARLONI CALAME C, MONTAGNA G, NICROSINI O, et al. The BABAYAGA event generator[J]. Nuclear Physics B - Proceedings Supplements, 2004, 131: 48-55.
- [262] ALWALL J, HERQUET M, MALTONI F, et al. MadGraph 5: going beyond[J/OL]. Journal of High Energy Physics, 2011, 2011(6). <https://doi.org/10.1007/jhep06%282011%29128>. DOI: [10.1007/jhep06\(2011\)128](https://doi.org/10.1007/jhep06(2011)128).
- [263] CHEN T, GUESTRIN C. XGBoost[C/OL]// Proceedings of the 22nd ACM SIGKDD International Conference on Knowledge Discovery and Data Mining. ACM, 2016. <https://doi.org/10.1145/2939672.2939785>. DOI: [10.1145/2939672.2939785](https://doi.org/10.1145/2939672.2939785).
- [264] HE K, ZHANG X, REN S, et al. Deep Residual Learning for Image Recognition[Z]. 2015. arXiv: [1512.03385](https://arxiv.org/abs/1512.03385) [[cs.CV](https://arxiv.org/abs/1512.03385)].
- [265] GONG S, MENG Q, ZHANG J, et al. An efficient Lorentz equivariant graph neural network for jet tagging[J/OL]. Journal of High Energy Physics, 2022, 2022(7). <https://doi.org/10.1007/jhep07%5C%282022%5C%29030>. DOI: [10.1007/jhep07\(2022\)030](https://doi.org/10.1007/jhep07(2022)030).
- [266] SMILJANIC I, JELISAVCIC I B, KACAREVIC G, et al. Systematic uncertainties in integrated luminosity measurement at CEPC[J]. 2020. arXiv: [2010.15061](https://arxiv.org/abs/2010.15061)

- [physics.ins-det].
- [267] LIU J, LIU Z, WANG L T. Enhancing Long-Lived Particles Searches at the LHC with Precision Timing Information[J/OL]. Phys. Rev. Lett., 2019, 122: 131801. <https://link.aps.org/doi/10.1103/PhysRevLett.122.131801>. DOI: [10.1103/PhysRevLett.122.131801](https://doi.org/10.1103/PhysRevLett.122.131801).
- [268] JEANTY L, NOSLER L, POTTER C. Sensitivity to decays of long-lived dark photons at the ILC (A Snowmass White Paper)[Z]. 2022. arXiv: [2203.08347](https://arxiv.org/abs/2203.08347) [hep-ph].
- [269] AIHARA H, et al. The International Linear Collider. A Global Project[J]. 2019. arXiv: [1901.09829](https://arxiv.org/abs/1901.09829) [hep-ex].
- [270] ABADA A, et al. FCC Physics Opportunities: Future Circular Collider Conceptual Design Report Volume 1[J]. 2019, 79(6): 474. DOI: [10.1140/epjc/s10052-019-6904-3](https://doi.org/10.1140/epjc/s10052-019-6904-3).
- [271] De BLAS J, et al. The CLIC Potential for New Physics[J]. 2018, 3/2018. arXiv: [1812.02093](https://arxiv.org/abs/1812.02093) [hep-ph]. DOI: [10.23731/CYRM-2018-003](https://doi.org/10.23731/CYRM-2018-003).
- [272] HOOPER D, FINKBEINER D P, DOBLER G. Possible evidence for dark matter annihilations from the excess microwave emission around the center of the Galaxy seen by the Wilkinson Microwave Anisotropy Probe[J/OL]. Phys. Rev. D, 2007, 76: 083012. <https://link.aps.org/doi/10.1103/PhysRevD.76.083012>. DOI: [10.1103/PhysRevD.76.083012](https://doi.org/10.1103/PhysRevD.76.083012).
- [273] COLLABORATION P. Planck 2013 results. XXII. Constraints on inflation[J]. A&A, 2014, 571: A22.
- [274] GRIEST K, KAMIONKOWSKI M. Unitarity limits on the mass and radius of dark-matter particles[J/OL]. Phys. Rev. Lett., 1990, 64: 615-618. <https://link.aps.org/doi/10.1103/PhysRevLett.64.615>. DOI: [10.1103/PhysRevLett.64.615](https://doi.org/10.1103/PhysRevLett.64.615).
- [275] HO C M, SCHERRER R J. Limits on MeV dark matter from the effective number of neutrinos[J/OL]. Phys. Rev. D, 2013, 87: 023505. <https://link.aps.org/doi/10.1103/PhysRevD.87.023505>. DOI: [10.1103/PhysRevD.87.023505](https://doi.org/10.1103/PhysRevD.87.023505).
- [276] NOLLETT K M, STEIGMAN G. BBN and the CMB constrain light, electromagnetically coupled WIMPs[J/OL]. Phys. Rev. D, 2014, 89: 083508. <https://link.aps.org/doi/10.1103/PhysRevD.89.083508>. DOI: [10.1103/PhysRevD.89.083508](https://doi.org/10.1103/PhysRevD.89.083508).

- [277] NOLLETT K M, STEIGMAN G. BBN and the CMB constrain neutrino coupled light WIMPs[J/OL]. Phys. Rev. D, 2015, 91: 083505. <https://link.aps.org/doi/10.1103/PhysRevD.91.083505>. DOI: [10.1103/PhysRevD.91.083505](https://doi.org/10.1103/PhysRevD.91.083505).
- [278] GREEN D, RAJENDRAN S. The cosmology of sub-MeV dark matter[J]. Journal of High Energy Physics, 2017, 2017(10): 13.
- [279] STEIGMAN G. Equivalent neutrinos, light WIMPs, and the chimera of dark radiation[J/OL]. Phys. Rev. D, 2013, 87: 103517. <https://link.aps.org/doi/10.1103/PhysRevD.87.103517>. DOI: [10.1103/PhysRevD.87.103517](https://doi.org/10.1103/PhysRevD.87.103517).
- [280] BÆHM C, DOLAN M J, MCCABE C. A lower bound on the mass of cold thermal dark matter from Planck[J]. Journal of Cosmology and Astroparticle Physics, 2013, 2013(08): 041.
- [281] CLOWE D, BRADAČ M, GONZALEZ A H, et al. A Direct Empirical Proof of the Existence of Dark Matter*[J]. The Astrophysical Journal, 2006, 648(2): L109.
- [282] ALEMANN F. Latest results from the DAMPE space mission[Z]. 2022. arXiv: [2209.06014](https://arxiv.org/abs/2209.06014) [astro-ph.HE].
- [283] GIOVACCHINI F, CASAUS J, OLIVA A. The AMS-02 RICH detector: Status and physics results[J]. Nuclear Instruments and Methods in Physics Research Section A: Accelerators, Spectrometers, Detectors and Associated Equipment, 2020, 952: 161797.
- [284] BEHR J K. Searches for Dark Matter with the ATLAS and CMS Experiments using LHC Run 2 (2015–2018) Data[R/OL]. Geneva: CERN, 2021. <https://cds.cern.ch/record/2790201>.
- [285] MENG Y, WANG Z, TAO Y, et al. Dark Matter Search Results from the PandaX-4T Commissioning Run[J/OL]. Phys. Rev. Lett., 2021, 127: 261802. <https://link.aps.org/doi/10.1103/PhysRevLett.127.261802>. DOI: [10.1103/PhysRevLett.127.261802](https://doi.org/10.1103/PhysRevLett.127.261802).
- [286] BILLARD J, BOULAY M, CEBRIÁN S, et al. Direct detection of dark matter—APPEC committee report*[J]. Reports on Progress in Physics, 2022, 85(5): 056201.
- [287] HOLDOM B. Two U(1)'s and ϵ charge shifts[J]. Physics Letters B, 1986, 166(2): 196-198.
- [288] FOOT R, HE X G. Comment on ZZ' mixing in extended gauge theories[J]. Physics Letters B, 1991, 267(4): 509-512.

- [289] FUYUTO K, HE X G, LI G, et al. *CP*-violating dark photon interaction[J/OL]. Phys. Rev. D, 2020, 101: 075016. <https://link.aps.org/doi/10.1103/PhysRevD.101.075016>. DOI: [10.1103/PhysRevD.101.075016](https://doi.org/10.1103/PhysRevD.101.075016).
- [290] CHOI G J, YANAGIDA T T, YOKOZAKI N. Dark photon dark matter in the minimal B-L model[J]. Journal of High Energy Physics, 2021, 2021(1): 57.
- [291] IZAGUIRRE E, KRNJAIC G, SCHUSTER P, et al. Testing GeV-scale dark matter with fixed-target missing momentum experiments[J/OL]. Phys. Rev. D, 2015, 91: 094026. <https://link.aps.org/doi/10.1103/PhysRevD.91.094026>. DOI: [10.1103/PhysRevD.91.094026](https://doi.org/10.1103/PhysRevD.91.094026).
- [292] GRAHAM M, HEARTY C, WILLIAMS M. Searches for Dark Photons at Accelerators[J]. Annual Review of Nuclear and Particle Science, 2021, 71(1): 37-58.
- [293] ANDREAS S, NIEBUHR C, RINGWALD A. New limits on hidden photons from past electron beam dumps[J/OL]. Phys. Rev. D, 2012, 86: 095019. <https://link.aps.org/doi/10.1103/PhysRevD.86.095019>. DOI: [10.1103/PhysRevD.86.095019](https://doi.org/10.1103/PhysRevD.86.095019).
- [294] BJORKEN J D, ESSIG R, SCHUSTER P, et al. New fixed-target experiments to search for dark gauge forces[J/OL]. Phys. Rev. D, 2009, 80: 075018. <https://link.aps.org/doi/10.1103/PhysRevD.80.075018>. DOI: [10.1103/PhysRevD.80.075018](https://doi.org/10.1103/PhysRevD.80.075018).
- [295] FABBRICHESI M, GABRIELLI E, LANFRANCHI G. The Physics of the Dark Photon[M/OL]. Springer International Publishing, 2021. <https://doi.org/10.1007/978-3-030-62519-1>. DOI: [10.1007/978-3-030-62519-1](https://doi.org/10.1007/978-3-030-62519-1).
- [296] WAN J, LENG Y, GAO B, et al. Simulation of wire scanner for high repetition free electron laser facilities[J]. Nuclear Instruments and Methods in Physics Research Section A: Accelerators, Spectrometers, Detectors and Associated Equipment, 2022, 1026: 166200.
- [297] ZHAO Z T, FENG C, ZHANG K Q. Two-stage EEHG for coherent hard X-ray generation based on a superconducting linac[J]. Nuclear Science and Techniques, 2017, 28(8): 117.
- [298] ZHAO Z, FENG C, CHEN J, et al. Two-beam based two-stage EEHG-FEL for coherent hard X-ray generation[J]. Science Bulletin, 2016, 61(9): 720-727.
- [299] BELYAEV A, CHRISTENSEN N D, PUKHOV A. CalcHEP 3.4 for collider physics within and beyond the Standard Model[J]. Computer Physics Communications, 2013,

- 184(7): 1729-1769.
- [300] COLLABORATION T N. Search for vector mediator of dark matter production in invisible decay mode[J/OL]. Phys. Rev. D, 2018, 97: 072002. <https://link.aps.org/doi/10.1103/PhysRevD.97.072002>. DOI: [10.1103/PhysRevD.97.072002](https://doi.org/10.1103/PhysRevD.97.072002).
- [301] DENIVERVILLE P, POSPELOV M, RITZ A. Observing a light dark matter beam with neutrino experiments[J/OL]. Phys. Rev. D, 2011, 84: 075020. <https://link.aps.org/doi/10.1103/PhysRevD.84.075020>. DOI: [10.1103/PhysRevD.84.075020](https://doi.org/10.1103/PhysRevD.84.075020).
- [302] BATELL B, POSPELOV M, RITZ A. Exploring portals to a hidden sector through fixed targets[J/OL]. Phys. Rev. D, 2009, 80: 095024. <https://link.aps.org/doi/10.1103/PhysRevD.80.095024>. DOI: [10.1103/PhysRevD.80.095024](https://doi.org/10.1103/PhysRevD.80.095024).
- [303] BATELL B, ESSIG R, SURUJON Z. Strong Constraints on Sub-GeV Dark Sectors from SLAC Beam Dump E137[J/OL]. Phys. Rev. Lett., 2014, 113: 171802. <https://link.aps.org/doi/10.1103/PhysRevLett.113.171802>. DOI: [10.1103/PhysRevLett.113.171802](https://doi.org/10.1103/PhysRevLett.113.171802).
- [304] COLLABORATION B. Search for Invisible Decays of a Dark Photon Produced in e^+e^- Collisions at BaBar[J/OL]. Phys. Rev. Lett., 2017, 119: 131804. <https://link.aps.org/doi/10.1103/PhysRevLett.119.131804>. DOI: [10.1103/PhysRevLett.119.131804](https://doi.org/10.1103/PhysRevLett.119.131804).
- [305] AGUILAR-AREVALO A A, BACKFISH M, BASHYAL A, et al. Dark Matter Search in a Proton Beam Dump with MiniBooNE[J/OL]. Phys. Rev. Lett., 2017, 118: 221803. <https://link.aps.org/doi/10.1103/PhysRevLett.118.221803>. DOI: [10.1103/PhysRevLett.118.221803](https://doi.org/10.1103/PhysRevLett.118.221803).
- [306] ESSIG R, MANALAYSAY A, MARDON J, et al. First Direct Detection Limits on Sub-GeV Dark Matter from XENON10[J/OL]. Phys. Rev. Lett., 2012, 109: 021301. <https://link.aps.org/doi/10.1103/PhysRevLett.109.021301>. DOI: [10.1103/PhysRevLett.109.021301](https://doi.org/10.1103/PhysRevLett.109.021301).
- [307] ÅKESSON T, BLINOV N, BRYNGEMARK L, et al. A high efficiency photon veto for the Light Dark Matter eXperiment[J]. Journal of High Energy Physics, 2020, 2020(4): 3.

Appendix A DarkSHINE Experiment

Over the last few decades, the Standard Model (SM) has been extraordinarily successful in corroborating a multitude of experimental outcomes in particle colliders. Nevertheless, certain phenomena point to the SM being a low-energy effective theory, implying the necessity of new physics beyond the SM. Strong astronomical and cosmological evidence attests to the existence of dark matter (DM), which constitutes approximately five times the mass of ordinary baryonic matter^[272-273]. This necessitates the exploration of DM to uncover physics beyond the SM.

One prevalent hypothesis postulates DM's origin in the early universe via thermal equilibrium, eventually leading to a stable density due to universal expansion and consequent temperature reduction; this is termed the *freeze-out* mechanism^[274-278]. The DM mass in this scenario ranges from MeV to tens of TeV to match the observed DM density^[279-280].

DM is primarily studied through its gravitational interactions in astronomical observations^[281]. However, questions about its mass and interaction mechanisms with both gravitational and SM forces remain open. Complementary approaches include space experiments such as DAMPE^[282] and AMS^[283], collider setups like the LHC^[284], and underground detectors like PandaX^[285]. Most of these focus on weakly interacting massive particles (WIMPs), which have so far yielded no evidence, constraining a significant portion of DM parameter space in the GeV–TeV mass range^[286].

The domain of sub-GeV DM particles remains relatively unexplored. One intriguing hypothesis posits that DM might engage in interactions through a novel *dark force*, analogous to electromagnetism in ordinary matter, mediated by a dark photon (A')^[287-288]. This mediator can couple to photons via a kinetic mixing parameter ϵ , enabling interactions between DM and SM particles^[289-290].

In the study at hand, dark photons are produced via electron-nucleon interactions in an electron-on-fixed-target experiment. These dark photons subsequently decay into DM candidates that elude detection, manifesting as missing momentum. For dark photons in the MeV–GeV mass range, this methodology enhances the constraints on the kinetic mixing parameter ϵ ^[291]. Given the low production rates of dark photons, this work employs GEANT4 simulations^[52-53] of 2.5 billion inclusive electron-on-target events and specialized background

samples. Discriminative variables include the count of reconstructed tracks and the energy deposition in both electromagnetic and hadronic calorimeters.

A.1 Theory Assumption

Although the dark photon does not engage in direct coupling with particles in the Standard Model (SM), it can manifest a minimal coupling to the electromagnetic current owing to the kinetic mixing of the SM hypercharge and the A' field strength tensor. The Lagrangian corresponding to this scenario is articulated as

$$L = L_{\text{SM}} + \varepsilon F^{\mu\nu} F'_{\mu\nu} + \frac{1}{4} F'^{\mu\nu} F'_{\mu\nu} + m_{A'}^2 A'^\mu A'_\mu,$$

where $m_{A'}$ denotes the dark photon mass, A'_μ signifies the dark photon field, and $F'_{\mu\nu}$ is its associated field strength tensor. The kinetic mixing parameter ε varies from 10^{-8} to 10^{-2} depending on the mass point^[292].

Dark photons can be produced in laboratory conditions and can either decay into detectable SM end states or elusive dark sector final states, contingent on whether $m_{A'} > 2m_\chi$. The minimal dark photon model incorporates merely three undetermined parameters: ε , $m_{A'}$, and the decay branching ratio to the dark sector, which is conventionally taken as either zero or unity. This investigation narrows its focus to the parameter space defined by $[m_{A'}, \varepsilon]$, presuming a 100% decay branching ratio of dark photons to dark matter.

Four primary mechanisms of dark photon production are highlighted, with three possible decay modes, as illustrated in figure A-1 (left): bremsstrahlung in fixed-target experiments ($eZ \rightarrow eZA'$ and $pZ \rightarrow pZA'$), annihilation in e^+e^- colliders ($e^+e^- \rightarrow A'\gamma$), decays of mesons ($\pi^0 \rightarrow A'\gamma$ or $\eta \rightarrow A'\gamma$), and the Drell-Yan process ($q\bar{q} \rightarrow A'$)^[293].

The cross-section for bremsstrahlung production is governed by

$$\frac{d\sigma}{dx_e} = 4\alpha^3 \varepsilon^2 \xi \sqrt{1 - \frac{m_{A'}^2}{E_e^2} \frac{1 - x_e + \frac{x_e^2}{3}}{m_{A'}^2 \frac{1-x_e}{x_e} + m_e^2 x_e}},$$

where $x_e = \frac{E_{A'}}{E_e}$ represents the energy fraction of the incoming electron carried by the dark photon. The effective photon flux ξ is

$$\xi(E_e, m_{A'}, Z, A) = \int_{t_{\min}}^{t_{\max}} dt \frac{t - t_{\min}}{t^2} G_2(t),$$

where t_{\min} and t_{\max} are defined in the text^[294].

If the dark photon decays into dark matter ($A' \rightarrow \chi\bar{\chi}$) are kinematically permissible, i.e., $m_{A'} > 2m_\chi$, the partial widths for these decays are given by

$$\Gamma(A' \rightarrow \chi\bar{\chi}) = \frac{1}{3}\alpha_D m_{A'} \sqrt{1 - \frac{4m_\chi^2}{m_{A'}^2}} \left(1 + \frac{2m_\chi^2}{m_{A'}^2}\right).$$

For an incident electron with 8 GeV energy and assuming $\varepsilon = 1$, Figure A-2 delineates the cross-section as a function of $m_{A'}$.

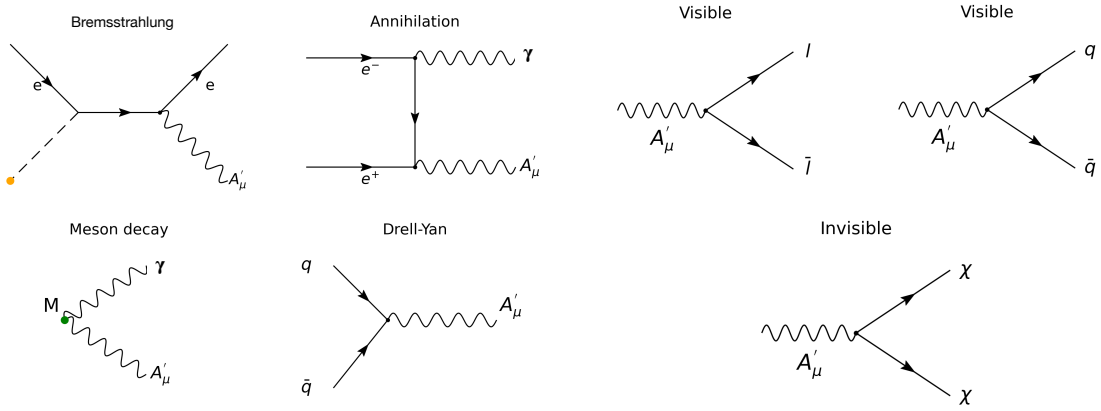


Figure A-1 *Left: Production of dark photons: bremsstrahlung, annihilation, meson decay, and Drell-Yan.*^[295] *Right: Decay of the massive dark photon into visible (SM leptons or hadrons) and invisible (DM) modes.*^[295]

A.2 Experimental Setup

A.2.1 SHINE Facility

In this investigation, a high-frequency electron beam is utilized, which is furnished by the under-construction Shanghai High Repetition-Rate XFEL and Extreme Light Facility (SHINE)^[296-298]. The SHINE facility is designed to generate a beam with an energy level of 8 GeV and a frequency of 1 MHz. Figure A-3 illustrates the configuration of the SHINE linac and the various kicker systems, including those designated for the Free Electron Lasers (FEL-I, FEL-II, FEL-III) and for the present experiment. Specifically, SHINE's microwave system, operating at 1.3 GHz, supplies 1.3 billion buckets per second. For every set of 1300 buckets, a 100 pC charge of electrons is loaded into a single bucket, which corresponds to a

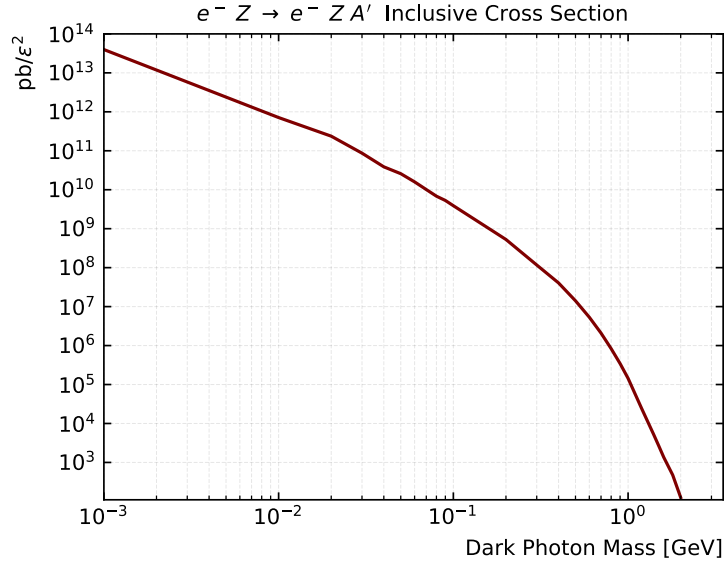


Figure A–2 Inclusive cross section of dark photon bremsstrahlung from electron interacting with tungsten target, which is produced by Calcchep and is normalized to $\varepsilon = 1$, with 8 GeV beam energy.

frequency of 1 MHz. This produces a bunch population of 6.25×10^8 electrons, which is too high for efficient dark photon detection.

To remedy this, a specialized single-electron beamline is proposed to be incorporated into the existing SHINE linac. This additional beamline aims to make use of the empty buckets by injecting a single electron into each. Post-acceleration, these electrons are distributed by a dedicated kicker system. When considering the response time of the kicker and the detection systems, an effective rate of 10 MHz is achieved. This configuration is projected to yield around 3×10^{14} electron-on-target (EOT) events during a single year of commissioning for the DarkSHINE experiment.

A.2.2 Detector Design

The detector for the DarkSHINE experiment is composed of three primary sub-detector systems: a silicon tracker, an electromagnetic calorimeter (denoted as ECAL), and a hadronic calorimeter (referred to as HCAL). Figure A-4 provides a schematic representation of these systems in spatial relation to each other. Along the direction of the incident electron from left to right, one first encounters a dipole magnet, depicted in red with a blue brace in the figure. The magnet operates at a field strength of 1.5 T. Situated at the center of this magnet

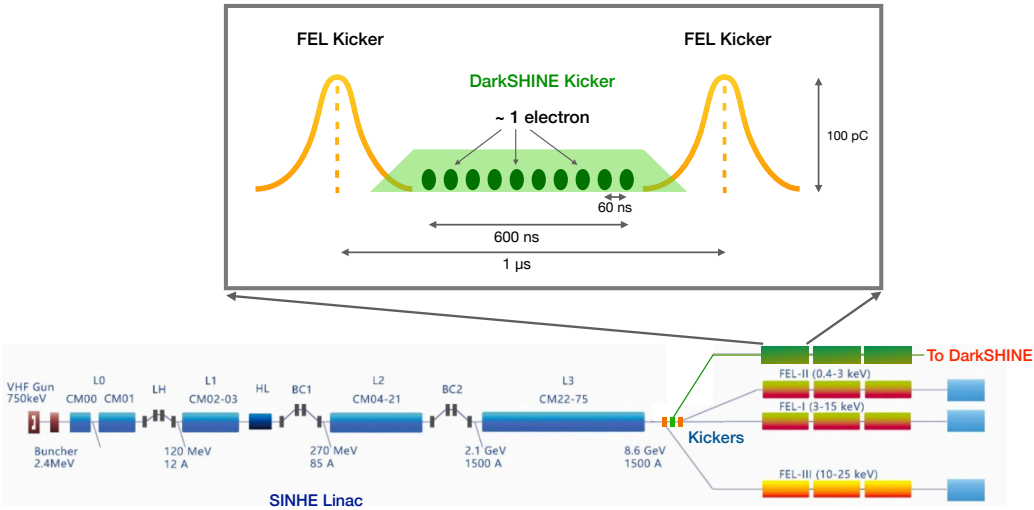


Figure A–3 Schematic representation of the beamline and kicker systems.

is the tagging tracker, which is designed to identify and tag particles. Adjacent to the edge of the magnet lies the recoil tracker. The experimental target is strategically positioned in the middle of these tracking systems. Following the recoil tracker, the ECAL is placed, and it is subsequently succeeded by the HCAL. The parameters based on the geometry of these sub-detectors are summarized in Table A–1, which serves as the baseline setup for this study.

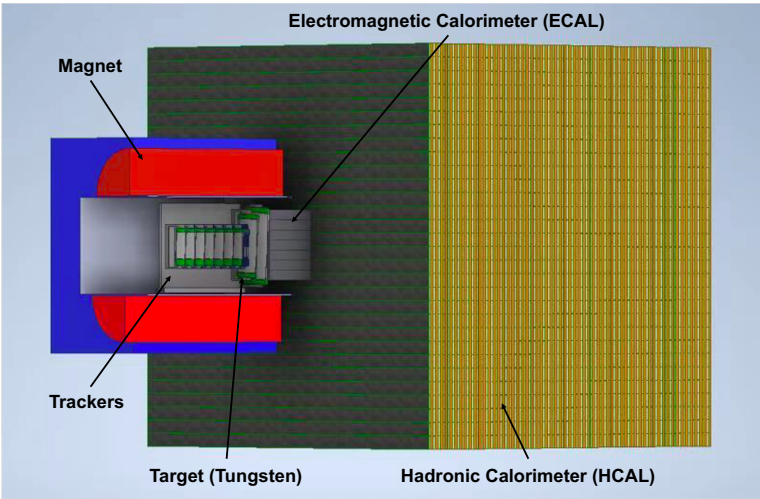


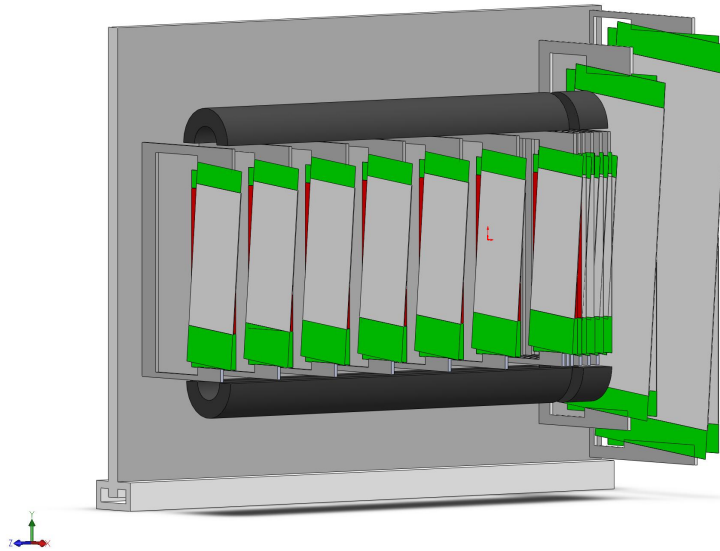
Figure A–4 Schematic layout of the detector and its components.

The DarkSHINE experiment incorporates a sophisticated tracking system embedded within

Node	Centre (mm)		Size (mm)		Arrangement	Comments
	z	x	y	z		
Tagging tracker	-307.783	200	400	600.216	7 layers	Second layer rotation: 0.1 rad
Target	0	100	200	0.35	-	
Recoil tracker	94.032	500	800	172.714	6 layers	Second layer rotation: 0.1 rad
ECAL	408.539	506	506	454.3	$20 \times 20 \times 11$ cells	-
HCAL	2660.69	4029.51	4029.51	4048.01	$4 \times 4 \times 1$ modules	-

Table A-1 The detector geometry overview.

a dipole magnet generating a magnetic field of 1.5 T. A silicon-based tracker is employed for the purpose of reconstructing both incident and recoil electron trajectories, thereby enabling the calculation of their respective momenta. Illustrated in Figure A-5, the tagging tracker comprises seven layers of silicon strip detectors, while the recoil tracker is designed with six such layers. Situated between these two tracking modules is a tungsten (W) target with a decay length of $0.1X_0$. To enhance the spatial resolution, each layer of both tracking modules accommodates two silicon strip sensors, which are oriented at a small angle of 100 mrad relative to one another. This configuration facilitates the precise measurement of particle positions in the x-y plane. The system achieves an impressive horizontal resolution of approximately $6 \mu\text{m}$ and a vertical resolution of around $60 \mu\text{m}$.

**Figure A-5 Illustration of tracking system components.**

The DarkSHINE experiment features a high-resolution electromagnetic calorimeter (ECAL) situated immediately downstream of the recoil tracker. This ECAL is designed to capture and reconstruct the energy deposition of incident particles. The scintillation material chosen for this application is LYSO(Ce) crystal, selected for its advantageous properties, such as high light yield, rapid decay time, and minimal electronic noise. The ECAL is comprised of a $20 \times 20 \times 11$ array of these LYSO crystals. Each individual crystal has a cross-sectional area measuring $2.5 \times 2.5 \text{ cm}^2$ and a length of 4 cm. The total decay length facilitated by this LYSO array amounts to $44 X_0$, ensuring that final state electrons and photons are fully absorbed, thereby allowing for a complete energy reconstruction. The energy resolution of the LYSO crystal array has been experimentally determined to be approximately 10% when calibrated using a ^{22}Na radioactive source.

Subsequent to the ECAL a hadronic calorimeter (HCAL) is installed to capture and veto hadronic background, with a particular emphasis on muon elimination. The HCAL is engineered as a scintillator-based sampling calorimeter featuring steel absorbers. It has dimensions of $100 \text{ cm} \times 100 \text{ cm}$ in the x-y plane. Each of the scintillators in HCAL is encapsulated in a carbon envelope and contains a centrally located wavelength-shifting fiber, enhancing its detection capabilities.

A.3 Simulation

This study employs simulations based on the baseline detector geometry delineated in Sec. A.2. The incident electron energy is fixed at 8 GeV. Signal samples are generated parametrically as functions of the dark photon mass. Both inclusive backgrounds and key rare processes, such as photon–nuclear interactions, electron–nuclear interactions, and photon decays to muon pairs, are simulated to enhance the understanding and quantification of background events. Additional background contributions deemed negligible are explored in Sec. A.5.3.

The DarkSHINE Software framework consolidates multiple functionalities, including detector simulation, digitization, event display, event reconstruction, and data analysis. It employs a proprietary data structure model for seamless data flow across various computational stages. GEANT4 v10.6.0^[52,53] serves as the simulation engine, specifically tailored for the DarkSHINE detector.

A.3.1 Signal Sample Production

Dark photon signal events are generated using CalcHEP v3.4^[299], while GEANT4 v10.6.0 is utilized for detector simulation. A total of 25 signal samples are produced, each comprising 1×10^5 events, across a range of dark photon masses denoted as $m_{A'}$, varying from 1 MeV to 2000 MeV.

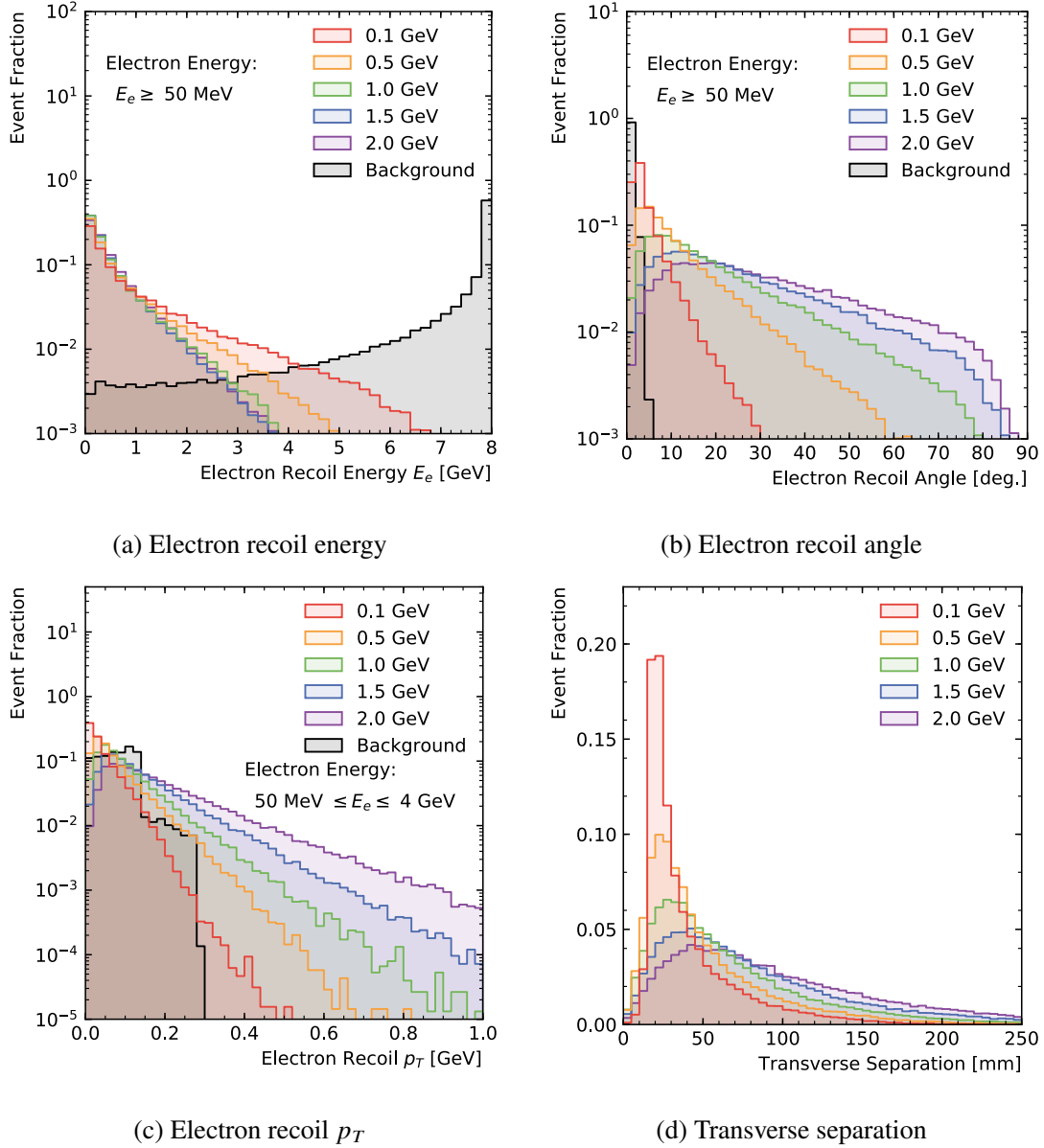


Figure A-6 Kinematic distributions of recoil electron variables, juxtaposing signal samples with an inclusive background sample.

Figure A-6 exhibits the kinematic distributions of the signal and inclusive background. Signal events primarily transfer their momentum to the dark photon, leading to a recoil electron with typically less than a quarter of the initial momentum. Conversely, in background events, the recoil electron retains most of the incident momentum. Hence, imposing a cut on the recoil electron momentum proves pivotal for signal region delineation. For increasing dark photon masses in signal events, the recoil electron angle and transverse momentum, on average, manifest higher values, in contrast to their smaller magnitudes in background events. The transverse momentum in the background concentrates around 100 MeV due to the magnetic field's 1.5 T strength. Upon inspection of the transverse separation in the signal events, higher dark photon mass tends to yield greater average distances.

A.3.2 Background Sample Production

Figure A-7 illustrates the hierarchy of major background processes, along with their corresponding relative rates. Predominantly, incident electrons traverse the target without undergoing any interaction. However, approximately 6.7% of these electrons emit hard bremsstrahlung photons, leading to a final state comprising a recoil electron and a photon. Subsequently, these bremsstrahlung photons can engage in photon–nuclear interactions with the materials of ECAL and the target, occurring with relative rates of 2.31×10^{-4} and 1.37×10^{-6} with respect to the inclusive rate, respectively. Furthermore, the bremsstrahlung photons can undergo conversions, resulting in muon pairs at ECAL and the target, with relative rates of 1.63×10^{-6} and 1.50×10^{-8} , respectively. Although bremsstrahlung photons can also yield electron pairs at a substantially high rate, these electrons are readily identifiable and reconstructable by the tracking system and ECAL. Apart from the aforementioned processes instigated by hard bremsstrahlung photons, electron–nuclear interactions involving the materials of ECAL and the target also contribute significantly to the background, with relative rates of 3.25×10^{-6} and 5.10×10^{-7} .

An inclusive background sample comprising 2.5×10^9 events was generated for this study. In addition, six rare processes were also simulated, the statistics of which, along with the corresponding EOTs, are detailed in Table A-2.

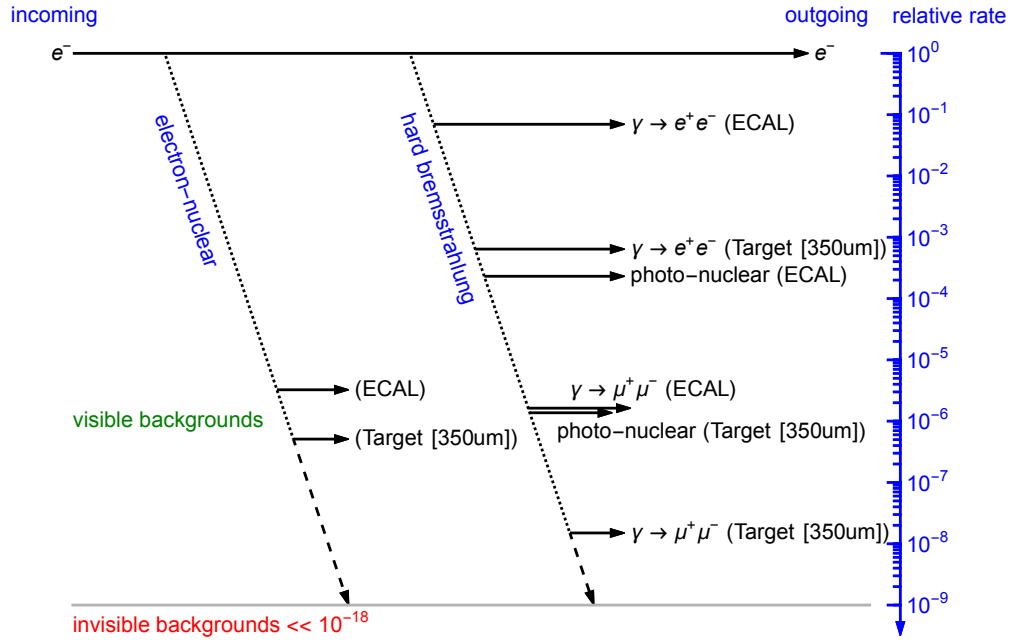


Figure A-7 Schematic depiction of the principal background processes and their associated relative rates. These rates serve as branching ratios and are tabulated in Table A-2.

Process	Generate Events	Branching Ratio	EOTs
Inclusive	2.5×10^9	1.0	2.5×10^9
Bremsstrahlung	1×10^7	6.70×10^{-2}	1.5×10^8
GMM_target	1×10^7	$1.5(\pm 0.5) \times 10^{-8}$	4.3×10^{14}
GMM_ECAL	1×10^7	$1.63(\pm 0.06) \times 10^{-6}$	6.0×10^{12}
PN_target	1×10^7	$1.37(\pm 0.05) \times 10^{-6}$	4.0×10^{12}
PN_ECAL	1×10^8	$2.31(\pm 0.01) \times 10^{-4}$	4.4×10^{11}
EN_target	1×10^8	$5.1(\pm 0.3) \times 10^{-7}$	1.6×10^{12}
EN_ECAL	1×10^7	$3.25(\pm 0.08) \times 10^{-6}$	1.8×10^{12}

Table A-2 Summary of background sample production, specifying branching ratios and corresponding EOTs for each rare process. The branching ratios are derived from the inclusive sample, conditioned on the energy of the electron being greater than 4 GeV.

A.4 Signal Region Definition

Informed by the distribution of background processes as illustrated in figure [A-7](#), we construct a set of event selection criteria, leveraging the following detector variables:

- Count of reconstructed tracks in the tagging tracker, denoted as $N_{\text{trk}}^{\text{tag,rec}} = 1$;
- Disparity in electron momentum, represented as $p_{\text{tag}} - p_{\text{rec}} > 4 \text{ GeV}$;
- Cumulative energy measured in ECAL, quantified by $E_{\text{ECAL}}^{\text{total}} < 2.5 \text{ GeV}$;
- Aggregate energy observed in HCAL, not exceeding $E_{\text{HCAL}}^{\text{total}} < 0.1 \text{ GeV}$;
- Peak energy registered in an individual HCAL cell, confined to $E_{\text{HCAL}}^{\text{MaxCell}} < 2 \text{ MeV}$.

Subsequent analysis confirms that these thresholds are optimized to effectively mitigate background events while retaining high signal sensitivity.

Focusing on tracking data, it is observed that dark photon signal events typically manifest as a solitary reconstructed track in both the tagging and recoil trackers. The momentum difference between these two tracks, depicted in the top-left quadrant of figure [A-8](#), clearly segregates signal from background. Specifically, in the signal case, the 'missing momentum'—attributed to the dark photon—tends to be higher, whereas it decays rapidly in background scenarios dominated by hard bremsstrahlung events. To exclude such background contamination effectively, a preselection criterion on missing momentum, $p_{\text{tag}} - p_{\text{rec}} > 4 \text{ GeV}$, is instituted.

Pivoting to the calorimeter system, Figure [A-8](#) contains several significant plots. Subfigure (a) shows the difference in momentum between the tagging and recoil electrons ($P_{\text{tag}} - P_{\text{rec}}$) for the inclusive background, as well as for signal samples of 1 MeV, 10 MeV, 100 MeV, and 1000 MeV. Subfigures (b, c, d) display the two-dimensional distribution of total energy in ECAL and HCAL for the inclusive background and the 10 MeV and 1000 MeV signal samples, respectively.

In the case where a dark photon decays into a Dark Matter (DM) pair, the decay products would evade detection, leaving no energy trace in ECAL and HCAL. Conversely, background processes generally register substantial energy deposits in these calorimeters, especially hadronic backgrounds which are predominantly absorbed in HCAL. Hence, judicious selection criteria based on the total and maximum cell energy in HCAL can effectively filter out such backgrounds while maintaining high signal fidelity.

To enhance the analytical sensitivity, cuts on HCAL energy are rigorously optimized. In

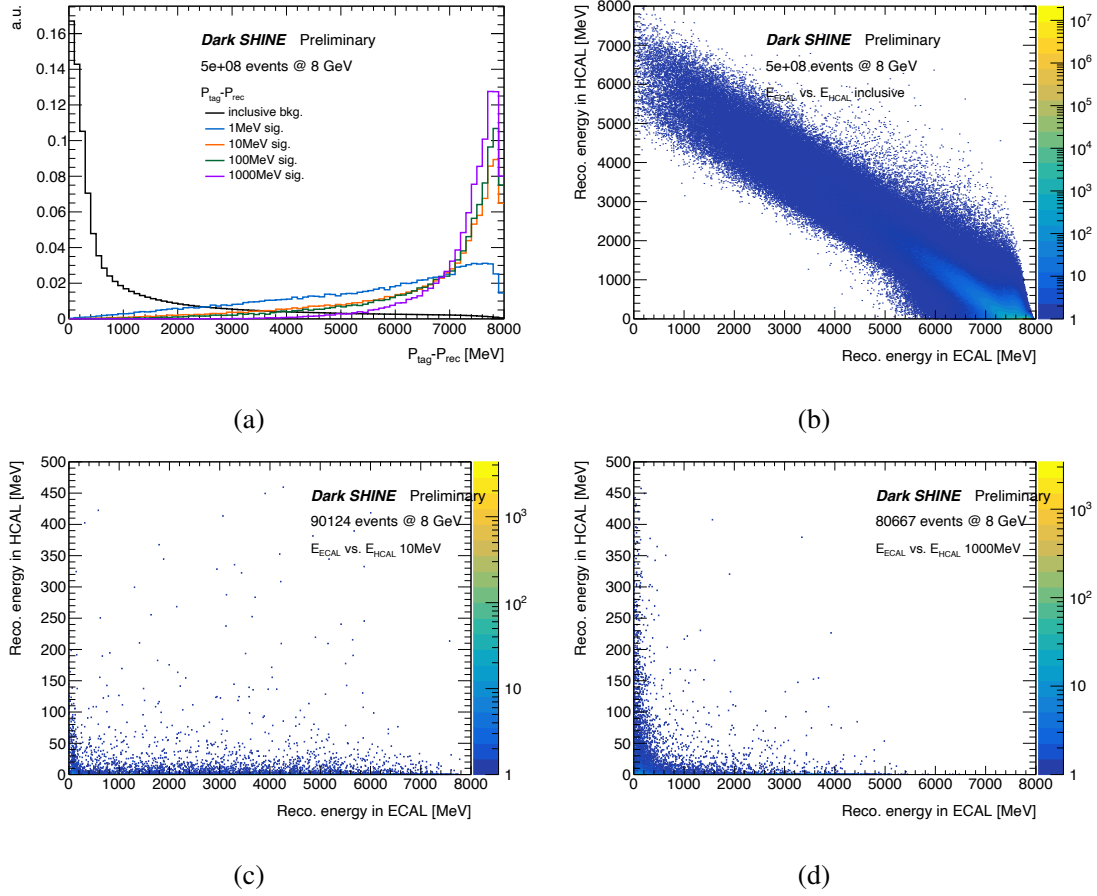


Figure A-8 Distributions of key variables for different signal and background samples.

typical dark photon signal scenarios, no energy deposition in HCAL is expected, thereby necessitating stringent HCAL veto criteria to suppress specific backgrounds, including $\gamma \rightarrow \mu\mu$ events and hadronic final states. The acceptance efficiency, as a function of HCAL energy, is depicted in Figure A-9 for a simulated 10 MeV signal sample. Here, the total HCAL energy cut varies from 5 MeV to 100 MeV, and the maximum cell energy in HCAL varies from 1 MeV to 20 MeV. Within this energy range, the efficiency remains relatively invariant. Specifically, the 10 MeV signal sample experiences a signal efficiency increase from 61% to 63% when the cut combination of $(E_{\text{HCAL}}^{\text{total}}, E_{\text{HCAL}}^{\text{MaxCell}})$ is relaxed from (5 MeV, 1 MeV) to (100 MeV, 10 MeV). Approximately a 1–2% efficiency improvement is also observed for other signal samples. Consequently, the final cut values chosen for optimal background suppression are $E_{\text{HCAL}}^{\text{total}} < 100$ MeV and $E_{\text{HCAL}}^{\text{MaxCell}} < 2$ MeV.

As depicted in Figure A-10, the acceptance efficiencies for various simulated signal sam-

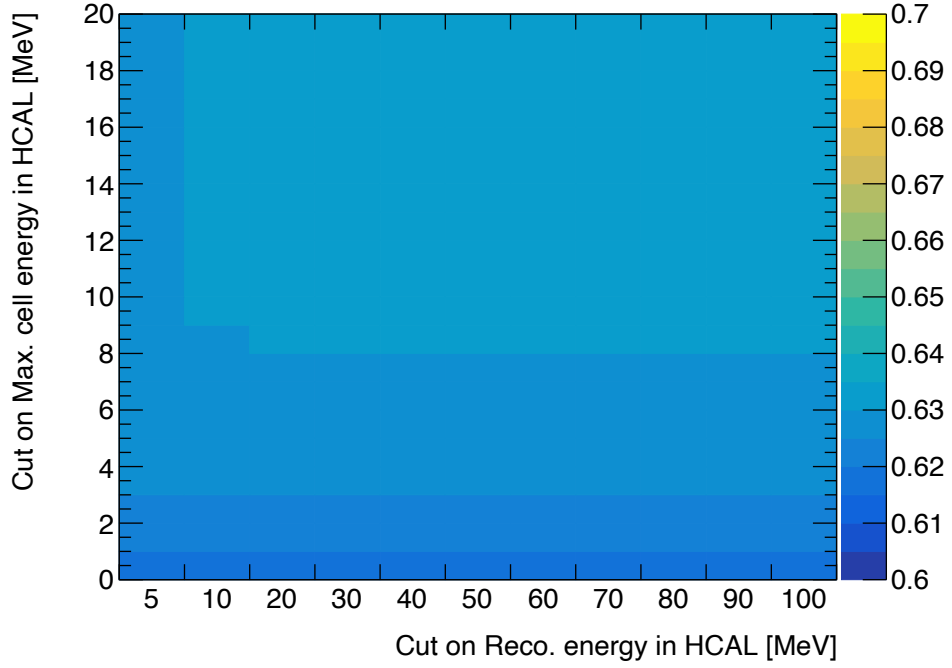
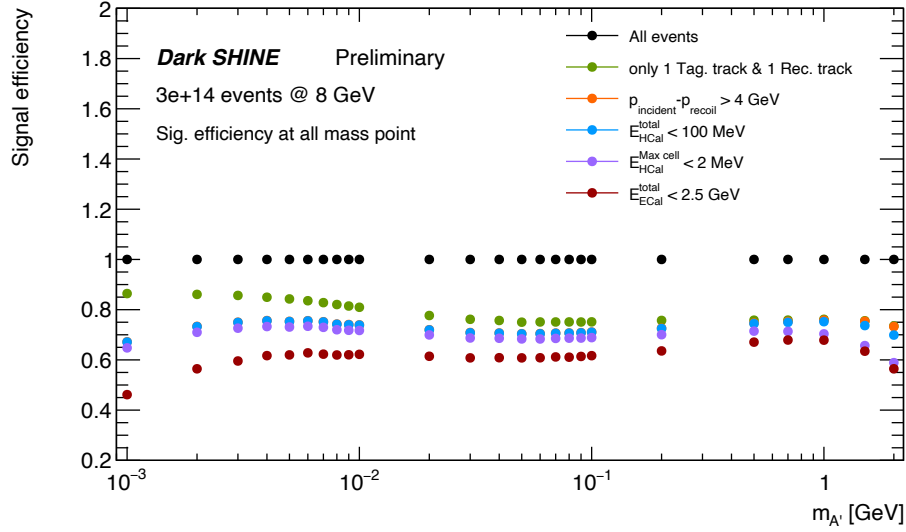


Figure A-9 Efficiency vs. HCAL energy for the 10 MeV signal.

ples are plotted as a function of the dark photon mass, $m_{A'}$. Overall, high signal efficiencies surpassing 60% are sustained across most of the $m_{A'}$ range subsequent to the application of all selection criteria. However, the efficiencies witness a decline to approximately 50% when $m_{A'}$ is in the range of a few MeV or above 1 GeV. For the lower $m_{A'}$ values, the prevailing ECAL and HCAL energy cuts might be excessively stringent, thereby suggesting the need for tailored optimization. Additionally, events with large incident or recoil angles are likely to bypass the ECAL and directly impact the HCAL due to specific geometric configurations at the simulation level. This phenomenon becomes increasingly prevalent for larger $m_{A'}$ values and results in their rejection by the HCAL energy cuts, thereby leading to diminished selection efficiencies.

To summarize, a comprehensive overview of the background cut flow and corresponding selection efficiencies are documented in Tables [A-3](#) and [A-4](#), respectively.

Figure A-10 Dark photon signal efficiencies across $m_{A'}$.

	EN_ECAL	PN_ECAL	GMM_ECAL	EN_target	PN_target	GMM_target	hard_brem	inclusive
total events	2.48×10^7	1.66×10^8	1.74×10^7	1.09×10^8	1.05×10^7	1.05×10^7	1.02×10^7	2.50×10^9
only 1 track	1.46×10^7	1.17×10^8	1.52×10^7	6.38×10^6	6.17×10^5	77	8.03×10^6	2.11×10^9
$p_{tag} - p_{rec} > 4 \text{ GeV}$	1091	5531	707	6.08×10^6	5.73×10^5	1	7.19×10^6	1.20×10^8
$E_{HCAL}^{total} < 100 \text{ MeV}$	135	1348	0	322135	75501	0	1.19×10^8	2.89×10^7
$E_{HCAL}^{MaxCell} < 10 \text{ MeV}$	56	676	0	141808	27949	0	1.12×10^8	2.72×10^7
$E_{HCAL}^{MaxCell} < 2 \text{ MeV}$	30	363	0	63644	9999	0	1.01×10^8	2.46×10^7
$E_{ECAL}^{total} < 2.5 \text{ GeV}$	0	0	0	0	0	0	0	0

Table A-3 Event cut flow for each background sample in Table A-2. The number of events remaining after each cut is listed in the table.

A.5 Background Estimation

As evidenced by the background cut flow tables (Tables A-3 and A-4), none of the 2.5×10^9 simulated inclusive background events survive the selection criteria, mirroring the outcome for each of the rare background processes. To project the background yields for a one-year operation of the DarkSHINE experiment, corresponding to 3×10^{14} EOTs, an initial investigation into the background rejection efficiency within side-band regions is mandated, subsequently facilitating extrapolations into the signal region.

To this end, rare background samples of substantial statistical heft, ranging from 10^{11}

	EN_ECAL	PN_ECAL	GMM_ECAL	EN_target	PN_target	GMM_target	hard_brem	inclusive
total events	100%	100%	100%	100%	100%	100%	100%	100%
only 1 track	58.87%	70.48%	87.36%	5.85%	5.88%	$< 10^{-3}\%$	78.73%	84.40%
$p_{tag} - p_{rec} > 4 \text{ GeV}$	0.0044%	0.0033%	0.0041%	5.58%	5.46%	$< 10^{-5}\%$	70.49%	4.80%
$E_{HCAL}^{total} < 100 \text{ MeV}$	$< 10^{-3}\%$	$< 10^{-3}\%$	0%	0.30%	0.72%	0%	69.61%	4.76%
$E_{HCAL}^{MaxCell} < 10 \text{ MeV}$	$< 10^{-3}\%$	$< 10^{-3}\%$	0%	0.13%	0.27%	0%	65.00%	4.48%
$E_{HCAL}^{MaxCell} < 2 \text{ MeV}$	$< 10^{-3}\%$	$< 10^{-3}\%$	0%	0.058%	0.095%	0%	58.14%	4.04%
$E_{ECAL}^{total} < 2.5 \text{ GeV}$	0%	0%	0%	0%	0%	0%	0%	0%

Table A–4 Event cut flow for each background sample in Table A–2. The selection efficiencies of each cut are listed in the table.

to 10^{12} EOTs as per Table A–2, are deployed for the extraction of anticipated background yields via the fitting of event ratios at prespecified ECAL energy thresholds. For verification purposes, this extrapolation strategy is reciprocally applied to both the inclusive background sample and a series of low-beam energy samples.

Section A.5.1 elaborates on the extrapolation methodology specific to rare background processes. Section A.5.2 furnishes details concerning the validation via inclusive background simulation. Further, Sec. A.5.3 deliberates on rare backgrounds featuring neutrinos in their final states. A summarial discourse on background estimation is presented in Sec. A.5.4.

A.5.1 Extrapolation from rare processes simulation

Figure A–11 depicts the event ratios as a function of energy cut values on ECAL for cases with only one tagged track and one recoil track. The data points for six rare background processes (EN_ECAL, EN_target, PN_ECAL, PN_target, GMM_ECAL, and GMM_target) are exhibited, each scaled in accordance with its corresponding branching ratio. In terms of event ratios, the individually generated samples for each of these rare processes align well with their inclusive background counterparts. The composite of these six processes, represented by gray circles, is derived from the rare background samples, whereas the gray dots are obtained from the inclusive background samples. Notably, concordance between these summed fractions is observed, particularly in regions of high energy where statistical robustness is sufficient. A nominal ECAL energy cut at 2.5 GeV is denoted by a blue dashed line.

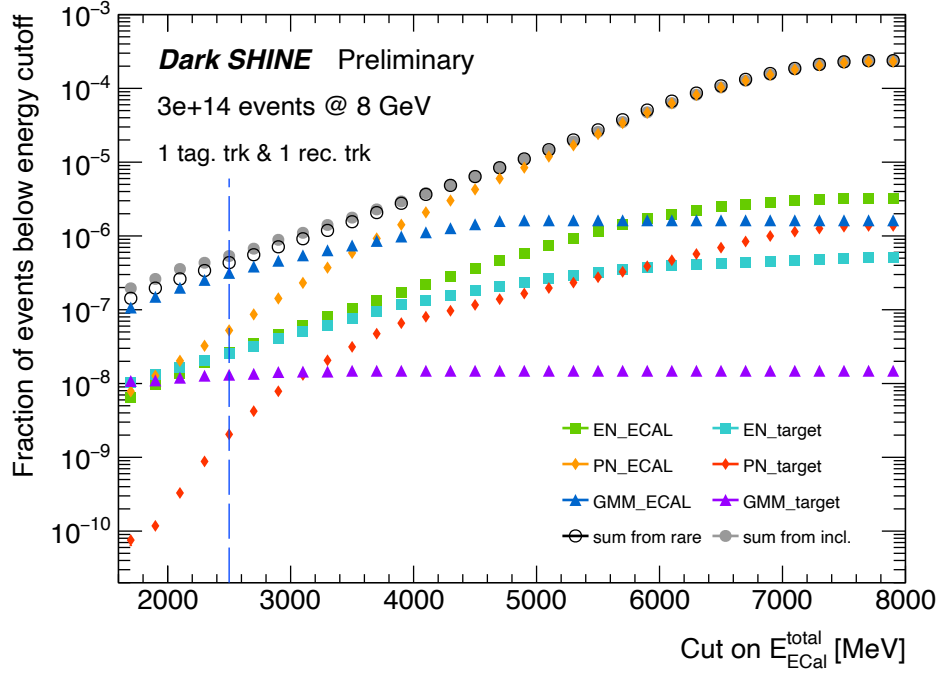


Figure A-11 Event ratio as a function of ECAL energy cut.

The expected background yield at a given ECAL energy cut is computed from the corresponding event ratio. For instance, with an event ratio below 10^{-14} at an energy cut x , it can be inferred that fewer than one background event will remain in a sample of 10^{14} events when imposing the condition $E_{ECAL}^{total} < x$ MeV. To derive the comprehensive background yield within the signal region, the full set of selections delineated in Sec. A.4 must be applied. However, the limited statistics preclude a straightforward extrapolation. The efficacy of HCAL energy cuts results in the depletion of statistics for most processes displayed in Figure A-11, particularly below the nominal ECAL energy cut of 2.5 GeV. Therefore, both high-statistics rare background samples and an extrapolation methodology are employed to extend event ratio trends into low-energy regimes. This approach facilitates the evaluation of background yields for each of the six rare processes, the sum of which serves as the final background yield after validation.

GMM processes are comparatively easier to eliminate. Given the present statistical breadth, no events from GMM_ECAl (6×10^{12} EOTs) or GMM_target (4.3×10^{14} EOTs) survive the signal region selection per Table A-3. As shown in Figure A-11, the event ratio for the GMM channel is largely unaffected by ECAL energy cuts. Most of the energy is deposited in the

HCAL due to the muon pair. Application of HCAL energy cuts results in a residual GMM event fraction less than 10^{-6} , validating its exclusion from this analysis.

Figure A-12 illustrates background extrapolation plots, showing the fraction of events below certain energy cutoffs for four key processes: EN_ECAL, EN_target, PN_ECAL, and PN_target. These fractions are scaled according to their respective branching ratios. The function $e^{a \log(x)+b}$ is fitted to these fractions, where x is the ECAL energy cut value, and a and b are free parameters.

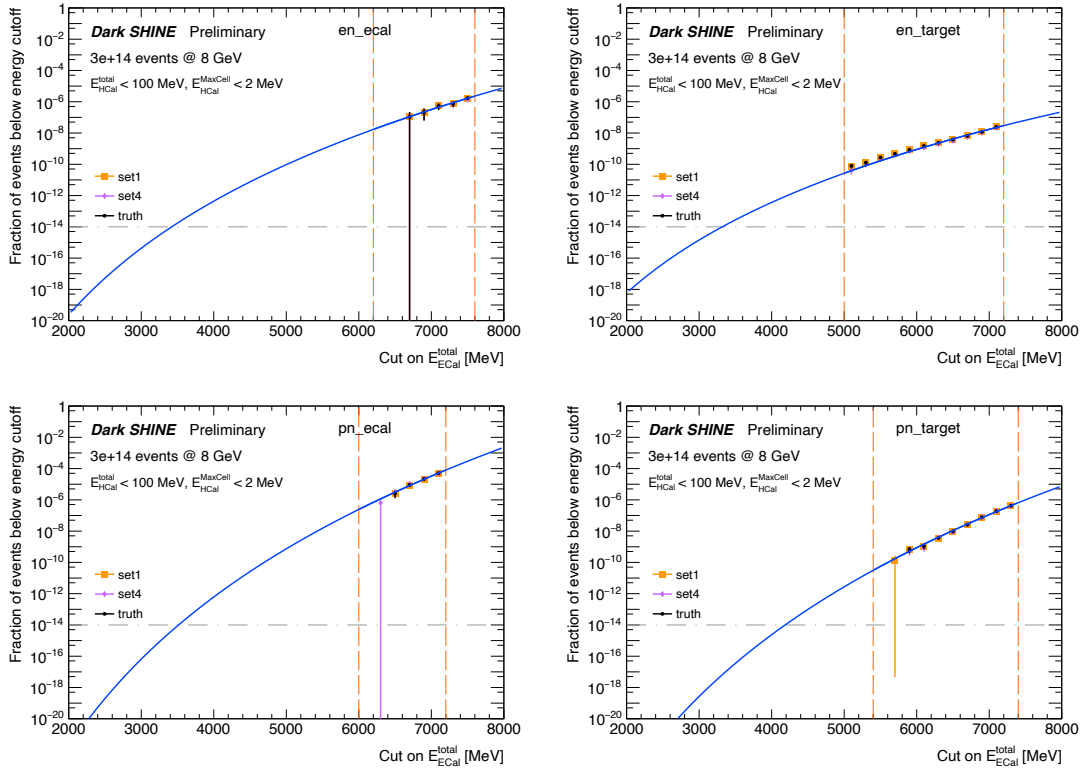


Figure A-12 Background extrapolation plots for four key processes.

Rare process	EN_ECAL	EN_target	PN_ECAL	PN_target	GMM
Estimated yield	0.0016	0.013	5.93×10^{-5}	2.53×10^{-7}	0

Table A-5 Expected number of each background process, estimated from the extrapolation method. The background yields listed in the table correspond to 3×10^{14} EOTs.

To obtain the background yield at $E_{ECAL}^{total} = 2.5$ GeV for the remaining four processes, an exponential-logarithmic function is employed to fit the event ratio while maintaining all

other signal region cuts. It should be highlighted that each background channel exhibits distinct cut efficiencies, necessitating individualized functional forms and parameter tuning. Figure A-12 displays the fit extrapolations for the EN_ECAL, EN_target, PN_ECAL, and PN_target channels. All the criteria defining the signal region, with the exception of the ECAL energy cut, are applied. The fractions for each channel are scaled in accordance with their respective branching ratios. The blue solid line in the plots represents the fitted function, which satisfactorily captures the form of the event ratio within the fit range delineated by the orange dashed lines. The estimated background yields for these channels are summarized in Table A-5. The aggregated background yield for these rare processes is calculated to be approximately 0.015 upon summing their extrapolated yields.

A.5.2 Validation from inclusive background simulation

The baseline background yield is primarily derived from the rare processes; however, for cross-validation, an inclusive background sample is also analyzed, as depicted in Figure A-13. Here, the event ratio curve is fitted using an exponential-quadratic function of the form e^{ax^2+bx+c} , resulting in an expected background yield of 2.53×10^{-3} when all signal region criteria are applied. The low statistics in the low-energy region prompt further validation efforts.

Additional inclusive background samples, each with 1×10^7 events, are generated at discrete electron beam energies ranging from 3 to 7.5 GeV. The event selection criteria are adapted to suit these lower-energy beams, with the missing momentum requirement now set to exceed half of the beam energy. The energy cuts in the HCAL detector are temporarily relaxed to $E_{HCAL}^{total} < 100$ MeV and $E_{HCAL}^{MaxCell} < 20$ MeV to preserve adequate statistics. The event fractions from these samples are scaled and aligned to corroborate with the 8 GeV sample, forming the basis for a direct extrapolation method shown in Figure A-14.

To obtain background yields conforming to the signal region conditions, a scale factor is established between the fit outcomes for different HCAL maximum cell energy cuts. Figure A-15 illustrates the fitting procedure for the more relaxed HCAL cut of $E_{HCAL}^{MaxCell} < 20$ MeV. The scaling process yields an extrapolated background estimate of 9.23×10^{-3} for 3×10^{14} EOTs, corroborating the results of the original fit extrapolation method.

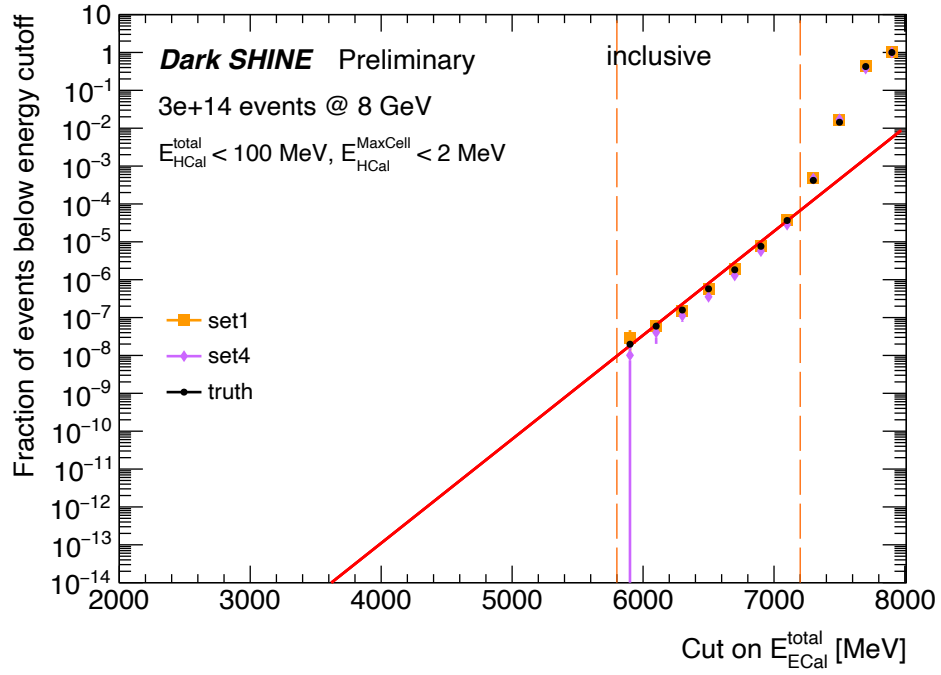


Figure A-13 Background Extrapolation from Inclusive Sample

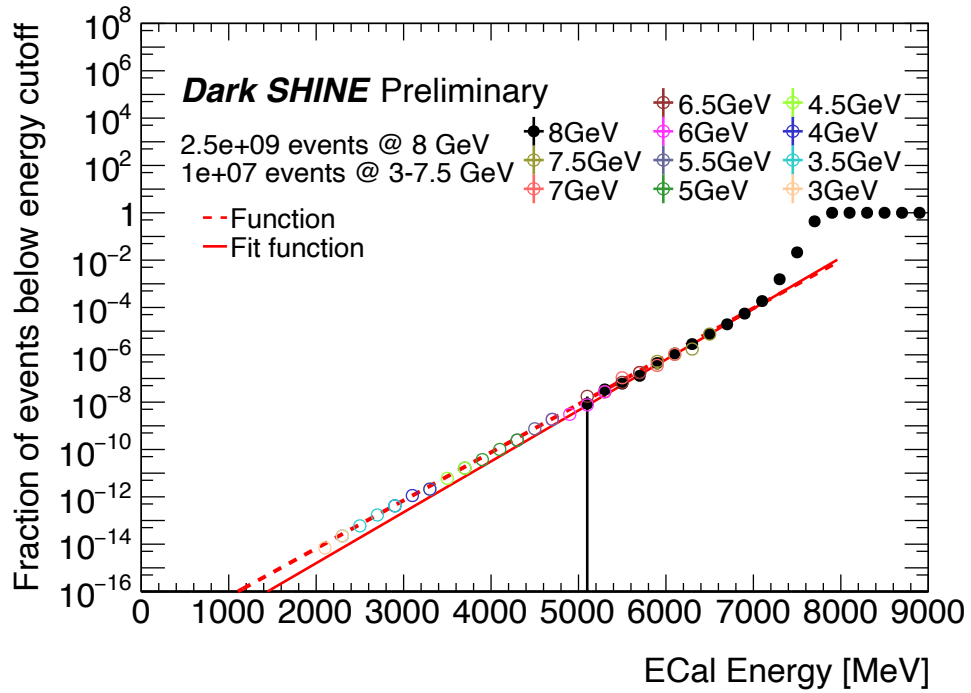


Figure A-14 Background Extrapolation Validation

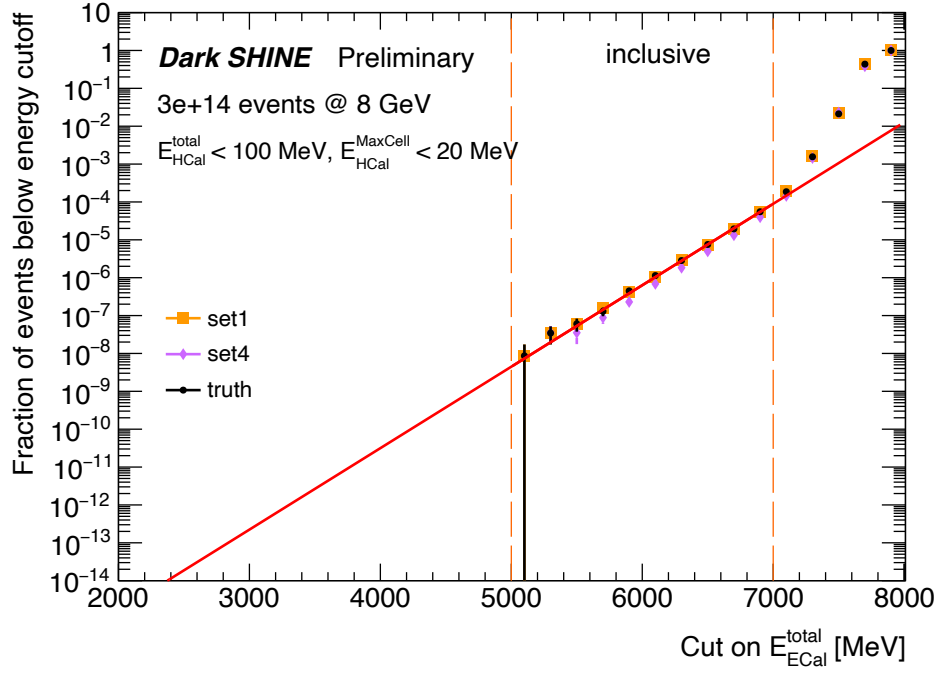


Figure A-15 Background Extrapolation with Relaxed HCAL Cut

A.5.3 Invisible background estimation

Neutrino backgrounds originating from specific production reactions constitute a critical source of irreducible backgrounds, indistinguishable from the signal processes. According to Section IV of [291], there are primarily two leading reactions to consider. The first encompasses Moller scattering followed by charged-current quasi-elastic (CCQE) reactions, mathematically denoted as $e^-e^- \rightarrow e^-e^-$ and $e^-p \rightarrow \nu_e n$. For an incident electron energy of 10 GeV with a W target, the Moller cross-section σ_{Moller} is roughly 0.4 b and σ_{CCQE} is 8 fb per nucleon. Given that DarkSHINE employs a 0.035-cm W target, this results in an estimated 10^{-4} events per 10^{14} EOTs. The second category involves neutrino pair production, $e^-N \rightarrow e^-N\nu\bar{\nu}$, with a cross-section of 0.03 fb, yielding 6×10^{-6} events per 10^{14} EOTs. Notably, DarkSHINE utilizes an 8 GeV incident electron energy, which implies that the above ratios serve as upper limits for this experiment.

In addition to these irreducible reactions, two other background scenarios are outlined in [291]: bremsstrahlung \oplus CCQE and charge current exchange with exclusive $e^-p \rightarrow \nu n \pi_0$. Both yield approximately 0.1 event per 10^{14} EOTs in DarkSHINE but can be effectively dis-

The irreducible reaction	Moller scattering	neutrino pair production
estimated yield	3×10^{-4}	$< 1.8 \times 10^{-5}$
The irreducible reaction	Bremsstrahlung \oplus CCQE	charge current exchange
estimated yield	0.3	0.3

Table A-6 Summary of Invisible Backgrounds

regarded due to their inability to pass the one-track criterion, which forms part of the signal region selection.

Furthermore, during the analysis, a small number of events were observed that left no energy deposition in ECAL. Specifically, 2 out of 1×10^7 hard bremsstrahlung samples and 6 out of 5×10^8 inclusive samples exhibited this characteristic. These events were traced back to photons produced via hard bremsstrahlung, which managed to traverse the gaps between ECAL cells to deposit energy exclusively in HCAL. The minimum energy deposition noted in HCAL was 527.7 MeV. Such events are effortlessly discarded through the application of HCAL energy cuts.

A.5.4 Background Estimation Summary

To consolidate our understanding of the background processes, we summarize the expected numbers of background events in the sensitivity study. These numbers are derived from multiple avenues: event cut flow, background extrapolation methods, and the invisible background estimation. Table A-7 displays the yield for each method, corresponding to a total exposure of 3×10^{14} EOTs. It should be noted that the cumulative yield from the rare background processes is conservatively high but is in agreement with the validation conducted on the inclusive sample.

Method	Cut Flow	Rare Extrapolation	Inclusive Extrapolation	Inclusive Validation	Invisible Background
Yield	0	1.5×10^{-2}	2.53×10^{-3}	9.23×10^{-3}	Negligible

Table A-7 Summary of Background Yields

A.6 Sensitivity study

The relationship between the kinetic mixing parameter ε and the expected signal yield N_{sig} is governed by the formula:

$$N_{\text{sig}} = \sigma_{A'} \times 0.1X_0 \times L \times N_A / M_W \times 10^{-36} \times \varepsilon^2,$$

where $\sigma_{A'}$ is the production cross section for a dark photon of mass $m_{A'}$ (see Figure A-2), $0.1X_0 = 0.676 \text{ g/cm}^2$ denotes the thickness of the tungsten target, $L = 3 \times 10^{14} \text{ EOTs}$ signifies the number of events, N_A is the Avogadro constant, and $M_W = 184$ represents the atomic mass of tungsten.

Given the low estimated background yield elaborated in Section A.5, it is reasonable to model all observed events as background following a Poisson distribution. Therefore, the upper limit on signal times acceptance efficiency at 90%-CL is

$$s_{\text{up}} \times \varepsilon_{\text{sig}} = \frac{1}{2} F_{\chi^2}^{-1}(1 - \alpha; 2(n_{\text{obs}} + 1)) - b,$$

where ε_{sig} is the acceptance efficiency, dependent on $m_{A'}$ (see Figure A-10), and $n_{\text{obs}} = b = 0.015$ is the constant background yield. This leads to upper limits on ε^2 :

$$\varepsilon^2 = s_{\text{up}} / \varepsilon_{\text{sig}} \times \sigma_{A'} \times 0.1X_0 \times L \times N_A / M_W \times 10^{-36}.$$

The current constraints and sensitivity estimates on ε^2 as a function of $m_{A'}$ are displayed in Figure A-16. This figure visualizes the expected upper limits on ε^2 for different data collection periods: $3 \times 10^{14} \text{ EOTs}$ (1 year), $9 \times 10^{14} \text{ EOTs}$ (3 years), and $1.5 \times 10^{15} \text{ EOTs}$ (5 years). Results from other experiments are also integrated for comparison.

In our investigation, we focus on the projected sensitivity in the dimensionless interaction strength $y = \varepsilon^2 \alpha_D (m_\chi / m_{A'})^4$ as a function of Dark Matter (DM) mass m_χ . We adopt the conventional assumptions that $m_{A'} = 3m_\chi$ and $\alpha_D = 0.5$. Figure A-17 illustrates this sensitivity, with the calculated projections for the data collected by the DarkSHINE experiment under various conditions of event numbers: 3×10^{14} , 9×10^{14} , 1.5×10^{15} , and 10^{16} EOTs .

The results indicate promising prospects for the DarkSHINE experiment. For example, with a data-taking duration of at least one year, the DarkSHINE experiment will likely commence probing the existence of thermal relic DM in the MeV mass range. Existing and anticipated constraints are also plotted for comparison [300-306].

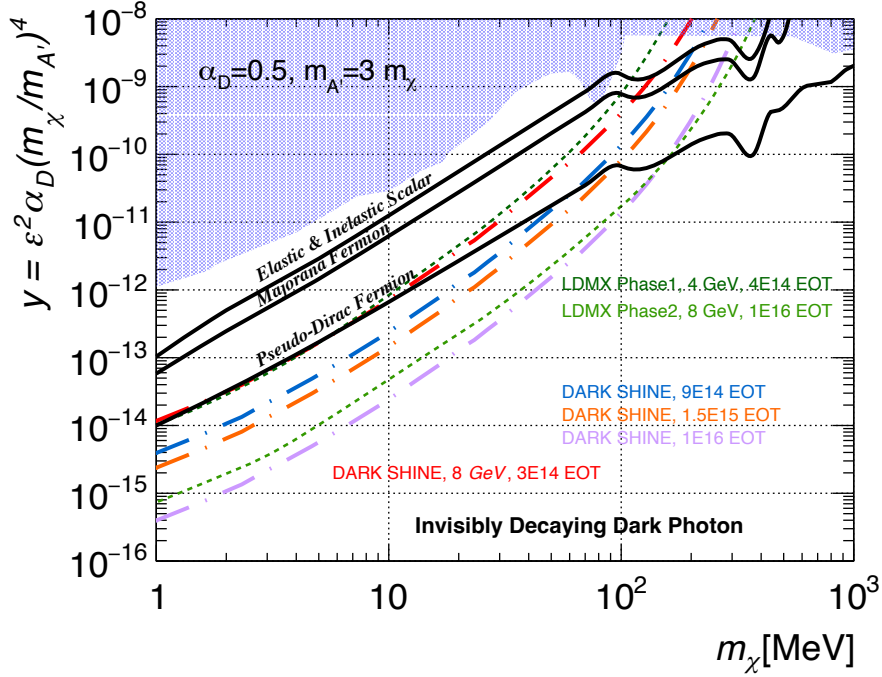


Figure A-17 Projected 90% CL exclusion limits on y at different event numbers (DarkSHINE experiment).

A.7 Summary

This paper investigates the search for the invisible decay of dark photons in fixed-target DarkSHINE experiments utilizing electron beams. Through rigorous simulation methods, we have scrutinized both signal and background signatures. The optimized signal region was identified to minimize background contributions while maximizing signal acceptance efficiency.

For the background estimation, simulated samples were employed to study the contribution from various processes. Due to statistical limitations, an extrapolation method is invoked for a more accurate estimation, and its validity is confirmed through inclusive samples. Under these considerations, the expected background yield in the optimized signal region is computed to be 0.015 for 3×10^{14} electrons on target (EOTs).

Subsequently, upper limits at the 90% confidence level were derived for the kinetic mixing parameter ε^2 , as a function of the dark photon mass $m_{A'}$. These limits were calculated for

varying electron-on-target scenarios: 3×10^{14} EOTs, 9×10^{14} EOTs, 1.5×10^{15} EOTs, and 10^{16} EOTs, corresponding respectively to 1 year, 3 years, and 5 years of data collection, including the Phase II upgrade.

Finally, a comparative analysis with operational and prospective experiments yields highly competitive results. Specifically, the sensitivity of the DarkSHINE experiment is sufficient to probe, and potentially exclude, parameter spaces for models involving elastic and inelastic scalars, Majorana fermions, and pseudo-Dirac fermions.

Acknowledgements

正如古语所言：“山不厌高，海不厌深。”这句话深刻地映射了我在上海交通大学物理与天文学院粒子所的博士学习生涯。在这四年半的时间里，我始终追求着学术上的高山和知识的深海，始终致力于追求卓越和创新，努力突破传统思维的限制，拓宽学术视野。就像山峰永远向着更高的天空挑战，海洋永远探索着更深的蔚蓝，我在博士学习过程中也是如此，永远渴望着更深入的理解和更高级的研究。在这段旅程中，我得到了许多导师和同侪的悉心指导与支持。他们的智慧和激励，如同山的坚韧和海的广阔，引领我不断突破自我，勇往直前。我要特别在此，向他们表达我最诚挚的感谢：

首先，我要感谢我的导师，上海交通大学物理与天文学院粒子所的李亮教授。我从本科二年级就跟随李亮老师学习，是我在粒子物理领域的领路人，也是我博士生涯中最重要的导师，他对我学术研究和生活都给予了极大的关心和帮助。在我博士期间，李老师对我的研究工作给予了充分的自由，同时也给予了我极大的鼓励和支持。李老师最具有代表性的特点就是对文字的精益求精，他对我论文和报告都进行了反复的修改和指导，从语法到框架，从逻辑到细节，从内容到形式，他都给予了我极大的帮助。每周举办的各种组会，促进李老师的学生们互相了解，交流学术，充分关心每一个同学的科研进度。李老师支持学生出国交流，在他的帮助下，我成功申请到了国家自然科学基金委的奖学金，并在 2021 年 12 月至 2023 年 9 月期间在法国 Université Paris Cité 跟随者 Gregorio Bernardi 博士进行联合培养。可以说，在李老师的带领下，我在学术上得到了极大的提升，使我的博士学术生涯丰富充实，精神状态良好。

同时，我也要感谢我的联合培养导师，Université Paris Cité 的 Gregorio Bernardi 博士。Gregorio 是一个非常和蔼的，经验非常丰富，在粒子物理领域相当有名望的科学家。在我在法国的联合培养期间，Gregorio 对我的研究工作给予了充分的自由，同时也给予了我极大的鼓励和支持。在他的资助下，我经常往返巴黎和 CERN，参与多次学术交流会议以及培训学校等等，极大拓展了我的视野，以及给予了我与不同的国际合作者交流的机会。在他百忙之中，专门抽空从巴黎飞来上海，参加我的毕业答辩，给予了我莫大的鼓励。

其次，我要感谢在我的博士生涯中的所有项目中参与的老师 and 同学们。我的主要分析是 ATLAS 实验上的双希格斯玻色子的寻找，得到了 ATLAS 实验的许多老师和同学的帮助。在 $HH \rightarrow \text{multilepton}$ 的分析道中，对我帮助最大的是分析的联络人，方亚泉老师和 Yesenia Hernandez Jimenez 博士。他们作为分析的联络人，积极推动了整

个分析的进展，同时也经常给我的分析提出深刻独到的建议。同时也感谢分析组中一起工作的 Santosh Parajuli, 郭方毅, 辛水艇, Babar Ali, Bartek, 张凯栗, 李池昊等同事。在 $HH \rightarrow b\bar{b}\tau^+\tau^-$ 的分析中, 感谢一直指导我的分析联络人 Brian Moser 博士。他是非常有经验, 想法丰富的研究人员, 引领我完成了在 $b\bar{b}\tau^+\tau^-$ 中的分析。在 **HH+H Combination** 的分析中, 我要特别感谢分析的联络人张瑞博士, 他非常耐心地从各个角度指导我。我是第一次接触联合分析的工作, 他不厌其烦地从每一个细节教我, 使我能够顺利完成这个分析。同时也要感谢同组一起工作的李昌樵博士, 作为上海交通大学粒子所的博士后, 带领我们成为第一个完成 **HH+H Combination** 的分析组。**DarkSHINE** 实验也贯穿了我的整个博士生涯。这是由杨海军教授发起的上海交通大学的自主实验。我们从零开始, 一步步研发整个实验计划。现任华南师范大学副教授的胡继峰师兄在一开始, 细心指导我如何写各种模拟程序, 帮助我构建完成了这个 **DarkSHINE** 软件框架。同时也感谢之后大力推进这个项目的李数老师, 许金祥老师以及刘坤老师。

在我的整个博士生涯中, 许多学弟学妹也给我的学术研究和生活带来了帮助, 支持与欢乐。感谢陈翔, 莫岑, 卢泽加, 唐剑男, 胡舒阳, 朱逸凡, 沈秋平, 李京, 王子睿, 陈纪元, 王震, 刘丹宁, 刘齐斌, 朱栩量, 赵芷钰, 周柏宏, 刘康, 余典, 杨林, 刘汗青, 李家琳, 王曦, 张翔科, 吕濛, 何征霆, 洪江流, 郭俊超等各位同学。

同时, 也要感谢安玉晨, 冯硕和车思奇几位挚友, 在我认真科研工作的时候, 极力邀请我打游戏, 使我能够在紧张的科研工作之余, 放松心情, 享受生活。也要感谢我的女友周美辰, 在我法国研学的 2 年中度过了欢乐的时光。她的陪伴和鼓励, 使我能够在异国他乡, 不断追求自己的学术梦想。

在最后, 也要感谢我的父母和亲人, 他们的无条件的爱和支持是我在攻读博士学位过程中最坚实的后盾。在遇到挑战和困难时, 是他们给予了我无限的鼓励 and 力量, 让我能够坚持不懈地追求我的学术梦想。

List of Research Achievements

Scholarly paper

- [1] Chen, J., Chen, JY., Chen, JF. et al. Prospective study of light dark matter search with a newly proposed DarkSHINE experiment. *Sci. China Phys. Mech. Astron.* 66, 211062 (2023).
- [2] The ATLAS Collaboration. Constraints on the Higgs boson self-coupling from single- and double-Higgs production with the ATLAS detector using pp collisions at $\sqrt{s} = 13$ TeV. *Physics Letters B*, 843, 137745 (2023).
- [3] The ATLAS Collaboration. Search for non-resonant Higgs boson pair production in final states with leptons and photons in proton-proton collisions at $\sqrt{s} = 13$ TeV with the ATLAS detector. ANA-HDBS-2019-04 (to be submitted to XXXX).
- [4] The ATLAS Collaboration. Search for the non-resonant production of Higgs boson pairs via gluon fusion and vector-boson fusion in the $b\bar{b}\tau^+\tau^-$ final state in proton-proton collisions at $\sqrt{s} = 13$ TeV with the ATLAS detector. ANA-HDBS-2019-27 (to be submitted to XXXX).
- [5] Zhang, Y., et al. Search for Long-lived Particles at Future Lepton Colliders Using Deep Learning Techniques. (to be submitted to XXXX).